Magnetic properties of the unconventional superconductors epsilon-Fe, FeSe and Ca2CuO2Cl2 investigated by x-ray and neutron scattering

Blair Wilfred Lebert

THÈSE DE DOCTORAT
DE L'UNIVERSITÉ PIERRE ET MARIE CURIE

Spécialité : Physique

École doctorale : Physique et Chimie des Matériaux (ED 397)

réalisée

à l'Institut de minéralogie, de physique des matériaux et de cosmochimie

présentée par

Blair LEBERT

pour obtenir le grade de :

DOCTEUR DE L'UNIVERSITÉ PIERRE ET MARIE CURIE

Sujet de la thèse :

Propriétés magnétiques des supraconducteurs non conventionnels epsilon-Fe, FeSe, et $Ca_2CuO_2Cl_2$ étudiés par diffusion des rayons X et des neutrons

(Magnetic properties of the unconventional superconductors epsilon-Fe, FeSe and $Ca_2CuO_2Cl_2$ investigated by x-ray and neutron scattering)

soutenue le 26 janvier 2018

devant le jury composé de :

M.	Rudolf RÜFFER	Rapporteur
M.	Ricardo LOBO	Rapporteur
M.	Maurizio SACCHI	Examinateur
M^{me}	Marie-Aude MÉASSON	Examinatrice
M.	Matthieu LE TACON	Examinateur
M.	Stefan KLOTZ	Invité
M.	Jean-Pascal RUEFF	Co-directeur
M.	Matteo D'ASTUTO	Directeur

Acknowledgments

A thesis is not a thesis without a supervisor. In my case, I was lucky enough to have not one, but two, incredibly kind and knowledgeable supervisors with complementary expertise. The past three years I have had the pleasure of working under the guidance of Matteo d'Astuto and Jean-Pascal Rueff. I would often hear horror stories from other doctoral students about their supervisors and I would feel guilty that I was monopolizing two great supervisors. A joke I repeated often was that having two supervisors was like having divorced parents — if one of them said something I did not like, I would simply take the RER to/from Paris to hopefully get the response I wanted from the other! In all honesty, they gave me an incredible amount of freedom, yet they were always available whenever I had a question. They both even invited me into their homes to meet their wonderful families. I was never one for paperwork or planning very far ahead, so I am very grateful to them for helping me navigate the convoluted system of France+academia and search for post-doctoral opportunities. I look forward to working together in future collaborations.

I would like to thank Matteo in particular for his encouragement at times when I felt overwhelmed and the many, many coffees I owe him! He always was encouraging me to broaden my horizons and would have me participate in other experiments unrelated to my thesis such as an ARPES experiment with Zailan, an IXS experiment with Victor, and many INS experiments with him. A final thanks is warranted for the opportunities he presented to me to travel the world for many conferences, schools, and experiments.

I was a member of the DEMARE team run by Andrea Gauzzi at IMPMC. I would like to thank him for organizing our group meeting where we could share our results in an informal environment and practice our formal presentations, as well as all the other group members for their feedback and help including Christophe Bellin, Yannick Klein, Oleksandr Kurakevych, Yann Le Godec, William Sacks, Marine Verseils, William Sacks, Silvia Pandolfi, Gilbert Umugabe, and Hancheng Yang.

I was a member of the GALAXIES beamline at SOLEIL and I would like to thank everyone who has come and went which I had the pleasure of conversing with both professionally and personally including James Ablett, Denis Ceolin, Dominique Prieur, Julien Rault, Benedikt Lassalle, and Yuki Utsumi. I would like to thank James Ablett especially who was often the local contact on my experiments and taught me the intricacies of the GALAXIES beamline.

A local contact is often a thankless job, therefore I would like to rectify the situation and thank all the local contacts who have helped make my experiments a success, in particular Andi Barbour, Flora Yakhou, Alessandro Nicolaou, Satoshi Tsutsui, and John-Paul Castellan.

Hicham Moutaabbid, Benoît Baptiste, Ludovic Delbes, Keevin Béneut, Yoann Guarnelli,

Phillipe Rosier, and Dominique Prieur were all key in providing technical support.

The CCOC samples we used were made generously by Masaki Azuma, Ikuya Yamada, Hajime Yamamoto, and David Santos-Cottin, while Pierre Toulemonde and the team at Institut Néel supplied our FeSe crystals.

Much thanks is needed for Alain Polian, Gilles Le Marchand, and Stefan Klotz for teaching me the ropes of high pressure science.

I would like to thank Michele Casula for help with ab-initio calculations including many human and CPU hours! As well I would like to thank Amélie Juhin for stimulating conversations and Tommaso Gorni for taking on the mantle of the epsilon-iron calculations.

The complexity of condensed matter physics pales in comparison to French administration, therefore I cannot thank enough Danielle Radas and Ali Dhibi for their help with purchases and trips. I would also like to thank Nicolas Menguy for last minute signatures which really saved my behind.

Synchrotron and neutron experiments require a team and I was lucky to have worked in some great teams during my thesis which made the long hours seem like minutes. I will not attempt to list everyone who helped during experiments since I am sure I will miss many, however a few key members who come to mind are Mark Dean, Hu Miao, John-Paul Castellan, Yvan Sidis, Pierre Toulemonde, Victor Balédent, Simo Huotari, Mary Upton, Stefan Klotz, James Ablett, Alessandro Nicolaou, Kari Ruotsalainen, and Christophe Bellin.

All of my fellow doctoral students were a source of constant moral support. I would like to thank my office mates over the years: Johan, Mario, Wenyi, Andrea, Ali, and especially Eduardo for his amazing coffee. Without listing all of the students I would like to thank in particular Guilherme, David, Nadeja, Manoj, Aisha, and Eric. Marine and I had a special give (Python) and take (Fullprof) relationship which helped a lot during my thesis. Zailan and I worked together on a few experiments and it was a pleasure to learn from her. Finally a big shout-out goes to the denizens of Baker St. for many hopful discussions, especially the Old Man and the Princess.

Finally, I would like to thank all my friends and family for helping me relax and enjoy the finer things in life. My parents have supported and encouraged me on this journey from the very beginning. I will always remember conversations in front of a fire in Canada with my father, sipping Calvados and looking at the stars while we discuss life. My mother was never good with expressions or Scrabble, but her advice has always been spot-on (even if I only realized it years later). However, one piece of advice she likes to give I can now declare categorically false: “Nothing good ever happens after midnight”. To that effect, I present this thesis as exhibit A, and meeting the love of my life as exhibit B. Thank you for everything my love.

Contents

Résumé long

Ce résumé long synthétise la théorie, les techniques et les matériaux étudiés durant ma thèse, y compris les résultats. Un résumé court est également disponible sur la quatrième de couverture. Les références sont disponibles dans leurs sections respectives dans le texte principal.

Introduction

La découverte de supraconducteurs à fermions lourds en 1978 a bouleversé notre compréhension de la supraconductivité, car le comportement de ces matériaux ne pouvait s'expliquer par la théorie conventionnelle BCS de la supraconductivité médiée par les phonons. Initialement, ces supraconducteurs "non conventionnels" étaient simplement une curiosité scientifique en raison de leurs températures critiques extrêmement faibles (T_c). La découverte des cuprates a démontré au contraire l'importance de la supraconductivité non conventionnelle, inaugurant un nouvel "âge d'or" où la supraconductivité à température ambiante semblait à portée de main. Force est de constater que malgré trois décennies de recherche, la supraconductivité à température ambiante reste insaisissable. Cela est dû en partie au manque d'une théorie microscopique prédictive du ou des mécanisme(s) supraconducteur(s) dans les supraconducteurs non conventionnels. Néanmoins, de nombreuses propriétés et tendances des supraconducteurs non conventionnels ont été révélées. Un parfait exemple est la proximité omniprésente du magnétisme avec la supraconductivité dans toutes les classes de composés suggérant l'importance des fluctuations de spin dans le mécanisme d'appariement des électrons.

Dans cette thèse, j'ai étudié trois supraconducteurs non conventionnels différents : le cuprate à base d'éléments léger à haute T_c "cuprate" $Ca_2CuO_2Cl_2$, la phase ϵ-fer à haute pression, et β-FeSe. Bien que ceux-ci proviennent de trois familles différentes de supraconducteurs, ils présentent tous une phase magnétique à proximité de leur phase supraconductrice (Fig. 1). Le but de ma thèse était d'étudier le magnétisme dans ces matériaux, bien qu'une quantité surprenante d'informations sur la supraconductivité dans ces matériaux puisse être spéculée à partir de nos résultats.

La problématique

La question à laquelle nous voudrions vraiment répondre est : quel est le mécanisme microscopique derrière la supraconductivité non conventionnelle dans ces matériaux ? Cependant, cette question dépasse de loin la compréhension par le commun des mortels qui suit un programme de doctorat de trois ans. Nous aimerions donc répondre à la question : quel est l'état

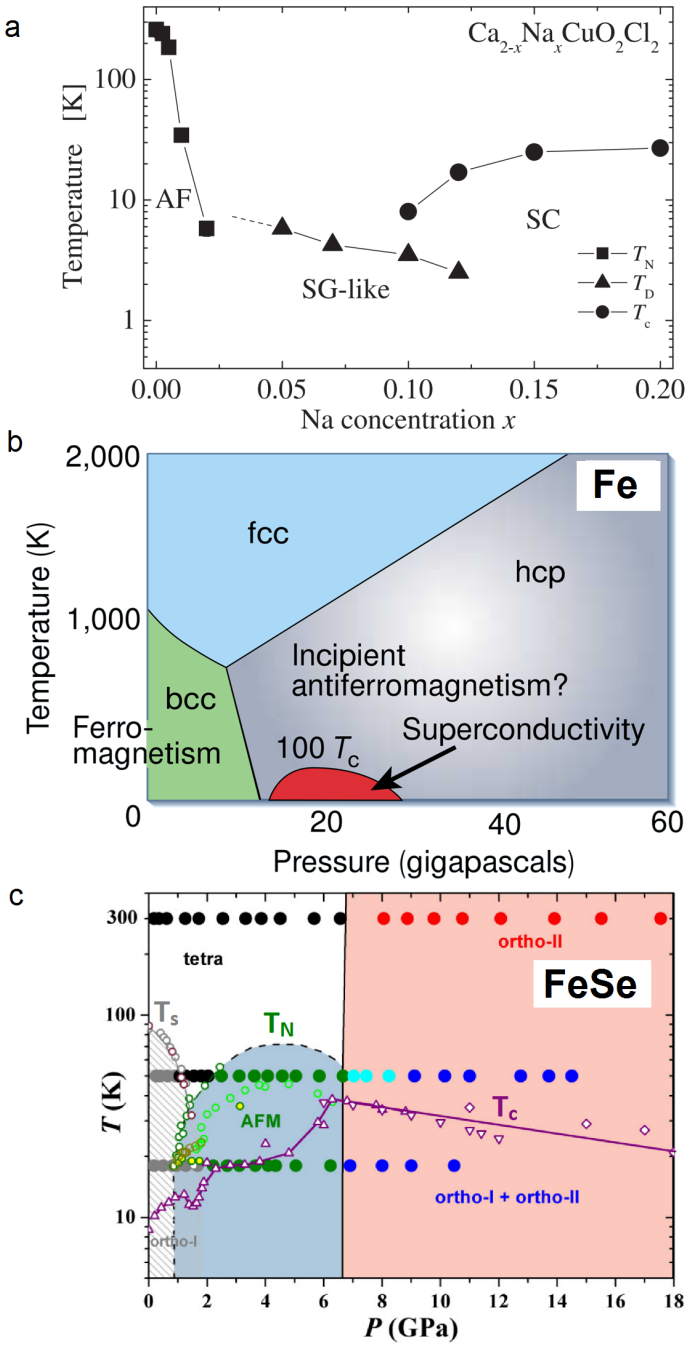

FIGURE 1 : Diagrammes de phase des trois supraconducteurs non conventionnels étudiés dans cette thèse. De haut en bas : (a) Le composé parent antiferromagnétique $Ca_2CuO_2Cl_2$ peut être dopé avec des trous par Na ce qui conduit à la disparition rapide de l'antiferromagnétisme 3D à longue portée (AF) et finalement à l'apparition de la supraconductivité (SC) [1]. (b) Le fer ferromagnétique subit une transition structurelle sous pression vers ϵ-fer dont l'état magnétique est fortement débattu, ainsi que son lien possible avec la supraconductivité dans cette région de pression [2]. (c) Le FeSe compressé montre une interaction étroite entre les ordres nématiques (T_s), magnétiques (T_N), supraconducteurs (T_c) [3]. Voir Chapitre III, IV, et V pour plus de détails sur le diagramme de phase de $Ca_2CuO_2Cl_2$, Fe, et FeSe respectivement.

magnétique de ces trois matériaux et comment se rapporte-t-il à la supraconductivité ? Plus précisément, nous voulons répondre aux questions suivantes :

- Comment les excitations magnétiques, qui sont supposées jouer un rôle important dans la supraconductivité, varient-elles à travers le diagramme de phase du système $Ca_2CuO_2Cl_2$ par rapport aux autres cuprates de haute T_c ?
- Quel est l'état magnétique de la phase ϵ-fer à haute pression et a-t-il un lien avec sa supraconductivité ?
- Quel est le lien entre les ordres structurels, magnétiques et supraconducteurs de β-FeSe pendant sa transition structurelle à haute pression ?

Concepts théoriques

Un bref rappel théorique est traité dans le Chapitre I. Les supraconducteurs non conventionnels appartiennent à la classe des "matériaux quantiques" qui présentent des phénomènes émergents remarquables. Ces matériaux ne peuvent pas être compris en utilisant l'approche monoélectronique traditionnelle puisque la corrélation entre les électrons est non négligeable et conduit à un comportement collectif imprévisible. Un exemple par excellence de ce comportement est la supraconductivité, où les électrons s'attirent, plutôt que de se repousser, pour se condenser dans un état superfluide. Cet état supraconducteur a une résistivité électrique nulle en dessous d'une certaine température critique (T_c), tant que la densité de courant électrique et le champ magnétique externe sont également inférieurs à une limite critique. De même, les supraconducteurs expulsent les champs magnétiques internes de leur volume lorsqu'ils sont refroidis au-dessous de T_c par l'effet dit de Meissner. Le mécanisme microscopique des supraconducteurs classiques a été codifié dans la théorie de Bardeen, Cooper et Schrieffer (BCS) dans laquelle une interaction arbitrairement forte entre les électrons provoque la formation par les électrons de "paires de Cooper" quasi-bosoniques qui se condensent dans un état superfluide. La théorie BCS (et ses extensions) expliquait très bien les matériaux supraconducteurs connus de l'époque, principalement des métaux purs et des alliages, où les phonons médiaient l'appariement de Cooper en fournissant la force d'attraction entre les électrons.

Les supraconducteurs non conventionnels ne peuvent pas être expliqués par les théories classiques de type BCS / BCS médiées par des phonons. La corrélation électronique dans les matériaux quantiques conduit à d'autres comportements collectifs que la supraconductivité, comme le magnétisme. Il n'est donc pas complètement aberrant de trouver le magnétisme à proximité de la supraconductivité, même si dans les supraconducteurs classiques, les impuretés magnétiques détruisent la supraconductivité. Néanmoins, l'ordre magnétique est connu pour concurrencer la supraconductivité, même dans les supraconducteurs non conventionnels. Cependant, comme nous le montre le diagramme de phase sous pression ou dopage, ces matériaux présentent souvent des régions avec des états fondamentaux magnétiques (et non magnétiques) dégénérés, où les fluctuations magnétiques quantiques associées joueraient un rôle essentiel dans l'appariement de Cooper. Dans les supraconducteurs à fermions lourds, la compétition entre l'effet Kondo et l'interaction RKKY à basses températures crée un point critique quantique où les états fondamentaux magnétiques et non magnétiques sont dégénérés, induisant ainsi des fluctuations de spin quantique impliquées dans leur supraconductivité.

Certains de ces composés sont ferromagnétiques, non sans rappeler le diagramme de phase du fer métallique. Les supraconducteurs à base d'oxyde de cuivre (cuprate) à haute T_c ont également des fluctuations de spin comme l'un des principaux candidats pour la médiation par paire de Cooper. Les cuprates sont des structures quasi-2D avec un ou plusieurs plans CuO_2 séparés par une couche de réservoir de charge utilisée pour le dopage. Les composés parents non dopés sont antiferromagnétiques avec un fort échange intra-planaire (super-échange Cu-O-Cu) et un faible échange inter-planaire. L'ordre antiferromagnétique 3D est rapidement détruit lors du dopage, cependant de fortes corrélations antiferromagnétiques demeurent dans le ou les plans CuO_2 où la supraconductivité est supposée se manifester. Le groupe le plus récent de supraconducteurs non conventionnels est celui des supraconducteurs à base de Fe (FeSC). L'existence de la supraconductivité dans ces composés est, à première vue, surprenante en raison du puissant magnétisme du fer qui devrait déstabiliser la supraconductivité. Les FeSC sont aussi parfois appelés pnictides de fer (avec P ou As) ou chalcogénures (avec S, Se ou Te). Les FeSC ont une structure quasi-2D similaire aux cuprates avec des couches de FeSe, siège de la supraconductivité, séparées par des couches de réservoir de charge. Les FeSC ont typiquement des T_c inférieurs aux cuprates car ils ont un ordre antiferromagnétique coexistant et en concurrence avec la supraconductivité. Il existe un débat sur le mécanisme dominant derrière l'appariement de Cooper dans les FeSC entre les fluctuations de spin et les fluctuations orbitales dues à la nématicité.

Techniques expérimentales

Les principales techniques expérimentales que j'ai utilisées sont expliquées dans le chapitre II. Ma thèse portait sur l'utilisation de sondes à neutrons et à rayons X pour étudier les propriétés électroniques, magnétiques et structurelles des matériaux. Ces expériences, en particulier sous pression, sont irréalisables ou impossibles en laboratoire. Par conséquent, les expériences utilisent des installations de rayons X ou de neutrons. J'ai utilisé des sources de rayonnement synchrotron, principalement SOLEIL et ESRF, pour réaliser les expériences de diffusion de rayons X décrites ci-dessous. Les sources synchrotron produisent des faisceaux de rayons X très brillants basés sur le principe qu'une particule chargée (les électrons habituellement pour les synchrotrons, parfois les positrons) émet un rayonnement électromagnétique lorsqu'elle est accélérée. Les neutrons sont produits avec une source de spallation ou de réacteur. Nous avons utilisé une source de réacteur nucléaire (ILL) qui produit de grandes quantités de neutrons pendant la fission nucléaire. Ces installations à grande échelle, et leurs instruments associés, ou "stations expérimentales", sont des outils importants pour étudier les systèmes de matière condensée, car ils fournissent des informations qui sont impossibles avec des expériences en laboratoire. Il n'y a jamais eu de période plus excitante pour ces études avec le nombre croissant d'établissements dans le monde, l'ouverture de nouvelles voies de recherche à mesure que les instruments atteignent des résolutions record et la possibilité d'études extrêmement résolues dans le temps avec développement de lasers à électrons libres à rayons X (le successeur des synchrotrons).

Techniques à haute pression

La haute pression est un paramètre externe très utile pour ajuster les degrés de liberté magnétique, structurel et électronique puisqu'elle est "propre", en ce sens que, contrairement

au dopage ou à la température, elle n'introduit pas de désordre dans le système. Le principe de la technique est l'analogie classique des hauts-talons : on applique une pression modérée sur une grande surface dont la force est transmise à travers une matière dure à une petite surface, amplifiant ainsi la pression. Dans cette thèse, nous avons utilisé uniquement des cellules de pression uniaxiales (cellules à enclumes diamants) qui sont constituées de deux diamants opposés servant à appliquer la pression sur l'échantillon. Pour atteindre la haute pression, nous avons utilisé des diamants monocristallins et des diamants frittés pour des études de haute pression de rayons X et de neutrons respectivement. Deux autres composants clés des cellules sont les joints, qui empêchent l'extrusion de l'échantillon à l'extérieur de la zone de haute pression, et le milieu transmetteur de pression, qui contribue à fournir un environnement (quasi)-hydrostatique.

Spectroscopie d'absorption des rayons X (XAS)

La spectroscopie d'absorption des rayons X est une technique qui implique l'excitation d'un électron de coeur dans un état de valence vide. Elle fournit des informations structurelles et électroniques sur l'environnement local de l'atome cible. XAS est effectué en mesurant la transmission à travers un échantillon tout en faisant varier l'énergie incidente à travers un "seuil d'absorption", qui correspond à l'énergie minimale pour ioniser les électrons de cœur d'un niveau particulier. Une autre façon de mesurer indirectement l'absorption est de mesurer l'intensité de fluorescence (totale ou partielle) ou l'intensité des électrons qui varie avec l'absorption. Nous avons utilisé XAS pour étudier le fer dans β-FeSe en utilisant le rendement de fluorescence partielle, ou PFY-XAS au seuil K du Fe. Il s'agit d'une technique de photon-in / photon-out et est donc compatible avec des études de haute pression puisque le seuil K d'absorption de Fe est $\approx$ 7112 eV. Nous mesurons le PFY-XAS en mesurant l'émission (voir XES ci-dessous) Fe Kβ ($3p \rightarrow 1s$), ce qui conduit à un effet d'amincissement spectral dû au trou moins profond de $3p$ dans l'état final par rapport au niveau plus profond de $1s$. La méthode est également connus sous le nom HERFD. XAS, de même que XES et RIXS, discutés ci-dessous, ont l'avantage d'être sensibles à l'état massif et d'être sélectifs des éléments et sites sondés.

Spectroscopie d'émission des rayons X (XES)

La spectroscopie d'émission de rayons X, également connue sous le nom de fluorescence X, consiste à exciter un électron de coeur dans le continuum par effet des photons X incidents, puis de mesurer les rayons X émis lors de la désexcitation radiative du système. Nous utilisons un type spécifique de XES appelé Fe Kβ XES pour étudier le Fe et le FeSe comprimés. Les rayons X incidents et émis en Fe Kβ XES sont tous les deux des rayons X durs, donc applicables dans des études à haute pression. L'émission Kβ ($3p \rightarrow 1s$) du fer a une ligne principale (K$\beta_{1,3}$) ainsi qu'un satellite à plus faible énergie. Ce satellite, connu sous le nom de Kβ', est sensible au moment angulaire de spin $3d$ et peut donc être utilisé pour suivre l'état de spin ou déterminer semi-quantitativement le moment magnétique.

Diffusion de rayons X inélastique résonante (RIXS)

La diffusion inélastique résonante des rayons X est une autre technique de photon-in photon-out qui peut être considérée comme XAS, excitation d'un électron de coeur vers un état in-

occupé, suivie par XES, émission d'un rayons X. Cependant, la situation est plus complexe puisque les deux processus sont cohérents, ce qui conduit à une section efficace compliquée où l'état intermédiaire peut créer des excitations intrinsèques dans le matériau. Ces excitations peuvent être sondées avec RIXS en mesurant la variation de l'énergie et de la quantité de mouvement du rayon émis. L'utilisation de la résonance peut considérablement augmenter la section efficace inélastique de plusieurs ordres de grandeur. La technique RIXS principalement utilisée dans cette thèse est la méthode directe RIXS au seuil Cu L_3 ($2p_{3/2}$) pour étudier les excitations magnétiques dans le système $Ca_2CuO_2Cl_2$. Dans les cuprates, la configuration électronique des ions Cu est $3d^9$ de sorte qu'il n'y a qu'un seul trou dans le niveau $3d_{x^2-y^2}$. Dans le processus RIXS au seuil L_3 du Cu, un électron $2p_{3/2}$ est excité vers les états $3d$, créant un état intermédiaire hautement énergétique. Le couplage spin-orbite fort du trou de cœur permet l'échange du moment cinétique du photon avec le moment angulaire de rotation du trou dans l'état final. Ceci induit une excitation de spin (spin flip) qui se propage à travers le réseau par super-échange.

Diffraction de neutrons sur poudre (NPD)

La diffraction des neutrons peut être utilisée pour déterminer la structure nucléaire et magnétique des matériaux. La technique utilise des neutrons thermiques qui ont une longueur d'onde de Broglie comparable à l'espacement atomique dans la matière condensée. En utilisant la loi de Bragg, nous pouvons déterminer l'espacement du réseau. Les neutrons portent un spin et interagissent directement avec les moments magnétiques et par conséquent NPD a des pics magnétiques de Bragg d'une intensité comparable à celle des pics nucléaires (contrairement à la diffusion magnétique des rayons X). NPD est particulièrement adaptée pour rechercher l'ordre antiferromagnétique puisque les supercellules antiferromagnétiques impliquent des pics magnétiques de Bragg loin des pics nucléaires de Bragg vers des angles de diffusion inférieurs où le facteur de forme magnétique est le plus grand (en raison de l'étendue du nuage d'électrons). Nous avons utilisé la diffraction de neutrons sur poudre pour rechercher l'ordre antiferromagnétique dans Fe et FeSe sous pression.

Magnétisme dans les supraconducteurs non conventionnels

Les trois matériaux que j'ai étudiés seront maintenant présentés avec leurs principaux résultats. Celles-ci sont traitées plus en détail dans le chapitre III, IV, et V pour $Ca_2CuO_2Cl_2$, ϵ-fer, et FeSe respectivement.

$Ca_2CuO_2Cl_2$

La nature corrélée des électrons dans les cuprates rend extrêmement complexe la compréhension des mécanismes de la supraconductivité. Il y a une surabondance de théories prétendant expliquer le mécanisme, mais elles ne peuvent pas expliquer tous les résultats expérimentaux disponibles, probablement parce qu'elles s'appuient sur des cadres simplifiés pour traiter la corrélation électronique. Une solution consiste à utiliser des calculs à plusieurs corps, qui sont rendus possibles grâce aux progrès constants des capacités de calculs suivant la loi de Moore. Dans ce cadre, on aimerait idéalement étudier le composé le plus simple qui capture encore toute la physique pertinente des cuprates.

C'est dans ce contexte que nous avons choisi d'étudier le système oxychlorure de cuivre $Ca_2CuO_2Cl_2$, présenté dans le chapitre III. Ce système peut être dopé avec Na, K ou des lacunes et présente les mêmes propriétés que celles observées dans les cuprates (Fig. 1). La raison peut être observée sur la structure de la figure Fig. 2 : le $Ca_2CuO_2Cl_2$ système a la même structure quasi-2D de couche que les cuprates avec des plans CuO_2 séparés par des couches de réservoir de charge. Les oxygènes apicaux des cuprates sont remplacés par du chlore, ce qui fait de ce système un oxychlorure de cuivre, mais les propriétés magnétiques et supraconductrices importantes des cuprates proviennent des plans de CuO_2 qui restent inchangés. Ce système offre de nombreux avantages aux calculs ab-initio : il a une structure tétragonale simple sans distorsions orthorhombiques du réseau ou des plans de CuO_2, et ce à toutes les températures et dopages ; La présence d'éléments légers simplifie les calculs en raison du nombre réduit d'électrons ; et, il a un chlore apical qui donne aux plans CuO_2 une nature encore plus quasi-2D.

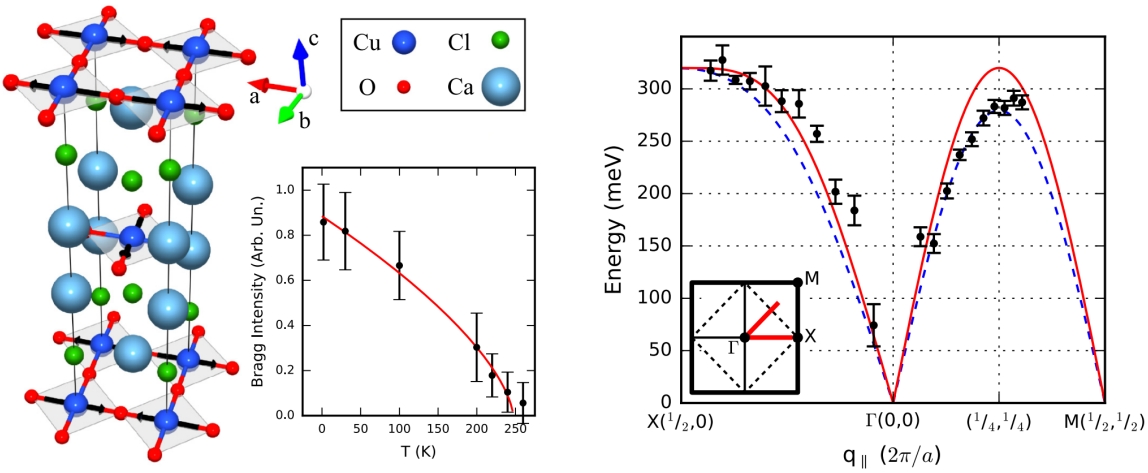

FIGURE 2 : (À gauche) Structure cristalline tétragonale de $Ca_2CuO_2Cl_2$. La coordination carrée du cuivre avec ses quatre ions oxygène les plus proches voisins dans les plans CuO_2 est montrée. Les ions chlore sont situés dans le site apical au-dessus et en dessous du cuivre. L'encart montre nos données de diffraction des neutrons mesurant la température Néel. (À droite) Nos résultats de dispersion de magnons pour $Ca_2CuO_2Cl_2$ mesurés en utilisant RIXS au seuil L_3 du Cu. [4]. La ligne rouge continue est un calcul pour un modèle de Heisenberg 2D spin-1/2 classique avec un échange de plus proche voisin, et la ligne bleue en pointillés est un calcul incluant d'autres termes d'échange. L'encart montre la zone 2D Brillouin montrant les points de haute symétrie. La première limite de la zone Brillouin est représentée par un carré noir épais, tandis que la limite de la zone Brillouin magnétique est représentée par une ligne pointillée. La région où nous avons mesuré est représentée par deux lignes rouges épaisses le long de Γ-X and Γ-M.

L'étude principale sur $Ca_2CuO_2Cl_2$ dans cette thèse (Article 1, Sec. III.3) est la mesure de la dispersion des ondes de spin (magnons dans l'approche de seconde quantification) dans le composé parent non dopé $Ca_2CuO_2Cl_2$. Le composé non dopé, comme dans tous les cuprates, est un antiferromagnétique 2D spin-1/2. L'étude de ce composé d'origine est importante pour caractériser les paramètres de superéchange entre les spins du Cu, qui

varie peu avec le dopage et est un ingrédient important dans de nombreuses théories sur sa supraconductivité. Nos résultats principaux sont résumés dans la figure Fig. 2 qui montre la dispersion de magnons dans $Ca_2CuO_2Cl_2$ mesurée le long des deux directions de haute symétrie en utilisant RIXS au seuil L_3 du Cu. A notre connaissance, c'est la première étude de la dispersion de magnons de $Ca_2CuO_2Cl_2$, ou même de l'échange de plus proche voisin J. Nous avons extrait $J = 135$ meV en utilisant un modèle Heisenberg 2D plus proche voisin (ligne rouge), mais il existe une différence d'énergie claire entre les deux limites de zone, ce qui indique la nécessité d'inclure d'autres termes d'échange. L'inclusion d'autres termes d'échange paramétrés avec un modèle de Hubbard à 1 bande donne un meilleur ajustement pour les énergies de limite de zone (ligne pointillée bleue) mais change très peu l'estimation de super-échange, $J = 141$ meV. Les résultats d'une étude à haute résolution de cette dispersion sont présentés dans Sec. III.4 où notre modèle s'adapte beaucoup mieux en raison de la résolution améliorée et de la préparation d'échantillons.

$Ca_2CuO_2Cl_2$ est extrêmement hygroscopique et seulement disponible en petits monocristaux. Nos résultats montrent la puissance de RIXS au seuil L_3 du Cu pour étudier les excitations de spin dans les cuprates, car des mesures similaires utilisant la diffusion inélastique des neutrons seraient pratiquement impossibles en raison de la faible masse (et de la difficulté de co-alignement des cristaux hygroscopiques) et des neutrons épithermaux nécessaires pour cette gamme d'énergie. En Sec. III.4 je présente aussi très brièvement une exploitation plus poussée de cette technique pour mesurer la dépendance avec le dopage des excitations magnétiques dans le système $Ca_2CuO_2Cl_2$. De plus, des résultats préliminaires sur le bimagnon utilisant différentes techniques et une recherche de l'ordre de chargement dans $Ca_2CuO_2Cl_2$ sont brièvement présentés. Dans l'ensemble, nous avons travaillé pour fournir des points de référence pour les futurs calculs à plusieurs corps, afin de combler enfin le fossé entre théorie et expérience dans les cuprates. L'accord avec d'autres systèmes de cuprates est prometteur car il souligne que $Ca_2CuO_2Cl_2$ est un bon modèle pour les cuprates.

Fer sous pression

Le fer a longtemps été un matériau de prédilection de la communauté des hautes pressions en raison de sa signification géophysique. En effet, le fer est l'un des rares matériaux étudiés à de telles pressions et températures extrêmes pour simuler les conditions du cœur de la Terre. Les études sur le fer repoussent constamment les limites de la physique de la haute pression, mais la région de basse pression de son diagramme de phase reste mystérieuse. L'état magnétique de la région de basse pression de ϵ-fer a été étudié minutieusement avec la théorie et l'expérience, mais les résultats sont souvent paradoxaux et font l'objet de débats depuis des décennies. La découverte de la supraconductivité non conventionnelle dans cette région de pression a encore souligné la nécessité de découvrir la nature magnétique de ϵ-fer, ce qui était le but de notre étude dans le chapitre IV.

Sous la compression, le fer subit une transition structurelle d'une structure cubique centrée (bcc) vers une structure hexagonale compacte (hcp), les phases α et ϵ respectivement. Le ferromagnétisme bien connu du fer disparaît aussi pendant la transition structurale mais l'état magnétique de ϵ-fer n'est pas clair. La spectroscopie Mössbauer à basse température ne détecte aucun magnétisme dans ϵ-fer, mais un pic Raman anormal suggère une symétrie brisée due au magnétisme. De plus, les calculs de premier principe prédisent de façon constante un état fondamental antiferromagnétique et les mesures de spectroscopie d'émis-

sion de rayons X trouvent un moment magnétique après la transition α-ϵ qu'ils appellent un "reste". Il existe deux théories concurrentes pour décrire ces résultats paradoxaux : un état antiferromagnétique spécial appelé afmII et les fluctuations de spin. La première est compatible avec les mesures de Mössbauer en raison d'un champ magnétique hyperfin fortuitement petit et explique aussi le mode anormal de Raman. La structure afmII et la dépendance de la pression prédite pour le moment magnétique sont montrées sur la figure Fig. 3. Cette dernière explication des fluctuations de spin est également intéressante car des études théoriques ont montré qu'elles sont nécessaires pour expliquer le comportement du dôme supraconducteur dans ϵ-fer.

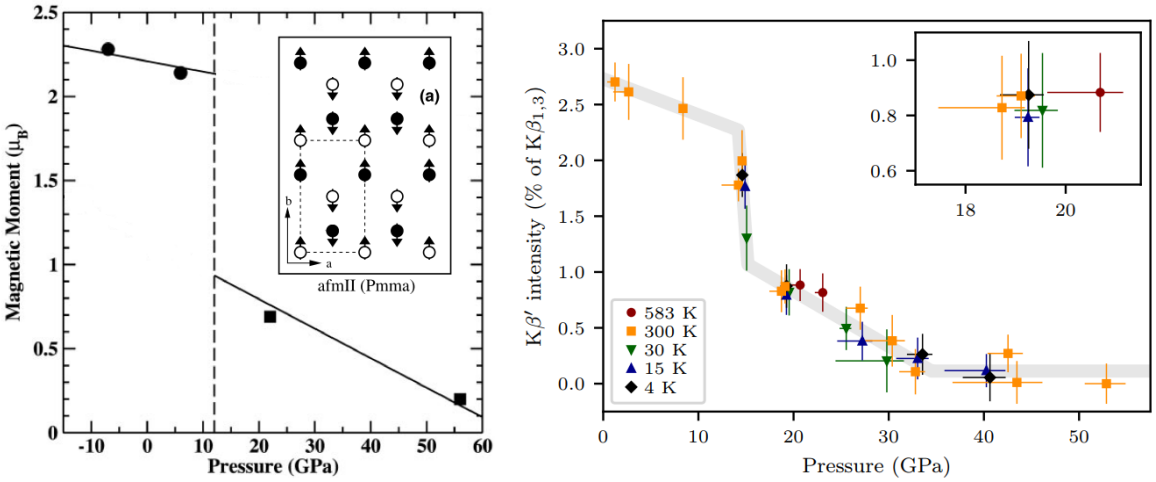

FIGURE 3 : (À gauche) Le moment magnétique prédit de l'état ϵ-fer, dont la configuration est montrée dans l'encadré [5, 6]. Les atomes à z = 1/4 (3/4) sont affichés avec un symbole fin (plein) et les flèches indiquent spin up et spin down (À droite) Dépendance de la pression de l'intensité du satellite par spectroscopie d'émission Kβ. L'intensité Kβ' sert comme une approximation semi-quantitative du moment angulaire de spin $3d$ qui est approximativement le moment magnétique dans le fer dû au gel du moment orbital. L'encart montre un zoom de la région dense autour de 20 GPa. Les lignes grises sont des guides pour l'oeil.

Dans cette thèse, je présente une étude XES & NPD du fer comprimé afin d'étudier ces deux explications possibles (Article 2, Sec. IV.2). Nous avons effectué Kβ XES avec un amélioration des statistiques, de milieu transmetteur de pression, et du traitement des données. Les résultats sont montrés sur la figure Fig. 3 où nous pouvons clairement voir un changement brusque de l'intensité du satellite à la transition structurelle. Par conséquent, nous pouvons clairement identifier que le moment magnétique dans cette région est intrinsèque à la phase ϵ, et n'est pas un vestige de la phase α. Le moment magnétique disparaît au-dessus de 30 GPa, soit la même pression que la supraconductivité, ce qui concorde avec l'existence de fluctuations de spin qui induisent la supraconductivité dans ϵ-fer. Néanmoins, la tendance qualitative entre les prédictions afmII et nos résultats est frappante. Nous avons étudié l'existence de l'état afmII, et plus généralement de tout état antiferromagnétique statique, en utilisant la diffraction de neutrons sur poudre à des conditions simultanées haute pression / basse température (technique décrite dans l'article 4, Sec. A). Nous mettons une limite supérieure sur le moment magnétique dans une phase hypothétique afmII qui est

quatre fois plus faible que les prédictions ab-initio et l'estimation du moment à partir de nos résultats XES.

Nos résultats argumentent fortement contre l'existence d'un afmII statique dans ϵ-fer, mais à la fin peut-être les deux explications, afmII statique et des fluctuations de spin, sont-elles partiellement correctes ? Dans Sec. IV.3, je mentionne très brièvement quelques calculs théoriques sur lesquels nous travaillons et qui pointent vers de nombreux états fondamentaux dégénérés de type afmII en raison de la frustration géométrique du réseau hcp à l'antiferromagnétisme. Ces états dégénérés induiraient des fluctuations de spin quantique, que nous trouvons en fait varier non seulement dans la direction, mais aussi dans l'intensité. Nos résultats montrent que la similitude dans les diagrammes de phase du fer et d'autres supraconducteurs ferromagnétiques (typiquement des supraconducteurs à fermions lourds) n'est que superficielle. Le ferromagnétisme du fer est perdu pendant la transition vers ϵ-fer et il ne joue aucun rôle dans la supraconductivité de ϵ-fer. Cependant, lors des mesures du dôme supraconducteur, des restes ferriques ferromagnétiques α-fer juste après la transition pourraient être à l'origine de la diminution de T_c sur le côté gauche du dôme.

FeSe sous pression

FeSe a deux polymorphes stables aux conditions ambiantes, cependant nous ne nous intéressons qu'au polymorphe tétragonal β-FeSe, que nous appelons simplement FeSe, puisqu'il appartient à la famille des supraconducteurs à base de Fe (FeSC). FeSe a une structure simple composée uniquement de couches quasi-2D FeSe (Fig. 4). C'est aussi l'un des rares FeSC où la supraconductivité existe dans des conditions ambiantes sans ordre antiferromagnétique à longue portée. Ces deux caractéristiques font de FeSe un composé unique pour étudier la supraconductivité dans les FeSCs. La T_c de FeSe est plutôt modeste (7–8 K) mais elle est augmentée en utilisant des monocouches, par effet d'intercalation, et / ou pression. Le diagramme de phase sous pression (Fig. 1) montre la relation complexe entre les ordres magnétiques, nématiques et supraconducteurs. Dans le chapitre V, notre étude du FeSe sous pression est présentée où nous essayons de démêler ces ordres entrelacés.

La température critique du FeSe augmente de quatre fois lorsqu'il est comprimé et son évolution est non monotone. Il semble y avoir une anticorrélation entre les températures Néel (T_N) et critique (T_c) qui crée deux anomalies T_c distinctes autour de 1–2 GPa and 6–8 GPa. La première anomalie T_c a été étudiée en détail, tandis que la dernière anomalie T_c l'est moins. Dans cette région de pression de 6–8 GPa, il y a aussi une transition structurelle irréversible, de premier ordre, de la phase ortho-I à la phase ortho-II (Fig. 4). La phase ortho-I est pseudo-tétragonale et les atomes de Fe ont une coordination T_d, c'est-à-dire qu'il y a juste une légère distorsion orthorhombique dans le plan ab induite par la némacité dans FeSe sous T_s et T_N. D'autre part, la structure ortho-II forme un réseau 3D où les atomes de Fe ont une coordination O_h. La région de pression de l'anomalie T_c simultanée à haute pression, la diminution de T_N, et la transition ortho-I à ortho-II ont été au centre de cette thèse (article 3, Sec. V.2). Comme dans le fer, nous avons utilisé Kβ XES et NPD pour étudier les changements électroniques et magnétiques durant cette transition, mais nous avons aussi effectué des mesures XAS pour étudier les changements structurels et électroniques. Les résultats sont montrés sur la Fig. 4 où l'on peut voir les signaux XAS A et XES tous deux changer radicalement autour de 7 GPa. Le signal XAS A provient du pré-pic qui change avec la coordination de l'atome de Fe, ce qui nous permet de suivre la transition structurelle attendue.

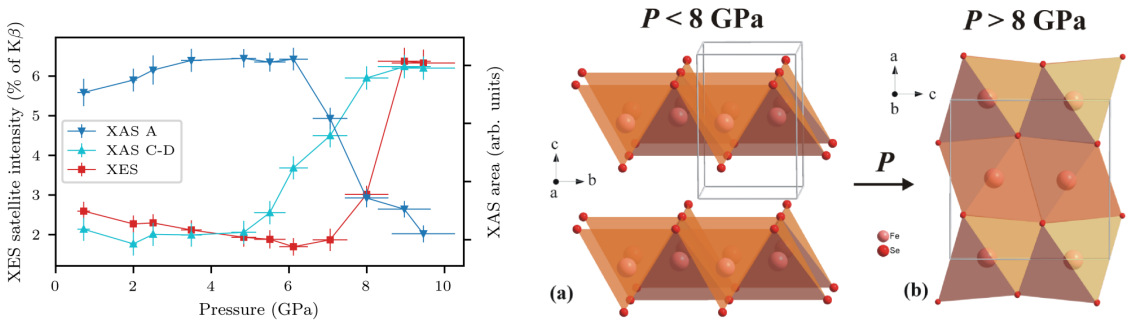

FIGURE 4 : (À gauche) La dépendance en pression des spectres d'émission de rayons X (XES) et absorption de rayons X (XAS) dans FeSe [7]. XAS A est la zone du pré-pic et XAS C-D est la zone située entre la caractéristique C-D dans la région proche du bord (voir la Sec. V.2). (À droite) Phases basse pression et haute pression de FeSe [3]. (a) La phase basse pression a une structure tétragonale de type PbO ($P4/nmm$) et est composée de couches de tétraèdres de $FeSe_4$ partagés par les bords. La phase ortho-I basse pression et basse température ($Cmma$) est similaire à l'exception d'une légère distorsion orthorhombique dans le plan ab. (b) La structure ortho-II de type MnP à haute pression ($Pnma$) est composée de chaînes d'octaèdres $FeSe_6$ à faces partagées. (Notez le changement d'axes entre les deux figures)

Le signal XES montre un comportement complètement inattendu allant à un état bas-spin à haut-spin. Une simulation des spectres XAS de premier principe confirme notre attribution d'un état de spin élevé à l'ortho-II. La transition structurelle et magnétique semble être concomitante. La stabilité d'un état de bas spin avec coordination T_d est probablement due aux effets de corrélation dépendant de la bande récemment prédits dans les supraconducteurs à base de Fe. Une transition bas-spin à haut-spin sous pression est extraordinaire car l'augmentation de la bande passante sous pression induit généralement la transition inverse. Cependant, il n'est peut-être pas si surprenant en raison du changement structurel drastique quasi-2D à 3D entre ortho-I et ortho-II. Ceci est considéré plus en détail dans Sec. V.3. Dans cette section, je discute également de l'augmentation observée dans la région proche du bord des spectres XAS (XAS C-D) avant la transition à 5 GPa, ce qui correspond au début de la dernière augmentation de T_c. Je spécule que la phase ortho-II à haut spin coexiste avec la phase ortho-I supraconductrice à l'échelle nanométrique. Comme dans le $K_xFe_{2-y}Se_2$ intercalé, les transitions entre ces phases à haut spin et à bas spin créent des fluctuations de spin qui peuvent augmenter la supraconductivité. Ceci pourrait induire une augmentation de T_c quand il y a une minorité d'ortho-II, cependant alors que les domaines ortho-II deviennent majoritaires, les mesures de transport sont dominées par la diffusion électronique due aux différents domaines et T_c est difficile à déterminer.

Nous avons également effectué des mesures de diffraction de poudre de neutrons sur FeSe, qui sont discutées dans les informations supplémentaires de l'article 3 (Sec. V.2). Malheureusement, nous n'avons pas pu mesurer une transition ortho-I à ortho-II claire afin de rechercher l'ordre antiferromagnétique en ortho-II. La raison pour laquelle je spécule dans Sec.V.3 est probablement due à l'utilisation de poudre de FeSe au lieu de monocristaux. Néanmoins, nos mesures NPD dans la phase ortho-I donnent des limites supérieures plus fortes sur le

moment magnétique pour les deux principales configurations afm proposées. Nous trouvons qu'une configuration afm colinéaire de type bande est plus probable, comme dans d'autres supraconducteurs FeSC à base de FeAs, plutôt qu'une configuration afm bicollinéaire.

Conclusions

Je présente une variété de mesures expérimentales dans cette thèse, principalement liées au magnétisme, appliquées à trois supraconducteurs non conventionnels complètement différents. Mes résultats soulignent la connexion intime entre le magnétisme et la supraconductivité qui semble omniprésente dans les supraconducteurs non conventionnels. Les principaux résultats de ces études sont :

- La dispersion de magnons dans le composé parent non dopé $Ca_2CuO_2Cl_2$ est mesurée et nous estimons le paramètre de superéchange $J = 141$ meV. Nos mesures à haute résolution sont bien adaptées à d'autres termes d'échange paramétrés par un modèle Hubbard à une bande.

- Nous fournissons un un jeu de données caractérisant les excitations magnétiques dans le système $Ca_2CuO_2Cl_2$ utiles pour la comparaison avec de futurs calculs à plusieurs corps. Ces résultats comprennent la dépendance au dopage du paramagnon et une étude approfondie du bimagnon en utilisant une multitude de techniques. Nous trouvons également les premiers indices d'ordre de charge dans l'état massif dans le système $Ca_2CuO_2Cl_2$.

- Nos résultats de diffraction de neutron sur poudre sur ϵ-fer réfute l'existence d'un ordre afmII statique. Par conséquent, nous trouvons que des fluctuations de spin doivent exister afin d'expliquer les résultats expérimentaux précédents.

- Le moment magnétique de ϵ-fer estimé par spectroscopie d'émission de rayons X tend vers zéro entre 30–40 GPa, la même région où l'état supraconducteur disparaît. Ceci supporte fortement les théories prédites précédentes de l'appariement de Cooper médiées par les fluctuations de spin dans ϵ-fer.

- Nos calculs préliminaires suggèrent que les fluctuations de spin apparaissent dans ϵ-fer en raison des états fondamentaux dégénérés dans le réseau hcp géométriquement frustré.

- Nous trouvons une transition impromptue de l'état bas spin à haut spin dans FeSe associée à sa transition structurelle. L'origine de cet effet inhabituel est bien expliqué par les effets de corrélation dépendant de la bande récemment prédits dans les supraconducteurs à base de Fe.

- Une signature spectroscopique de l'augmentation de T_c dans FeSe autour de 5 GPa est trouvée et doit être étudiée plus loin. Je spécule que la séparation à l'échelle nanométrique des états de spin faible et élevé induit des fluctuations de spin qui augmentent le T_c dans cette région.

- Les limites supérieures que nous avons fixées pour le moment magnétique de différentes configurations antiferromagnétiques dans la phase ortho-I de FeSe sont en accord avec

un arrangement colinéaire de type bande qui est commun avec d'autres supraconducteurs à base de FeSe.

Long abstract

This long abstract summarizes the theory, techniques, and materials studied in my thesis, including the results. A short abstract is also available on the back cover. References are available in their respective sections in the main text.

Introduction

The discovery of heavy fermion superconductors in 1978 was shocking since they were not explained by conventional phonon-mediated BCS theory. Initially, these "unconventional" superconductors were simply a scientific curiosity due to their unfortunately low critical temperatures (T_c). This notion was quickly overthrown with the discovery of high-T_c cuprate superconductors which ushered in a golden age where room-temperature superconductivity seemed just within reach. On the contrary, room-temperature superconductivity remains elusive as ever, despite three decades of research, partly since we lack predictive power from a microscopic theory of the superconducting mechanism(s) in unconventional superconductors. Nonetheless, many properties and trends of unconventional superconductors have been revealed. One prime example is the ubiquitous proximity of magnetism with superconductivity in all classes, from organic to iron-based, suggesting the importance of spin fluctuations in the pairing mechanism.

In this thesis I study three different unconventional superconductors: the light-element high-T_c "cuprate" $Ca_2CuO_2Cl_2$ system, high-pressure ϵ-iron, and β-FeSe. Although these are from three different families of superconductors, they all show magnetism in proximity to their superconducting phase (Fig. 5). The purpose of my thesis was to study magnetism in these materials, although a surprising amount of information about superconductivity in these materials can be speculated from our results.

Problematic

The question which we would really like to answer is: what is the microscopic mechanism behind unconventional superconductivity in these materials? However, this question is well beyond the grasp of (most) mere mortals doing a three-year doctoral program, therefore we would like to answer the question: what is the magnetic state of these three materials and how does it relate to superconductivity? More specifically we want to address these specific questions about each unconventional superconductor:

- How do the magnetic excitations, which are thought to play an important role in superconductivity, vary across the phase diagram of the $Ca_2CuO_2Cl_2$ system compared

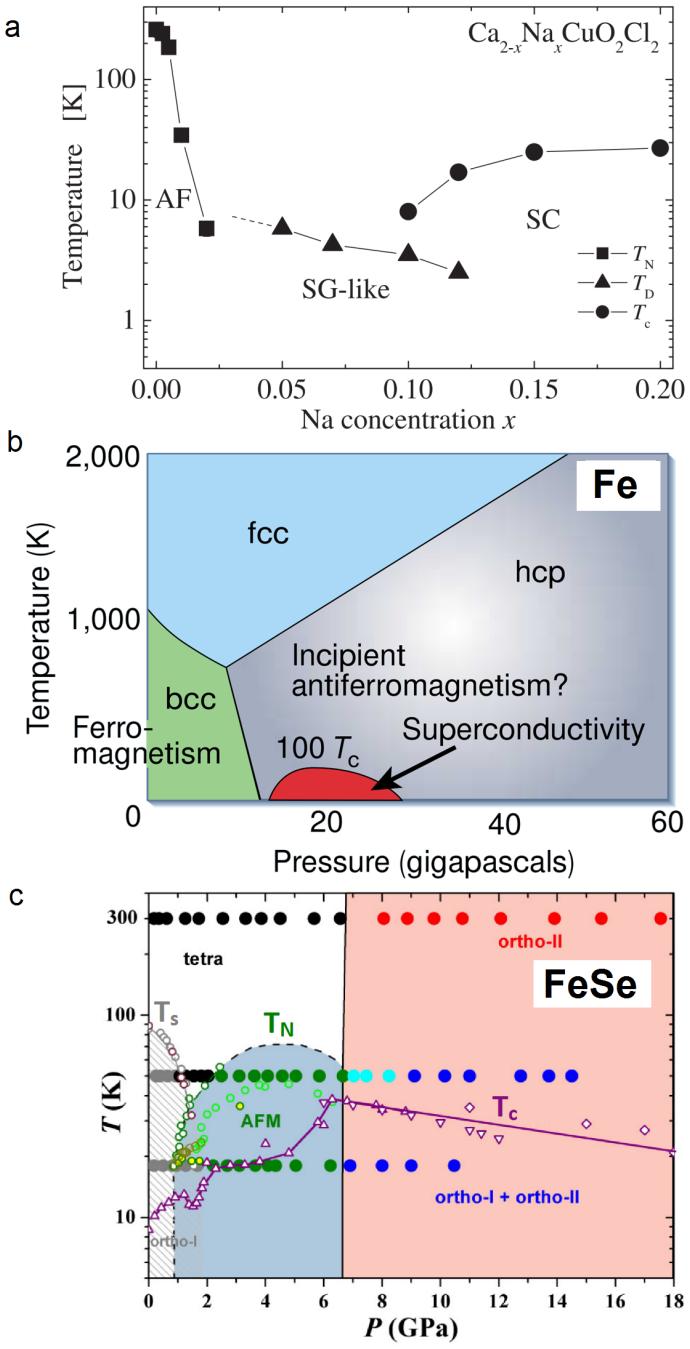

Figure 5: Phase diagrams of the three unconventional superconductors studied in this thesis. From top to bottom: (a) The antiferromagnetic parent compound $Ca_2CuO_2Cl_2$ can be hole-doped with Na which leads to the rapid disappearance of long-range 3D antiferromagnetism (AF) and eventually the appearance of superconductivity (SC) [1]. (b) Ferromagnetic iron undergoes a structural transition under pressure to ϵ-iron whose magnetic state is heavily debated, along with its possible link to superconductivity in this pressure region [2]. (c) Compressed FeSe shows a dramatic interplay between nematic (T_s), magnetic (T_N), superconducting (T_c) orders [3]. See Chapter III, IV, and V for more details about the phase diagram of $Ca_2CuO_2Cl_2$, Fe, and FeSe respectively.

to other high-T_c cuprates?

- What is the magnetic state of the high-pressure ϵ-iron phase and does it have a connection to its superconductivity?

- What is the connection between the structural, magnetic, and superconducting orders of β-FeSe during its high-pressure structural transition?

Theoretical concepts

A brief theoretical background is covered in Chapter I. Unconventional superconductors belong to the class of "quantum materials" which show remarkable emergent phenomena. These materials cannot be understood using the traditional monoelectronic approach since the correlation between electrons is non-negligible and leads to unpredictable collective behavior. A quintessential example of this behavior is superconductivity, where electrons attract, rather than repulse, one another and condense into a superfluid state. This superconducting state has zero electrical resistivity below a certain critical temperature (T_c), as long as the electrical current density and external magnetic field are also below a critical limit. As well, superconductors expel internal magnetic fields from their bulk when cooled below T_c by the so-called Meissner effect. The microscopic mechanism of the early superconductors was codified in the Bardeen, Cooper and Schrieffer (BCS) theory in which arbitrarily-strong interaction between electrons causes them to form quasi-bosonic "Cooper pairs" which condense in a superfluid state. The BCS theory (and its extensions) explained very well the known superconducting materials of the era, mostly pure metals and alloys, where phonons mediated the Cooper pairing by providing the attractive force between electrons.

Unconventional superconductors cannot be explained by traditional phonon-mediated BCS(-like) theories. Electronic correlation in quantum materials leads to other collective behavior besides superconductivity, such as magnetism, therefore it is is not completely unnatural to find magnetism in the proximity of superconductivity even though in conventional superconductors magnetic impurities are known to destroy superconductivity. Nonetheless, magnetic order is still known to compete with superconductivity, even in the unconventional superconductors. However, as the material is tuned either through doping or pressure there are regions in the phase diagram with degenerate magnetic (and nonmagnetic) ground states, where the associated quantum magnetic fluctuations are thought to play an integral role in the Cooper pairing.

In the heavy fermion superconductors the competition between the Kondo effect and the RKKY interaction at low temperatures creates a quantum critical point where the magnetic and non-magnetic ground states are degenerate, thereby inducing quantum spin fluctuations which are thought to be involved in their superconductivity. There are a few heavy fermion superconductors which have ferromagnetism, which invokes thoughts of the metallic iron's phase diagram. The high-T_c copper oxide (cuprate) superconductors also have spin fluctuations as one of the leading candidates for Cooper pair mediation. The cuprates are quasi-2D structures with CuO_2 plane(s) separated by a charge reservoir layer used for doping. The undoped parent compounds are antiferromagnetic with large intra-planar exchange (Cu-O-Cu super-exchange) and weak inter-planar exchange. The 3D antiferromagnetic order is quickly destroyed upon doping, however strong antiferromagnetic correlations remain in the

CuO_2 plane(s) where superconductivity is believed to manifest itself. The newest group of unconventional superconductors is the Fe-based superconductors (FeSC). They were quite a surprise since the strong magnetism of iron was thought to be antagonistic to superconductivity. The FeSCs are also sometimes referred to as iron pnictides (with P or As) or chalcogenides (with S, Se, or Te). FeSCs have a quasi-2D structure similar to the cuprates with FeSe layers, the seat of superconductivity, separated by charge reservoir layers. The FeSCs typically have lower T_c than the cuprates since they have antiferromagnetic order coexisting and competing with superconductivity. There is debate over the dominant mechanism behind the Cooper pairing in the FeSCs between spin fluctuations and orbital fluctuations due to nematicity.

Experimental techniques

The main experimental techniques I used are explained in Chapter II. My thesis focused on using x-ray and neutron probes to study the electronic, magnetic, and structural properties of materials. These experiments, especially under pressure, are infeasible or impossible in a laboratory setting. Therefore, the experiments make use of x-ray or neutron facilities. I used synchrotron light sources, principally SOLEIL and ESRF, to perform the x-ray scattering experiments described below. Synchrotron sources produce highly brilliant x-ray beams based on the principle that a charged particle (electrons usually for synchrotrons, sometimes positrons) emits electromagnetic radiation upon acceleration. Neutrons are produced on a large scale with either a spallation or continuous nuclear fission reactor source. We used a nuclear reactor source (ILL) which produces large quantities of neutrons during nuclear fission. These facilities, and their associated instruments, or "endstations", are important tools to study condensed matter systems since they provide information often unavailable with laboratory experiments. There has never been a more exciting time for these studies with the number of facilities increasing around the world, the opening of new research avenues as instruments reach record-breaking resolutions, and the possibility of extreme time-resolved studies with the development of of x-ray free electron lasers.

High pressure techniques

High pressure is a very useful external parameter to tune the magnetic, structural and electronic degrees of freedom since its is "clean", in that unlike doping or temperature it does not introduce disorder into the system. The principle of the technique is the classic high-heel analogy: one applies a moderate pressure over a large surface area whose force is transmitted through a hard material to a small surface, thus amplifying the pressure. In this thesis we only use uniaxial pressure devices which have two opposed "anvils" that squeeze our sample. To reach high pressure requires hard materials, therefore we used single crystal diamonds or sintered diamond for x-ray and neutron high-pressure studies respectively. Two other key components are the gaskets, which prevent the sample from extruding outside the high-pressure region, and the pressure transmitting medium, which helps provide a (quasi)-hydrostatic environment.

X-ray absorption spectroscopy (XAS)

X-ray absorption spectroscopy is a technique which involves the excitation of a core electron into an empty valence state. It provides structural and electronic information about the local environment of the target atom. XAS is performed by measuring the transmission through a sample while varying the incident energy across a so-called absorption edge, which corresponds to the minimum energy to excite a certain atomic core level to the lowest unoccupied valence state. Another way of indirectly measuring the absorption is to measure the (total or partial) fluorescence intensity or electron intensity which scale with absorption. We used XAS to study iron in β-FeSe using the partial-fluorescence yield method (PFY-XAS). This is a photon-in photon-out technique and is therefore compatible with high-pressure studies since the absorption edge of Fe is $\approx$ 7112 eV. We measure the PFY-XAS by measuring the emission (see XES below) of the Fe Kβ ($3p \rightarrow 1s$) emission, which leads to an intrinsic sharpening effect due to the shallower $3p$ core hole left in the final state with respect to the deeper $1s$ level (also known as HERFD).

X-ray emission spectroscopy (XES)

X-ray emission spectroscopy, also known as x-ray fluorescence, excites a core electron into the continuum (non-resonant) with an x-ray and then measures the emitted x-ray when the excited system decays to fill the core hole. We use a specific type of XES called Fe Kβ XES to study compressed Fe and FeSe. The incident and emitted x-rays in Fe Kβ XES are both hard x-rays, therefore it is compatible with high-pressure studies. The Kβ emission ($3p \rightarrow 1s$) from iron has a mainline (K$\beta_{1,3}$) as well as a lower-energy satellite. This satellite, known as Kβ', is sensitive to the $3d$ spin angular momentum and thus can be used to follow the spin state or semi-quantitatively determine the spin magnetic moment.

Resonant inelastic x-ray scattering (RIXS)

Resonant inelastic x-ray scattering is another photon-in photon-out technique which can be thought of as XAS, excitation of a core electron to an unoccupied state, followed by XES, emission of an x-ray as an electron decays to fill the initial core hole. However, the situation is more complex since the two processes are coherent which leads to a complicated cross section where the intermediate state can create intrinsic excitations in the material. These excitations can be probed with RIXS by measuring the change in energy and momentum of the emitted x-ray. The use of resonance can greatly increase the inelastic cross section by many orders of magnitude. The main RIXS technique used in this thesis is direct RIXS at the Cu L$_3$-edge ($2p_{3/2}$) to study magnetic excitations in the $Ca_2CuO_2Cl_2$ system. In the cuprates the Cu ions electronic configuration is $3d^9$ such that there is only one hole in the $3d_{x^2-y^2}$ level. In Cu L$_3$-edge RIXS a $2p_{3/2}$ core electron is excited to fill this hole, creating a highly energetic intermediate state. The strong-spin orbit coupling of the core hole allows the exchange of the photon's orbital angular momentum with the spin angular momentum of the hole in the final state, which creates a spin flip that propagates throughout the lattice via the super-exchange.

Neutron powder diffraction (NPD)

Neutron powder diffraction can be used to determine the nuclear and magnetic structure of materials. The technique uses thermal neutrons which have a de Broglie wavelength comparable to atomic spacing in condensed matter. Using Bragg's law we can determine the lattice spacing. Neutron carry a spin and interact directly with magnetic moments and therefore NPD has magnetic Bragg peaks with intensity comparable to that of nuclear peaks (unlike x-ray magnetic scattering). NPD is especially suited to look for antiferromagnetic order since antiferromagnetic supercells imply magnetic Bragg peaks away from nuclear Bragg peaks towards lower scattering angles where the magnetic form factor is greatest (due to spatial extent of the valence electrons). We used neutron powder diffraction to search for antiferromagnetic order in Fe and FeSe under pressure.

Magnetism in unconventional superconductors

The three materials I studied will now be introduced along with their main results. These are covered in more detail in Chapter III, IV, and V for $Ca_2CuO_2Cl_2$, ϵ-iron, and β-FeSe respectively.

$Ca_2CuO_2Cl_2$

The correlated nature of electrons in the cuprates makes unraveling their superconducting mechanism extremely difficult. There is an overabundance of theories claiming to explain the mechanism, however they cannot adequately explain all available experimental results, likely since they rely on simplified frameworks to treat electronic correlation. One solution is to use many-body calculations, which is becoming more viable everyday due to advances in techniques and the steady march of Moore's law. In this case, one would like to study the simplest compound which still captures all the relevant physics of cuprates.

It is in this context that we chose to study the copper oxychloride $Ca_2CuO_2Cl_2$ system, which is presented in Chapter III. This system can be hole-doped with either Na, K, or vacancies and exhibits the same properties seen in the cuprates (Fig. 5). The reason why can be seen by looking at its structure in Fig. 6: the $Ca_2CuO_2Cl_2$ system has the same quasi-2D layer structure as the cuprates with CuO_2 planes separated by charge reservoir layers. The apical oxygens of the cuprates, is replaced with chlorine, making this system a copper oxychloride, yet the important magnetic and superconducting properties of the cuprates arise from the CuO_2 planes which rest unchanged. This system offers many advantages to first-principles calculations, such as: it has a simple tetragonal structure free of orthorhombic distortions and buckling of the CuO_2 planes at all temperatures and doping; it has only low mass atoms which is a boon due to the reduced number of electrons; and, it has apical chlorines which gives the CuO_2 planes an even more quasi-2D nature.

The main study on $Ca_2CuO_2Cl_2$ in this thesis (Article 1, Sec. III.3) is the measurement of the dispersion of spin waves (magnons in the second quantization approach) in the undoped parent compound $Ca_2CuO_2Cl_2$. The undoped compound, as in all cuprates, is a spin-1/2 2D antiferromagnet. The study of this parent compound is important to characterize the super-exchange parameters between the Cu spins, which varies little with doping and is an important ingredient in many theories about its superconductivity. Our main results are

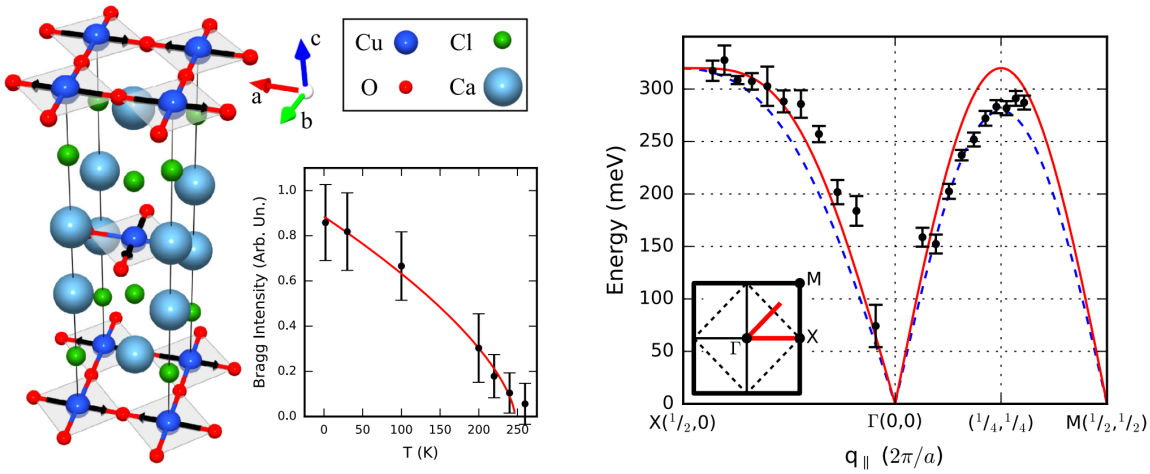

Figure 6: (Left) Tetragonal crystal structure of $Ca_2CuO_2Cl_2$. The square coordination of copper with its four nearest-neighbor oxygen ions in the CuO_2 planes is shown. The chlorine ions are located in the apical sites above and below the copper. The inset shows our neutron diffraction data measuring the Néel temperature. (Right) Our magnon dispersion results for $Ca_2CuO_2Cl_2$ measured using Cu L_3-edge RIXS [4]. The red, continuous line is a calculation for a classical spin-1/2 2D Heisenberg model with nearest-neighbor exchange, and the blue, dashed line is a calculation including further exchange terms. The inset shows the 2D Brillouin zone showing the high-symmetry points. The first Brillouin zone boundary is represented by a thick black square, while the magnetic Brillouin zone boundary is represented by a dashed line. The region where we measured is shown as two thick red lines along Γ-X and Γ-M.

summarized in Fig. 6 which shows the magnon dispersion in $Ca_2CuO_2Cl_2$ measured along the two high-symmetry directions using Cu L_3-edge RIXS. To the best of our knowledge, this was the first report on the magnon dispersion of $Ca_2CuO_2Cl_2$, or even the nearest-neighbor exchange J. We extracted $J = 135$ meV using a nearest-neighbor 2D Heisenberg model (red line), however there is a clear energy difference between the two zone boundaries which indicates the need to include further exchange terms. The inclusion of further exchange terms parameterized with a 1-band Hubbard model gives a better fit for the zone boundary energies (blue dashed line) but changes the super-exchange estimation very little, $J = 141$ meV. The results of a high-resolution study of this dispersion is presented in Sec. III.4 where our model fits much better due to improved resolution and sample preparation.

$Ca_2CuO_2Cl_2$ is extremely hygroscopic and only available in small single crystals. Our results show the power of Cu L_3-edge RIXS to study spin excitations in the cuprates, since similar measurements using inelastic neutron scattering would be nigh impossible due to the low mass (and difficulty of co-aligning hygroscopic crystals) and small cross-section of epithermal neutrons which are needed for this energy range. I present very briefly in Sec. III.4 further exploitation of this technique to measure the doping dependence of magnetic excitations in the $Ca_2CuO_2Cl_2$ system. As well, preliminary results looking at the bimagnon using different techniques and a search for charge order in $Ca_2CuO_2Cl_2$ are briefly presented. Overall, we have been working to provide benchmarks for future many-body calculations, in

order to finally bridge the gap between theory and experiment in the cuprates. The agreement with other cuprate systems so far is promising since it emphasizes that $Ca_2CuO_2Cl_2$ is a good model for the cuprates.

Iron under pressure

Iron has been a favorite material of the high pressure community for a long time due to its geophysical significance. Indeed, iron is one of the few materials which has been studied to such extreme pressures and temperatures in order to simulate the conditions of the Earth's core. Studies on iron are constantly pushing the boundaries of high pressure physics, however the low pressure region of its phase diagram still holds a mystery. The magnetic state of the low-pressure region of ϵ-iron has been studied thoroughly with theory and experiment, yet the results are often paradoxical and have been under debate for decades. The discovery of unconventional superconductivity in this pressure region further emphasized the need to uncover the magnetic nature of ϵ-iron, which was the goal of our study in Chapter IV.

Under compression iron undergoes a structural transition from a body-centered cubic (bcc) structure to a hexagonal close-packed (hcp) structure, the α and ϵ phases respectively. The well-known ferromagnetism of iron also disappears during the structural transition but the magnetic state of ϵ-iron is unclear. Low-temperature Mössbauer spectroscopy does not detect any magnetism in ϵ-iron, yet an anomalous Raman peak suggests broken symmetry due to magnetism. Furthermore, first-principles calculations consistently predict an antiferromagnetic ground state and recent x-ray emission spectroscopy measurements find a magnetic moment after the α-ϵ transition which they called a "remnant". There are two competing theories to describe these paradoxical results: a special antiferromagnetic state called afmII and spin fluctuations. The former is compatible with Mössbauer measurements due to a fortuitously small magnetic hyperfine field and also explains the anomalous Raman mode. The afmII structure and predicted pressure dependence for the magnetic moment are shown in Fig. 7. The latter explanation of spin fluctuations is also attractive since theoretical studies find they are needed to explain the behavior of the superconducting dome in ϵ-iron.

In this thesis, I present an XES & NPD study of compressed iron in order to investigate these two possible explanations (Article 2, Sec. IV.2). We performed Kβ XES with improved statistics, pressure transmitting medium, and data treatment. The results are shown in Fig. 7 where we can clearly see a sharp change in the satellite intensity at the structural transition. Therefore, the magnetic moment in this region is intrinsic to the ϵ phase, and is not a remnant of the α phase. The magnetic moment disappears above 30 GPa, the same as superconductivity, which agrees with the existence of spin fluctuations which mediate superconductivity in ϵ-iron. Nonetheless, the qualitative trend between the afmII predictions and our results are striking. We investigated the existence of the afmII state, and more generally any static antiferromagnetic state, using neutron powder diffraction at record simultaneous high-pressure/low-temperature conditions (technique described in Article 4, App. A). We put an upper limit on the magnetic moment in a hypothetical afmII phase which is four times lower than first-principles predictions and an estimate from our XES results.

Our results strongly argue against the existence of a static afmII configuration in ϵ-iron, however in the end perhaps both explanations are partially correct? In Sec. IV.3 some preliminary theoretical calculations are briefly mentioned which point towards many degenerate afmII-like ground states due to the geometrical frustration of the hcp lattice with respect

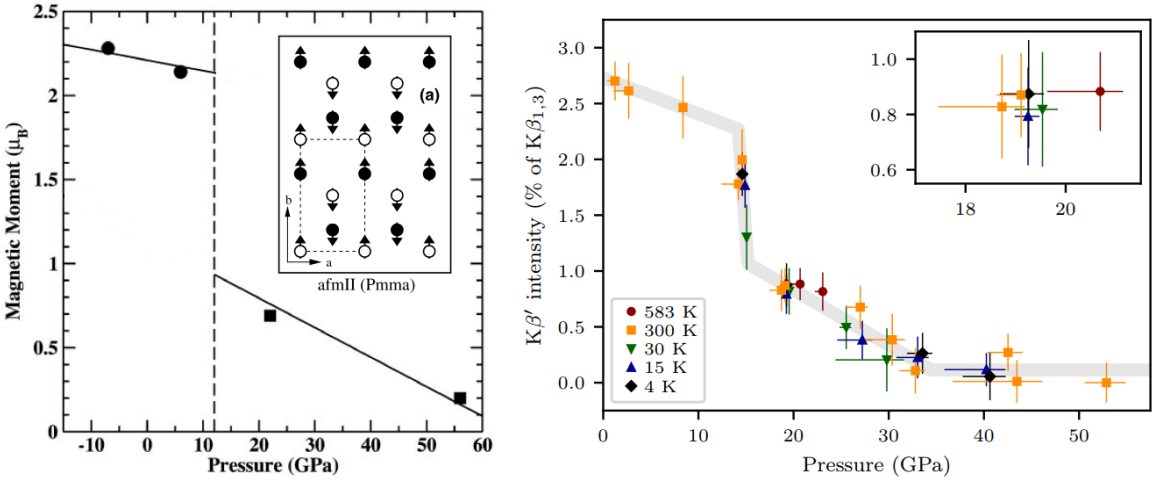

Figure 7: (Left) The predicted magnetic moment of the afmII state in ϵ-iron, whose configuration is shown in the inset [5, 6]. Atoms at z = 1/4 (3/4) are shown with open (closed) symbols and the arrows indicate spin up and spin down (Right) Pressure dependence of satellite intensity using Kβ x-ray emission spectroscopy. The Kβ' intensity acts as semi-quantitative proxy to the $3d$ spin angular momentum which is approximately the magnetic moment in iron due to orbital quenching. The inset shows a zoom of the dense region around 20 GPa. The gray lines are guides for the eye.

to antiferromagnetism. These degenerate states would induce quantum spin fluctuations, which we find actually vary not only in direction, but also in intensity. Our results show that the similarity in the phase diagrams of iron and other ferromagnetic superconductors (typically heavy fermion superconductors) is only superficial. Iron's ferromagnetism is lost during the transition to ϵ-iron and it plays no role in ϵ-iron's superconductivity. However, during measurements of the superconducting dome minority ferromagnetic α-iron remnants just after the transition could suppress T_c on the low-pressure side of the dome.

FeSe under pressure

FeSe has two stable polymorphs at ambient conditions, however we are only interested in the tetragonal polymorph β-FeSe (referred to as simply FeSe in this thesis) since it belongs to the family of Fe-based superconductors (FeSC). FeSe has a simple structure consisting solely of quasi-2D FeSe layers (Fig. 8). It also is one of the few FeSC where superconductivity exists at ambient conditions without long-range antiferromagnetic order. These two features make FeSe a unique compound to study superconductivity in FeSCs. The T_c of FeSe is rather modest (7–8 K) however it is increased by using monolayers, intercalation, and/or pressure. The phase diagram under pressure (Fig. 5) shows the complex relation between magnetic, nematic, and superconducting orders. In Chapter V, our study of FeSe under pressure is presented where we try to unravel these intertwined orders.

The critical temperature of FeSe increases four-fold when compressed and its evolution is non-monotonic. There seems to be an anticorrelation between the Néel (T_N) and critical (T_c) temperatures which creates two distinct T_c anomalies around 1–2 GPa and 6–8 GPa.

The former T_c anomaly has been studied in detail, while the latter T_c anomaly less so. In this 6–8 GPa pressure region there is also an irreversible, first-order structural transition from the ortho-I to the ortho-II phase (Fig. 8). The ortho-I phase is pseudo-tetragonal and the Fe atoms have T_d coordination, i.e. there is just a slight orthorhombic distortion in the *ab*-plane induced by nematicity in FeSe below T_s and T_N. On the other hand, the ortho-II structure forms a 3D network where the Fe atoms have O_h coordination.

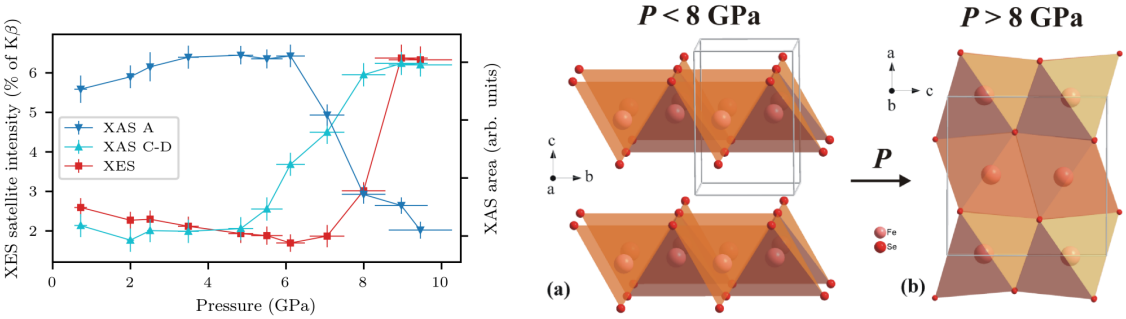

Figure 8: (Left) The pressure dependence of our x-ray emission spectroscopy (XES) and x-ray absorption spectroscopy (XAS) results on FeSe [7]. XAS A is the area of the pre-peak and XAS C-D is the area between feature C-D in the near-edge region (see Sec. V.2). (Right) Low-pressure and high-pressure phases of FeSe [3]. (a) The low-pressure phase has a tetragonal PbO-type ($P4/nmm$) structure and is composed of layers of edge-shared $FeSe_4$ tetrahedra. The low-pressure, low-temperature ortho-I phase ($Cmma$) is similar except for a slight orthorhombic distortion in the *ab*-plane. (b) The high-pressure, MnP-type ortho-II structure ($Pnma$) is composed of chains of face-shared $FeSe_6$ octahedra. Note the change of axes between the two drawings.

The pressure region of the simultaneous high-pressure T_c anomaly, decrease in T_N, and ortho-I to ortho-II transition was the focus of this thesis (Article 3, Sec. V.2). As in iron, we used Kβ XES and NPD to study the electronic and magnetic changes during this transition, however we also performed XAS to study the structural and electronic changes. The results are shown in Fig. 8 where we can see the XAS A and XES signals both change dramatically around 7 GPa. The XAS A signal is from the pre-peak which changes with the Fe atom's coordination, allowing us to follow the expected structural transition. The XES signal shows a completely unexpected behavior going from a low-spin to high-spin state. A first-principles simulation of the XAS spectra confirms our assignment of a high-spin state to ortho-II. The structural and magnetic transition seem to be concomitant. The stability of a low-spin state with T_d coordination is likely due to the recently predicted band-dependent correlation effects in Fe-based superconductors.

A low-spin to high-spin transition under pressure is extraordinary since the increased bandwidth under pressure usually induces the opposite transition. However, perhaps it is not so surprising due to the drastic quasi-2D to 3D structural change between ortho-I and ortho-II. This is considered in more detail in Sec. V.3. In this section I also discuss the observed increase in the near-edge region of the XAS spectra (XAS C-D) before the transition at 5 GPa, which corresponds to the onset of the last T_c increase. I speculate that the high-spin ortho-II phase coexists with the superconducting ortho-I phase on a nanoscale. As in

the intercalated $K_xFe_{2-y}Se_2$, the transitions between these high- and low-spin phases creates spin fluctuations which can enhance superconductivity. This gives a rise in T_c when there is a minority of ortho-II, however as more ortho-II domains appear the transport measurements are dominated by electronic scattering at these phase boundaries and the T_c is difficult to determine.

We also performed neutron powder diffraction measurements on FeSe, which are discussed in the Supplementary Information of Article 3 (Sec. V.2). Unfortunately we could not measure a clear ortho-I to ortho-II transition in order to search for antiferromagnetic order in ortho-II. I speculate in in Sec.V.3 that this is likely due to the use of FeSe powder instead of single crystals. Nonetheless, our NPD measurements in the ortho-I phase give stronger upper limits on the magnetic moment for the two main proposed afm configurations. We find that a stripe-type collinear afm configuration is most likely as in other FeAs-based FeSC superconductors, rather than a bicollinear afm configuration.

Conclusions

I present a variety of experimental measurements in this thesis, mostly related to magnetism, applied to three completely different unconventional superconductors. My results emphasize the intimate connection between magnetism and superconductivity which seems ubiquitous in unconventional superconductors. The main results of these studies are:

- The magnon dispersion in the undoped parent compound $Ca_2CuO_2Cl_2$ is measured and we estimate the super-exchange parameter $J = 141$ meV. Our high-resolution measurements are well-fit with further exchange terms parameterized by a one-band Hubbard model.

- We provide a set of benchmarks characterizing magnetic excitations in the $Ca_2CuO_2Cl_2$ system for comparison with future many-body calculations. These results include the doping dependence of the paramagnon and an extensive study of the bimagnon using a multitude of techniques. We also find the first hints of bulk charge order in the $Ca_2CuO_2Cl_2$ system.

- Our neutron powder diffraction results on ϵ-iron rebuts the existence of static afmII order. Therefore, we find spin fluctuations must exist in order to explain previous experimental results.

- The magnetic moment in ϵ-iron measured with x-ray emission spectroscopy tends towards zero between 30–40 GPa, the same region where the superconducting state disappears. This strongly supports the previous predicted theories of Cooper pairing mediated by spin fluctuations in ϵ-iron.

- Our preliminary calculations suggest that spin fluctuations arise in ϵ-iron due to degenerate ground states in the geometrically frustrated hcp lattice.

- We find an unforeseen low-spin to high-spin transition in FeSe associated with its structural transition. The origin of this unusual effect is explained well by recently predicted band-dependent correlation effects in Fe-based superconductors.

- A spectroscopic signature of the increased T_c in FeSe around 5 GPa is found and needs to be investigated further. I speculate that nanoscale separation of the low- and high-spin states induces spin fluctuations which enhance the T_c in this region.
- The upper limits we set for the magnetic moment of different antiferromagnetic configurations in the ortho-I phase of FeSe agree with a stripe-type collinear arrangement which is in common with other FeSe-based superconductors.

Chapter I
Background

I.1 Introduction

The liquefaction of helium in 1908 by Heike Kamerlingh Onnes kicked off a revolution in condensed matter physics which continues to this day and has reverberated throughout all branches of physics. This achievement opened up the possibility of low-temperature experiments – helium has a boiling point of 4.2 K at atmospheric pressure, which can be lowered further by pumping (see App. A for one novel use). Using this technique, Kamerlingh Onnes later discovered that the electrical resistance of mercury abruptly vanishes below 4.15 K, the so-called critical temperature T_c [8]. This novel phenomenon is now known[1] as superconductivity and in the the following years, several other elemental and compound/alloy superconductors with increasing T_c were discovered (see Fig. I.1 for a selection). The microscopic mechanism behind superconductivity remained a mystery for nearly 50 years, until 1957 when Bardeen, Cooper and Schrieffer (BCS) posited a theory in which interaction between electrons and phonons caused electrons to form quasi-bosonic "Cooper pairs" which condense into a superfluid state. This BCS theory and its extensions explained very well the known superconducting materials of the era.

However, theoreticians could not rest on their laurels for long, since the heavy fermion superconductors discovered in 1978 were surprisingly unexplainable by conventional phonon-mediated BCS theory. Initially, these "unconventional" superconductors were simply a scientific curiosity due to their unfortunately low critical temperatures. This notion was quickly overthrown with the serendipitous discovery of high-T_c copper oxide (cuprate) superconductors in 1986 which ushered in a golden age where room-temperature superconductivity seemed just around the corner. On the contrary, room-temperature superconductivity remains elusive despite three decades of research. Once again theory is lagging behind experiment and there is no agreement on the microscopic mechanism(s) behind unconventional superconductivity.

The lack of predictive power from a complete theory has not quelled discoveries in the field of superconductivity, both unconventional and conventional. The search for a transparent oxide semi-conductor inadvertently lead to the discovery of a new unconventional superconductor $LaFeAsO_{1-x}F_x$ (T_c =26 K) in 2008, the first of many iron-based supercon-

[1] Kamerlingh Onnes originally dubbed the phenomenon as supraconductivity which is the term still used today in French

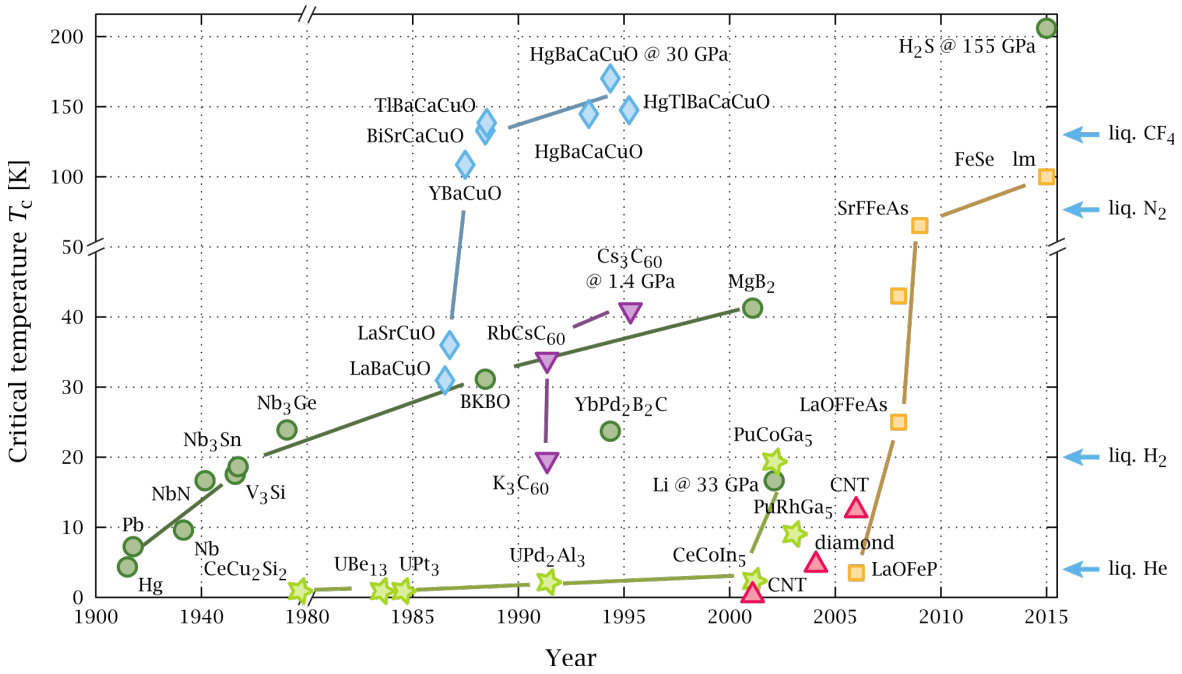

Figure I.1: A timeline of the critical temperatures of a representative sample of different superconducting families [9]. Green circles: conventional, green stars: heavy-fermion, blue diamonds: cuprate, purple inverted triangles: fullerenes, red triangles: covalent (CNT = carbon nanotubes), yellow squares: iron-based. Note the discontinuity at 50-100 K along the y-axis and and 1940-1980 along the x-axis.

ductors (FeSC) [10]. On the conventional side, the sulfur hydride system under pressure was found to have $T_c = 203$ K in 2013 [11]. This critical temperature shattered the previous T_c record of 138 K for $Hg_{0.8}Tl_{0.2}Ba_2Ca_2Cu_3O_{8+\delta}$ at ambient pressure [12] and 164 K for $Hg_{1-x}Pb_xBa_2Ca_2Cu_3O_{8+\delta}$ at high pressures [13]. As well, many properties and trends of unconventional superconductors have been revealed. One prime example is the ubiquitous proximity of magnetism with superconductivity in all classes, from organic to iron-based superconductors (see phase diagrams in Sec. I.4 for examples).

The proximity (or coexistence) of magnetism with superconductivity may seem antithetical at first glance, since magnetic impurities interrupt the necessary Cooper pairing in conventional superconductors. On the other hand, unconventional superconductors all belong to a class of materials known as "quantum materials" [14], which show remarkable emergent phenomena including magnetism and superconductivity. These materials cannot be understood using the traditional monoelectronic approach since the correlation between electrons is non-negligible and leads to unpredictable cooperative behavior. Their properties are very sensitive to the Fermi surface and can be "tuned" through doping or external pressure. Many of these properties are only manifested at low temperature — again returning to the enormous impact of low-temperature experiments ushered in by Kamerlingh Onnes. Therefore, a common tool to study quantum materials is studying the temperature dependence of the emergent phenomena as a function of the tuning parameter (doping/pressure) in the form of phase diagrams. These studies reveal that magnetism is never far away from

unconventional superconductivity. In these materials magnetic order is found to compete with superconductivity. However, there are also regions with degenerate magnetic (and non-magnetic) ground states, where the associated quantum magnetic fluctuations are thought to play an integral role in the Cooper pairing of unconventional superconductors.

The goal of my thesis was to investigate magnetism in unconventional superconductors in order to gain insight into their intertwined relationship. I studied three different materials from three different classes of unconventional superconductors.

The first compound studied was the copper oxychloride family $Ca_2CuO_2Cl_2$, which due to its simple structure and light elements is an ideal model for the cuprate family. I studied magnetic excitations in the antiferromagnetic parent compound using Cu L_3-edge RIXS. I will also present preliminary results investigating its phonons, bimagnon, doping dependence, and charge order. Our goal is to provide a benchmark for future many-body calculations, which are more feasible for low-Z $Ca_2CuO_2Cl_2$, in order to finally bridge the gap between theory and experiment in the cuprates.

The second compound I studied was the high-pressure phase of metallic iron known as ϵ-iron. This phase exhibits unconventional superconductivity from $\approx$ 15 GPa to 30–40 GPa and magnetic fluctuations are thought to play an important role. However, the magnetic state of ϵ-iron is heavily debated and the proximity of the low-pressure ferromagnetic phase invokes thoughts of ferromagnetic heavy-fermion superconductors such as UGe_2. We used x-ray emission spectroscopy and neutron powder diffraction to study ϵ-iron on the atomic and long-range levels respectively. We performed neutron powder diffraction on ϵ-iron for the first time, while our x-ray emission spectroscopy results were a significant improvement over previous studies.

The last compound I studied was the iron chalcogenide superconductor FeSe under pressure. Regarding its structure and stoichiometry, it is the simplest of the Fe-based superconductor family, however its phase diagram shows a complex interplay of magnetic, nematic, and superconducting orders. It is a rare case where an antiferromagnetic region coexists directly in the middle of a superconducting "dome". The pressure evolution of the critical temperature correlates with the antiferromagnetic order with competition between two orders, as seen also in the cuprates. We used x-ray emission spectroscopy to follow the magnetic state's pressure evolution, as well as neutron powder diffraction in the low pressure region to elucidate the antiferromagnetic ordering.

This thesis is organized in six sections. Chapter 1 gives an overview of correlated electron systems, magnetism, and superconductivity. Chapter 2 presents the experimental methods I used to study magnetism in these materials. The unconventional superconductors $Ca_2CuO_2Cl_2$, ϵ-iron, and FeSe are discussed in Chapter 3, 4, and 5 repsectively. Finally, my conclusions are presented Chapter 6.

I.2 Correlated $3d$ electron systems and magnetism

The review Rueff & Shukla [15] was used as the primary reference for this section.

The materials considered in this thesis are composed of the $3d$ transition metals Fe or Cu, which have incompletely filled d shells. The $3d$ orbitals are fairly localized and the electrons in these narrow bands can no longer be thought of as uncorrelated electrons in a Fermi

"sea". The strong correlation between neighboring electrons means that simple one-electron theories which rely on a mean-field are no longer applicable. The collective behavior of the electrons can lead to the emergence of novel behavior such as Mott insulator, pseudogap, electronic stripe, electronic nematicity, heavy electron, superconducting, or any non-Fermi liquid behavior.

In general, the $3d$ electrons behave both as delocalized, itinerant electron systems and localized, correlated electrons. For example, iron has an itinerant character since it is metallic, yet its magnetism is well-described in a localized picture of spins filling $3d$ orbitals.

An understanding of these systems can be gained using the simple yet powerful Hubbard model. The Mott-Hubbard Hamiltonian for a single band is given by:

$$\mathcal{H} = \sum_{i,j,\sigma} t_{ij} a^{\dagger}_{i\sigma} a_{j\sigma} + U \sum_{i} n_{i\uparrow} n_{j\downarrow}$$

The first term is the kinetic energy of the system, where $a^{\dagger}_{i\sigma}(a_{i\sigma})$ creates (annihilates) an electron of spin σ at site i, and $n_{i\sigma} = a^{\dagger}_{i\sigma} a_{i\sigma}$. This represents the intersite hopping of an electron from one site to another and is governed by the energy scale t_{ij}. The second term is the interaction energy when a site is doubly-occupied due to the on-site Coulomb repulsion U.

The hopping t is related to the bandwidth W, since a smaller bandwidth reduces the hopping energy. With strongly correlated electrons this model shows that when $U/W > 1$ the system is more localized, while when $U/W < 1$ the system is more delocalized. If the band is half-filled or less, the hopping is disfavored due to the strong Coulomb repulsion at the new site. This splits the band into an upper and lower Hubbard band separated by the energy U, and leads to an insulating state.

In transition-metal compounds the $3d$ ions are coordinated by ligand atoms such as oxygen. The ligands create a crystal electric field (CEF) around the $3d$ ion which is felt differently by the orbitals due to their orientation which lifts their degeneracy in a process known as crystal field splitting (Fig. I.2). In a system with octahedral coordination (O_h), the splitting between the e_g and t_{2g} bands is called $10Dq$, or Δ_o. In a system with tetrahedral coordination (T_d), the e_g band is below the t_{2g} band and their splitting is lowered to $\Delta_t = 0.44$ Δ_o [16]. Different ligand configurations will naturally lead to different crystal field splitting. Another consequence of the crystal electric field in $3d$ metal systems is the "quenching" of the orbital angular momentum , therefore the $3d$ magnetic moment is determined principally by the spin moment. The orbitals of the ligand are also affected by this process and the energy difference between the metal band and the ligand band is known as the charge transfer energy Δ. With correlations the energy scale of Δ, W, and U can create different types of insulators such as a Mott-Hubbard insulator or a charge transfer insulator (see Sec. I.4.2 for an example).

I.3 Superconductivity

The books of Kittel [17], Levy [18], and Tinkham [19] were used as the primary references for this section.

The physical property which gives superconductivity its name is zero electrical resistivity below a critical temperature, T_c. Above T_c the material is in the "normal state", while below

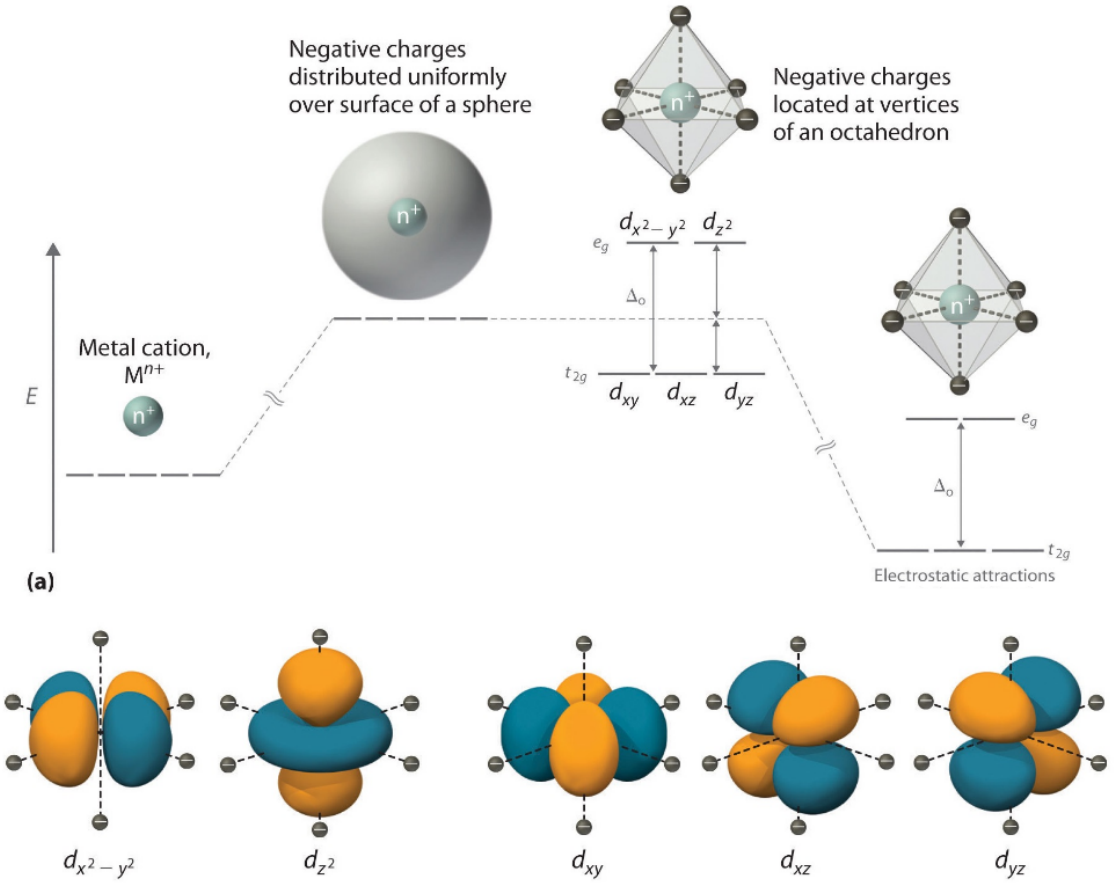

Figure I.2: Overview of crystal field splitting in octahedral coordination [16]. (Top) A uniform, spherical distribution of negative charge surrounding a metal ion increases the energy of all orbitals due to electrostatic repulsion. When the negative charges are octahedrally coordinated (O_h) the energy of the $d_{x^2-y^2}$ and d_{z^2} orbitals increases due to repulsion since they point directly towards the charges, while the energy of the d_{xy}, d_{xz}, and d_{yz} orbitals decreases (see bottom image). These orbitals form two degenerate bands called e_g and t_{2g} respectively. The overall electrostatic attraction decreases the energy of all the orbitals but the splitting remains.

T_c it is in the "superconducting state". This superconducting state is characterized by the creation of Cooper pairs which condense into a coherent superfluid state and can lead to other remarkable properties besides zero resistivity such as its unique magnetic response.

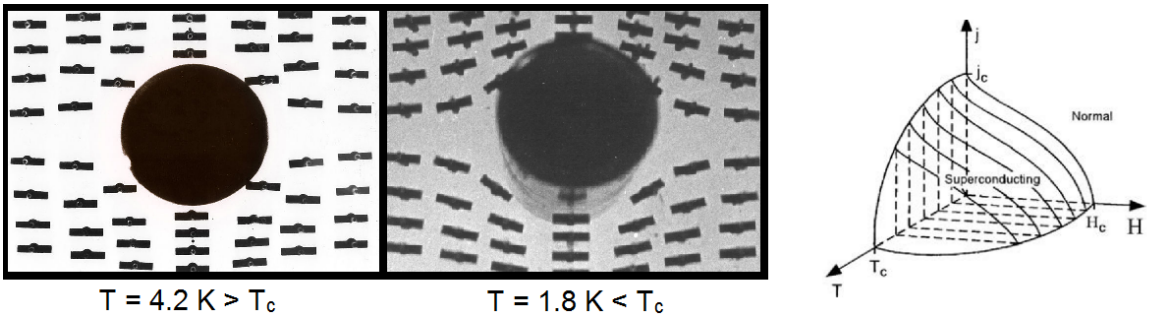

Figure I.3: (Left) Experimental demonstration of the Meissner effect in tin [20]. The magnetic field of 8 mT is visualized with small compasses. The first photo is taken in the normal state above $T_c = 3.72$ K where the magnetic flux penetrates the tin cylinder, while the second photo is after cooling into the superconducting state where the magnetic flux has been expelled. (Right) A 3D phase diagram of a type-I superconductor showing its sensitivity to temperature, current density, and applied magnetic field [21].

As a superconductor is cooled from the normal to the superconducting state it expels any magnetic field which was applied in the normal state. This is a unique property of a superconductor and cannot be explained simply by a hypothetical "perfect" conductor. A perfect conductor naturally leads to a perfect diamagnet since it will oppose external fields according to Lenz's law — a change in applied field induces currents opposing this change which persist due to zero resistance. This interpretation relies on changes in the external field, therefore one would expect an external field applied in the normal state to remain in the superconducting state. On the contrary, experiments show that the magnetic fields are expelled from the superconductor below T_c by the so-called Meissner effect (Fig. I.3). This effect refers to the spontaneous creation of persistent surface currents below T_c which create an internal magnetic field that compensates the magnetization. These internal fields cause the magnetic field to decay exponentially to zero away from the surface. The length scale of this decay is an important characteristic length called the London penetration depth (see further below). As the external field is increased, a superconductor will even break down to the normal state above a critical field H_c, or similarly a critical current density j_c (Fig. I.3). The break down occurs since the condensate formed by Cooper pairs only lowers the free energy of the system a finite amount and increasing the external magnetic field or current density increases the free energy of the superconducting state until eventually the normal state is energetically favored.

The response of a superconductor to an external magnetic field can be broken down into two classes. The scenario described above only applies to a relatively small number of superconductors known as type-I superconductors, or "soft" superconductors due to their low critical fields. Their critical fields are on the order of 1 mT, therefore their practical applications are limited. Type-I superconductors are principally pure elements (but not all pure elements are type-I), although there are some exceptions such as $TaSi_2$, KBi_2, and boron-doped SiC. The magnetization versus applied magnetic field in Fig. I.4 (a) shows this

scenario of a complete Meissner effect where the magnetization completely cancels the applied magnetic field until a critical field, above which the system collapses to the normal state. The second class is type-II superconductors, or "hard" superconductors, and their magnetization curves are shown in Fig. I.4 (b). They have a lower and an upper critical field, H_{c1} and H_{c2} respectively. Below H_{c1} they have a complete Meissner effect, however between H_{c1} and H_{c2} there is an incomplete Meissner effect. The system here is in a mixed state of normal and superconducting regions called a vortex state. The magnetic field penetrates the superconductor in the normal region while the surrounding superconducting region has induced vortex "shielding" current around the tubes. The density of vortices increases with applied magnetic field until eventually the superconducting state collapses above H_{c2}. The value of H_{c2} is much larger than H_c, typically on the order of a few tens of Tesla, which makes type-II superconductors desirable for high field and current applications. The majority of all superconductors are type-II, in particular almost all unconventional superconductors fall into this category.

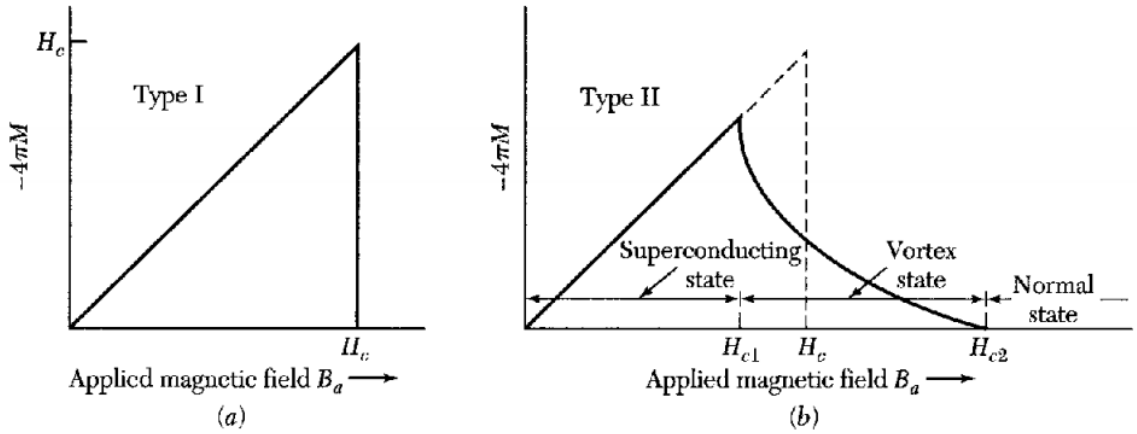

Figure I.4: (CGS units used) Magnetization versus applied magnetic field for type-I and type-II superconductors [17]. A type-I superconductor shows perfect diamagnetism until H_c where it reverts to its normal state and there is total field penetration and non-zero resistivity. A type-II superconductor has an additional mixed state known as the vortex state which allows partial field penetration but still exhibits zero resistivity (see text for details).

The London theory is phenomenological theory which describes the electromagnetic behavior of superconductors on the basis of a two-fluid concept. There is a superfluid and normal fluid density which satisfy charge neutrality, $n_s + n_n = n$, where n is the total local charge density. The superfluid current density is proposed to satisfy the London equation:

$$\nabla \times \mathbf{j_s} = -\frac{1}{\mu_0 \lambda_L^2}\mathbf{B}$$

where λ_L is the London penetration depth. Using $\nabla \times \mathbf{B} = \mu_0 \mathbf{j}$ from Maxwell's equations, taking the curl on both sides, and combining with the London equation we find $\nabla^2 \mathbf{B} = \mathbf{B}/\lambda_L^2$. This equation described the Meissner effect since a uniform solution is forbidden unless $\mathbf{B} = 0$. Solving the equation at a plane boundary with a magnetic field parallel to the surface

we see the field decays exponentially according to $B(x) = B(0)e^{-x/\lambda_L}$. In the context of BCS theory, $\lambda_L = (\epsilon_0 mc^2/nq^2)^{1/2}$ and is typically around 500 Å in a pure superconductor.

The Ginzburg-Landau (GL) is another phenomenological theory which is based on the the Landau theory of continuous transition. A macroscopic order parameter representing the condensate can be expressed as $\psi = |\psi|e^{i\phi}$, where $|\psi|^2 = n_s$. The GL equations can be derived using the variational principle and from these equations emerges two important characteristic lengths: the London penetration depth, λ_L, and the intrinsic coherence length, ξ_0. The coherence length describes the spatial extent of the Cooper pair. The ratio of these lengths is the dimensionless GL parameter $\kappa = \lambda_L/\xi_0$. It is shown that for type-I superconductors, $\kappa < 1/\sqrt{2}$, and for type-II superconductors, $\kappa > 1/\sqrt{2}$. This is the so-called "clean limit" when the electron mean free path, ℓ, is larger than the coherence length. In the "dirty limit" for small ℓ the GL parameter reduces to $\kappa = \lambda_L/\ell$.

A band gap in the superconducting state is implied by the existence of a critical temperature (and magnetic field) as well as the exponential increase in heat capacity near the critical temperature. Direct measurements of the band gap, $E_g(T)$, find that it decreases towards zero at T_c and that its maximal value $E_g(0)$ scales linearly with T_c according to $E_g \approx 3.5kT_c$. The weakening E_g with temperature suggests a binding energy and therefore there are two or more bound particles in the superconducting state. Indeed, Cooper showed that arbitrarily small attractions between electrons in a metal allows electron to form bound pairs with individual binding energies of Δ_{SC}. These Cooper pairs are quasi-bosons and no longer obey the Pauli exclusion principle, thus they condense to a ground state of paired electrons creating a superconducting gap $E_g = 2\Delta_{SC}$. The concept of a condensate forming due to coupling of electrons to a bosonic mode was initially described by BCS theory. The theory is general and the boson mode is not specified. As well, BCS theory is only valid in the weak coupling limit when the coupling parameter, λ, describing the strength of the electron-boson attractive interaction is small ($\lambda << 1$). Other theories were later derived from BCS theory which can describe an arbitrarily strong electron-boson coupling in superconductors [22].

Experiments using different isotopes of elements found that T_c is inversely proportional to the square of the isotopic mass. This result suggested that electron-phonon coupling provides the "glue" for Cooper pairs in these materials. Indeed, BCS theory with phonons finds a BCS condensate with Cooper pairs forming a singlet state with opposite momentum and spin. This phonon-mediated, *s*-wave superconductivity described by BCS theory or its extensions is now known as classical, or conventional, superconductivity. The predictions from BCS theory explain qualitatively most of the results found in conventional superconductors, ranging from the Meissner effect to the isotope effect.

I.4 Unconventional superconductivity

Unconventional superconductors possess all the physical properties outlined in the previous chapter, however they can no longer be described using BCS theory (or its derivatives) with *s*-wave, phonon-mediated pairing. As well, they are usually not well-described by GL theory since they typically have small intrinsic coherence lengths such that $\kappa >> 1$. It is generally agreed nonetheless that a condensation of bound Cooper pairs is still the driving force behind their superconductivity. However, the boson(s) involved in the Cooper pairing in each individual material/class is still under debate and includes magnetic, valence, and

nematic fluctuations. Unconventional superconductors are also usually non-isotropic, that is the symmetry of the wave function of the Cooper pairs has higher angular momentum such as p-wave or d-wave, rather than the isotropic s-wave pairing usually found in conventional superconductors.

I will discuss three classes of unconventional superconductors in historical order: heavy-fermion, cuprates, and Fe-based superconductors. The heavy-fermion systems are presented briefly since a number of these systems have ferromagnetism bordering superconductivity like in ϵ-iron. The cuprates will be discussed, mainly in the context of hole-doped cuprates, with a focus on their antiferromagnetic order which persists upon doping as magnetic excitations. In general, magnetic excitations are thought to play an important role in the Cooper pairing of the cuprates. Finally, the Fe-based superconductors will be discussed emphasizing their differences with the cuprates. Unlike the cuprates the Fe-based superconductor parent compounds are multiband "bad" metals, but like the cuprates they have a quasi-2D structure and antiferromagnetism near superconducting order. These systems have the added complexity of nematic order, which some theories suggest could also be an important ingredient for their superconductivity. These are just three classes of unconventional superconductors which show the intimate connection between magnetic and superconducting order, however the same is seen in all the other known unconventional superconductors.

I.4.1 Heavy fermion superconductors

The review of Steglich et al. [23] was used as the primary reference for this section.

Heavy fermion systems are intermetallic compounds which contain rare earth or actinide elements. The $4f$ or $5f$ valence electrons are in partially-filled bands which act as localized moments due to the small extent of the f-orbitals. These moments interact with the conduction electrons through the the exchange J in two different manners. The first interaction is the so-called Kondo effect where the conduction electrons are polarized via the exchange to compensate the moment and form non-magnetic singlet states. The second effect is the Rudermann-Kittel-Kasuya-Yosida (RKKY) interaction which couples neighboring f moments indirectly through the conduction electrons via the exchange leading to (anti)ferromagnetic ordering.

Both of these interactions have characteristic temperatures which scale with J. Furthermore, the exchange J can be varied with pressure and by exploring the pressure-temperature phase diagram we find that the system can be tuned to be magnetic or non-magnetic. As the boundary between these two regions approaches 0 K a magnetic quantum critical point (QCP) exists where the two ground states are degenerate leading to quantum magnetic fluctuations [25]. Superconductivity usually exists at these QCPs and its origin is theorized to be due to the magnetic fluctuations, although further research is still needed. The intersection between antiferromagnetism and superconductivity at a QCP can be seen for $CePd_2Si_2$ in Fig. I.5. In this figure we also see the case of UGe_2 which has ferromagnetism near the superconducting dome, although the position of the two cannot be explained by the QCP concept.

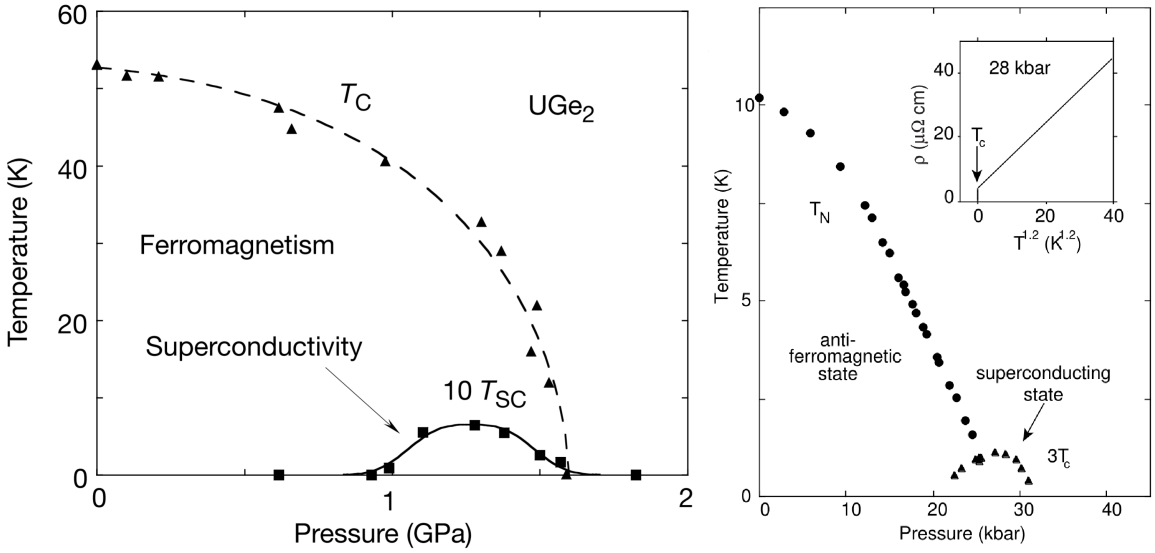

Figure I.5: Temperature-pressure phase diagrams of UGe_2 on the left [24] and $CePd_2Si_2$ on the right [25]. Superconductivity emerges as the anti(ferromagnetism) ordering temperature tends towards absolute zero.

I.4.2 Copper oxide superconductors

The reviews of Orenstein & Millis [26], Scalapino [27], Tranquada [28], and Keimer et al. [29] were used as the primary references for this section.

The copper oxide, or cuprate, superconductors' crystal structures are based on the cubic perovskite structure with tetragonal or orthorhombic distortions (Fig. I.6). This structure is layered, or quasi-2D, and its key feature is the CuO_2 planes where superconductivity occurs. The number of directly adjacent CuO_2 planes can vary for different cuprates and an increased number of planes is known to increase the T_c of the materials up until 3 layers. The copper oxide planes are separated by metal oxide layer, also known as the "charge reservoir" layer since chemical substitution, varying oxygen content, and/or creating vacancies in this layer transfer electrons or holes to the CuO_2 layers via the weak ionic bonds.

The cuprates can be divided into two classes based on whether they are electron- or hole-doped. I will focus on the latter class, using the prototypical La_2CuO_4 system as a concrete example since its parent compound at ambient temperature has a similar structure to the $Ca_2CuO_2Cl_2$ system which I studied (Fig. I.6). The La_2CuO_4 system can be doped in various ways, however we will focus on chemical substitution of La by Sr, i.e. $La_{2-x}Sr_xCuO_4$. The divalent Sr ions contribute one less electron than the trivalent La ions. The CuO_2 subunit has a formal charge of 2- and can therefore donate an electron to the charge reservoir layer to balance the charge difference due to substitution, effectively hole-doping the CuO_2 planes. The density of holes (electrons) per Cu is denoted a p (n), or more generally as the carrier concentration x.

The important phases of the hole-doped cuprates are shown in the temperature and carrier concentration phase diagram in Fig. I.7. The parent compound in cuprates is an an-

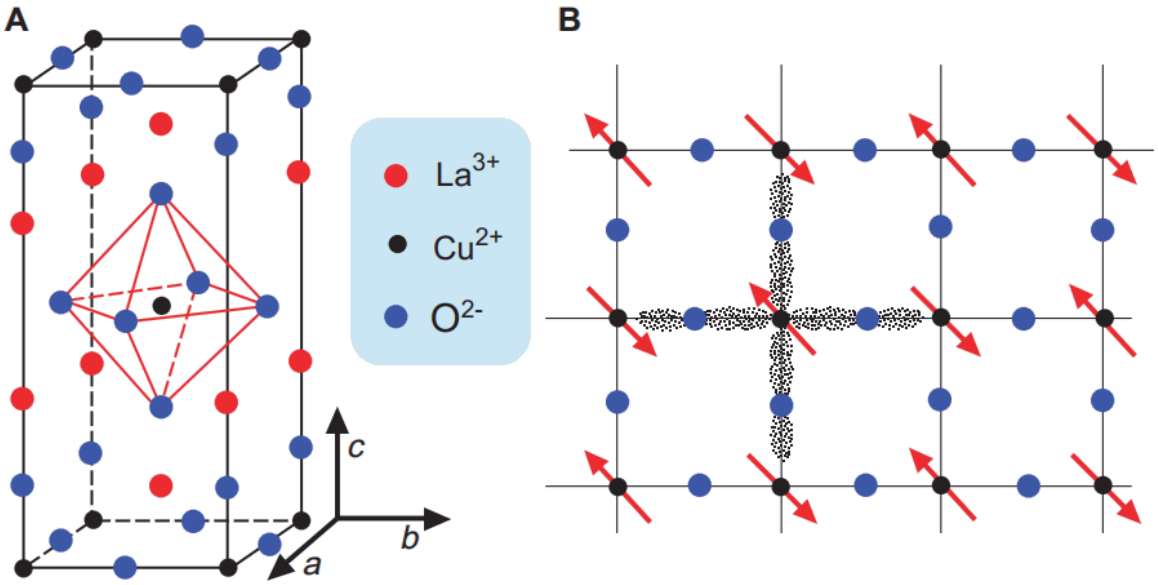

Figure I.6: Diagram from Ref. [26]. (A) Crystal structure of La_2CuO_4 parent compound (B) Schematic of CuO_2 plane which is believed to be the seat of superconductivity. Red arrows indicate antiferromagnetic alignment of neighboring spins in parent compound. The speckled shading indicates extent of O $2p_\sigma$ orbitals, which are important for superexchange in the parent compound and carrier motion in the doped compound.

tiferromagnetic charge-transfer insulator (see further below). At low temperatures, the antiferromagnetic order is rapidly destroyed upon doping with holes (x = 0.02 in $La_{2-x}Sr_xCuO_4$). The introduction of even more holes into the CuO_2 planes eventually leads to superconductivity. The superconducting critical temperature T_c forms a dome shape with a maximum around x = 0.16. Finally, the cuprate enters a Fermi liquid regime ("normal metal") after enough charge carriers are introduced into the CuO_2 planes. There are two other phases above T_c, the so-called pseudogap and "strange metal" phases. The former is characterized by the opening of a soft gap on the underdoped side of the phase diagram below a crossover temperature T^* which is well above T_c in the underdoped side of the phase diagram. Transport measurements in the strange metal phase shows that it exhibits non-Fermi liquid behavior which is consistent with 2D antiferromagnetic fluctuations within this region.

This phase diagram is intentionally simple and shows all the main features of the hole-doped cuprates. However, there are many aspects of the hole-doped cuprate phase diagram which remain controversial and are beyond the scope of this thesis. For example, the temperature behavior of the pseudogap phase varies depending on the author. The temperature T^* will either continue down through the superconducting dome towards a QCP at absolute zero, or it will follow the T_c dome and disappear upon entering the normal metal phase. The green region in Fig. I.7 represents a complicated 2D short-range magnetic order which persists after the lose of 3D commensurate magnetism due to the strong in-plane exchange. As well, charge order seems ubiquitous in the hole-doped cuprates and is observed in this underdoped region of the phase diagram. The properties of these spin- and charge-density

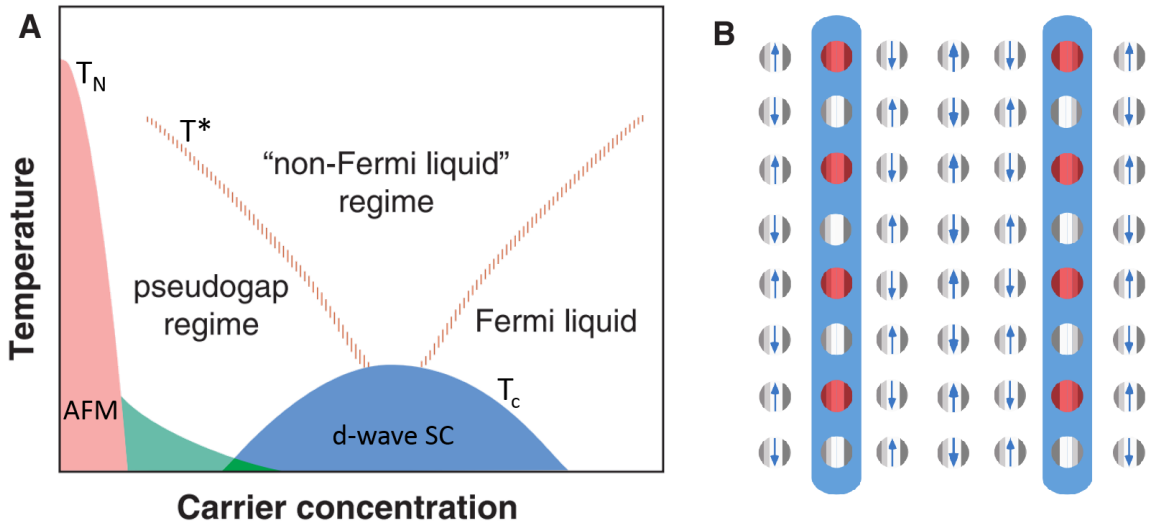

Figure I.7: Diagram modified from Ref. [26]. (A) Schematic phase diagram of hole-doped cuprate. The pink area is the long-range commensurate antiferromagnetic (AFM) phase delineated by T_N. The blue area is the d-wave superconducting (SC) phase delineated by T_c. The SC phase has a maximum at an optimal doping of roughly x = 0.16 hole concentration and the left and right sides are referred to as underdoped and overdoped respectively. The green area is a 2D spin density wave which exists between AFM and SC phases, and in some materials even extends into the SC phase. The crossover temperatures indicating new electronic properties in the normal state are shown as shaded lines. (B) Illustration of stripe ordering with excess holes forming stripes. Oxygen ions have been omitted and silver (red) indicates one (two) holes in the $3d_{x^2-y^2}$ orbital of the copper ions. Therefore the stripes have $1e^-$ per two Cu sites, or in other words the $3d_{x^2-y^2}$ band is quarter-filled in these stripes. The spin direction is shown by blue arrows and we can see that the stripes form an antiphase boundary for the spin density wave.

waves (SDW/CDW) in the underdoped region depends on the cuprate and also varies with the quality. In the $La_{2-x}Sr_xCuO_4$ system there are fluctuating "stripes" observed as shown in Fig. I.7. The excess holes tend to localize in stripes which separate domains of locally commensurate SDW. These stripes arise from frustration of the desire of holes to be separated from local spins and long-range Coulomb repulsion. The connection between stripes and superconductivity is still an open question, however static stripes seem to compete with the superconducting state. Stripes can become pinned due to structural distortions, such as when Nd is substituted for Sr in $La_{2-x}Sr_xCuO_4$, as well as in general at x = 1/8 doping which is commensurate to the lattice for one hole per two sites in a stripe. At this doping, there is a lowering of the T_c, the so-called 1/8 anomaly, which seems to indicate a competition between long-range SDW/CDW order and superconductivity. Nonetheless, a role in the superconducting mechanism for the short-range SDW/CDW is still debated.

The weak bonding out of the CuO_2 plane leads to a distortion of the octahedral ligand coordination of copper. The out-of-plane ligands (oxygen in La_2CuO_4), the so-called apical ligands, have bond lengths which are longer than in-plane leading to distorted octahedra

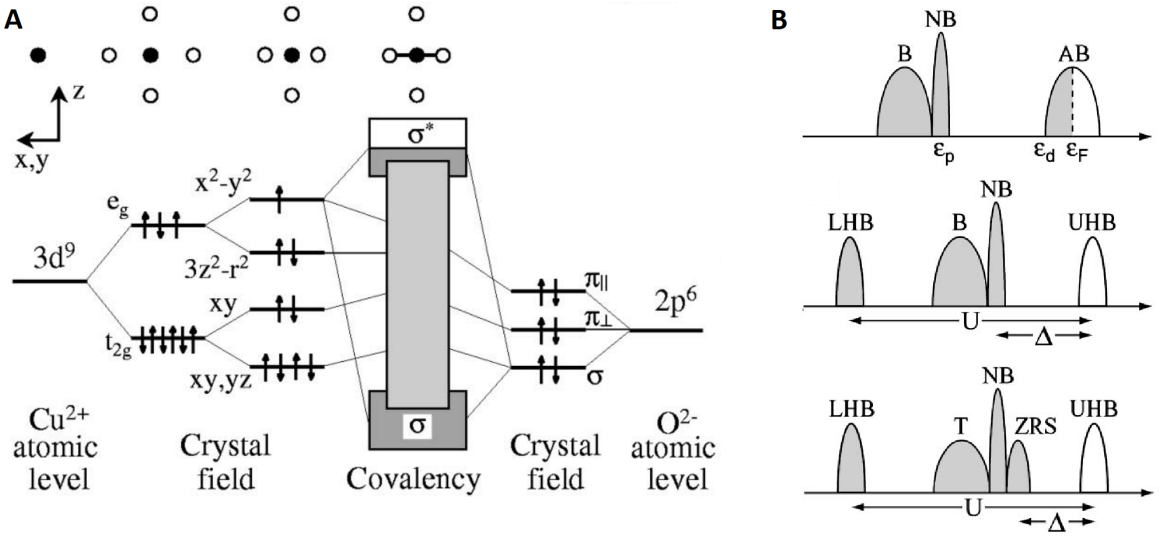

Figure I.8: (A) Energy level diagram in undoped parent compound showing the crystal-field splitting and hybridization which creates the Cu-O bands [27]. Hybridization of the Cu $3d_{x^2-y^2}$ and O $2p_\sigma$ atomic orbitals create σ^* anti-bonding (AB) and σ non-bonding (NB) bands separated by a charge transfer energy Δ. (B) The anti-bonding band is separated into a lower and upper Hubbard band (LHB and UHB) due to electronic correlations U. The cuprate parent compounds are charge transfer insulators ($U > \Delta > W$) because the gap is determined by the Δ as the LHB lays below the NB band. Further hybridization of the UHB with the NB band causes a splitting of the NB band into triplet and Zhang-Rice singlet states.

which are elongated along the c-axis. This elongation lowers the energy of the $3d_{z^2}$ orbital and breaks the e_g degeneracy (Fig. I.2 & I.8), therefore in the undoped parent compound the $3d^9$ electronic configuration leads to a single hole in the $3d_{x^2-y^2}$ orbital. Hybridization of this orbital with the O $2p_\sigma$ orbital creates an anti-bonding (AB) band at the Fermi level separated by the charge transfer energy Δ from the non-bonding (NB) band. According to band theory, the half-filled AB band at the Fermi level indicates a paramagnetic metal. However, the AB band is split into a lower and upper Hubbard band (LHB & UHB) due to the on-site Coulomb repulsion. The process by which the cuprates become charge transfer insulators is illustrated in Fig. I.8.

A three band Hubbard model should be used because of the hybridization, however a single band Hubbard model captures the insulating antiferromagnetic behavior of the parent compounds. The bandwidth in the tight-binding approach for a 2D lattice is $W = 8t$. In the strong-coupling limit $U \gg t$ and therefore we see localized behavior ($U/W > 1$) as the electrons do not hop to avoid the energy penalty from double occupancy (U). We can rewrite the Hubbard model from Sec. I.2 considering only nearest-neighbor (NN) hopping:

$$\mathcal{H} = -t \sum_{\langle ij \rangle, \sigma} a^\dagger_{i\sigma} a_{j\sigma} + U \sum_i n_{i\uparrow} n_{j\downarrow}$$

Where $\langle ij \rangle$ indicates NN hopping. The antiferromagnetic ordering results from virtual hop-

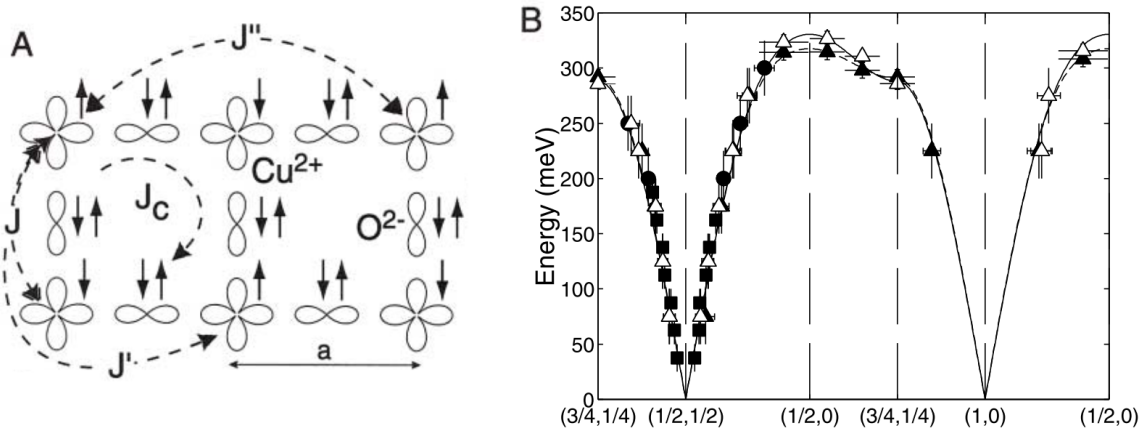

Figure I.9: Figures from Ref. [30]. (A) The exchange terms of an effective Heisenberg model given by expanding a perturbation series of the single band Hubbard model to four hopping terms. $J = 4t^2/U$, $J' = J'' = 4t^4/U^3$, and $J_c = 80t^4/U^3$. (B) Experimental spin wave dispersion measured at 10 K (open symbols) and 295 K (closed symbols). Solid (dashed) line shows the fit for T = 10 K (295 K) with the effective Heisenberg model parameterized by $U = 2.2$ and $t = 0.3$ ($U = 2.9$ and $t = 0.33$).

ping of electrons to neighboring sites and back in order to lower their kinetic energy since this is only possible with antiparallel NN alignment due to the Pauli exclusion principle. The effective Heisenberg exchange this creates between neighboring spins is the superexchange energy $J = 4t^2/U$. The electrons can move coherently which gives further exchange terms. Expanding the perturbation series of the Hubbard Hamiltonian to four hops (t^4) gives the exchange mechanisms shown in Fig. I.9. This figure also shows the agreement of the experimental spin wave dispersion with that calculated from spin wave theory using a Heisenberg model with the exchange values determined by U and t.

These antiferromagnetic correlations which persist even upon doping seem to have a strong impact on the electronic properties of the pseudogap and superconducting phases. Unlike conventional superconductors which have an isotropic gap (s-wave) the gap in the cuprates is anisotropic with a predominant $d_{x^2-y^2}$ type symmetry (d-wave). In this symmetry the gap energy is expressed by $\Delta_{SC}(\mathbf{k}) = (\Delta_0/2)[\cos(\mathbf{k_x}a) - \cos(\mathbf{k_y}a)]$, where $k = (k_x, k_y)$ is the wavevector in the Brillouin zone and $\Delta_0 = E_g$ is the maximal band gap value at absolute zero (Fig. I.10). From this equation we see that the gap is completely open parallel to the Cu-O-Cu bonds (anti-nodal direction) and it is closed at 45° from this along the nodal direction. This symmetry is observed over the entire superconducting dome, although the gap energy diminishes at higher dopings. The pseudogap is maximum along the anti-nodal direction like the superconducting gap, however it becomes gapless along the nodal direction forms so-called Fermi arcs. The evolution from a superconducting gap to a soft gap in the pseudogap regime along the anti-nodal direction is shown in Fig. I.10. The origin of this pseudogap is debated within the community, with some suggesting it is related to the antiferromagnetic fluctuations in this region, while others believe it is due to a different unknown competing order. The connection of the pseudogap with superconductivity is also heavily debated. Some authors believe that the pseudogap lies at the origin of superconductivity. There are

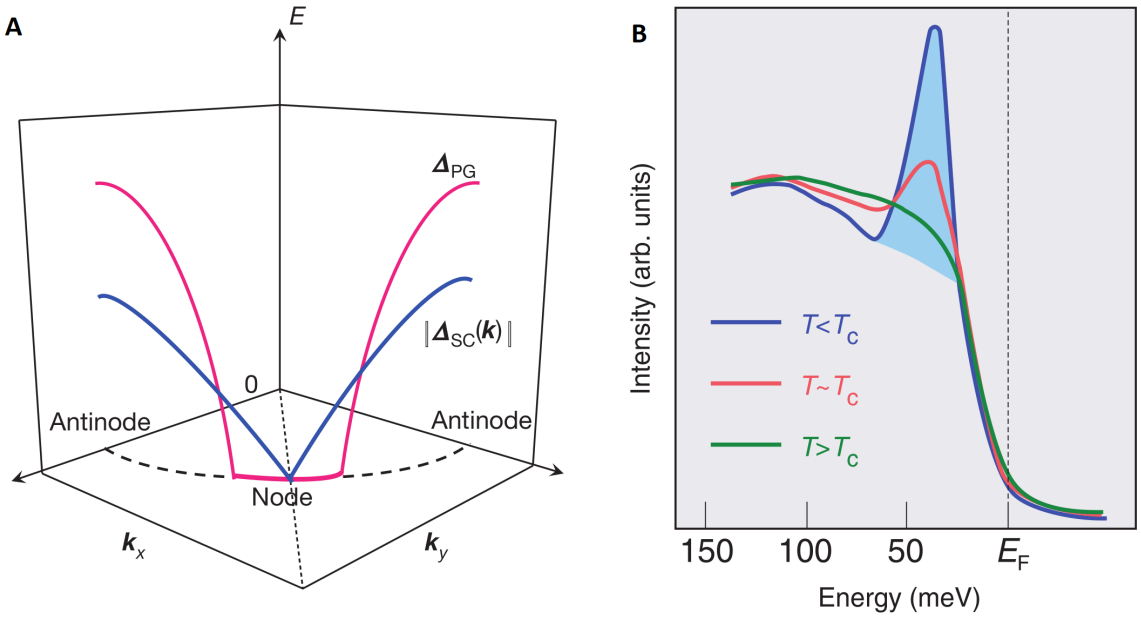

Figure I.10: (A) Angular dependence of the superconducting gap energy (blue) and pseudogap energy (red) in one quadrant of Brillouin zone [29] (B) Evolution of superconducting gap to pseudogap in underdoped cuprate shown by photoemission intensity from ARPES spectra near the anti-nodal point as a function of energy relative to the Fermi energy. [26]. The intensity is proportional to the electron population. The sharp peak in the superconducting region ($T < T_c$) is interpreted as a well-defined electronic excitation. This excitation disappears above T_c but a "soft" gap remains in the pseudogap region.

also many other theories regarding the origin of superconductivity in the cuprates, many of which rely on spin fluctuations as the bosonic glue for Cooper pairing.

I.4.3 Iron-based superconductors

The reviews of Paglione & Greene [31] and Chubukov & Hirschfeld [32] were used as the primary references for this section.

The iron-based superconductors (FeSC) can be separated into two classes: the iron pnictides and iron chalcogenides. The basic building block in both classes is a quasi-2D lattice of iron cations joined by either pnictogen (Group 15 elements: P or As) or chalcogen (Group 16 elements: Se, S, or Te) anions in a nearly tetrahedral coordination which creates a staggered arrangement of these anions above and below the iron plane (Fig. I.11). Much like the cuprates, these layers have strong covalent (and in FeSC also metallic) bonds and are believed to be the seat of superconductivity. Except in the 11 systems (FeSe, FeS, and FeTe), these layers are stacked together along the c-axis through ionic bonds to "blocking layers" consisting alkali, alkaline-earth or rare-earth and oxygen/fluorine atoms. All of the known structures, see Fig. I.11 for some examples, have a tetragonal structure at room temperature which distorts to an orthorhombic structure at lower temperature.

The arrangement of the pnictogen/chalcogen anions above and below the iron plane is

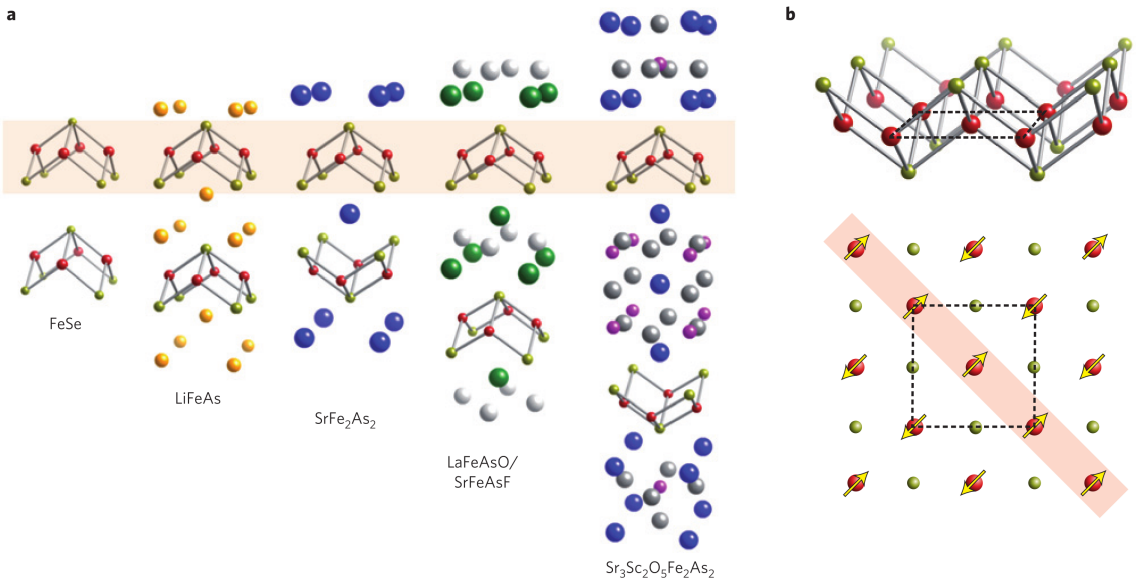

Figure I.11: Crystallographic and magnetic structures of the iron-based superconductors [31] (a) Representative examples of some FeSC families are shown from left to right: the 11, 111, 122, 1111, and quinternary families. (b) The iron layer common to all FeSC with pnictogen/chalcogen anions above and below the planes. The 2D unit cell is shown as a dashed line. The antiferromagnetic stripe structure is shown in the bottom right.

different than the planar CuO_2 planes (albeit there is slight buckling/distortions in some cuprates). In these layers there is strong metallic bonding between Fe-Fe and Fe-As sites, as well as interlayer As-As bonds in the 122 system, such that the geometry of the $FeAs_4$ tetrahedra is of integral importance to the electronic and magnetic properties in FeSCs. The tetrahedral bond angles in particular seem to be important for optimizing the T_c in these materials. Another difference with the cuprates is the fact that substitution can also occur directly in the iron layer.

The last major difference is that the FeSC parent compounds are metallic multiband systems (Fe^{2+}, $3d^6$), rather than insulating single-band systems (Cu^{2+}, $3d^9$) as in the cuprates. The electronic structure of FeSCs can be described as 2D metallic sheets made of hybrid bands from the Fe $3d$ states and the p orbitals of the anion sitting in a quasi-ionic framework from the blocking layers. The system is metallic although with a low carrier concentration and is therefore often called a "bad metal". The multiband nature is seen in the Fermi surface where there exists at least two hole pockets around $\mathbf{k} = (0,0)$ and two electron pockets at $\mathbf{k} = (\pm\pi,\pm\pi)$ in the folded Brillouin representation. This representation is used because there exists two inequivalent pnictogen/chalcogen anion sites above and below the iron plane as seen by the unit cell drawn in Fig. I.11 with two Fe atoms.

The FeSCs generic phase diagram is shown in Fig. I.13. The magnetic state at low temperature is commensurate antiferromagnetic ordering. An afm stripe configuration, as shown in Fig. I.11, is believed to be common to all FeSCs. The terminology spin density wave (SDW) is used in the phase diagram to emphasize the fact that it is itinerant magnetism rather than localized moments (as in the cuprates). The stripe configuration breaks spin

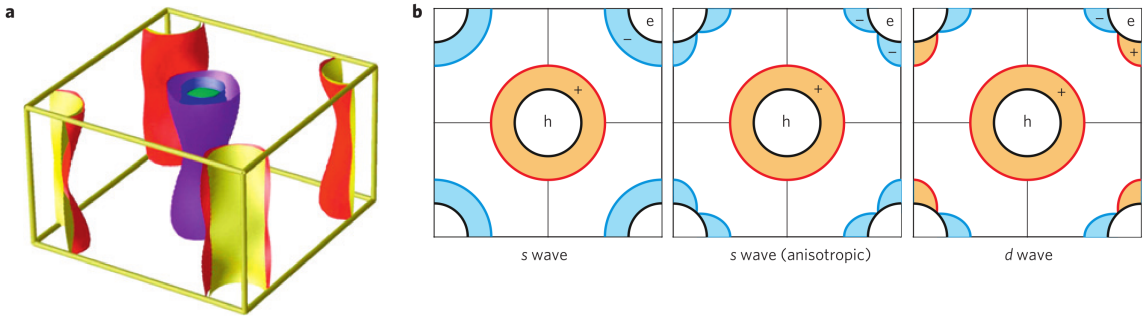

Figure I.12: Fermi surfaces and superconducting order parameter symmetry of $BaFe_{1.8}Co_{0.2}As_2$ [31]. (a) Fermi surfaces calculated with DFT show quasi-2D hole-like Fermi surface pockets (purple and blue) around the $\mathbf{k} = (0,0)$ and electron-like Fermi surface pockets at $\mathbf{k} = (\pm\pi, \pm\pi)$ (yellow and red). (b) Schematic 2D Brillouin zone projection with multiple bands reduced to a single hole (h) pocket and electron (e) pocket. Three possible ordering parameter symmetries are shown with the superconducting gap shown as shaded areas with red (hole) or blue (electron).

rotational symmetry, as well as an additional twofold discrete symmetry due to the two orthogonal directions along which the stripes may align. The lattice has an associated break in symmetry due to spin-orbit coupling and becomes orthorhombic in the magnetic phase (although some systems have a small region with SDW order and tetragonal symmetry preserved). In many FeSCs a so-called nematic phase precedes the SDW ordered phase, in which rotational symmetry is broken, yet time-reversal and translational symmetry are preserved. The origin of the nematic phase is debated between phonon, orbital, or spin fluctuation driven order. As a FeSC is tuned it will eventually enter a superconducting state.

The phase diagram can vary dramatically between different FeSC and the SDW, nematic, and superconducting orders can all coexist at low doping in some materials. One example is that in $LaFeAsO_{1-x}F_x$ the superconducting and magnetic phases are well separated. Another example is that FeSe without any tuning has its superconducting phase existing without SDW order (but with nematic order). The tuning in FeSCs is definitely not as clear in the cuprates, for example the phase diagram can be tuned with nominally isovalent substitution! It seems that the charge carrier concentration, structural parameters, disorder, chemical bonding, and density all play an important role in tuning the FeSC and that the key effect is changing the relative sizes of the hole and electron pockets.

The symmetry of the superconducting gap is still debated among the FeSC community (Fig. I.12). Two proposed symmetries are the isotropic s-wave symmetry as in conventional superconductors or the $d_{x^2-y^2}$ symmetry as in the cuprates. However, the multiband nature of the FeSCs lends itself to another symmetry known as $s^{\pm}$ which is currently the leading candidate. This is an anisotropic s-wave state in which the superconducting order parameter changes sign between electron and hole Fermi surfaces. The FeSCs are much more varied than their cuprate cousins and thus the suggested theories about their superconductivity are likewise extremely varied. Nonetheless, it seems likely that the antiferromagnetic correlations play an important role.

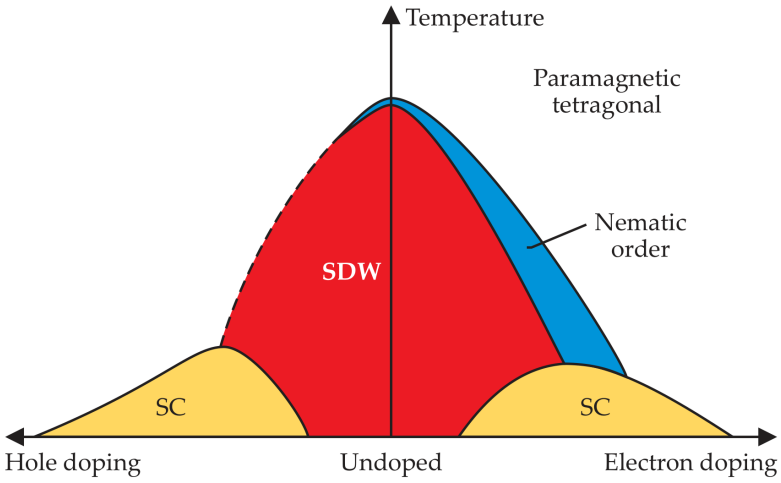

Figure I.13: Schematic temperature-doping phase diagram of FeSCs. A commensurate antiferromagnetic spin density wave (SDW) phase is shown in red, superconducting phase in yellow, and nematic phase in blue. A second-order (first-order) transition is shown as dashed (solid) lines. The three phases can coexist at small doping and low temperatures.

Chapter II

Experimental methods

II.1 Introduction

The book by Silvia [23] and the review by Rueff & Shukla [15] were used as the primary references in this section.

Scattering techniques are powerful tools used regularly in condensed matter physics to study a material's electronic/magnetic structure and dynamics. They work by illuminating a sample with a probe and then observing how the probe is altered upon leaving the material, or observing what new particles are created. In this thesis we only consider when the incident and scattered particle are the same type (see Fig. II.1 for simplified scheme). The most popular probes in condensed matter physics are neutrons, photons, and electrons. These probes each have their own strengths and weaknesses and together they form an important toolkit for the condensed matter physicist.

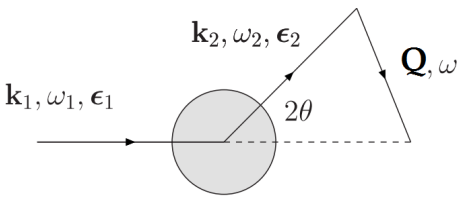

Figure II.1: A typical scattering process where the incident and scattered particle are of the same type [15]. The incident (scattered) particles momentum ($\hbar\mathbf{k}$), energy ($\hbar\omega$), and polarization (ϵ) are shown as 1 (2). The transferred momentum and energy are given by $\mathbf{Q}$ and ω respectively.

The momentum and energy transferred during the scattering process is expressed as $\hbar\mathbf{q} = \hbar\mathbf{k_1} - \hbar\mathbf{k_2}$ and $\hbar\omega = \hbar\omega_1 - \hbar\omega_2$ respectively. The scattering can be elastic ($|\mathbf{k_1}| = |\mathbf{k_2}|$) or inelastic ($|\mathbf{k_1}| \neq |\mathbf{k_2}|$), as well as either coherent or incoherent. The probes I used in this thesis were neutrons and x-ray photons, and the momentum condition for elastic scattering automatically implies $\omega_1 = \omega_2$ due to the energy-momentum relations for a non-relativistic neutron, $\hbar\omega = \hbar^2|\mathbf{k}|^2/2m$, and a photon $\hbar\omega = \hbar|\mathbf{k}|c$. Scattering with neutrons or x-rays are complementary and can probe different length/momentum and energy/time scales as

shown Fig. II.2. The length scale is important when performing coherent elastic scattering, which leads to the well-know phenomenon of diffraction due to constructive interference. In this case one should use a probe with a wavelength similar to the inter-atomic spacing, i.e. a few angströms. On the other hand, for inelastic scattering we are interested in the momentum and energy we can transfer to/from the sample. X-rays have energies well above the energy of any collective excitations and therefore are only limited by their resolution. Inelastic neutron scattering (INS) instruments have a much higher energy resolution, however advances in inelastic x-ray scattering (IXS) instrumentation are closing this gap, at least for energy ranges of collective excitations which interest us, such as phonons and magnons. On the other hand, x-rays have momentum restrictions in the soft x-ray regime. When x-rays scatter, $k_1 \approx k_2$, and the transferred momentum is $|\mathbf{Q}| \approx 2k_1 sin(\theta)$. The maximum momentum transfer in back scattering ($2\theta = 180°$) is $q = 2k_1$. For our Cu L_3-edge RIXS measurements (Sec.III.3) we have $\hbar\omega_1 = 930$ eV which corresponds to $q_{max} \approx 0.93$ Å$^{-}1$ which limits our access in the Brillouin zone (see Sec.III.4.2 for a comparison with other x-ray edges). Practically, neutrons are somewhat limited in energy for INS. Typically thermal neutrons of 15–100 meV are used which limits the energy transfer. To reach higher energies one can use epithermal neutrons but these experiments are demanding since the incident flux and interaction cross-section drop dramatically with increased energy. INS does not have any major limitation for momentum transfer in solids, but it is interesting to note the quadratic behavior in Fig. II.2 due to its kinematic relation.

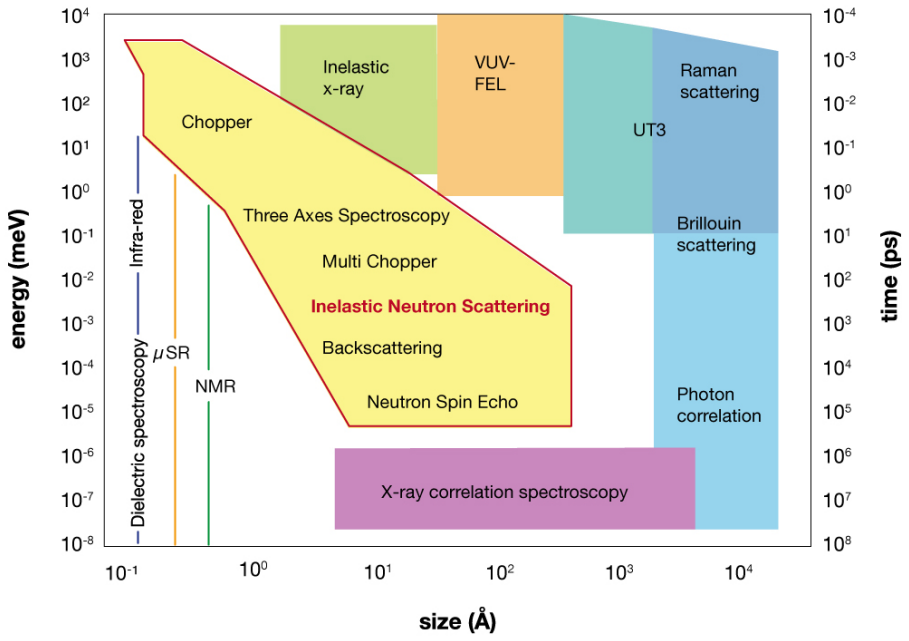

Figure II.2: Visualization of energy-momentum space available using a variety of techniques [33]. Momentum can be inferred from $k = 2\pi/size$, so that lower momentum is on the right of the figure and higher momentum is on the left.

Another key difference between neutrons and x-rays is their atomic scattering factors

(Fig. II.3). X-rays scatter off the electron clouds surrounding atoms and their atomic form factor scales roughly with the number of electrons Z. As well, the electron density is smeared in space such that the atomic form factor decreases at increased scattering angles. Neutrons have two separate scattering mechanism: nuclear and magnetic. They can scatter off the nucleus via the strong force or scatter off magnetic moments via a dipole-dipole interaction with the magnetic moment of the neutron. The nuclear scattering is constant in scattering angle since the nucleus at this scale is a point source. This constant atomic scattering factor, or scattering length b, is shown in Fig. II.3 for the coherent portion and we see there is no clear trend. This makes neutrons a powerful tool to study low-Z elements which are hard with x-rays. The magnetic scattering is from the valence electrons and therefore the scattering factor decreases with increased scattering angle. The magnetic and nuclear scattering at lower scattering angles are often comparable in neutron scattering. The last important difference between neutron and x-rays is their other interactions with matter. X-rays can interact with matter in other ways, such as the photoelectric effect, and are attenuated (hard x-rays less so) much more than neutrons. These effects also tend to produce heat in the sample which can lead to the destruction of the sample while neutron scattering is non-destructive.

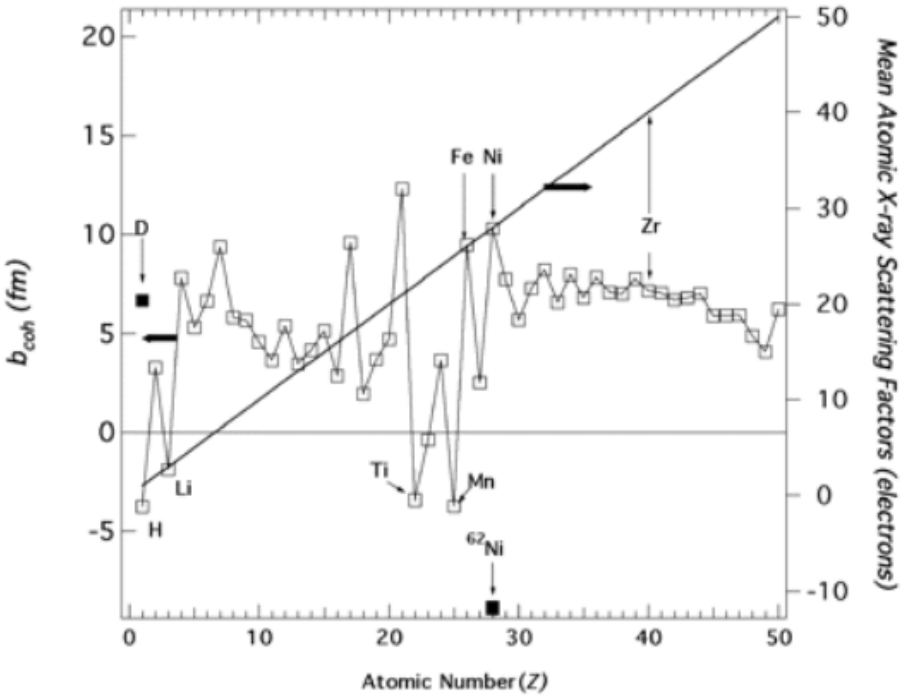

Figure II.3: A comparison of the scattering factors for neutron (nuclear) scattering and x-ray scattering [34].

The next sections will discuss x-ray core level spectroscopies (Sec. II.2) and neutron powder diffraction (Sec. II.3). The x-ray section discusses the three main techniques I used in general, and then in the specific context of the studies performed in this thesis. These techniques were x-ray absorption spectroscopy (Sec. II.2.1), x-ray emission spectroscopy (Sec. II.2.2),

and resonant inelastic x-ray scattering (Sec. II.2.3). I will discuss these techniques theoretically since a separate section is dedicated to the the discussion of x-ray generation and instrumentation, in the context of the GALAXIES beamline (Sec. II.2.4). A brief overview of neutron powder diffraction theory and instrumentation is presented in Sec. II.3. Finally, high pressure techniques will be introduced generally in Sec. II.4 and the use of diamond anvil cells for x-ray studies (Sec. II.4.1) and Paris-Edinburgh cells for neutron studies (Sec. II.4.2) will be discussed separately.

II.2 X-ray core level spectroscopy

The book by Silvia [23] and the review by Rueff & Shukla [15] were used as the primary references in this section.

The core level electrons are those which occupy completely filled inner bands well below the Fermi level, which are therefore not involved with bonding or electronic structure. We can excite or ionize these core level electrons with x-rays which have an energy higher than their binding energy. The binding energy of a specific core orbital is known as an "edge" due to the characteristic step when looking at absorption vs. x-ray energy graphs. In the x-ray community the core levels and associated fluorescence lines are named according to Barkla notation (Fig. II.4).

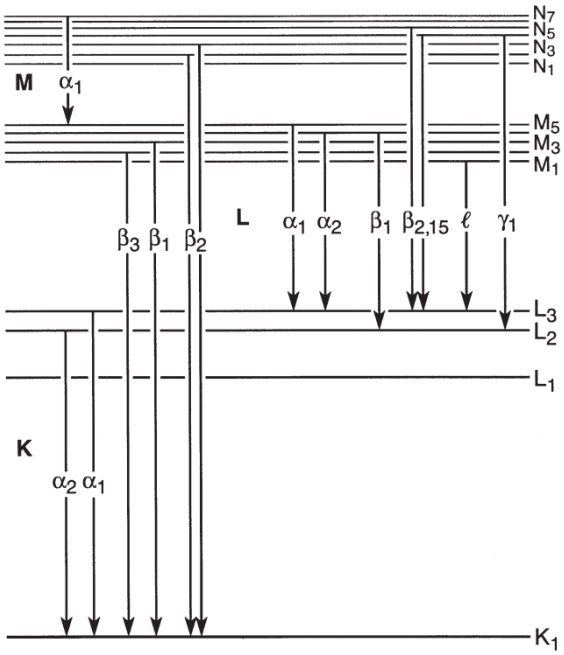

Figure II.4: Energy levels and associated transitions on a line diagram using Barkla notation [35].

X-ray core hole spectroscopies create a core hole, and thus an excited state, which then decays in order to fill the core hole. The creation and decay processes are shown in Fig. II.5, along with their associated spectroscopy techniques. In this thesis only photon-in photon-out

techniques will be considered. To create a core hole we promote a core electron either to an unoccupied valence level with an x-ray of the appropriate energy or we excite the electron into the continuum using an x-ray with an energy much larger than the absorption edge. The decay of a core hole occurs by x-ray fluorescence when an electron from a higher energy level fills the lower energy level core hole. This leaves a hole in the final state, but the atom will eventually return to its ground state through cascade of these events. These two processes can be studied as a function of energy in what is known as XAS and XES. The electron transitions are dominated by the electric dipole allowed transitions, however electric quadrupole transitions are important for many techniques. X-rays are roughly separated into soft and hard x-rays, which have a lower and higher energy respectively. They probe different core levels: for example, we used hard x-rays ($\approx$ 7112 eV) to measure at the Fe K-edge, while we used soft x-rays ($\approx$ 930 eV) to measure at the Cu L_3-edge. See Sec. II.2.4 for more information soft and hard x-rays.

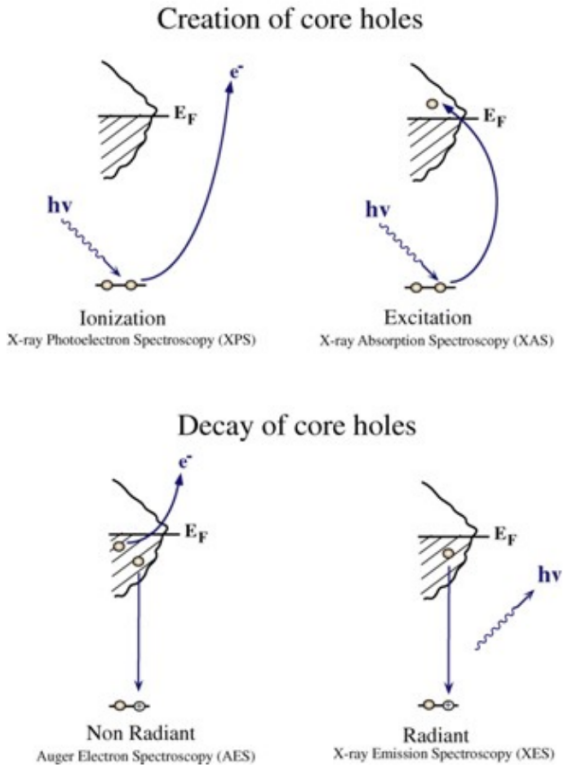

Figure II.5: X-ray core level spectroscopies involve the creation of core holes through ionization (photoelectric effect) or excitation and/or the decay of core holes, either through the Auger process or fluorescence [36].

The creation and destruction of core holes occurs on the same atom, therefore it is a local probe which is element- and orbital-selective. In the hard x-ray regime these photon-in photon-out techniques have the advantage of being compatible with challenging sample environments such as cryostats or high pressure cells. We leverage this advantage to measure Fe K-edge XAS and XES using a diamond anvil cell. Photon-in photon-out techniques also have the advantage of being bulk-sensitive since photons escape/enter the material with a

much larger penetration depth than electrons.

II.2.1 X-ray absorption spectroscopy (XAS)

The book by Silvia [23] and the reviews by Rueff & Shukla [15] and Glatzel & Bergmann [37] were used as the primary references in this section.

X-ray absorption spectroscopy is a photon-in photon-out technique which provides information about the local electronic and structural environment. The technique can be performed by measuring the transmission through a sample. And alternate method is to use the fluorescence or electron yield from the sample as a proxy for absorption. The technique is traditionally separated into regions as shown in Fig. II.6 for XAS at a K-edge. The lower energy side of the spectrum corresponds to transitions into unoccupied electron levels and is known x-ray absorption near-edge spectroscopy (XANES). The higher energy side of the spectrum corresponds to multiple-scattering interference between photo-electrons and is known as x-ray absorption fine structure (EXAFS).

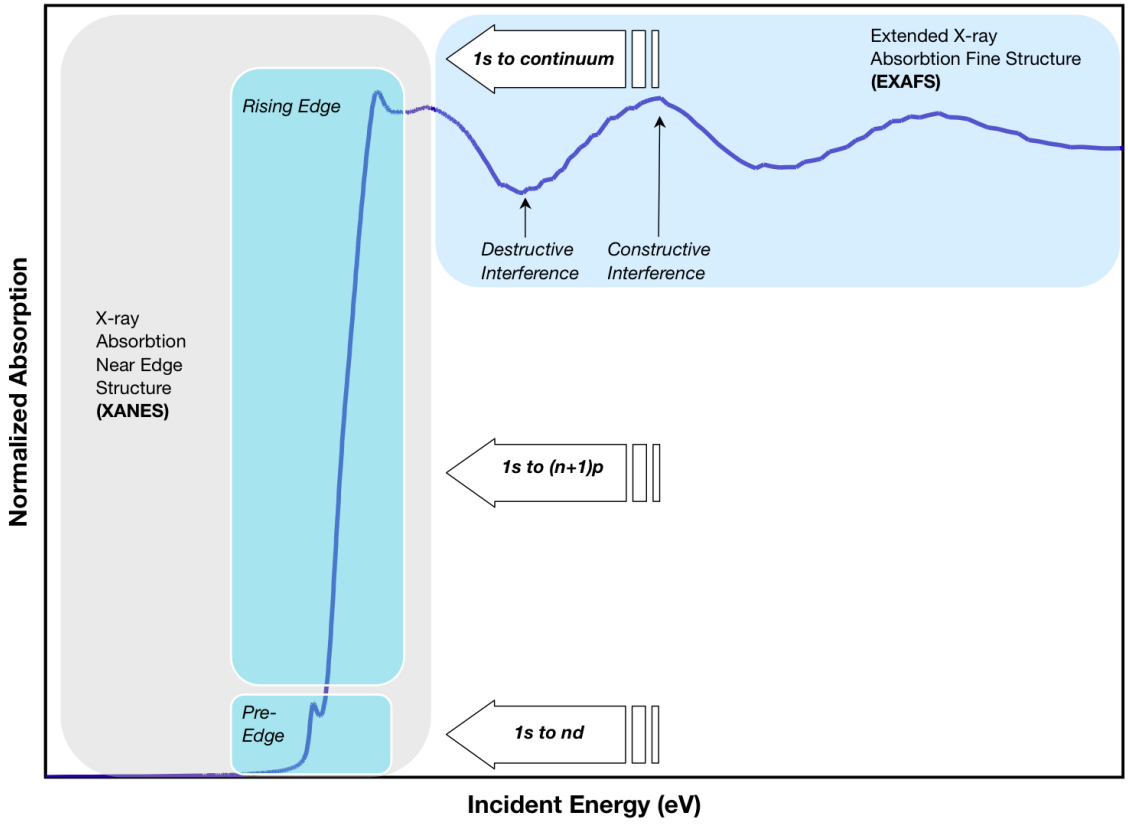

Figure II.6: An example of a K-edge x-ray absorption spectrum [38]. The XANES and EXAFS regions are shown, as well as the specific transitions which are probed in the pre-edge and rising edge regions.

The XANES region provides important information about the local electronic structure, including chemicals bonds and valence, oxidation state, types of ligands, and site symmetry.

The interpretation is not straight-forward and requires calibration to well-known reference compounds with the same target atoms. In $3d$ transition metal compounds, the pre-edge is due to $1s \rightarrow 3d$ quadrupole transitions or $1s \rightarrow 3d$-np hybrid bands. The pre-peak is intimately related to the atom's local symmetry — as the atom becomes less centrosymmetric the pre-peak increases due to increased mixing of the d and p states. The EXAFS region provides information about the local structure such as the number and distance of neighboring atoms. The interpretation of EXAFS spectra is not straight-forward either, however in general the interference oscillations distance relates to the distance of neighboring atoms and their amplitude relates to the number of nearest neighbors. A Fourier transform of the EXAFS region gives directly the radial distribution function. More insight into both these regions can be gained by using first-principles modeling software, such as FDMNES.

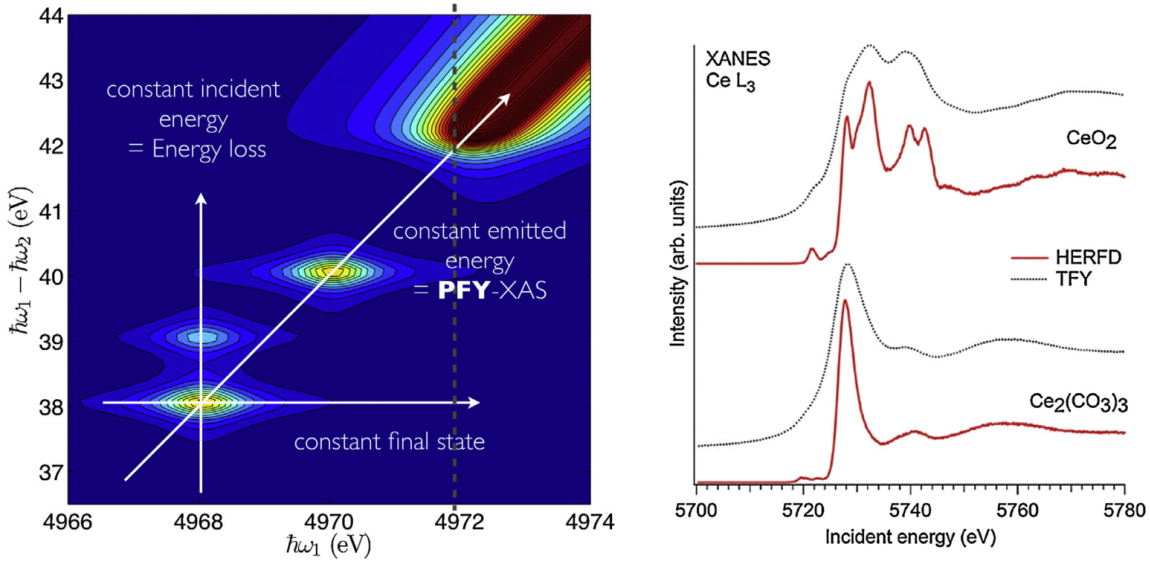

Figure II.7: (Left) A typical RIXS intensity map as a function of incident ($\hbar\omega_1$) and transfer ($\hbar\omega_1 - \hbar\omega_2$) energies [39]. When we perform RIXS to study elementary excitations, such as magnons, we use a constant incident energy at a specific resonance (4968 eV in this example) and measure the energy loss in order to find the energy of the elementary excitations. To perform PFY-XAS we look at a fluorescence line (constant emitted energy) such that as we scan the incident energy we move diagonally along the RIXS map. (Right) Measurements with the PFY and TFY modes in Ce L_3-edge XAS Ce oxides highlight the intrinsic line sharpening effect due to the shallow core hole in the final state when performing PFY-XAS.

PFY-XAS at the Fe K-edge

We performed our XAS measurement in the partial fluorescence yield (PFY) mode instead of total fluorescence yield (TFY). The technique is shown in Fig. II.7 along with a comparison between the two modes. We measured the K$\beta_{1,3}$ fluorescence (see Sec. II.2.2) as we scanned the incident energy across the Fe K-edge. This technique improves the resolution of XAS beyond the natural lifetime broadening and is therefore also referred to as high energy-resolution fluorescence-detected X-ray absorption spectroscopy (HERFD-XAS). The

sharpening effect is due to the appearance of the final state lifetime in the resonant inelastic x-ray scattering (RIXS) cross-section.

In the Kramers-Heisenberg formula the lifetime broadening is given by Lorentzian functions with a width of Γ_n and Γ_f for the intermediate and final states respectively. The total lifetime broadening with PFY-XAS is approximately $\Gamma_{PFY} = (1/\Gamma_n^2 + 1/\Gamma_f^2)^{-1}$. Generally the intermediate state has a shorter lifetime than the final state, or in other words $\Gamma_n >> \Gamma_f$. This creates a sharpening effect as the total lifetime broadening is dominated by the smaller lifetime broadening of the final state, $\Gamma_{PFY} \approx \Gamma_f$. It is important to note that PFY-XAS does not measure exactly the true XAS, since subtle interference effects between the absorption and emission paths at resonance can appear.

II.2.2 X-ray emission spectroscopy (XES)

The book by Silvia [23] and the reviews by Rueff & Shukla [15] and Glatzel & Bergmann [37] were used as the primary references in this section.

We consider here the non-resonant case of x-ray emission spectroscopy. A nice analogy is that just as the previously discussed XAS measured the unoccupied states of our system, XES measures the occupied states of our system. The process starts by the creation of a core hole either by excitation or ionization (Fig. II.5) which creates an intermediate state. The intermediate state can take on different electronic configurations due to interactions with the core hole. The excited state decays as an electron in an occupied state decays to fill the initial core hole and emits an x-ray. The decay process can also be accompanied by final state effects due to Coulomb and exchange interactions with the core hole in the final state. This XES process is insensitive to momentum transfer since the coherence between the incident and emitted x-ray is lost, thus it does not appear in the XES cross-section.

Fe Kβ spectroscopy

Fe Kβ spectroscopy is one example where final state effects are very important. The process for an isolated Fe^{3+} ion ([Ar]$3d^5$ electron configuration) is shown in Fig. II.8. In this case the $3p$-$3d$ exchange interaction creates a lower energy satellite peak. The $3p$ core hole left in the final state acts a local probe of the unpaired $3d$ electrons (Fig. II.9). The intense mainline is called K$\beta_{1,3}$ and the satellite is called the Kβ' peak. The situation in real materials is much more complex. The process can be calculated in $3d$ metal oxides using the crystal field multiplet approach, which finds a complex multiplet distribution. Nonetheless, experimental studies of $3d$ metal oxides find that the satellite intensity scales almost linearly with the $3d$ spin angular momentum and can be extracted using a phenomenological approach (see below). As well, spin-resolved XAS studies have shown the satellite region to be dominated by transitions of unpaired $3d$ spin-up electrons. These facts leads us to justify our phenomenological approach to Fe and FeSe, even though they are much more complicated being itinerant systems with somewhat localized $3d$ orbitals. Our results are only semi-quantitative but the trends we find seem to support this assignment. Finally we stress that this technique measures the unpaired $3d$ occupation only, therefore it provides no information about magnetic moment's direction or spatial correlations.

The phenomenological approach that was popularized for the $3d$ transition metal oxides is the integrated absolute difference (IAD_C) [40]. The subscript C refers to aligning the

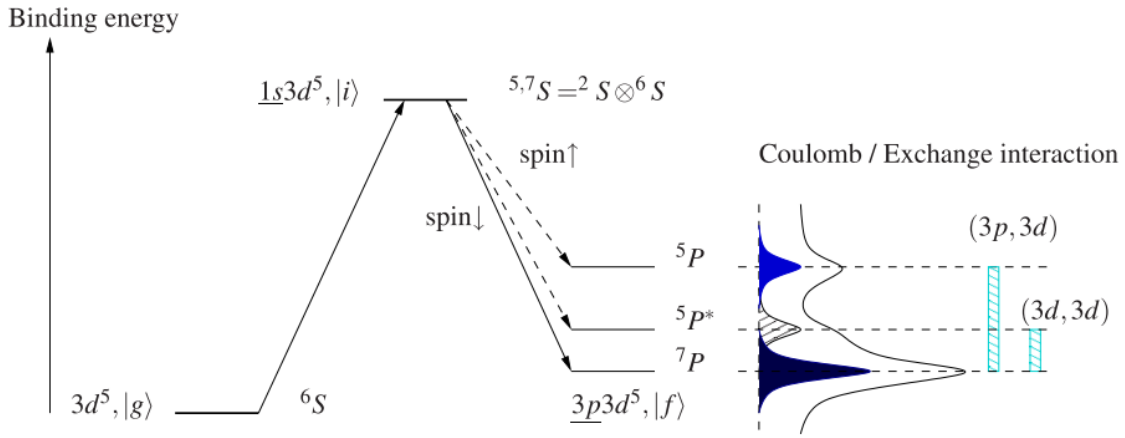

Figure II.8: An idealized Kβ emission process shown in a configuration level scheme for a $3d^5$ ion [15]. Note the difference in terminology: initial, intermediate, and final states denoted with g, i, and f instead of i, n, f.

spectra using the center of mass and normalizing by the area. This technique is exactly how it sounds: one takes the difference of a spectra with a reference spectra (i.e. the gray area in Fig. II.9), takes the absolute value, and integrates. It is shown that during a low to high spin transition in $3d$ transition metals oxides, this technique is the best at determining the proportion of coexisting high spin and low spin states during a transition (Fig. II.9). The derivation is exact in this coexisting case and it is shown that the signal to noise ratio is reduced by using the whole spectra.

Using the notation of Vanko *et al.* shown in Fig. II.9, we used a variation of the $\mathrm{I}(\mathrm{K}\beta')_{Pm}$ technique to treat the Kβ XES data from our high-pressure experiments on Fe and FeSe. This technique uses the integrated intensity of the difference in the satellite region, where the subscript Pm indicates that first the spectra are shifted to the Kβ peak and normalized to its maximum. We actually performed a fit of the difference peak to better characterize the effects of statistical noise and follow changes in its width and position. Nonetheless the fit was performed with a Gaussian function whose width did not vary, therefore its is equivalent to the $\mathrm{I}(\mathrm{K}\beta')_{Pm}$ technique.

We believe that $\mathrm{I}(\mathrm{K}\beta')_{Pm}$ is superior to the IAD_C technique for treatment of our compressed Fe and FeSe data for multiple reasons. First, we are not measuring coexisting spin states during a transition, but rather slow changes in the $3d$ occupation as the $3d$ bands broaden under pressure. The exact treatment of IAD_C does not apply in this case. The second reason is that other high pressure studies show pressure-induced effects on the Kβ mainline unrelated to the $3d$ spin polarization, which tend to dominate and have an effect of "stretching" the pressure transition region seen with XES versus other measurements such as Mössbauer spectroscopy or XMCD. The center-of-mass and area are affected much more than Kβ peak intensity and position by small variations in the background unrelated to the XES process. This is even more important when combining spectra from different experimental runs. An improper shift of normalization leads to large dichoric effects in the difference spectrum around the Kβ mainline unrelated to the spin state. In the end, we are not claiming our measurements are quantitative since there is no theoretical basis. However,

on a semi-quantitative level the I(Kβ')$_{Pm}$ technique seems superior. We also note that even with the 3*d* transition metal oxides it was indistinguishable from IAD$_C$ for a shoulder-like satellite with high statistics. The Kβ spectra of itinerant systems needs a more theoretically grounded basis, which will soon be possible with first-principles computer codes such as OCEAN which use ground-state density-functional theory and the Bethe-Salpeter equation to simulate x-ray emission spectra [41, 42]. These studies will need experimental support, yet getting synchrotron time for them might be difficult, therefore the advent of lab-based spectrometers is a serendipitous development.

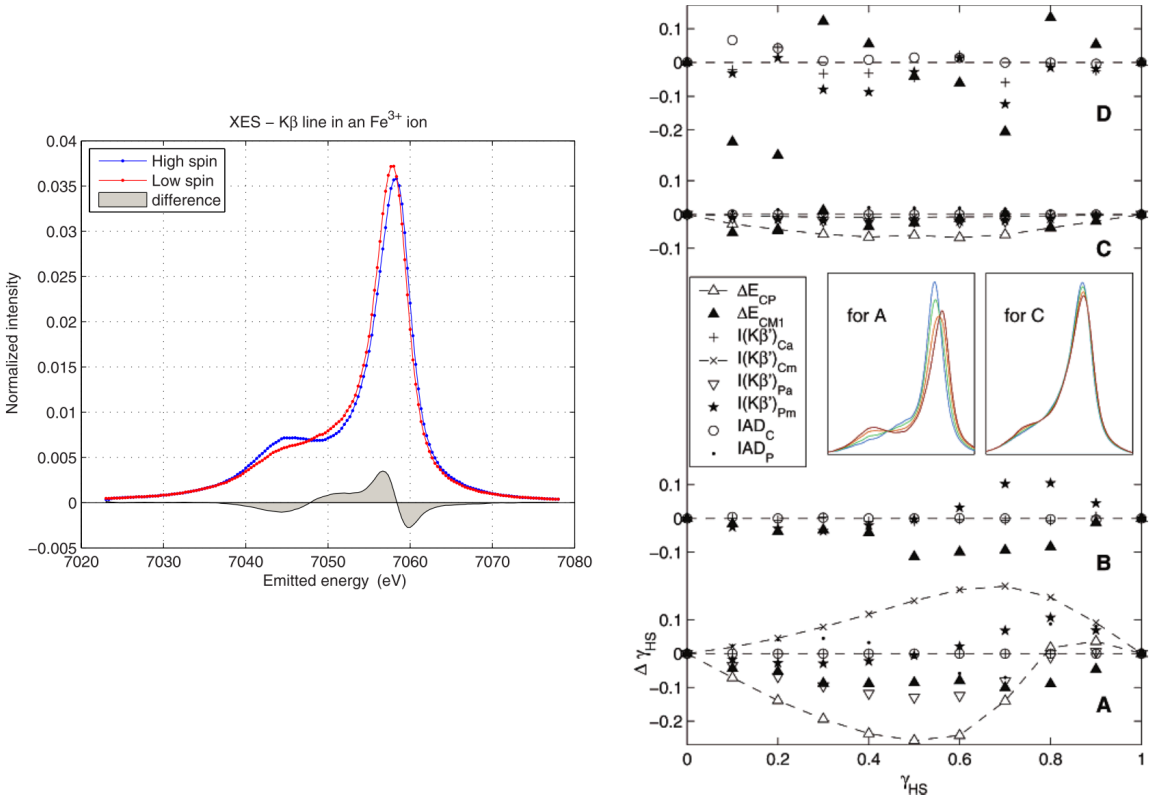

Figure II.9: (Left) An example of a Fe Kβ emission spectra measured in the high-spin and low-spin state of a $3d^5$ Fe-based molecular complex [15]. The spectra have been aligned by their center of mass and normalized by their area. The difference of the two states is shown in gray. (Right) A comparison of different phenomenological data treatments [40]. Simulated spectra are created by mixing weighted experimental spectra from a low-spin and high-spin state to simulate a transition. A and B are done on spectra with well-defined satellites, well C and D are done on spectra with shoulder-like satellites. A and C (B and D) are without (with) simulated statistical noise where only the most promising techniques are shown in B and D. The techniques discussed in the text are the IAD$_C$ (circle) and I(Kβ')$_{Pm}$ (star).

II.2.3 Resonant inelastic x-ray scattering (RIXS)

The books by Silvia [23] and Schülke [43] and the reviews by Rueff & Shukla [15] and Dean [44] were used as the primary references in this section.

Resonant inelastic x-ray scattering is another photon-in photon-out technique which can be thought of as a combination of XAS, excitation of a core electron to an unoccupied state, followed by XES, emission of an electron as the system decays to fill the core hole created by the XAS process. However, the situation is more complex since the two processes are coherent which leads to a complicated cross section where the intermediate state can create intrinsic excitations in the material (Fig. II.10). These excitations can be probed with RIXS by measuring the change in energy, momentum, and polarization of the emitted x-ray. The use of resonance increases the inelastic scattering cross section by many orders of magnitude. A common technique is to measure RIXS maps, where the energy loss ($\hbar\omega_1 - \hbar\omega_2$) is plotted as a function of incident energy ($\hbar\omega_1$). An simulated RIXS map is shown in Fig. II.7 and a measured RIXS map on $Ca_2CuO_2Cl_2$ is shown in Fig. 3 of Article 1 (Sec. III.3). Fluorescence features have a fixed emission ($\hbar\omega_2$) which creates diagonal features in the RIXS map. A typical RIXS measurement uses a fixed $\hbar\omega_1$ at a resonance feature of interest and studies excitations by measuring the outgoing x-rays energy loss. For example, in Fig. 3 of Article 1, a vertical slice at resonance of ≈ 930 eV, we can see going from lower to higher energy loss: quasi-elastic peak with unresolved phonons, magnons, *dd* excitations, and charge transfer excitations. The enhancement of inelastic scattering due to resonant conditions can be seen looking at a horizontal slice at a fixed energy loss.

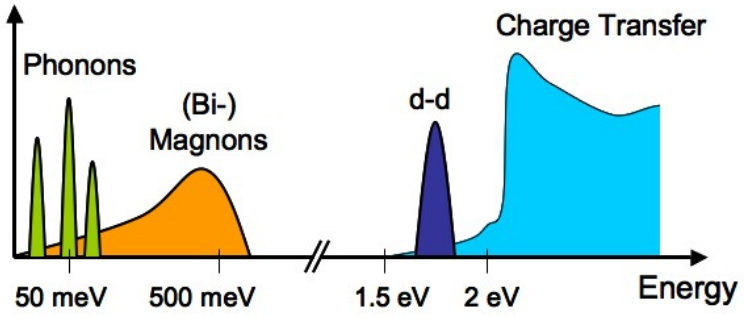

Figure II.10: Schematic energy loss diagram showing the types of elementary excitations which can be probed using RIXS with the the approximate energy scale of a correlated electron system [45].

There are two types of RIXS processes which can occur: direct and indirect. The direct RIXS process, otherwise known as resonant x-ray emission spectroscopy (RXES), refers to when a core electron is excited to a valence state followed by the decay of an electron from a different state (Fig. II.11). This process directly creates an elementary excitation with an energy corresponding to the difference between the incident and scattered x-rays $\hbar\omega_1 - \hbar\omega_2$. The indirect RIXS process (or direct recombination) is when the electron is promoted to a valence state well above the Fermi level, where it simply acts as a spectator before decaying to refill the core hole it created. Electronic excitations can be created in the intermediate state due to interactions between the strong core hole potential and the valence electrons, which

is probed as energy loss by the decaying spectator electron due to shifts of the electronic levels. The XAS and XES processes both must follow the dipole selection rules, which limits the possible excitations. If direct RIXS is possible according to the selection rules it is dominant, however indirect RIXS still has a minor contribution. As well, the intermediate state in direct RIXS can also be strongly influenced by the strong core hole potential, which is exploited in Cu L_3-edge RIXS to probe magnetic excitations.

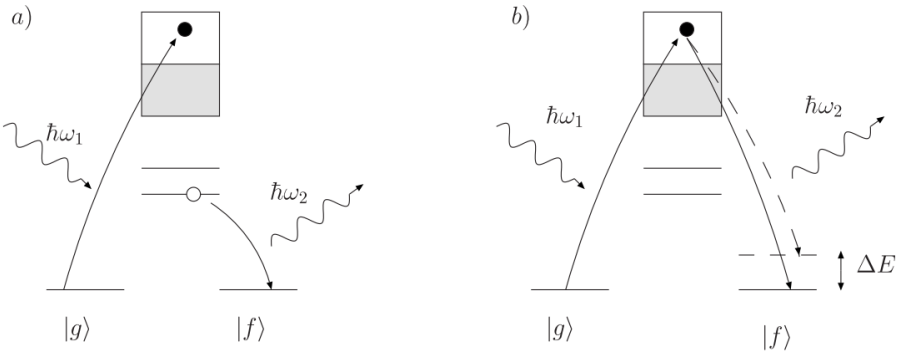

Figure II.11: (a) Direct RIXS. (b) Indirect RIXS. [15]

Cu L_3-edge RIXS

The main RIXS technique used in this thesis is direct RIXS at the Cu L_3-edge ($2p_{3/2}$) to study magnetic excitations in the $Ca_2CuO_2Cl_2$ system. In the cuprates the Cu ions electronic configuration is $3d^9$ such that there is only one hole in the $3d_{x^2-y^2}$ level. In Cu L_3-edge RIXS a $2p_{3/2}$ core electron is excited to fill this hole, creating a highly energetic intermediate state (Fig. II.12). The strong-spin orbit coupling of the core hole allows the exchange of the photon's orbital angular momentum with the spin angular momentum of the $3d_{x^2-y^2}$ electron final state. This process is known as a spin flip and creates a magnetic excitation which propagates through the lattice via the super-exchange.

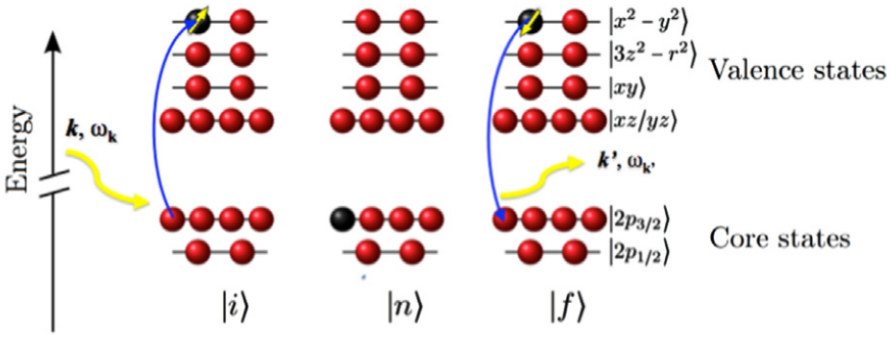

Figure II.12: The Cu L_3-edge RIXS process in cuprates [44].

Previously it was believed that the observation of magnons with Cu L_3-edge RIXS was forbidden in high-T_c cuprates, until it was theoretically demonstrated that it is allowed as

long as there is a non-zero projection of the spin in the CuO_2 plane. Luckily, the spins are always aligned in the CuO_2 plane for all known high-T_c cuprates, thus Cu L_3-edge RIXS can measure magnons in the cuprates. The RIXS geometry is drawn explicitly for grazing-in (grazing-out) in Fig. II.13 (Fig. 2, Article 1). These experiments consider the projection of the transferred momentum in the CuO_2 planes, while the out of plane momentum is assumed to be absorbed by other processes. The chosen geometry as well as incoming/outgoing x-ray polarization determine which excitations are probed on whether they are dipole allowed. As well, for magnons the polarization of the outgoing x-ray must rotate 90° degrees in order to conserve angular momentum when the spin flips. Therefore only the $\pi\sigma'$ and $\sigma\pi'$ channels will have spin flip contributions, where π (σ) is when the x-ray is linearly polarized in (out) of the scattering plane and the $'$ denotes the scattered polarization. Experiments have shown that the the grazing-out geometry with π polarization it the most sensitive to the spin flip channel. In the grazing-out geometry, the $\sigma\pi'$ and $\pi\pi'$ channels are dipole forbidden. Therefore, incident σ polarization probes do not probe spin flips since $\sigma\pi'$ is forbidden. On the contrary, the $\pi\sigma'$ spin flip channel is not forbidden with incident π polarization. We performed our experiments without polarization analysis of the scattered x-rays such that we have a contribution from the $\pi\pi'$ channel as well, however experiments using polarization analysis find that the $\pi\sigma'$ channel is dominant. The grazing-in experimental geometry probes a mixture of all channels and need polarization analysis to distinguish only spin flip contributions. The complicated cross-section can be used as an advantage. It has been shown that the bimagnon and magnon spectral contributions can be separated by measuring different geometry and polarization configurations and it is proposed to also determine the in-plane spin orientation from *dd* excitations.

This first experimental measurement [46] of (single) magnons in La_2CuO_4 is shown in Fig. II.13 and agrees well with spin wave calculations extrapolated from epithermal INS studies [30, 47]. This is experimental confirmation that RIXS is probing the magnetic dynamical structure factor, $S(\mathbf{Q},\omega)$. The weak interaction of neutrons with matter is advantageous for traversing challenging sample environments and also simplifies its cross-section such that $S(\mathbf{Q},\omega)$ can be determined unambiguously. However, this weak interaction, coupled with less neutron flux than x-ray flux, has the disadvantage of requiring large sample volumes. A rough estimate of count rate per volume finds that RIXS is 10^{11} times more sensitive than INS [44]. This allows Cu L_3-edge RIXS to be performed on very small samples, even down to 1 unit cell thick cuprate layers [48], and allows experimenters to fully probe the temperature and doping dependence of materials.

The study of magnons with Cu L_3-edge RIXS is a relatively new break-through which is only possible due to advances in instrumentation which increased the resolution by an order of magnitude in 10 years with a resolution of 130 meV on the SAXES beamline of SLS in 2008 [49]. This evolution continues with the current state-of-the-art being 30 meV on ID32 at the ESRF, while new instruments are being planned and constructed aiming at sub-10 meV resolution. These are exciting developments since it allows the measurement of phonons in the cuprates using RIXS. There are some theories which predict that the electron-phonon coupling can be extracted directly from these spectra by the relative scaling of phonon overtone peaks [50]. The electron-phonon coupling is an important parameter to constrain in order to determine the validity of theories which rely on phonons, by themselves or with magnetic excitations, to explain superconductivity in the cuprates [51, 52].

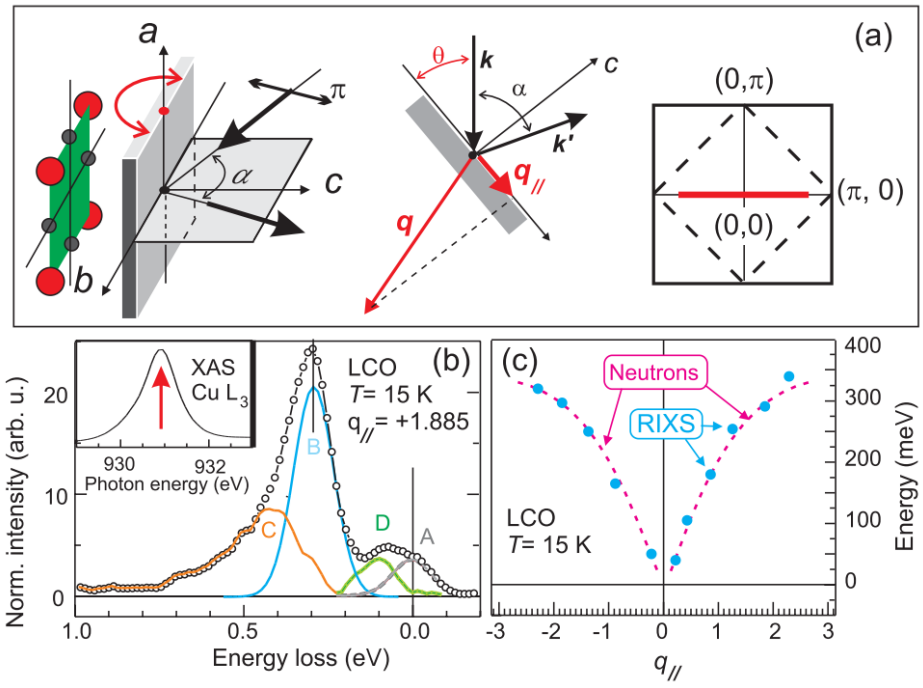

Figure II.13: Figure from Braicovich *et al.* [46]. (a) Experimental geometry shown for measuring along the $\langle \pi, 0 \rangle$ in-plane direction in the high-T_c cuprates. (b) Spectral features including A: elastic, B: magnon, C: multimagnon, and D: phonon. (c) The magnon dispersion measured with RIXS matches the dispersion from a model calculated from INS results.

II.2.4 X-ray generation and instrumentation

The book by Willmott [53] was used as the primary reference in this section.

Synchrotron light sources are desired for the x-ray experiments described above since they require a tunable monochromatic source and they are all very "photon hungry" second-order processes. Third-generation synchrotron light sources, or as used incorrectly in daily speech synchrotrons, are designed expressly for the purpose of producing high brilliance photon beams, ranging in energy from infrared to hard x-rays. They operate on the principle that an accelerating charge will lose energy by emitting electromagnetic radiation. Electrons are the particle of choice for modern synchrotrons, although positrons have been used in the past.

The main components of a third-generation synchrotron light source are shown Fig. II.14. The electrons are typically produced by thermionic emission in an electron gun (e-gun), after which they are accelerated with a linear accelerator (LINAC) to a moderate energy and enter the booster ring. In synchrotrons which use "top-up", such as SOLEIL, the electrons are gradually accelerated to their final energy in the booster ring before being "injected" in the main storage ring using a magnetic chicane. Top-up refers to the periodic injection of electrons from the booster into the storage ring to keep the storage ring current quasi-constant. The top-up operation was an important development which increased beamlines' stability since their optical elements are under a constant heat load. The storage ring is

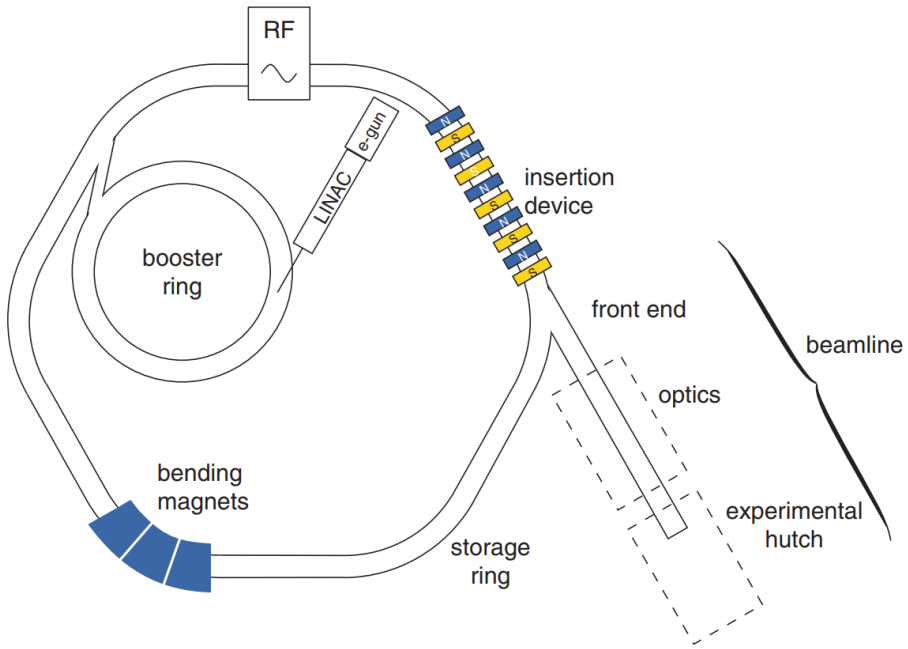

Figure II.14: A schematic showing the key components of a modern-day synchrotron light source, see text for details [53].

kept under ultra-high vacuum to avoid electron losses as the electron circulate the ring. The electrons are guided in a closed path along the storage ring by dipole-magnets (known as bending magnets, see Fig. II.15) due to the Lorentz force. The storage ring also has quadrupole and sextupole magnets to focus and correct chromatic aberrations respectively. The electrons lose energy as they circulate due to radiation at bending magnets and insertion devices. This energy is replenished along the electrons orbit by radio-frequency (RF) supplies which are synchronized with the electron orbit. In fact, this is the same technique used to gradually accelerate the electrons in the booster ring. When electron enter the RF cavity with the proper synchronization they are accelerated normally, while slower/faster electrons receive more/less acceleration. After a few cycles the electron beam will naturally form "bunches", which can also be leveraged to perform time-resolved experiments.

The kinetic energy of the electrons in the storage ring is on the order of a GeV making them relativistic. The electromagnetic emission profile from a relativistic electron under acceleration is a narrow cone in the direction of its motion, rather than an isotropic emission as in non-relativistic acceleration. We can see in Fig. II.15 the emission profiles for a bending magnet, as well as insertion devices known wigglers or undulators. A bending magnet produces intense polychromatic x-rays over a large swath of space due to the angular extent of the bending magnet. A wiggler improves upon a bending magnet by using a series of dipoles which causes the electrons to oscillate over a small range in the plane on the storage ring. The electromagnetic emission from each "wiggle" is summed and the small angular extent means increased flux and brilliance. Undulators operate on the same principle as wigglers, however their oscillatory paths are small enough that the electric fields from each oscillation overlap and interfere constructively increasing the brilliance. The constructive interference

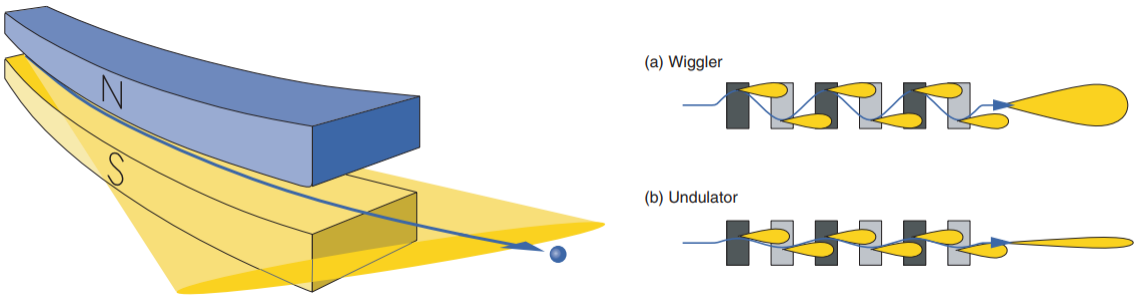

Figure II.15: The radiation profiles of bending magnets (left) and insertion devices (right) [53].

creates narrow bands of radiation consisting of a fundamental frequency and higher harmonics. The photon energy can be varied by modifying the magnetic field (changing the gap between dipoles) and using different harmonics.

The radiation from the bending magnet or insertion devices finally enters the optics hutch of a beamline through the "front end". The front end isolates the vacuum, defines the aperture, monitors beam position, and rejects unwanted radiation. After the front end is the optics hutch to focus and further monochromatize the photon beam, followed by the experimental hutch. The details of these are specific to the type of experiment and the energy of the photons. I used soft and hard x-rays in this thesis, which require radically different instrumentation. Soft x-rays have an energy of 100—1500 eV are are easily absorbed, therefore the beamlines, including the experimental portions, must take place in ultra-high vacuum. Furthermore, their optics are based on multi-layer mirrors and gratings. See Ref. [54] for an overview of the optics of the ADRESS beamline at the Swiss Light Source which was used for the measurements presented in Article 1 (Sec. III.3), as well as Ref. [49] for an overview of the SAXES soft x-ray RIXS spectrometer which was used.

GALAXIES beamline

The beamline review paper by Rueff et al. [55] and technique review by Rueff et al. [15] were used as the primary references in this section.

The instrumentation of a tender/hard x-ray beamline and RIXS spectrometer will be discussed in this section using the GALAXIES beamline of SOLEIL as an example. I used the RIXS end station of GALAXIES to perform two Fe Kβ XES experiments (Sec. IV.2 &V.2) as well as a Cu K-edge RIXS experiment (Sec. III.4). For the latter experiment, I was involved in the commissioning of equipment which will be discussed further below.

The GALAXIES beamline is designed to operate in tender/hard x-ray energy range (2.3–12 keV) and has a RIXS and HAXPES endstation. The RIXS endstation will be the focus of this discussion. The optical layout of the GALAXIES beamline is shown in Fig. II.16, all of which is under ultra-high vacuum to minimize absorption (however the RIXS spectrometer is in air). The source for the beamline is a U20 undulator (20 mm period, 1.96 m effective length) with $Nb_2Fe_{14}B$ permanent magnets (B_{max} = 1.04 T). The electrons oscillate in the plane of the storage rings and thus are polarized linear horizontal, although vertical

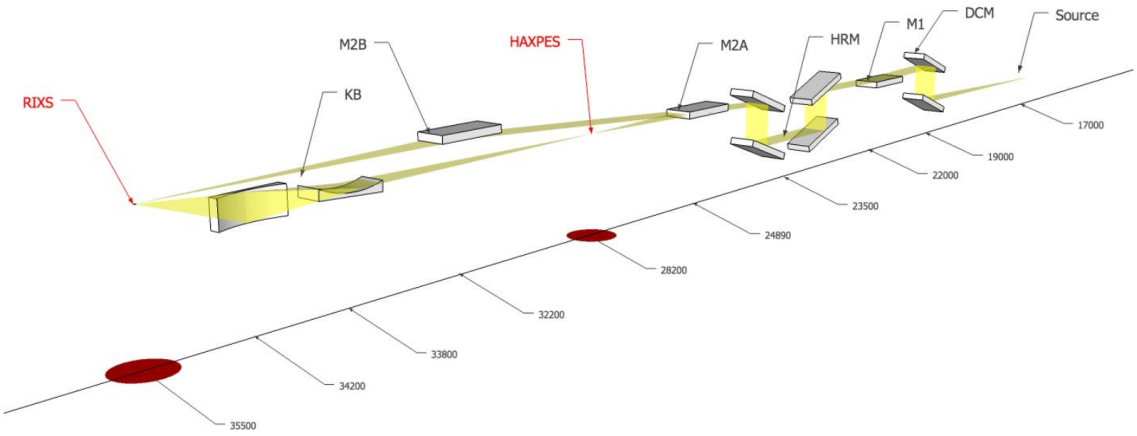

Figure II.16: The optical layout of the GALAXIES beamline [55]. **Source**: U20 undulator, **DCM**: double crystal monochromator, **M1**: spherical collimating and harmonic rejection mirror, **HRM**: high resolution 4-bounce monochromator, **M2A**: toroidal focusing mirror providing focused x-rays for HAXPES or a secondary source for the RIXS micro-focused mode, HAXPES end-station, **M2B**: toroidal focusing mirror for RIXS standard focalization mode, **KB**: Kirkpatrick-Baez mirrors for RIXS micro-focusing mode and RIXS end-station.

and circular polarization can be provided further downstream used a diamond quarter-wave plate. The x-rays enter the beamline through an aperture in the front end and are further monochromatized by a double crystal monochromator (DCM). The DCM uses a pair of Si(111) flat crystals and the energy is chosen by rotating the crystals according to Bragg's law. The use of two crystals is important since the position of the output beam does not change. The DCM takes all of the heat load from the undulator beam, therefore it is cooled indirectly using liquid nitrogen. In the future a high-resolution 4-bounce monochromator will be installed to further monochromatize the beam.

The rest of the optics in the beamline are mirrors, which operate on the principle of total external reflection due to the index of refraction slightly less than one of materials in this x-ray energy range. Total external reflection occurs below a certain critical angle and the design of GALAXIES is such that all the mirrors have a nominal grazing angle of 5 mrad. The mirrors are made from silicon substrates coated with 50 nm of Pd, C, and/or B_4C. The mirrors have a fixed curvature, instead of using benders, to increase the beamline stability. The first mirror, M1, is spherical and is used to collimate the beam and reject harmonics. The toroidal mirrors M2A and M2B, along with the Kirkpatrick-Baez (KB) mirrors, are used for focusing. The M2A mirror is used to focus on the HAXPES endstation and when it is removed the x-rays continue towards the M2B mirror which focuses on the RIXS endstation. This is the standard focalization for RIXS which provides 5×10^{13} photons/s/eV with a beam size of 35×80 (V $\times$ H) μm^2. An alternate focusing scheme can use the M2B mirror as a secondary source for the KB mirrors and provides 6×10^{12} photon/s/eV with a beam size of 15×15 μm^2. Along the beamline there is also beam cameras and monitors used for diagnostic and normalizing purposes.

On the spectrometer side, the energy discrimination is also done using a Bragg reflection from a crystal analyzer. The resolution is effected by the quality of the analyzer, therefore

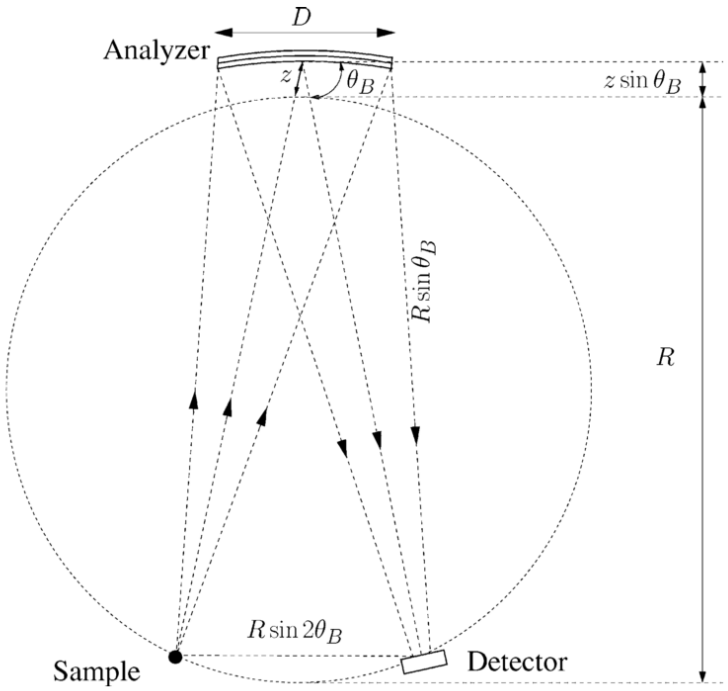

Figure II.17: Diagram of the Rowland circle geometry [56]. The analyzer's radius of curvature defines the diameter of Rowland circle, while the sample and detector positions determine the layout. Typically the analyzer is on the Rowland circle, however it can be moved along $z\sin\theta_B$ to increase the bandwidth.

silicon or germanium are usually chosen since their manufacturing process has been honed by the semiconductor industry over many decades. The GALAXIES spectrometer uses a Rowland circle in a Johann geometry which is shown in Fig. II.17. In this geometry, the radius of curvature of a spherical analyzer matches the diameter of the circle such that x-rays with the appropriate Bragg angle (θ_B), defined by the positions of the sample and detector, are reflected and focused on the detector. The Bragg condition can be expressed in convenient units as $E[\text{eV}] \approx 12398/2d[\text{Å}]\sin(\theta_B)$, where d is the lattice spacing of the analyzer reflection. Perfect focusing would require an analyzer entirely matching the Rowland circle, however this so-called Johansson curvature is difficult to produce. This difference is known as the Johann error and contributes to the instrument resolution according to $\Delta E_J/E = 0.5(r/R)^2\cot^2\theta_B$, where r is distance from the analyzer center. On GALAXIES we usually use a 1 m Rowland circle and 10 cm analyzers, therefore as an example, we find $\Delta E_J/E = 628$ meV with $\theta_B = 75°$ and $E = 7000$ eV. It should be noted that this gives the *maximum* energy shift due to the Johann aberration, but in practice the contribution to the FWHM of the resolution is less. For example, Huotari *et al.* [57] find a maximum energy shift of 8 meV, which agrees with formula using $\theta_B = 88.5°$, $r = 10$ cm, and $R = 1$ m, but the FWHM is less than 1 meV. The Johann error can be reduced by masking the analyzer, typically more along the direction of scattering. Another factor affecting the resolution is the source size ($\Delta\theta$): $\Delta E_g/E = \Delta\theta\cot\theta_B$.

The major limiting factor of the spectrometer resolution is the bending of the crystal

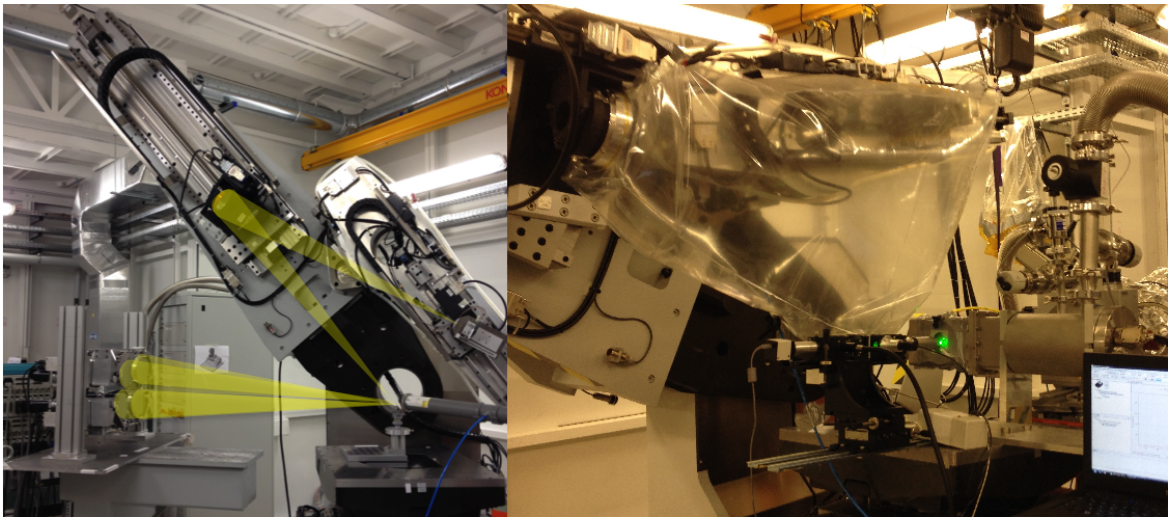

Figure II.18: (Left) Photo of the GALAXIES spectrometer using the single-analyzer arm for measurement. The direction of the x-ray emission from the sample to the single analyzer and then focused to the detector, all located on the Rowland circle are depicted by the yellow lines. Also shown is the multi-analyzer set-up mounted on a temporary support which has now been replaced with a permanent fixture. (Right) A photo showing in-situ pressure measurement. The spectrometer arms is raised to make room for the pressure ruby luminescence spectrometer. The cryostat pictured is a helium flow cryostat specially designed for high pressure cells to reduce vibrations. Also pictured is the helium bag which helps eliminate air absorption and scattering.

into a spherical form which results in elastic deformations. The energy resolution is given by $\Delta E_P/E = (\ell/R)|\cot^2\theta_B - \nu|$, where ℓ is the effective thickness of the crystal and ν is the its Poisson ratio. Although typically small theoretically, this value is large in practice due to extra strain during the gluing process. This can be improved with the anodic bonding technique or using slices to relieve the stress, however the intrinsic resolution is still too high for some applications. For example, an intrinsic resolution around 200 meV is found at 8979 eV with a 2-m radius Si(553) anodicly-bonded analyzer [58], which would be worse for a 1-m radius analyzer. Another solution is to use small cubes ($\approx$ 0.8 mm) to cover the spherical analyzer, the so-called diced analyzers. The individuals crystals are flat and thus without strain, but they are dispersive and will diffract at different Bragg angles. This contribution to the energy resolution is known as the finite-size effect: $\Delta E_f/E = (c/R)\cot\theta_B$. We can see that this effect, as well as the source and Johann error, all approach zero towards back scattering due to the $\cot\theta_B$ term. Indeed, nearly back scattering with diced analyzers is the modus operandi for non-resonant IXS experiments. In RIXS experiments we do not have flexibility over the incident and scattered energies, therefore there is usually no analyzers giving a Bragg reflection near back scattering. In this context, quartz and sapphire are being investigated by the community in order to create analyzers with a lot more available reflections since they have a reduced symmetry. An alternative technique is to still use diced analyzers out of back scattering, but coupled with a 2D detector in order to correct the dispersion [56, 57]. We used this technique to perform the first high-resolution experiments

on the GALAXIES beamline which is presented in more detail in App. B. That being said, it is still preferable to be as back scattering as possible to reduce Johann and source size contributions to the resolution.

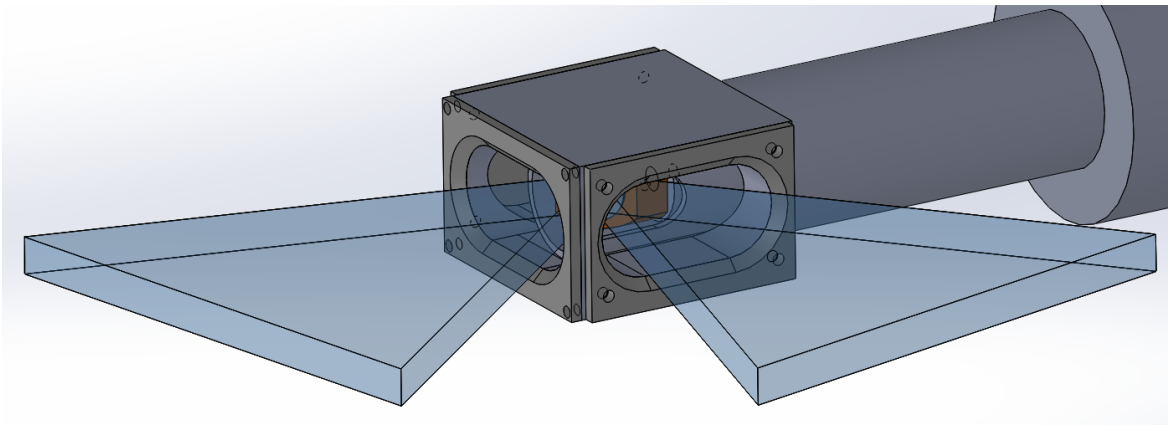

Figure II.19: Overview of my design for a new displex cover.

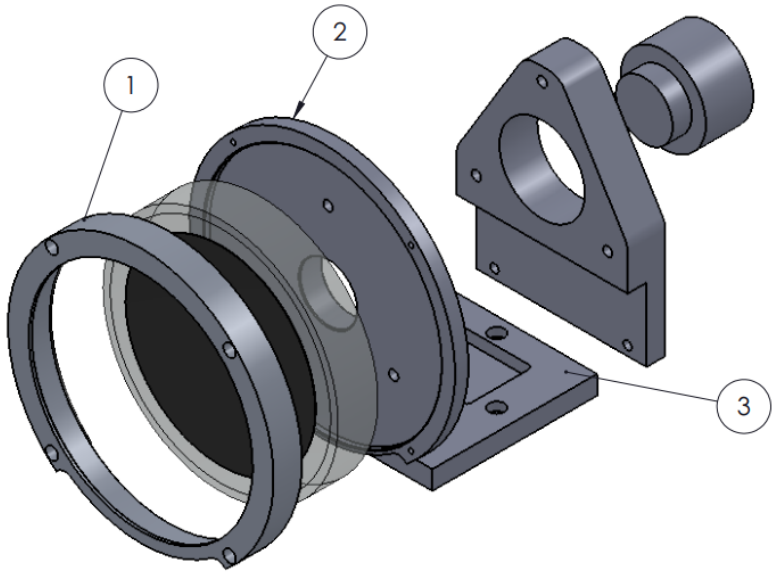

Figure II.20: Overview of my design for new analyzer holder. The base block needed to be cut away to keep the center of the analyzer on the center of rotation of the motors (and Rowland circle).

The theory discussed above put into practice is shown in Fig. II.18, where we see the single-analyzer arm and multi-analyzer setups of the GALAXIES spectrometer. The helium flow cryostat used for high pressure experiments is shown as well. I made a two notable contributions to the GALAXIES beamline during my thesis. The first was working on the commissioning of the high-resolution setup, which included working with two different 2D cameras, performing tests and commissioning, and writing Python code to treat the 2D

data. As well, a few mechanical modifications were needed. We used the displex of the beamline for the high-resolution experiment because the helium flow cryostat was too large and would collide with the camera at the Bragg angle we used. However, the displex head and sample holder needed to be completely redesigned and built for scattering at 90° which is ideal to reduce Thompson elastic scattering since the incident beam is linearly polarized in the horizontal plane. The design I made for the new cryostat head is shown in Fig. II.19, which maximized angular range while avoiding collisions with the spectrometer or beam output tube. The analyzer we borrowed for this experiment was a different standard than ours, 12.5 cm vs. 10 cm, which required a new analyzer mount shown in Fig. II.20. Another project I worked on was characterizing some problems that were noticed in the multi-analyzer which produced dips and oscillations in previous measurements (Fig. II.21). Tests with 2D detectors using a laser and x-ray beam determined the problem was with linear motors used to translate the crystals and keep them on the Rowland circle. This was determined by following the beam motion on the detectors and noting that when plotting the position as a function of these motors, the x and y directions oscillated 90° out of phase and with a period which matched the pitch of the screw drive. I characterized the extent of the motion to determine the required width of the slits to the APD point detector to avoid oscillations. I also tested a configuration where just the Bragg angle changed, i.e. the scan was performed slightly off the Rowland circle. These translation stages have recently been replaced with new translation stages from Newport.

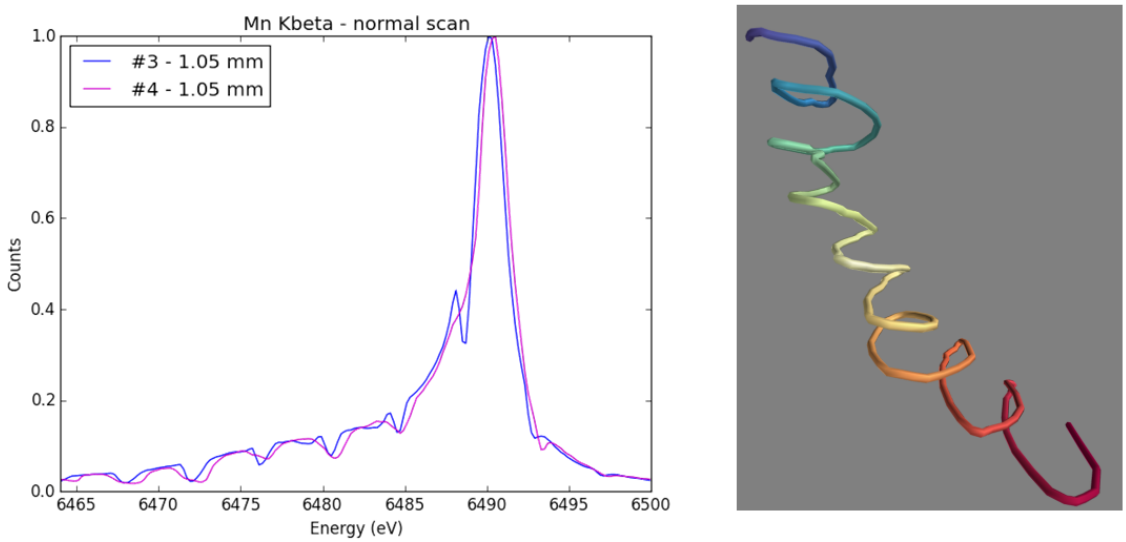

Figure II.21: (Left) ***Not representative of scan quality on GALAXIES***. Example of oscillations that were seen while scanning the analyzed energy with small slits using original translation stages. (Right) Visualization of the motion of the reflected beam seen on the 2D detector where the vertical direction represents energy (red to blue).

II.3 Neutron powder diffraction (NPD)

The beamline review paper by Hansen et al. [59] and the books by Copley [60] and Silvia [61] were used as the primary references in this section.

We will now turn to the use of neutron as probes of matter and discuss neutron powder diffraction. Diffraction from matter can be thought of as simply coherent, elastic scattering and is expressed using Bragg's law for solids. This law relates the distance between planes d (what we want to know), to the Bragg angle θ_B, wavelength λ, and order n (what we know) according to the equation $n\lambda = 2d\sin\theta_B$. The Bragg angle θ_B is half of the scattering angle 2θ. The process is elastic ($|\mathbf{k_1}| = |\mathbf{k_2}|$) which gives the following relations between the momentum transfer, d-spacing, and Bragg angle: $|\mathbf{Q}| = 2|\mathbf{k_i}|\sin\theta_B = 2\pi/d = 4\pi\sin\theta_B/\lambda$.

Nuclear scattering of neutron in solids is mediated by the strong force which operates over scales on the order of 10^{-15} m. In diffraction experiments the wavelength should be comparable to the interatomic distances, 10^{-10} m (we use 1.3 Å and 2.41 Å in our studies). This corresponds to thermal neutrons whose kinetic energy and wavelength are given in practical units as $E[\text{meV}] \approx 80.80/\lambda^2[\text{Å}]$. The wavelengths of these thermal neutrons are much larger than the nucleus, therefore they do not probe within the nucleus and thus neutron scattering is isotropic. The coherent nuclear scattering from an isolated atom is known as b_{coh} and is of the order of 10^{-15} = fm. This is known as the nuclear coherent scattering length. This value varies from element to element without a trend (and even isotope to isotope), unlike its analogous atomic form factor in x-rays. Neutrons also experience magnetic scattering due to the dipole-dipole interaction between their magnetic moment and that of the atom. The neutron's magnetic moment is $\mu_n = -1.041 \times 10^{-3}\mu_B$ and its gyromagnetic ratio is γ = -1.91. The magnetic scattering length is proportional to $\gamma r_e = -5.4 \times 10^{-15}$ m, where r_e is the classical electron radius. Therefore the magnetic and nuclear scattering lengths have comparable strengths.

A perfect powder represents equally all possible crystal orientations, such that an incident monochromatic source of neutrons will produce diffraction cones, subtended by θ_B, when the Bragg condition is fulfilled if they are not forbidden by symmetry. In our case, the incident neutrons are not polarized and the scattered neutrons' polarization and energy are not analyzed. The incoherent elastic scattering and the inelastic scattering will contribute to a background, along with any scattering from the sample environment. In this unpolarized case, there are no interference terms between nuclear and magnetic scattering such that the total structure factor is given by $S_{tot}(\mathbf{Q}) = S(\mathbf{Q}) + S_M(\mathbf{Q})\sin^2\alpha$. The angle α is between atomic magnetization vector and scattering vector. In the case of a periodic crystal the nuclear structure factor is:

$$S(\mathbf{Q}) = \frac{(2\pi)^3}{nV}\sum_{\mathbf{G}}\delta(\mathbf{Q}-\mathbf{G})\left|\sum_{j}^{n} b_j e^{-Q^2\langle u_j^2\rangle/2} e^{i\mathbf{Q}\cdot r_j}\right|^2$$

where n is the density, V is the volume, and $\mathbf{G}_{hk\ell} = h\mathbf{a}^* + k\mathbf{b}^* + \ell\mathbf{c}^*$ with h, k, ℓ as integers is the reciprocal lattice vectors. The first sum is over all the reciprocal lattice vectors where the delta function enforces the Bragg condition $\mathbf{Q} = \mathbf{G}_{hk\ell}$. The second sum is over the basis of the unit cell, where r_j is the position of atom j. It is this form factor squared which is responsible for forbidden reflections due to to destructive interference between certain

atoms in the basis. The Debye Waller factor in this isotropic case is given by $e^{-Q^2\langle u_j^2\rangle/2}$ and represents thermal disorder. The mean square displacement of the atom from its equilibrium position is given by $\langle u_j^2\rangle$. The overall effect of these vibrations is to shift intensity from the Bragg peaks into thermal diffuse scattering background.

The magnetic structure factor is similar except b_j is replaced by p_j. This magnetic scattering length is proportional to the atomic magnetic moment. It also has a Q-dependent factor which decreases at increased scattering vectors due to the electron distribution around the atom (like for x-rays and unlike for neutron nuclear scattering). Antiferromagnetic structures are perfect to measure with NPD since their supercells create reflections at lower scattering angles where the magnetic form factor is greatest. Another advantage is that some magnetic Braggs peaks will exist which do not overlap the nuclear Bragg peaks.

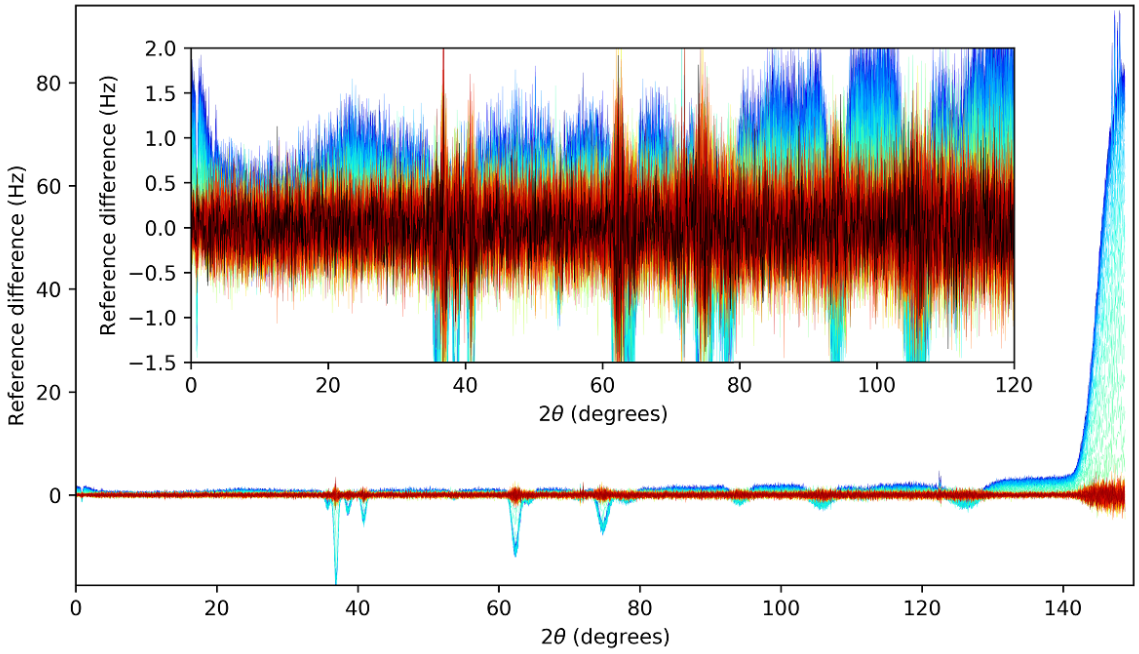

Figure II.22: Neutron powder diffraction measurements during cooling with stable 1.8 K diffraction pattern subtracted. The measurements increase in time from blue to red. The spectra at the beginning when there is still liquid helium in the neutron beam show scattering from the liquid helium, as well as increased absorption by the dips in the Bragg peaks.

The description of NPD here is quite simplistic and there are many other factors not considered, to name just a few: scattering-angle dependence of resolution function, preferred orientation, strain-induced peak broadening, anisotropic temperature factors, absorption and contributions from inelastic scattering. Also, the phase information is lost without the use of polarization and there can be many phases/compounds coexisting in a sample which creates overlapping peaks. Therefore, NPD data has the be treated with a model. We used the FULLPROF suite to perform Rietveld refinement to model our powder diffraction patterns. The program can take into account many of the complicating factors mentioned above. The Rietveld refinement method uses known models based on your input to simulate a diffraction pattern and then performs a least-squared fit of all the free parameters to best match the

experimental pattern. The method assumes that you already know a good deal about your structure(s) to make a reasonable guess of the model, otherwise structure determination using something such as LeBail fitting must be performed beforehand.

Preferred orientation refers to a middle ground between a perfect single crystal and perfect powder. This is the case when the polycrystalline grains have a non-isotropic distribution and the sample is sometimes called "textured" in this case. This is often the case under pressure, therefore it is an important parameter for our experiments on ϵ-iron and FeSe. Furthermore, finding the proper preferred orientation is important for when we simulate the expected magnetic diffraction pattern using FULLPROF because of the $\sin^2\alpha$ term related to magnetic scattering. If the magnetic moment of the atom is aligned with scattering wavevector there will be no magnteic scattering! In a perfect powder this term averages to a value of 2/3, but as we see in our ϵ-iron results the polycrystalline iron has a preferred orientation under pressure and must be taken into account when we perform our simulations.

Neutron powder diffraction is sensitive technique which can also measure incommensurate structures and short-range magnetic order. It can even measure the time-averaged radial distribution in disordered substances such as gases, liquids, and glasses. We actually inadvertently measured the time-averaged radial distribution of helium using the technique described in Sec. A. In Fig. II.22 we can see before the liquid helium evaporated below the neutron beam there is scattering contributions from the liquid helium. The first clear large peak is at $2\theta = 24.5°$. This agrees well with previous results [62] which find $2\theta = 21.3°$ with an incident wavelength of 1.08 Å. This agrees with the peak we see after making the conversion for the wavelength:

$$2\theta_2 = 2\sin^{-1}\left(\frac{\lambda_2}{\lambda_1}\sin\left(\frac{2\theta_1}{2}\right)\right) = 2\sin^{-1}\left(\frac{1.3\text{Å}}{1.08\text{Å}}\sin\left(\frac{21.3°}{2}\right)\right) = 24.3°$$

Neutrons are produced usually with a continuous nuclear reactor source or a spallation source. The instrumentation for the two dramatically differs so I will focus on the continuous nuclear reactor source which we used for our experiments. We performed our experiments at the Institut Laue-Langevin (ILL) which is one of the most intense neutron sources in the world. The reactor works through the fission of uranium in the process: ${}^{235}_{92}\mathrm{U}_{143} + \mathrm{n} \rightarrow [{}^{236}_{92}\mathrm{U}_{144}]^* \rightarrow \mathrm{X} + \mathrm{Y} + 2.44\mathrm{n}$. The uranium nucleus splits into two or more lighter nuclei, releases kinetic energy, gamma radiation, and 2.44 neutrons on average. The process is a self-sustaining nuclear reaction since a portion of the released neutrons will induce further nuclear fission events. Thermal neutrons are produced by "moderating" the highly-energetic neutrons from the fission reaction in heavy water.

We used the D20 high-intensity two-axis diffractometer with variable resolution beamline at the ILL. The instrument layout if shown in Fig. II.23 and more details can be found in Ref. [59]. A key feature of the D20 beamline is a curved linear position sensitive detector over a large 2θ range to simultaneously capture a large solid angle of the diffracted neutrons. Another feature is the fact that the D20 beamline is very close to the center of the reactor for the highest possible flux of neutrons. At a take-off angle of 42° with a Cu(200) monochromator there is the highest flux of 9.8×10^7 n cm^{-2} s^{-1}. The one disadvantage of using this mode is that the so-called $\lambda/2$ contamination which cannot be removed with a filter and contributes 0.3%. This contamination from the monochromator follows from Bragg's law with $n = 2$. Usually 0.3% is negligible for diffraction, however since we are looking for small magnetic Bragg peaks we must take this into consideration. The contamination

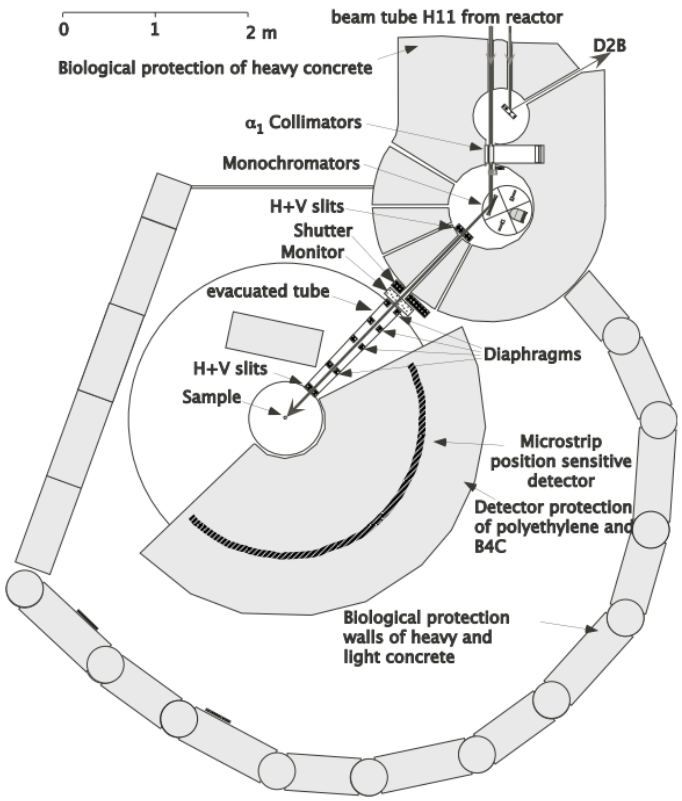

Figure II.23: Birds-eye view of the D20 spectrometer at the ILL [59].

is easily treated in FULLPROF using a secondary incident wavelength. The system used for high pressure and low temperature measurements is covered in more detail Sec. A.

II.4 High pressure

The review paper of Rueff et al. [15] was used as the primary reference in this section.

High pressure is useful for studying materials which are naturally under pressure, such as iron in the Earth's core. However, pressure in general is also an effective external parameter to study the change in electronic structure, hybridization, and magnetic properties of materials as their interatomic distance is compressed. Pressure has the advantage of tuning the system without inducing disorder, unlike doping or temperature. Another key difference between pressure and other external parameters is that it maps onto a much larger energy scale, at least an order of magnitude more than is possible with temperature. Finally, pressure-induced phase transitions can lead to interesting types of order since entropy is not involved, as in temperature-induced transitions. This phenomenon is seen clearly in the emergence of superconductivity in compressed heavy fermion superconductors discussed earlier. As well, other phenomenon are possible such as a magnetic collapse, metal-insulator transition, and valence changes.

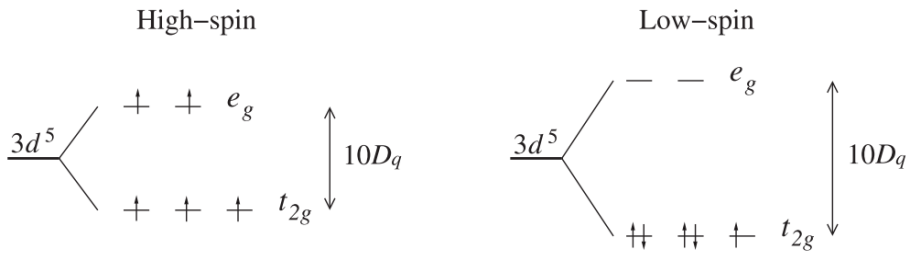

Figure II.24: A high-spin (S=5/2) to low-spin (1/2) transition occurs in a $3d^5$ metal ion in octahedral (O_h) symmetry as the crystal field strength ($10D_q$) increases under pressure [15].

The effect of pressure on magnetism in $3d$ ions can be pictured either in the itinerant Stoner picture or a localized picture. Starting with the Stoner picture, we can rewrite the Stoner criterion by noting that depending on the on-site Coulomb repulsion U the system will behave differently. At low U, the system behaves as a Pauli paramagnet, while at large U, the system becomes a ferromagnet. We express the Stoner criterion for ferromagnetism with respect to this critical Coulomb repulsion as $U_c n(\epsilon_F) > 1$. Under pressure the bandwidth W of the $3d$ electrons increases as they become progressively more delocalized, leading to a decrease in the density of states at the Fermi level $n(\epsilon_F)$ while the on-site Coulomb repulsion U is mostly unchanged since it is a local property. Therefore, eventually under pressure a ferromagnetic system will collapse to a paramagnetic system due to the increased $3d$ bandwidth. The same holds true in the localized picture which is shown Fig. II.24. In the localized picture, the ordering of spins in the $3d$ orbitals is determined by a competition between the magnetic exchange and the crystal electric field (CEF) strength. Once again, the magnetic exchange is localized and varies little with pressure, while the CEF strength increases under pressure as the atomic distances decrease. Upon compression this competition is eventually won by the CEF strength and the electrons prefer to order on the lowest energy level (Fig. II.24).

The maximum experimentally accessible pressure has increased dramatically in the last sixty years. The highest pressures were traditionally and still are achieved in dynamic pressure experiments which use shock waves. However, dynamic methods have limited applicability due to their transient and adiabatic nature. On the other hand, static pressure experiments maintain a constant pressure by applying a force to a sample in a pressure cell thereby allowing a wider variety of experiments. The containment within a pressure cell is the first major constraint and excludes techniques whose probe cannot traverse the pressure vessel. In particular, photoemission spectroscopies are impossible since electrons do not have sufficient penetration depth.

The opposed anvil pressure cell was invented by Bridgman, who through the use of harder and harder materials increased the achievable static pressure by several orders of magnitude up to 10 GPa. The key concept of an anvil pressure cell is the transmission of a moderate force applied over a relatively large surface to a smaller surface, thus "magnifying" the applied pressure by several orders of magnitude. The materials used to transmit the pressure must be hard in order to withstand the large pressure gradients, therefore the use of diamonds anvils was the next logical step due to their natural hardness. Using diamond

anvils, static pressures up to 300 GPa are routinely achieved and a maximum pressure of 640 GPa has been reported using micro-ball nanodiamond anvils [63]. A lucky coincidence of nature, diamonds are also transparent over a broad spectrum and therefore allow a variety of infrared, visible and x-ray spectroscopies.

There is a zoo of high pressure techniques depending on the application. In this thesis I will focus on these uniaxial, opposed-anvil pressure cells. The main components of the pressure cell are: an initial applied force, a hard material to transmit the applied force, a gasket to contain the sample volume, a pressure-transmitting medium (PTM) to transmit pressure within the sample volume, and a manometer. The choice of these components depends if one is using x-rays or neutrons, and to a lesser extent the type of experiment. For x-ray experiments we used diamond anvil cells (Sec. II.4.1) and for neutron experiments we used Paris-Edinburgh cells (Sec. II.4.2). The name "Paris-Edinburgh cell" is a bit of a misnomer, since it is actually referring to the use of a Paris-Edinburgh press to apply the pressure. This press uses helium gas pressing on a surface, just like the membrane-driven diamond anvil cells we used.

II.4.1 Diamond anvil cells (DAC)

The review paper of Jayaraman [64] was used as the primary reference in this section.

A basic schematic of a modern diamond anvil cell (DAC) is shown in Fig. II.25. Despite the many variations of DACs, they all share the same key features. The major difference between different DACs is their method of applying force on the diamonds. The force is applied on the larger surface of the diamond, the table, and transmitted to the smaller surface of the diamond, the culet. The metal gasket was a key innovation and performs two main functions. The most obvious function, looking at the diagram, is that it delineates the sample chamber volume and helps maintain hydrostaticity. A less apparent function is that the gasket supports the diamonds and helps reduce their pressure gradients. The support to reduce stress on the culet edges is shown more clearly in the zoom on the right side of Fig. II.25. The sample volume depends on the desired maximum pressure, however it is typically 10^{-2} mm^3 to 10^{-4} mm^3. This is a major constraint and excludes techniques which require relatively large volume, such as neutron spectroscopy. Besides the sample, this volume also typically contains a pressure transmitting medium and a pressure gauge. A pressure transmitting medium is used to maintain hydrostatic conditions while the pressure gauge is used to measure the static pressure within the cell.

We used a membrane diamond anvil cell [66] in our experiment, which uses compressed helium gas in a thin metallic membrane to provide the force. The advantages of using a membrane versus traditional mechanical techniques are numerous. The membrane applies a force symmetrically which keeps the diamonds parallel avoiding additional stress on the diamonds. The use of helium gas provides continuous, smooth, and accurate adjustments in pressure. Membrane DACs typically have a small form factor and large optical aperture due to the lack of mechanical components. Finally, membrane DACs are interfaced easily with other devices, such as cryostats, since only a gas feedthrough is needed.

Our particular incarnation of the membrane DAC uses the piston-cylinder design and is shown in Fig. II.26. The piston is inserted into the cylinder and the diamonds are in contact with each other through the gasket (not shown). The cap is threaded into the cylinder to

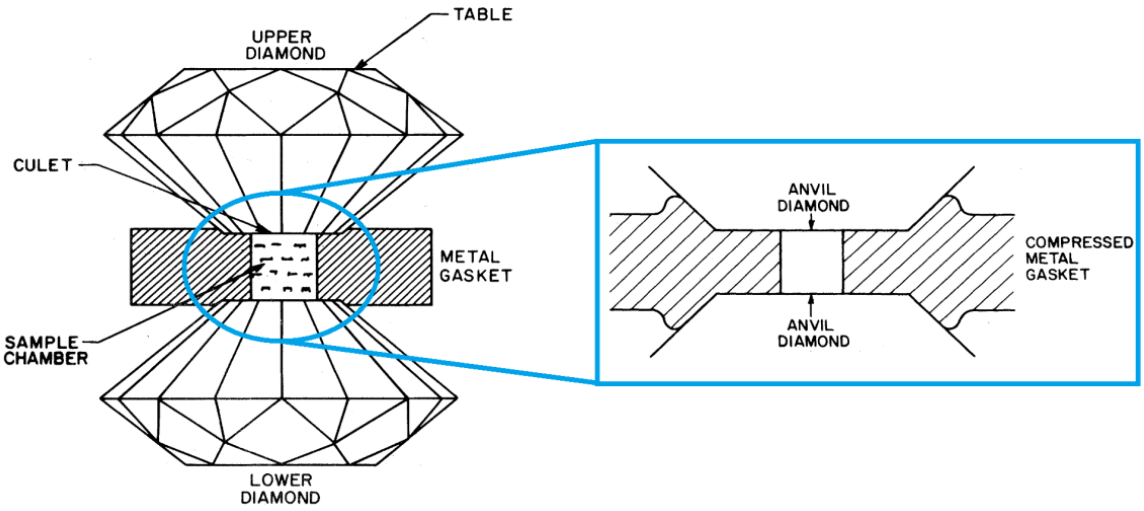

Figure II.25: Schematic of a diamond anvil cell showing the important features. See text for description. (Modified from Ref. [65]).

push the piston and mechanically force the diamonds towards each other. However, this is only done during the initial loading. Pressure changes during an experiment are performed using the membrane, which pushes the piston as the helium pressure is increased in the membrane. The cap, cylinder, and piston are all made out of a fairly hard material, stainless steel in our DAC, although different materials are needed for high temperature or magnetic measurements. The seat supports the table of the diamond and has a hole for optical access (below the bronze piece in the picture). The contact surface between the diamond and the seat is still relatively small so it also experiences a large pressure gradient. Therefore, the seat is made out of an extremely hard material also, in our case it was tungsten carbide. The bronze plate and copper ring are one way of mounting the diamond on the seat.

The choice of pressure transmitting medium depends on many factors. Liquids such as silicone oil or 4:1 methanol-ethanol mixture are very easy and fast, yet they have a low hydrostaticity limit. We used silicone oil for our FeSe experiment. The condensed noble gases are the most hydrostatic, with helium being the best. Unlike liquids, these gases are more difficult to use and must be loaded using high pressure gas loading or cryogenic loading. The boiling point of helium and neon are below that of nitrogen, while the boiling point of argon is above. Therefore, for our ϵ-iron experiment we chose to use argon as a compromise between hydrostaticity and simplicity since liquid nitrogen can be used for cryogenic loading. It is interesting to note that argon actually becomes solid at a much lower pressure (1.9 GPa) than 4:1 methanol-ethanol (9.8 GPa) [67, 68]. Nonetheless, argon stays "quasi-hydrostatic" because it forms a solid with weak bonding via the van der Waals interaction.

The general idea of cryogenic loading is to condense argon into a liquid by cooling it below its boiling point with liquid nitrogen. In order to let the liquid enter the sample volume, the cap is slightly unscrewed to create a small gap between the diamonds and gasket. Next, the DAC is placed in a chamber which is attached to a bottle of argon and a vacuum pump. The helium input of the DAC is attached with a capillary to an open microvalve then through a feedthrough in the chamber and finally to the membrane gas regulator. The microvalve is

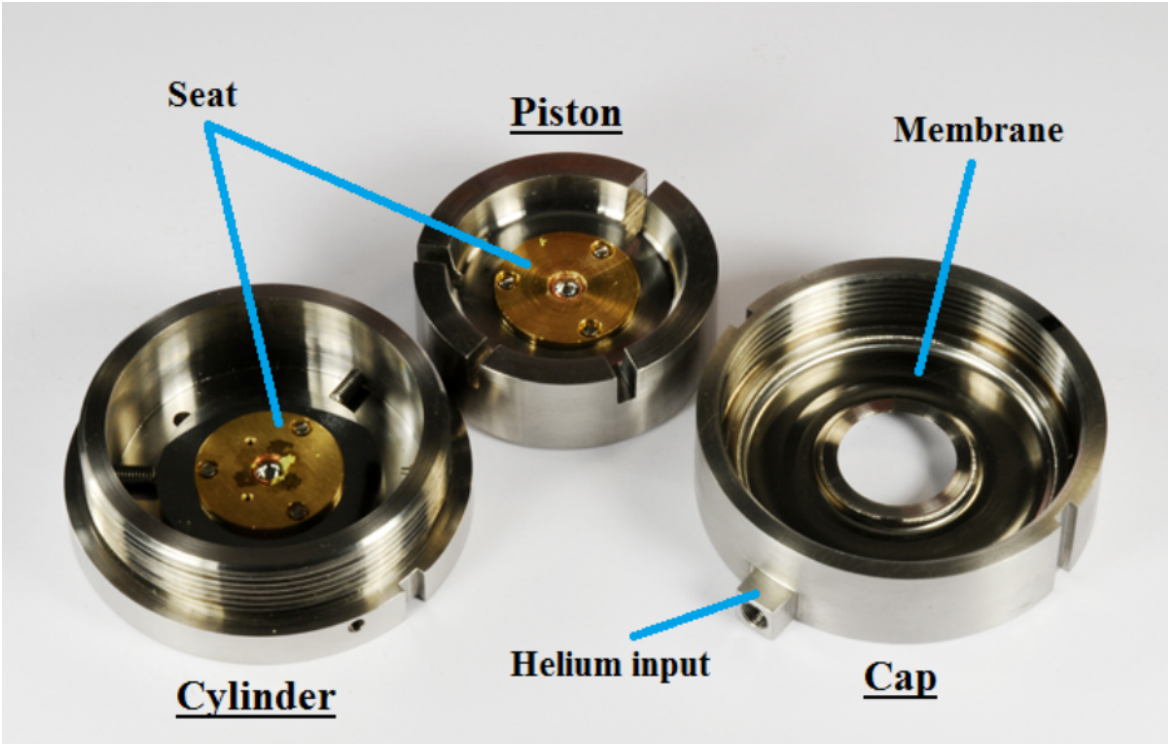

Figure II.26: Picture of a membrane diamond anvil cell. See text for description. (Modified from www.impmc.upmc.fr)

necessary to remove the feedthrough after loading and reattach the membrane regulator. The chamber is purged of ambient gases by repeatedly pumping the chamber and refilling it with argon. The vacuum pump is removed and the chamber is placed in liquid nitrogen, while maintaining a constant pressure of argon within the chamber. The argon slowly condenses until the liquid argon reaches the level of the sample volume. At this point, the pressure in the membrane is increased to push the diamonds together and trap the argon in the sample volume. The process is fairly straight-forward process, but there still is a bit of an art to cryogenic loading. The sample and pressure gauge can be lost if the cap is too loose, while if it is too tight then the argon cannot enter. As well, if the membrane pressure is too low the argon will not be loaded, yet too high and you can break the diamond. Additionally, we also had problems with the microvalves not working at cryogenic temperatures causing us to lose pressure on the membrane.

To measure the static pressure in the DAC one needs to measure something that has a calibrated change with pressure. The most accurate method is measuring the volume of a material with a well-known equation of state, such as copper or silver, using x-ray diffraction. This is not very convenient for most experimental setups, which is why using fluorescent gauges, which can be measured in-situ, is the most widely used method. This technique was first discovered using ruby [69], which is still the most widely used pressure gauge.

Ruby is simply α-alumina doped with chromium: Al_2O_3:Cr^{3+}. The chromium in ruby is excited with a green laser to an excited state and quickly decays non-radiatively to a

long-lived metastable state. The chromium decays further from this meta-stable state to the ground state, radiating a doublet with the so-called R1 and R2 lines. This fluorescence spectra is recorded using a dispersive spectrometer and fitted using two Lorentzian functions with a quadratic background. Although both of the R lines are sharp and strong, the R1 line is used since it is stronger. The R line wavelengths depend on the particular ruby (i.e chromium concentration), pressure, and temperature. In our particular case the R1 line at ambient temperature and pressure was 694.33 nm. The wavelength of the R1 line shifts to longer wavelengths as the pressure is increased. Below 30 GPa, the wavelength shift is approximately linear with a rate of $+0.365$ nm GPa^{-1}. A more refined ruby calibration from Ref. [70] was used in our experiments. Ruby luminescence presents multiple problems at higher temperatures. The major problem is that the signal-to-background ratio decreases and the R lines are barely measurable at 700 K [71]. As well, the R lines broaden with temperature and their overlap induces uncertainty when determining the wavelength. Finally, the temperature dependence of the wavelength shift in ruby is relatively large. Therefore, we used SrB_4O_7:Sm^{2+} for our measurements at 583 K since it counteracts all three drawbacks of ruby at high temperatures: it has good signal-to-background, it is a singlet instead of a doublet, and it has a small temperature shift. The fluorescence method is the exact same with this compound and can be excited with the same laser. The fluorescent transition of the excited samarium is a thin singlet line known as the 0-0 line. The pressure calibration we used is taken Ref. [71].

II.4.2 Paris-Edinburgh cells (PEC)

The book of Klotz [72] was used as the primary reference in this section.

The general concepts are the same for neutrons, therefore I will just briefly describe material considerations needed for high pressure with neutrons. The main difference is the increased volume needed due to the weak interaction of neutrons. This means the anvils are much bigger. We used a cubic boron nitride anvil with a steel retaining ring for the FeSe experiment and a sintered diamond anvil with tungsten carbide and steel retaining rings for the ϵ-iron experiment (to reach higher pressures). The larger volume also means that the press must supply much more force, which lead to the development of the Paris-Edinburgh (PE) press. Different PE press models can provide 50–500 tonnes to compresses samples from 1–100 mm^3. See Fig. II.27 for an example of the key components in the VX model. Another difference is the relatively large size of the incident neutron beam, unlike x-rays. We operated in the longitudinal scattering geometry (Fig. II.27) which means the retaining rings need to be shielded with cadmium to avoid Bragg reflections. The gaskets and anvil are in the neutron beam and cannot be avoided. Diamond has relatively few Bragg peaks due to its symmetry and it is easily modeled when performing Rietveld refinement. The gaskets use a TiZr alloy to avoid Bragg contributions. The coherent scattering length of Ti and Zr is -3.44 fm and +7.16 fm, respectively, therefore an alloy of the two materials with a Ti/Zr molar ratio of $7.16/3.44 = 2.1$ is null-scattering. Fig. II.27 shows the profiles of the two configurations we used. The top one has a single toroid and is used for larger volumes at low pressure (FeSe experiment), while the bottom one has a double toroid and is used for smaller volumes and higher pressures (ϵ-iron experiment).

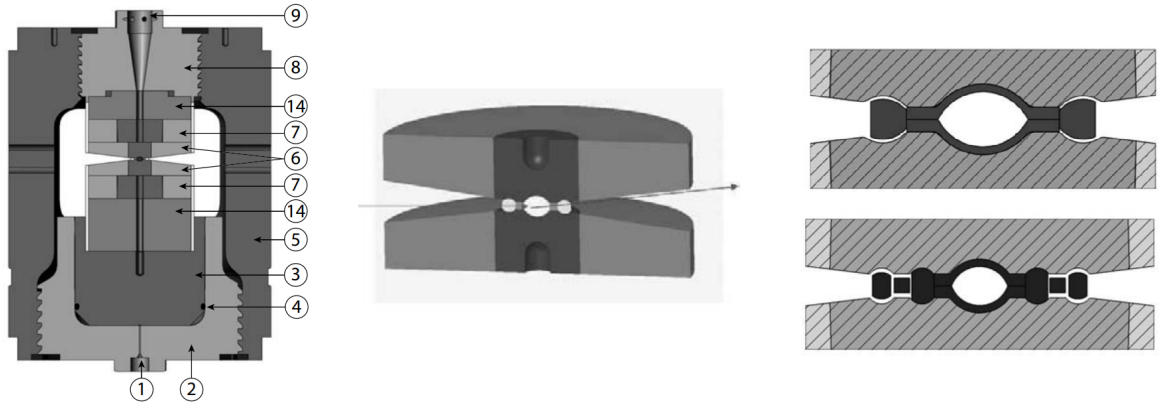

Figure II.27: Overview of Paris-Edinburgh cell [72]. (Left) Cross-section of VX PE press with 1: hydraulic fluid inlet, 2: cylinder, 3: piston, 4: O-ring seal, 5: load frame, 6: anvils, 7: TC backing plates (seats), 8: breech, 9: front collimator, 10: nut, 11: top platen, 12: tie rod, 13: backing disc, 14: steel spacer. (Middle) Longitudinal scattering geometry we used in our NPD experiments. (Right) The single- and double-toroidal anvil cells configurations with encapsulating hemispheres.

Chapter III

$Ca_2CuO_2Cl_2$ system: a light element model for cuprates

III.1 Introduction

Half of my thesis was devoted to studying magnetic excitations in the copper oxychloride system, $Ca_2CuO_2Cl_2$, which shares the same quadratic CuO_2 planes that are believed to be the seat of the superconductivity in the hole-doped cuprate superconductors[1]. This can be seen clearly by comparing its structure (Fig. 1. in Article 1, Sec. III.3) and phase diagram (Fig. III.1) to that of the prototypical cuprate system La_2CuO_4 described in Sec. I.4.2.

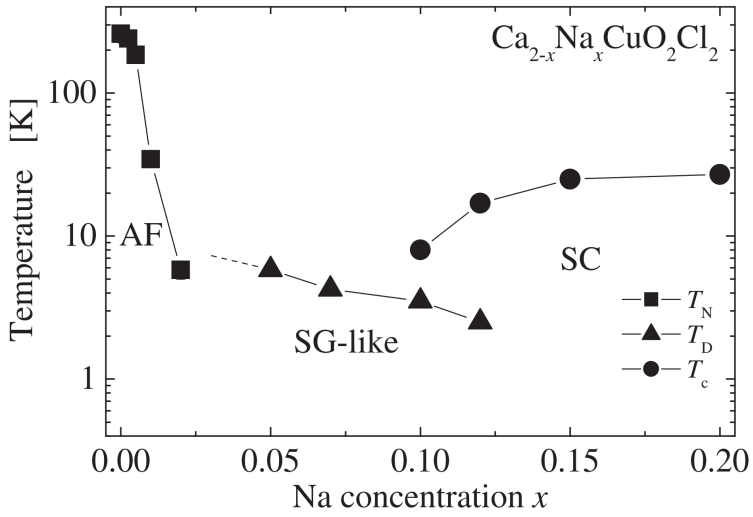

Figure III.1: Phase diagram of $Ca_{2-x}Na_xCuO_2Cl_2$ is the same as high-T_c cuprates [1]. The Na doping leads to the rapid disappearance of the antiferromagnetic phase (AF) followed by the appearance of the superconducting (SC) state. A spin-glass-like (SG-like) phase is found between the AF and SC states.

[1] $Ca_2CuO_2Cl_2$ is technically a copper oxychloride and not a copper oxide (cuprate). However, I will often refer to it as a high-T_c cuprate due to its similarity.

$Ca_2CuO_2Cl_2$ is a 1-layer "cuprate" with the same K_2NiF_4-type ($I4/mmm$) [73] structure as high-temperature La_2CuO_4 with the lanthanum atoms in the charge reservoir layer replaced by calcium and the apical oxygens of the CuO_6 octahedra replaced by chlorine. The system is typically doped with sodium ($Ca_{2-x}Na_xCuO_2Cl_2$) or vacancies ($Ca_{2-x}CuO_2Cl_2$) (Sec. III.2). Although the system has a rather modest critical temperature, it has many salient features which make it a model system to study the physics of CuO_2 planes in the cuprates:

- *Low-Z*: The system has much less electrons than other cuprates, i.e. copper is the heaviest atom, which is an experimental and theoretical advantage. In general, we expect higher inelastic signals compared to the cuprates because the photoelectric absorption scales as $\approx Z^4$ [74]. For *ab-initio* calculations the reduced number of electrons is also an advantage. In standard density functional theory high-Z atoms can pose a problem for pseudopotential optimization [74]. Furthermore, low-Z compounds are preferred by advanced many-body calculations which include correlation effects since they require an accurate treatment of spin-orbit coupling which can be difficult. This difficulty can be circumvented by using low-Z systems where relativistic effects can be neglected [75–77].

- *Simple structure*: The tetragonal symmetry is conserved at all dopings and temperatures – it is free of orthorhombic distortions and buckling of the CuO_2 planes [78].

- *Apical chlorine*: Its CuO_2 planes have a stronger 2D character since the apical Cl^- ions contribute less than apical O^{2-} ions to the CuO_2 planes electronic structure. X-ray photoemission spectroscopy finds the Cl $3p$ levels at ≈ 6 eV below the Fermi level [79], compared to ≈ 3 eV for the O $2p$ levels in cuprates with apical oxygen. Furthermore, the apical anion distance in $Ca_{2-x}Na_xCuO_2Cl_2$ and $La_{2-x}Sr_xCuO_4$ show opposite trends [80], therefore theories of superconductivity which rely on the Cu d_{z^2} band are unlikely.

These features truly make $Ca_2CuO_2Cl_2$ a model system to gain insight into the 30-year-old mystery of high-T_c cuprates by bridging the gap between theory and experiment. However, relatively little is known about the system from an experimental point of view – indeed, there is almost more publications about its synthesis than its characterization! One important reason is that the samples are only available as small single crystals which are quite hygroscopic (Sec. III.2). Nonetheless, the recent convergence of advances in Cu L_3-edge RIXS instrumentation/theory and many-body calculations, along with the steady march of Moore's law, makes us believe that it is an apt time to revisit the $Ca_2CuO_2Cl_2$ system.

As in the cuprates, undoped $Ca_2CuO_2Cl_2$ is an antiferromagnetic charge-transfer insulator [81]. Neutron diffraction found $T_N = 247 \pm 5$ K below which $Ca_2CuO_2Cl_2$ orders in a unique $\sqrt{2} \times \sqrt{2} \times 2$ magnetic cell [78]. The doubling of the c-axis is rare among the cuprates. The study was unable to determine neither the in-plane orientation of spins nor the ordering along the c-axis. Nonetheless, they find only two possible structures which are shown in Fig. III.3. According to dipolar calculations, the noncollinear helical model should have the Cu^{2+} spins in-plane along $\langle 100 \rangle$ and the collinear model should have the spins along $\langle 110 \rangle$. Inelastic neutron scattering studies of the magnetic excitations are infeasible due to the small crystal size, while co-alignment is difficult due to its hygroscopic nature. However, the recent developments in Cu L_3-edge RIXS opens up the study of magnetic excitations in this material for the first time.

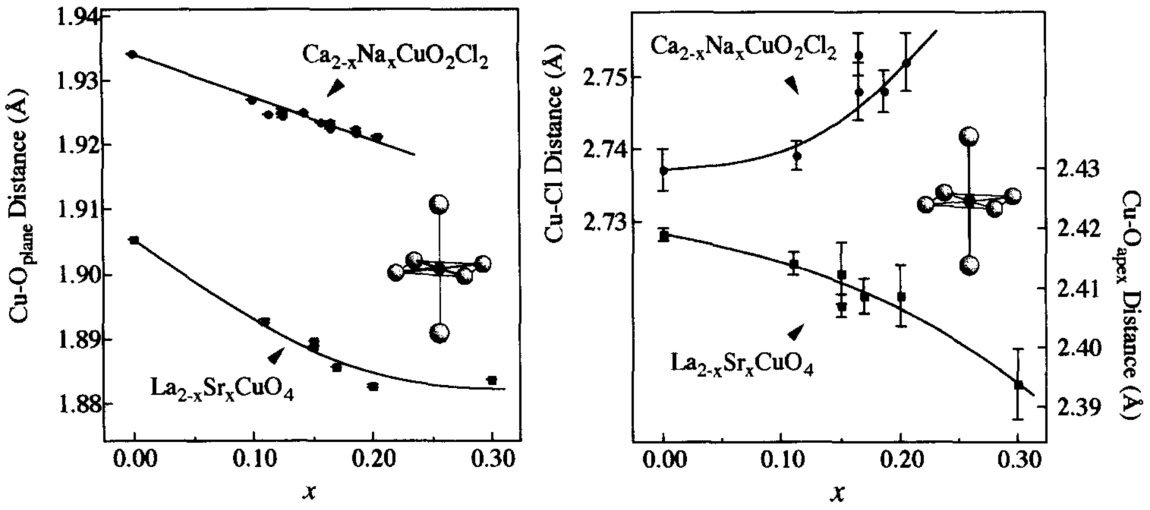

Figure III.2: Comparison of the local structure doping dependence for $Ca_{2-x}Na_xCuO_2Cl_2$ and $La_{2-x}Sr_xCuO_4$ [80]. The distance between CuO_2 planes (left) shows the same trend, although it is $\approx 10\%$ larger for $Ca_2CuO_2Cl_2$. However, the apical anion distances (right) in the two systems show the opposite trend with doping.

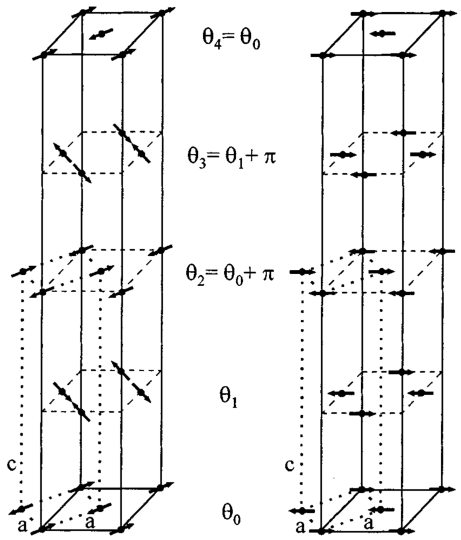

Figure III.3: Ref. [78] finds a $\sqrt{2} \times \sqrt{2} \times 2$ magnetic cell which is either a noncollinear helical structure (left) or a collinear structure (right). θ_0 is undetermined, however it is shown in the images as dipolar calculations predict for each structure.

In Article 1 (Sec. III.3) we measure the magnon dispersion in undoped $Ca_2CuO_2Cl_2$ and provide the first estimate of the superexchange parameter in this cuprate parent compound. This estimate is further refined in preliminary high-resolution Cu L_3-edge RIXS measurements presented in Sec. III.4.1. These results should also help us resolve the direction of the in-plane spin by a detailed study of the *dd*-excitations.

Previous studies on the cuprates, found that the magnons become paramagnons under doping as the long-range afm order is lost, however their spectral weight remains significant even into the overdoped region contrary to INS results [82]. This created friction between the RIXS and INS communities on whether $S(\mathbf{q}, \omega)$ is truly measured by RIXS in the doped cuprates since its cross-section is complicated. The disagreement is more or less resolved when one realizes that the two techniques probe entirely different portions of the Brillouin zone. This is because RIXS probes around Γ=(0,0) of the Brillouin zone, while INS probes around the afm ordering vector M=$(\pi/a,\pi/a)$. In fact, the area in reciprocal space which is believed to host magnetic excitations involved in Cooper pairing is probed by neither RIXS or INS [82]. Our preliminary measurements of the (para)magnon evolution in $Ca_{2-x}Na_xCuO_2Cl_2$ under doping is shown in Sec. III.4.1. As well, some preliminary results studying the bimagnon using Cu L_3-edge RIXS, Cu K-edge RIXS, O K-edge RIXS, and Raman spectroscopy are presented in Sec. III.4.2.

The $Ca_2CuO_2Cl_2$ system has excellent cleavability [83] which has made it a popular system for surface-sensitive studies such angle-resolved photoemission spectroscopy [84] and scanning tunneling microscopy and spectroscopy [85–87]. The latter has detected charge order in $Ca_{2-x}Na_xCuO_2Cl_2$, however no bulk signature of charge order has been found to date [88]. $Ca_{2-x}Na_xCuO_2Cl_2$ is also remarkable since its phase diagram does not show any T_c anomaly at 1/8 doping [89] which is characteristic of charge order pinning. Our recent results in the search for charge order will be discussed in Sec. III.4.4 after first presenting inelastic x-ray scattering measurements of phonon dispersion which suggest charge order exists (Sec. III.4.3).

III.2 $Ca_2CuO_2Cl_2$ crystals

A brief note on sample synthesis and working with these hygroscopic crystals is appropriate to emphasize the difficulty of working with the $Ca_2CuO_2Cl_2$ system. I was not involved with the sample synthesis (Sec. III.2.1), but became familiar with the techniques since I had to break the raw batches we received to find single crystals. Hygroscopic considerations and improvements we made in order to work with these crystals are described in Sec. III.2.2.

III.2.1 Physical properties

$Ca_2CuO_2Cl_2$ can be prepared at ambient pressure by a solid-state reaction of different powders with the correct stoichiometry by annealing at high temperatures in an inert gas atmosphere. For example, Ref. [90] used $CaCl_2$, CaO, and CuO at 1073 K, while Ref. [91] used a 1:1:2 molar ratio of Ca_2CuO_3, CuO, and $CaCl_2$ at 1023 K. Intermediate grindings are performed to ensure a homogeneous mixture and accelerate the reaction. X-ray diffraction finds the $I4/mmm$ space group with $a = b = 3.86735(2)$ Å and $c = 15.0412(1)$ Å [92].

Cuprates can be doped by substituting the cation in the charge reservoir with a different cation which has a similar ionic radius and lower oxidation state. For example, in

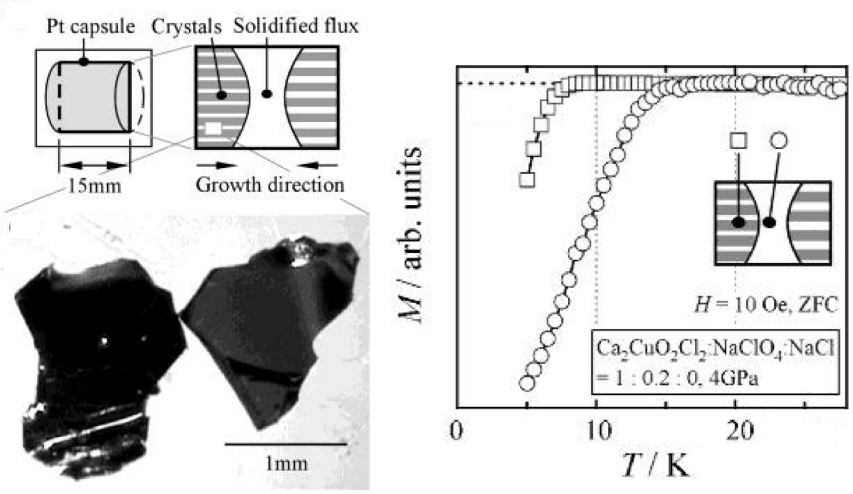

Figure III.4: Growth of $Ca_{2-x}Na_xCuO_2Cl_2$ crystals under high pressure [83]. A typical capsule used for high pressure synthesis is shown in the upper left, showing the growth of crystals is initiated from the ends of the capsule. Black and white image of typical single crystals are shown in the lower left. The right side shows the magnetization curves from a single crystal (squares) and from the flux (circles). The flux has a broader curve showing that it contains polycrystalline samples with different critical temperatures, while the single crystal shows a sharper drop corresponding to a single T_c.

$La_{2-x}Sr_xCuO_4$ we replace La^{3+} with Sr^{2+}. However, the $Ca_2CuO_2Cl_2$ system resisted initial attempts at chemical modification at ambient pressure. It was found that a high pressure and temperature synthesis route must be taken to dope the system [90]. High pressure synthesis is a bit of an art — the "recipes" for doping with Na [80, 83, 89–91, 93–95], K [96], or vacancies [92, 97] all vary slightly in their reactants, pressure application, and pressure-temperature schedule. An example of one recipe is the first synthesis [90] of $Ca_{2-x}Na_xCuO_2Cl_2$ where powders of $Ca_2CuO_2Cl_2$, CuO, and $NaClO_4$ are compressed into gold capsule and heated to 1173 K at 6 GPa. The $NaClO_4$ provides the dopant but the additional oxygen is also important for creating an oxidizing environment.

The compression is achieved with either a cubic-anvil-type or opposed-anvil-type high pressure device, depending on the desired pressure and volume. The applied pressure affects the level of doping (Fig. III.5), for example there is a solubility limit of x=0.21 at 5.5 GPa, although some slightly overdoped polycrystalline samples are created [83]. It is estimated that pressures of 10 GPa with larger volumes will be needed to create overdoped single crystals of $Ca_{2-x}Na_xCuO_2Cl_2$ [83]. These pressures are difficult to produce while keeping an adequate reactant volume. This is important since a press with a large enough volume is needed to create single crystals of a moderate size. Fig. III.4 shows how the crystals grow in the high pressure capsule, extracted single crystals, and magnetization curves taken from different points in the capsule. The crystals grow as very thin $\approx 1 \times 1$ mm^2 flat plaquettes, therefore INS yields are very low and despite a test on the 1T spectrometer (LLB/Karlsrhue) we were only able to extract the elastic component of the magnetic scattering (see Fig. 1 in Article 1). The *c*-axis is usually oriented perpendicular to the large surface, which makes alignment and mounting relatively easy since only the correct in-plane rotation of the sample

must be determined before mounting.

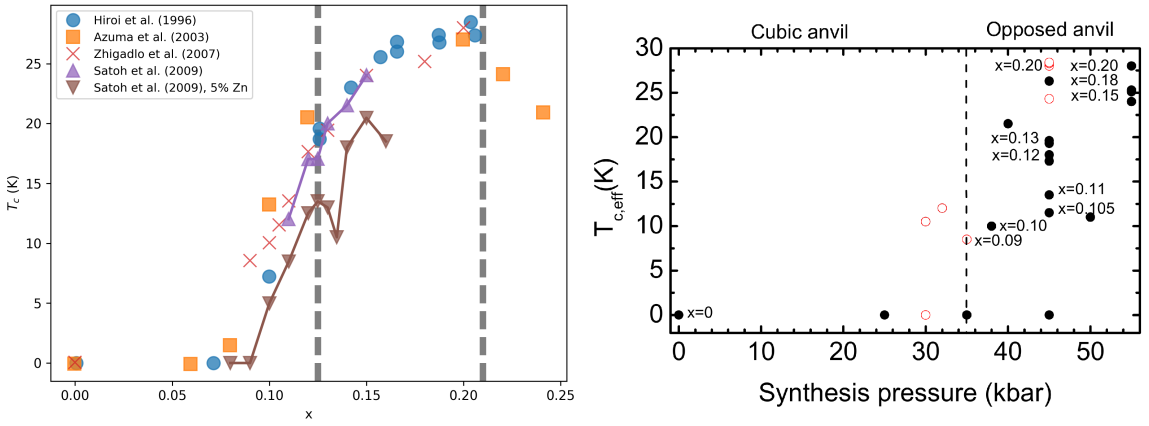

Figure III.5: (Left) Doping dependence of T_c for $Ca_{2-x}Na_xCuO_2Cl_2$ from Refs. [80, 91, 93, 95]. A vertical line is drawn to show 1/8 doping and a second line at x=0.21 to indicate the solubility limit at 5.5 GPa. The two points in the overdoped region were polycrystalline samples. (Right) The doping of $Ca_{2-x}Na_xCuO_2Cl_2$ as a function of synthesis pressure [91]. Closed (open) circles are polycrystalline (single crystal) samples.

A plot of the T_c as a function of Na doping is shown in Fig.III.5. We note that $Ca_{2-x}Na_xCuO_2Cl_2$ does not show the typical 1/8 anomaly [89] seen in other cuprates due to charge order (discussed further in Sec. III.4.4). The lattice constants of $Ca_{2-x}Na_xCuO_2Cl_2$ show inverted doping dependence: increased doping decreases a and increases c. Therefore, we can use our refined lattice constants from single crystal x-ray diffraction to estimate the doping of our crystals to double-check our magnetometric measurements.

Finally it is interesting to note that the T_c of $Ca_{2-x}CuO_2Cl_2$ is higher than $Ca_{2-x}Na_xCuO_2Cl_2$, showing a maximal T_c of 38 K which increases to 43 K upon annealing [92, 97]. The cause of the increased T_c is not clear, however one possible explanation is less disorder since vacancy doping is more efficient (2 holes per vacancy vs. 1 hole per Na). $Ca_{2-x}CuO_2Cl_2$ and $Ca_{2-x}Na_xCuO_2Cl_2$ show the same maximal doping despite the more efficient doping, which suggests an electrostatic limit in the doping process.

III.2.2 Working with hygroscopic crystals

The copper oxychloride crystals are extremely hygroscopic – the crystals react with water vapor in the air and form a blue hydroxide compound (Fig. III.6). The reaction speed is tough to quantify since the moisture in air can vary drastically (0.001%–5% [98]). We do not have a hygrometer and in either case they are notoriously difficult to calibrate. Nonetheless, any manipulation outside of a controlled environment is impossible when it is very humid. For example, our crystals are made in Japan and they cannot produce them during the monsoon season since they see hydroxide damage, even in the short amount of time it takes to transfer the samples from the press to a glovebox. On the other hand, the air is quite dry at synchrotron facilities, a side-effect of the air conditioning systems used to keep the experimental hall at a constant temperature. We have found that the samples can be

manipulated in air at these facilities for a few minutes without any sign of damage, although obviously we avoid this as much as possible.

Figure III.6: (Left) $Ca_2CuO_2Cl_2$ crystal shows hydroxide damage after performing x-ray diffraction for two hours, using a cryojet to protect the crystal.

We used a glovebox which was repurposed from its original use of loading diamond anvil cells. The glovebox is kept at least 150 Pa above ambient pressure with argon. The advantage of argon over the more traditional nitrogen is its mass. The lighter water molecules will be pushed towards the top of the glovebox, away from the working area, and out of glovebox through the gas outlet located on the top. We also keep desiccant in the working area and load lock to ensure dryness. The glovebox is manual, in that the only control we have is with a needle flow control valve attached to a Thorpe tube flowmeter. A constant flow was used while working with samples. When we were not working with samples, they were stored in hermetically-sealed plastic boxes filled with desiccant, which were placed inside a larger hermetically-sealed box with desiccant. The glovebox pressure was kept in a steady state at 150 Pa by opening the flow valve slightly to counteract any small leaks.

During my thesis I have improved the glovebox by:

- Adding an "air lock" in which the outlet feeds into a tube submerged in oil, which allowed the glovebox to be used alone (originally a second person was present to open and close the gas outlet). The air lock avoids air entering during brief moments of under-pressure and prevents over-pressure, since a pressure above 500 Pa would be enough to overcome the pressure from the oil and bubbles would be released.

- Performing a He leak check to find and repair a number of leaks.

- Adding a vacuum pump to the load lock chamber, which allowed us to perform purging cycles before passing anything in or out of the main chamber.

These improvements, along with diligent recycling of the desiccant, kept the glovebox completely dry. Samples could be left in the glovebox out of their storage boxes for over three days with no signs of hydroxide damage. The situation is more difficult when we need to

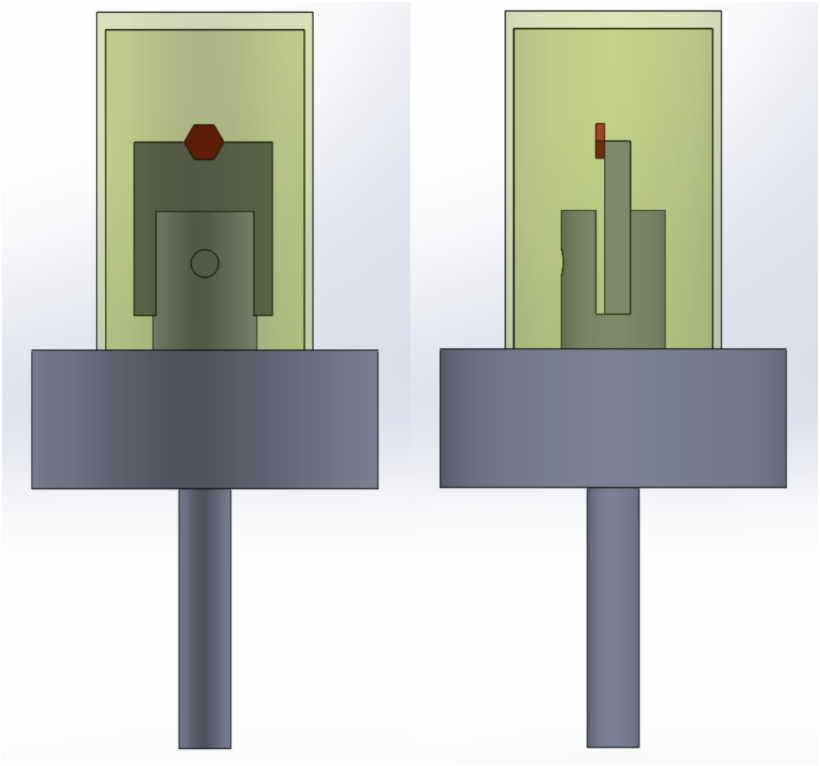

Figure III.7: A sample mount designed to protect the samples while performing x-ray diffraction.

characterize and align the samples. One simple solution is to protect the samples with an oil or grease. We tried paraffin oil and vacuum grease but the results were inconsistent. Furthermore, this technique is incompatible for UHV environments, which are required for soft x-ray experiments. We also tried using a cryojet which worked moderately well, however turbulent flow is difficult to avoid and we would often have hydroxide damage on the sides of the crystal (Fig. III.6). After these trials, we found two solutions which work consistently. The first is simply to sandwich the sample between two pieces of Kapton tape. The one initial disadvantage was that the sample was often damaged when trying to recover the sample! This was solved later by adding a piece of Kapton foil on both pieces of tape to avoid contact with the sample. This system was tested by performing x-ray diffraction before and after leaving the sample exposed for three days. I found no change in the diffraction pattern indicating the seal was good. Visual inspection after in the glovebox showed no blue hydroxide. We also took a powder diffractogram of a hydroxide sample in order to have reference. The second technique is done with sample mount shown in Fig. III.7. The sample is protected from the air by a Kapton tube sealed with glue at the top and by putty at the bottom. The

advantage of this mount is that the sample is already attached to a copper mount, so the orientation matrix can be transferred using the edge of the copper mount as a reference. As well, the sample was sure not to move during the measurements, like they did sometimes depending on their size with the double-tape technique. For magnetometric measurements the sample is in a sealed chamber with low pressure He gas, therefore no protection is needed during the measurement. Nonetheless, to avoid hydroxide formation during the loading and unloading we protected the capsule holding the sample with Parafilm.

III.3 Article 1: Resonant inelastic x-ray scattering study of spin-wave excitations in the cuprate parent compound $Ca_2CuO_2Cl_2$

Status: Published in *Physical Review B* **95**, 155110 [4] on 7 April 2017

Author contributions: The $Ca_2CuO_2Cl_2$ samples used in this study were synthesized by Runze Yu and Masaki Azuma. They were prepared for the experiment by Matteo d'Astuto with the help of Benoît Baptiste, Mark Dean, and Alessandro Nicolau. Resonant inelastic x-ray scattering at the Cu L_3-edge was performed on the ADRESS beamline at the Swiss Light Source by Matteo d'Astuto, Mark Dean, and Alessandro Nicolau with the help of the beamline staff Jonathan Pelliciari, Marco Dantz, and Thorsten Schmitt. Data treatment was done by Blair Lebert with the advice of Matteo d'Astuto, Mark Dean, Hu Miao, and Jonathan Pelliciari. The article was prepared by Blair Lebert with corrections/advice from Matteo d'Astutothe rest of the authors. Blair Lebert, Matteo d'Astuto, Hu Miao, and John-Paul Castellan characterized a different sample from the same batch using neutron scattering on the 1T spectrometer at Laboratoire Leon-Brillouin.

Resonant inelastic x-ray scattering study of spin-wave excitations in the cuprate parent compound $Ca_2CuO_2Cl_2$

B. W. Lebert,[1,2] M. P. M. Dean,[3] A. Nicolaou,[2] J. Pelliciari,[4] M. Dantz,[4] T. Schmitt,[4] R. Yu,[5] M. Azuma,[5] J.-P. Castellan,[6,7] H. Miao,[3] A. Gauzzi,[1] B. Baptiste,[1] and M. d'Astuto[1,*]

[1]*IMPMC-Sorbonne Universités, Université Pierre et Marie Curie, CNRS, IRD, MNHN 4, place Jussieu, 75252 Paris, France*

[2]*Synchrotron SOLEIL, L'Orme des Merisiers, Saint-Aubin, 91192 Gif-sur-Yvette Cedex, France*

[3]*Department of Condensed Matter Physics and Materials Science, Brookhaven National Laboratory, Upton, New York 11973, USA*

[4]*Swiss Light Source, Paul Scherrer Institut, CH-5232 Villigen PSI, Switzerland*

[5]*Materials and Structures Laboratory, Tokyo Institute of Technology, 4259 Nagatsuta, Midori, Yokohama 226-8503, Japan*

[6]*Laboratoire Léon Brillouin (CEA-CNRS), CEA-Saclay, F-91911 Gif-sur-Yvette, France*

[7]*Institute for Solid State Physics, Karlsruhe Institute of Technology, D-76021 Karlsruhe, Germany*

(Received 28 October 2016; revised manuscript received 7 March 2017; published 7 April 2017)

By means of resonant inelastic x-ray scattering at the Cu L_3 edge, we measured the spin-wave dispersion along $\langle 100\rangle$ and $\langle 110\rangle$ in the undoped cuprate $Ca_2CuO_2Cl_2$. The data yield a reliable estimate of the superexchange parameter $J = 135 \pm 4$ meV using a classical spin-1/2 two-dimensional Heisenberg model with nearest-neighbor interactions and including quantum fluctuations. Including further exchange interactions increases the estimate to $J = 141$ meV. The 40 meV dispersion between the magnetic Brillouin zone boundary points (1/2, 0) and (1/4, 1/4) indicates that next-nearest-neighbor interactions in this compound are intermediate between the values found in La_2CuO_4 and $Sr_2CuO_2Cl_2$. Due to the low-Z elements composing $Ca_2CuO_2Cl_2$, the present results may enable a reliable comparison with the predictions of quantum many-body calculations, which would improve our understanding of the role of magnetic excitations and of electronic correlations in cuprates.

DOI: 10.1103/PhysRevB.95.155110

I. INTRODUCTION

Magnetic excitations have been intensively studied in high-temperature superconducting (HTS) cuprates for their possible role in the pairing mechanism of these materials [1–4]. Although several studies have already been carried out by means of inelastic neutron scattering (INS) [3] on a number of cuprate compounds, the interpretation of the data remains highly controversial because of the lack of a theoretical understanding of electronic correlations in realistic systems.

Recently, Cu L_3 edge resonant inelastic x-ray scattering (RIXS) [5,6] has emerged as an alternative probe of the above excitations. This technique extends the energy range probed by INS to higher energies [7], and it also offers the advantage of measuring small single crystals. To the best of our knowledge, in HTS cuprates, RIXS has been hitherto employed to complete previous INS studies on well-known compounds. In the case of $La_{2-x}Sr_xCuO_4$, for example, the RIXS results found that magnetic excitations persist up to very high doping levels in regions of the Brillouin zone that are not easily probed by INS [8].

The purpose of the present work is to study by means of RIXS the HTS cuprate parent compound $Ca_2CuO_2Cl_2$ (CCOC), for which INS studies are infeasible because samples are only available as small, hygroscopic single crystals. This parent compound can be doped either with sodium, $Ca_{2-x}Na_xCuO_2Cl_2$ (Na-CCOC) [9,10], or with vacancies, $Ca_{2-x}CuO_2Cl_2$ [11]. The motivation of our study is the simplicity of their single-layer tetragonal structure and the absence of structural instabilities that often jeopardize the study of more common cuprates, such as the aforementioned $La_{2-x}Sr_xCuO_4$. Moreover, the $Ca_2CuO_2Cl_2$ system is the only HTS cuprate system composed exclusively of low Z ions, with copper being the heaviest. This is an advantage for standard *ab initio* density-functional-theory calculations, where large Z ions pose problems for pseudopotential optimization. This feature is even more advantageous for advanced theoretical methods suitable to take into account correlation effects, such as quantum Monte Carlo, since they require one to treat accurately the spin-orbit coupling. To circumvent this difficulty, these quantum many-body calculations are mainly applied to systems with light atoms, where relativistic effects are negligible [12–14]. Note that Ref. [14] treats in particular $Ca_2CuO_2Cl_2$, although without separating the different components of the magnetic exchange interaction. In this respect, $Ca_{2-x}CuO_2Cl_2$ and $Ca_{2-x}Na_xCuO_2Cl_2$ are the most suitable example of such low-Z systems among HTS cuprates. In addition, the superconducting compound $Ca_{2-x}Na_xCuO_2Cl_2$ has already been studied by means of photoemission and scanning tunneling spectroscopy [9,15,16], therefore a RIXS study is expected to provide further insight into the electronic excitation spectrum. In the present work, by means of RIXS, we study the spin-wave dispersion of $Ca_2CuO_2Cl_2$, the parent compound of the above HTS cuprate, and we extract the superexchange parameter J using two different models.

II. EXPERIMENTAL METHODS

A. Crystal growth and characterization

Single crystals of $Ca_2CuO_2Cl_2$ were grown from $CaCO_3$, CuO, and $CaCl_2$ by solid state reaction, as described in detail elsewhere [10,11]. As shown in Fig. 1, $Ca_2CuO_2Cl_2$ has a tetragonal K_2NiF_4-type structure ($I4/mmm$) [19] with alternate stacking of $(Ca,Cl)_2$ and CuO_2 layers. The lattice parameters at ambient conditions are $a = b = 3.867\,35(2)$ Å

*matteo.dastuto@impmc.upmc.fr

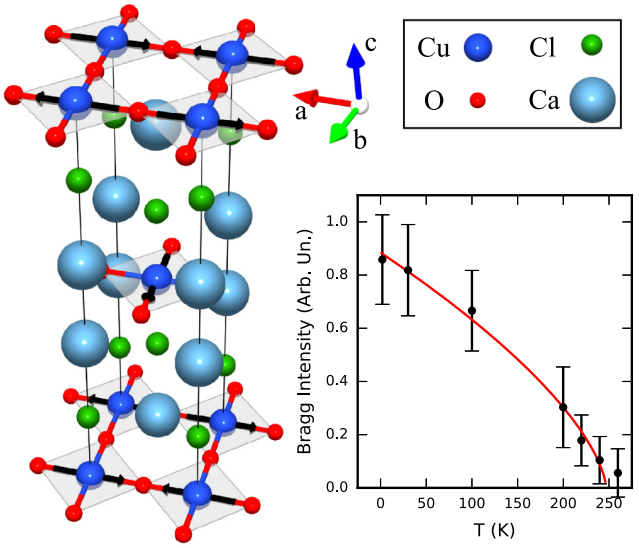

FIG. 1. Top left: Tetragonal crystal structure [17] of $Ca_2CuO_2Cl_2$ [11]. The square coordination of copper with its four nearest-neighbor oxygen ions in the CuO_2 planes is shown. The chlorine ions are located in the apical site above and below the copper. Black arrows indicate one of the possible magnetic structures consistent with neutron-diffraction data [18]. Bottom right: Temperature dependence of the fitted intensity of the averaged Bragg reflections $(\frac{1}{2},\frac{1}{2},\frac{5}{2})$ and $(\frac{1}{2},\frac{1}{2},\frac{7}{2})$ and a power-law fit (red).

and $c = 15.0412(1)$ Å [10,11]. The crystals are easily cleaved along the *ab* plane due to the weak ionic bonds between adjacent layers.

The single crystals of ≈2 mm width/height and ≈0.2 mm thickness were characterized using a commercial Bruker four-circle κ geometry diffractometer. A fixed Mo anode was used and the filtered $K\alpha$ emission was collimated at 0.2 mm (3 mrad). A cryogenic N_2 flux was used to isolate the sample from humidity. The measurements yield unit-cell parameters in agreement with the literature [10,11], and they also enabled us to determine the crystal orientation with respect to visible facets. The samples for RIXS measurements were subsequently glued on the holder with silver epoxy. Finally, ceramic posts were attached with the same epoxy in order to cleave the crystals in vacuum.

$Ca_2CuO_2Cl_2$ is an antiferromagnetic insulator with a Néel temperature of $T_N = 247 \pm 5$ K [18]. To check the magnetic state of the samples, we performed neutron scattering on the 1T spectrometer at Laboratoire Leon–Brillouin using a sample from the same batch used for the RIXS experiment. We measured very weak magnetic reflections at low temperature for $\mathbf{q} = (\frac{1}{2},\frac{1}{2},\frac{\ell}{2})$ with $\ell = 2n+1$ $(n = 0,\ldots,4)$, but none for $\ell = 0$, in agreement with Ref. [18]. The temperature dependence of the fitted Bragg intensity [average of the $(\frac{1}{2},\frac{1}{2},\frac{5}{2})$ and $(\frac{1}{2},\frac{1}{2},\frac{7}{2})$ reflections] is shown in the bottom right of Fig. 1, and a power-law fit finds $T_N = 247 \pm 6$ K.

B. Resonant inelastic x-ray scattering

RIXS measurements at the Cu L_3 edge (930 eV) were performed at the ADRESS beamline [21,22] of the Swiss Light Source using the SAXES spectrometer [23]. The samples were mounted in the ultrahigh-vacuum manipulator cryostat of the experimental station. By applying a force on the aforementioned ceramic posts, the samples were cleaved *in situ* under ultrahigh vacuum and low-temperature conditions to avoid hygroscopic damage of the cleaved surface. Their surface quality was confirmed by x-ray absorption spectroscopy. All spectra presented in this work were taken at 15 K.

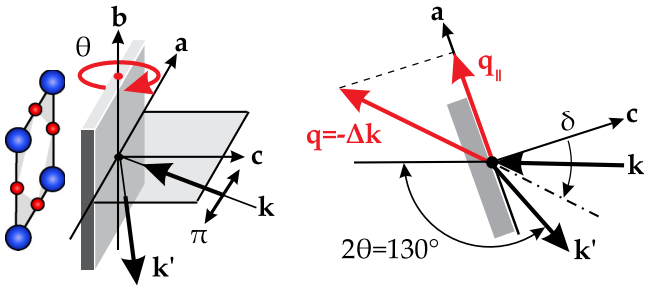

FIG. 2. RIXS geometry for measuring along ⟨100⟩ with π-polarization and grazing out emission (modified from Ref. [20]). The scattering angle 2θ is defined between the photon momentum of the incoming beam $\mathbf{k}$ and the direction where the analyzer collects the scattered beam $\mathbf{k}'$. 2θ and the azimuthal angles are fixed, whereas the incident angle can be changed by a rotation, θ, around the *b* axis. The incident angle defines δ, which is the angle between the sample normal $\mathbf{c}$ and the transferred momentum $\mathbf{q}$ (red arrow), so that $\delta = 0$ in specular reflection. The projection of $\mathbf{q}$ onto the sample's *ab* plane is denoted $\mathbf{q}_\parallel$, which is 0 for $\delta = 0$ and maximal for grazing geometries. Measurements along ⟨110⟩ are done with the sample rotated 45° around the *c* axis.

The experimental geometry is shown in Fig. 2 and was similar to previous RIXS studies on cuprate parent compounds [6]. We used π-polarized incident x rays and a grazing exit geometry in order to enhance the single magnon spectral weight [7,24–29]. The scattering angle was fixed at $2\theta = 130°$, giving a constant momentum transfer to the sample of $q = 2k\sin(\theta) = 0.85$ Å^{-1}. Although q is fixed, its component in the *ab* plane, $q_\parallel$, can be changed by rotating the sample about the vertical axis (*b* axis in Fig. 2). For a given rotation, θ, the deviation from specular reflection is given as $\delta = \theta_{\text{specular}} - \theta$, thus $q_\parallel = q\sin(\delta)$. The minimum (maximum) δ used was +5° (+55°) corresponding to $q_\parallel = +0.07$ Å^{-1} ($q_\parallel = +0.70$ Å^{-1}). Therefore, in terms of reciprocal-lattice units $(2\pi/a)$ in the *ab* plane, we measured $\mathbf{q}_\parallel$ from (0.05, 0) to (0.43, 0) along ⟨100⟩ and from (0.03, 0.03) to (0.3, 0.3) along ⟨110⟩. In other terms (Fig. 6, inset), we measured past the magnetic Brillouin zone along Γ-M, but well short of where thermal neutrons measure at $M = (1/2,1/2)$. Along Γ-X we measured very close to the first Brillouin zone edge at $X = (1/2,0)$.

III. RESULTS AND DISCUSSION

The RIXS map of $Ca_2CuO_2Cl_2$ at $\mathbf{q}_\parallel = (0.34,0)$ shown in Fig. 3 highlights the resonant behavior of the inelastic features. From lower- to higher-energy loss, one notes a midinfrared peak between 0.1 and 0.6 eV, *dd* excitations between 1 and 3 eV, and weak charge-transfer excitations at higher energies. A weak fluorescence line is visible at energies above the

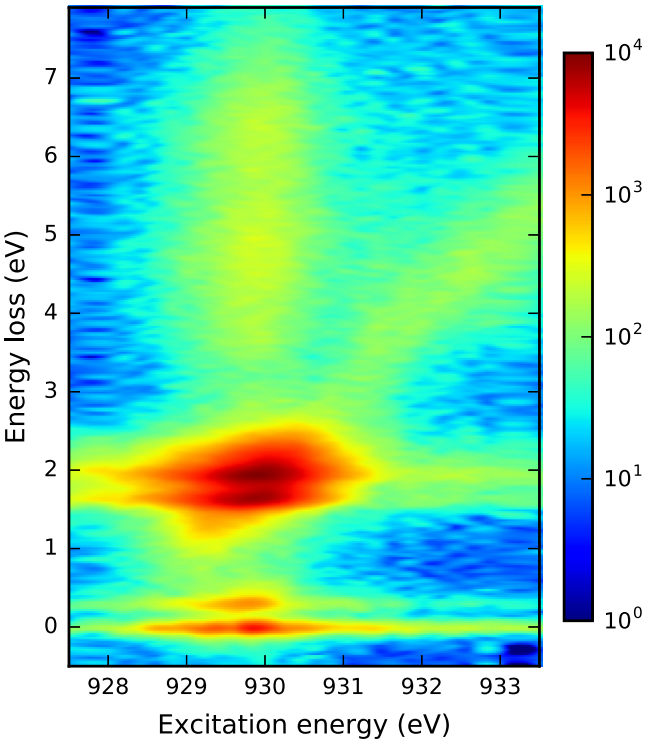

FIG. 3. RIXS map at $\mathbf{q}_\parallel = (0.34,0)$ with π incidence polarization showing the resonant behavior of the magnetic excitations, *dd* excitations, and charge-transfer excitations. Weak fluorescence is seen at high energy when the system is excited above the Cu L_3 edge threshold. The color map is a logarithmic scale in arbitrary intensity units.

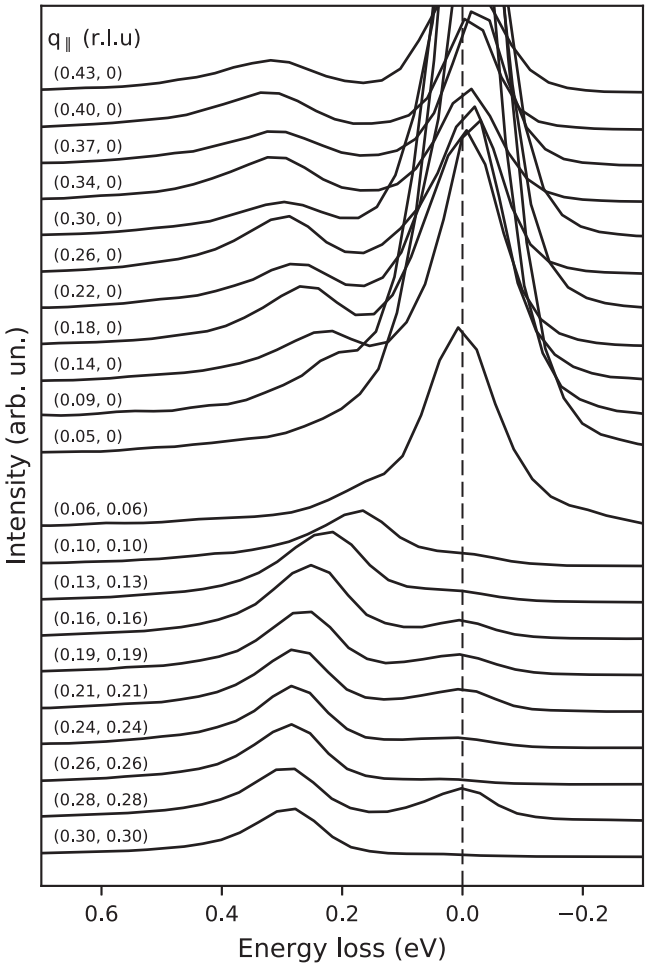

FIG. 4. RIXS spectra showing the dispersion of the magnetic excitations along ⟨100⟩ (top) and ⟨110⟩ (bottom). Spectra are normalized by their *dd* excitations.

Cu L_3 edge and intersects the *dd* excitations at resonance. The spectral weight from this fluorescence line at resonance is unknown, but it is likely of the same order as the *dd* excitations, as evidenced by the diagonal skew of the *dd* excitations.

Figure 4 shows the RIXS spectra obtained along both directions focusing on the midinfrared energy region, while Fig. 5(a) shows the full energy region for $\delta = +10$ and $+55$. The spectra are normalized to the area of the *dd* excitations to account for the geometrical changes of the RIXS cross section. There is an expected increase in elastic scattering near specular, i.e., at (0.09, 0) and (0.06, 0.06). However, the elastic line for the sample aligned along ⟨100⟩ was large for all momentum transfers. These variations are likely due to finite surface quality after cleaving and did not impede accurate fitting.

The midinfrared feature is assigned as a magnon with a higher-energy multimagnon continuum. This assignment was done considering its dispersion (Figs. 4 and 6) and past RIXS results on cuprate parent compounds in this experiment geometry [6,7]. Furthermore, in our case, magnetic excitations are the only excitation in the midinfrared energy region due to the ≈2 eV Mott gap. These spin excitations are the focus of our paper and are discussed below.

The apical chlorine in $Ca_2CuO_2Cl_2$ increases the tetragonal distortion much like for $Sr_2CuO_2Cl_2$, therefore based on Ref. [20] we assigned the *dd* excitation at 1.70 eV to Cu $3d_{xy}$, 1.99 eV to Cu $3d_{xz/yz}$, and higher energies in the shoulder to Cu $3d_{3z^2-r^2}$. The *dd* excitations were not well fit following the technique of Ref. [20], possibly due to fluorescence emission in this energy region or electron-phonon coupling [30].

The broad charge-transfer feature centered around 5.5 eV did not show dispersion or significant intensity variations, in agreement with Cu K edge RIXS [31]. The author of Ref. [31] assigned this feature as transitions to an excited state composed of symmetric contributions of a central Cu $3d_{x^2-y^2}$ orbital and the surrounding O $2p_\sigma$ orbitals. Cu K edge RIXS also found a dispersive Mott excitation from 2.35 to 3.06 eV along Γ-X and from 2.34 to 4.14 eV along Γ-M. Therefore, the Mott excitation will fall under the *dd* excitations for the majority of our momentum transfers, however the Mott excitation at ≈3.4 eV for $\mathbf{q}_\parallel = (0.3,0.3)$ is not visible in our results [Fig. 5(a)].

A typical fit of the midinfrared region is shown for $\mathbf{q}_\parallel = (0.21,0.21)$ in Fig. 5(b) and the extracted magnon dispersion is shown in Fig. 6. The resolution function was measured on carbon tape and was well described by a Lorentzian squared function of 130 meV full width at half-maximum. The elastic, phonon, and single magnon contributions were all resolution-limited. The multimagnon excitation continuum was modeled as the resolution function convolved with a step function with subsequent exponential decay toward higher-energy losses.

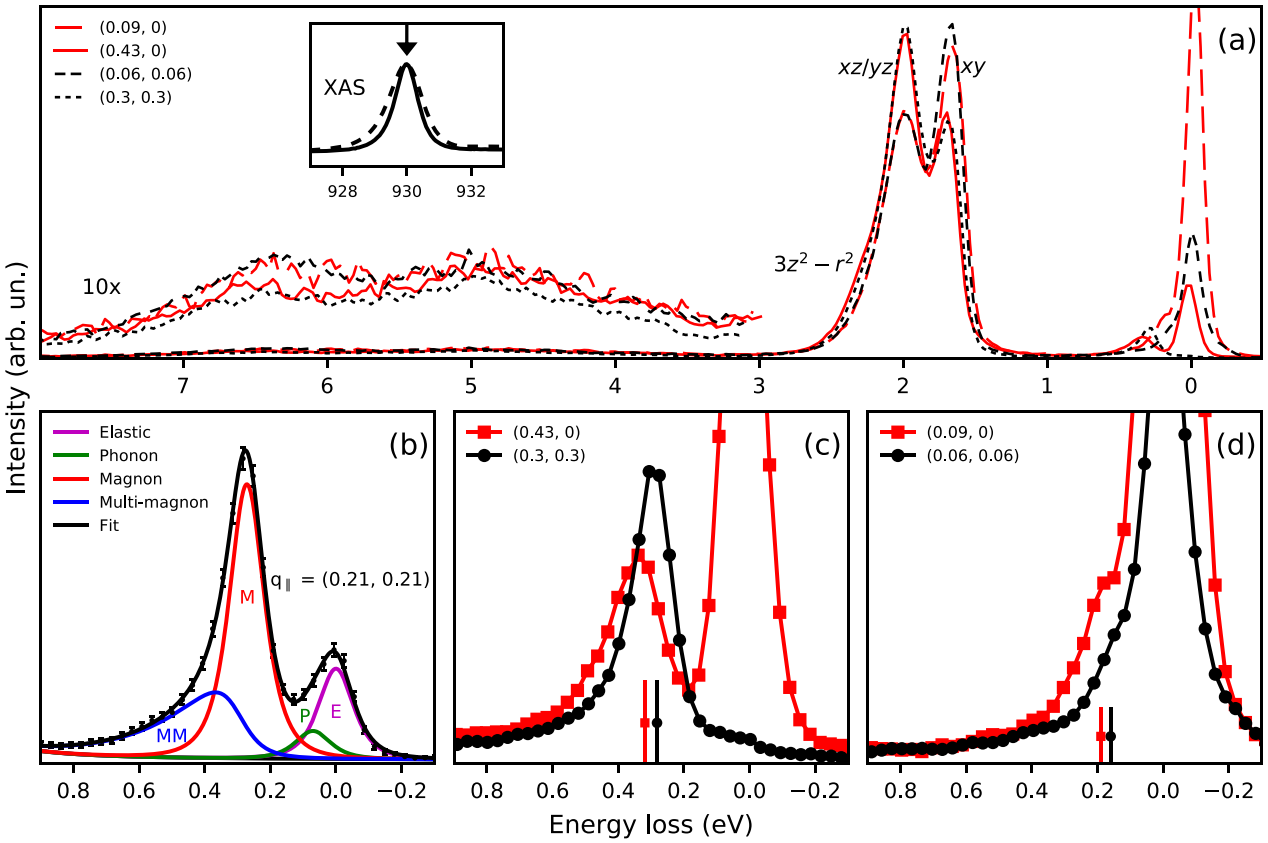

FIG. 5. Cu L_3 RIXS spectra of $Ca_2CuO_2Cl_2$ at different in-plane transferred momentum, $\mathbf{q}_\parallel$, expressed as (h, k) in reciprocal-lattice units. (a) Representative RIXS spectra along ⟨100⟩ (red) and ⟨110⟩ (black). All spectra have been normalized to the area of the *dd* excitations. The midinfrared regions of these spectra are shown in (c,d), where vertical bars represent the energy of a single magnon found by fitting. The inset shows TEY-XAS (solid) and TFY-XAS (dashed), with an arrow indicating incident energy for our RIXS measurements. (b) Example of the fitting procedure at $\mathbf{q}_\parallel = (0.21,0.21)$ shown as a black curve through data points. The elastic (E, magenta), phonon (P, green), and single magnon (M, red) peaks were resolution-limited, and the multimagnon (MM, blue) peak fitting is described in the text.

The background was a Lorentzian tail of the form $y = A(x - x_0)^{-2} + c$. The energy of the phonon contribution is found around 60–70 meV with respect to the elastic, or ∼15–17 THz, roughly corresponding to the Debye cutoff frequency ω_D of $Ca_2CuO_2Cl_2$ [32]. The major source of uncertainty for the magnon energy was determining the elastic energy, since the elastic line was irregular for the sample aligned along ⟨100⟩ and often too weak along ⟨110⟩. *dd* excitations in undoped layered cuprates are known to be nondispersive within current experimental accuracy [20], therefore the elastic energy was fixed with respect to the Cu $3d_{xz/yz}$ energy, which was found to be 1985 ± 5 meV from several spectra with well-defined elastic lines.

The experimental and calculated dispersion along the two high-symmetry directions is shown together in Fig. 6. We use a classical $S = 1/2$ 2D Heisenberg model with higher-order coupling to analyze our dispersion. The Hamiltonian is given by [33]

$$\mathcal{H} = J \sum_{\langle i,j \rangle} \mathbf{S}_i \cdot \mathbf{S}_j + J' \sum_{\langle i,i' \rangle} \mathbf{S}_i \cdot \mathbf{S}_{i'} + J'' \sum_{\langle i,i'' \rangle} \mathbf{S}_i \cdot \mathbf{S}_{i''} + J_c \sum_{\langle i,j,k,l \rangle} \{(\mathbf{S}_i \cdot \mathbf{S}_j)(\mathbf{S}_k \cdot \mathbf{S}_l) + (\mathbf{S}_i \cdot \mathbf{S}_l)(\mathbf{S}_k \cdot \mathbf{S}_j) - (\mathbf{S}_i \cdot \mathbf{S}_k)(\mathbf{S}_j \cdot \mathbf{S}_l)\},$$

where we include first-, second-, and third-nearest-neighbor exchange terms, as well as a ring exchange term (J, J', J'', and J_c). Within classic linear spin-wave theory [34,35], this leads to a dispersion relation given by [33] $\hbar\omega_\mathbf{q} = 2Z_C(\mathbf{q})\sqrt{A_\mathbf{q}^2 - B_\mathbf{q}^2}$, where $A_\mathbf{q}^2 = J - J_c/2 - (J' - J_c/4)(1 - \nu_h\nu_k) - J''[1 - (\nu_{2h} + \nu_{2k})/2]$, $B_\mathbf{q}^2 = (J - J_c/2)(\nu_h + \nu_k)/2$, $\nu_x = \cos(2\pi x)$, and $Z_C(\mathbf{q})$ is a spin renormalization factor [33,36].

As a first approximation, we consider only the first term in the Hamiltonian, which corresponds to only nearest-neighbor exchange. In this isotropic case, the dispersion relation above reduces to $\hbar\omega_\mathbf{q} = 2JZ_C\sqrt{1 - [\cos(2\pi h) + \cos(2\pi k)]^2/4}$, where $Z_c = 1.18$ is a constant [36]. The calculation for our data is shown in Fig. 6 as a solid red line, obtained both analytically and using the SPINWAVE code [35], as a check. The energy at the zone boundary peaks at $2JZ_C = 320 \pm 10$ meV, which gives $J = 135 \pm 4$ meV. For La_2CuO_4 and $Sr_2CuO_2Cl_2$, the zone boundary energy is 314 ± 7 and 310 meV, respectively, which corresponds to $J = 133 \pm 3$ and 131 meV, respectively [7,33].

Note the 40 ± 10 meV energy difference along the magnetic Brillouin zone boundary (MBZB) between X and M. This MBZB dispersion is an indication of non-negligible magnetic

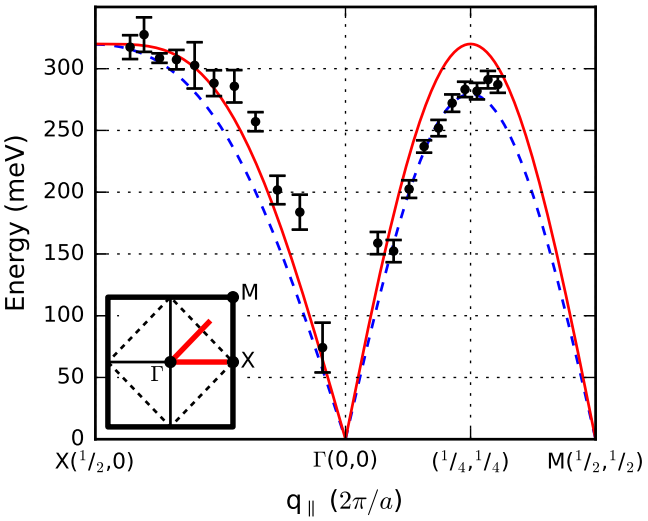

FIG. 6. Dispersion of $Ca_2CuO_2Cl_2$ measured using Cu L_3 RIXS. The red, continuous line is a calculation for a classical spin-1/2 2D Heisenberg model with nearest-neighbor exchange, and the blue, dashed line is a calculation including further exchange terms that is described in the text. Inset: 2D Brillouin zone showing high-symmetry points. The first Brillouin zone boundary is represented by a thick black square, while the magnetic Brillouin zone boundary is represented by a dashed line. The region where we measured is shown as two thick red lines along Γ-X and Γ-M.

interactions beyond nearest neighbors [7,33,37]. Following Ref. [33], we parametrize the above Hamiltonian with a single-band Hubbard model with U, the on-site repulsion, and t, the nearest-neighbor hopping. Expanding the Hubbard Hamiltonian to order t^4, we find $J = 4t^2/U - 24t^4/U^3$, $J_c = 80t^4/U^3$, and $J' = J'' = 4t^4/U^3$. We assume the spin renormalization is constant, $Z_c(\mathbf{q}) \approx Z_c$, which introduces an error less than the uncertainty of our data [33]. Within this model, it can be shown [38] that the maximum energy at X is given by $E_{\max} = 2Z_C(J - J_c/10)$ and the energy dispersion along the MBZB is given as $\Delta E_{\mathrm{MBZB}} = 3Z_C J_c/5$. We can use our experimental dispersion to fix $E_{\max} = 320$ meV and $\Delta E_{\mathrm{MBZB}} = 40$ meV, which uniquely determines $U = 2.2$ eV and $t = 295$ meV. The corresponding superexchange parameter is $J = 141$ meV, versus $J = 146$ meV for La_2CuO_4 and $J = 144$ meV for $Sr_2CuO_2Cl_2$. The calculated dispersion using these values is shown in Fig. 6 as a dashed blue line. The MBZB dispersion is well fit, however the energy along $\langle 100 \rangle$ is underestimated, indicating the need to include further hopping terms in the Hubbard model [37,39]. Furthermore, our values of U and t are unphysical, even if they are similar to those found in La_2CuO_4 at 10 K using this approach [33] ($U = 2.2$ eV and $t = 300$ meV). They are in disagreement with photoemission results [40], and $U = 7.5t$ is less than the tight-binding bandwidth [39] of $8t$. Inclusion of further hopping terms is beyond the scope of this paper, however they will not fundamentally change the determination of the superexchange parameter J.

The fact that all three cuprates discussed above have a very similar $E_{\max}$ is a bit surprising. The simplistic scaling relation [41] $J \propto {d_{\mathrm{NN}}}^4$ based on the intraplanar Cu NN distance would predict a 7% softening of $Ca_2CuO_2Cl_2$ with respect to La_2CuO_4 ($d_{\mathrm{NN}} = 3.803$ Å) [42] and an 11% hardening with respect to $Sr_2CuO_2Cl_2$ ($d_{\mathrm{NN}} = 3.975$ Å) [42].

On the other hand, these three cuprates have different ΔE_{MBZB}, with La_2CuO_4 being smaller (22 ± 10 meV) and $Sr_2CuO_2Cl_2$ being larger (70 meV). With further exchange terms [43] it is found that the dispersion scales as $(t'/t)^2$, where t' is the next-nearest-neighbor hopping. This second hopping term is typically decreased due to apical hybridization [44], therefore we would expect greater dispersion for longer apical bonds lengths. This is indeed the trend we see for these three compounds: $Sr_2CuO_2Cl_2$ (2.8612 Å) > $Ca_2CuO_2Cl_2$ (2.734 Å) > La_2CuO_4 (2.416 Å). If this interpretation is correct, then our assignment of the shoulder in the dd excitations to Cu $3d_{3z^2-r^2}$ is likely incorrect since we would then expect $E_{3z^2-r^2}$ for $Ca_2CuO_2Cl_2$ to be less than 1.97 eV ($Sr_2CuO_2Cl_2$) and more than 1.7 eV (La_2CuO_4) [20].

Although Ref. [14] did not report a value of J, the current uncertainty in QMC calculations allows a rough comparison between them and experiment. QMC calculations [12,13] have found $J = 160(13)$ meV for La_2CuO_4, $J = 140(20)$ meV for $CaCuO_2$, and $J = 159(14)$ meV for Ca_2CuO_3. The value found for La_2CuO_4 is quite different from its experimental value, possibly due to relativistic effects in the La atoms. $CaCuO_2$ and $Ca_2CuO_2Cl_2$ are both composed of CuO_2 planes with interplanar Ca atoms, however $CaCuO_2$ lacks any apical ligand. Nonetheless, its calculated value matches quite well our results above, much better than the Cu chain system of Ca_2CuO_3, which has apical oxygens, emphasizing the important role that the apical ligands play in intraplanar (chain) exchange.

IV. CONCLUSIONS

In conclusion, the present Cu L_3 edge RIXS study enabled us to determine the spin-wave dispersion along the two high-symmetry directions of $Ca_2CuO_2Cl_2$, an undoped antiferromagnetic HTS cuprate parent compound containing only low-Z elements. In a first approximation, the data are explained within a simple $S = 1/2$ 2D Heisenberg model with a nearest-neighbor exchange term $J = 135 \pm 4$ meV, taking into account spin quantum fluctuation renormalization. Including next-nearest-neighbor contributions, our estimate is increased to $J = 141$ meV. To the best of our knowledge, this is the first measurement of the spin-wave dispersion and of its zone-boundary energy in $Ca_2CuO_2Cl_2$, noting that INS experiments are currently infeasible, and two-magnon Raman scattering has not been performed yet. We believe that the present low-Z cuprate $Ca_2CuO_2Cl_2$ is an ideal playground for future quantum many-body theoretical models of HTS cuprates. Our RIXS results combined with the future results of these models will offer a unique comparison between experiment and state-of-the-art theory of correlated electron systems.

ACKNOWLEDGMENTS

The authors acknowledge the Paul Scherrer Institut, Villigen-PSI, Switzerland for provision of synchrotron radiation beamtime at beamline X03MA, "ADRESS" of the

Swiss Light Source, as well as LLB and KIT for providing neutron beamtime on the 1T spectrometer, and we would like to thank Yvan Sidis for his assistance. We are grateful to Jean-Pascal Rueff, Sylvain Petit, and Marco Moretti for fruitful discussions, as well as Lise-Marie Chamoreau from the "Plateforme Diffraction" at IPCM for help in crystallographic orientation. We are very grateful to Sylvain Petit for his help with the SPINWAVE code [35]. B.L. acknowledges financial support from the French state funds managed by the Agence Nationale de la Recherche (ANR) within the "Investissements d'Avenir" programme under reference ANR-11-IDEX-0004-02, and within the framework of the Cluster of Excellence MATISSE led by Sorbonne Université and from the LLB/SOLEIL Ph.D. fellowship program. This material is based upon work supported by the U.S. Department of Energy, Office of Basic Energy Sciences, Early Career Award Program under Award No. 1047478. Brookhaven National Laboratory was supported by the U.S. Department of Energy, Office of Science, Office of Basic Energy Sciences under Contract No. DE-SC00112704. J.P. and T.S. acknowledge financial support through the Dysenos AG by Kabelwerke Brugg AG Holding, Fachhochschule Nordwestschweiz, and the Paul Scherrer Institut. M.D. acknowledges financial support from the Swiss National Science Foundation within the D-A-CH programme (SNSF Research Grant No. 200021L 141325). The research leading to these results has received funding from the European Community's Seventh Framework Programme (FP7/2007-2013) under grant agreement n. °312284. This work was written on the collaborative OVERLEAF platform [45].

[1] D. J. Scalapino, Phys. Rep. **250**, 329 (1995).
[2] J. Orenstein and A. J. Millis, Science **288**, 468 (2000).
[3] Y. Sidis, S. Pailhès, B. Keimer, P. Bourges, C. Ulrich, and L. P. Regnault, Phys. Status Solidi B **241**, 1204 (2004).
[4] P. A. Lee, N. Nagaosa, and X.-G. Wen, Rev. Mod. Phys. **78**, 17 (2006).
[5] L. Braicovich, J. van den Brink, V. Bisogni, M. M. Sala, L. J. P. Ament, N. B. Brookes, G. M. De Luca, M. Salluzzo, T. Schmitt, V. N. Strocov *et al.*, Phys. Rev. Lett. **104**, 077002 (2010).
[6] M. P. M. Dean, J. Magn. Magn. Mater. **376**, 3 (2015).
[7] M. Guarise, B. Dalla Piazza, M. Moretti Sala, G. Ghiringhelli, L. Braicovich, H. Berger, J. N. Hancock, D. van der Marel, T. Schmitt, V. N. Strocov *et al.*, Phys. Rev. Lett. **105**, 157006 (2010).
[8] M. P. M. Dean, G. Dellea, R. S. Springell, F. Yakhou-Harris, K. Kummer, N. B. Brookes, X. Liu, Y.-J. Sun, J. Strle, T. Schmitt *et al.*, Nat. Mater. **12**, 1019 (2013). D. Meyers, H. Miao, A. C. Walters, V. Bisogni, R. S. Springell, M. d'Astuto, M. Dantz, J. Pelliciari, H. Y. Huang, J. Okamoto *et al.*, Phys. Rev. B **95**, 075139 (2017).
[9] Z. Hiroi, N. Kobayashi, and M. Takano, Nature (London) **371**, 139 (2002).
[10] Y. Kohsaka, M. Azuma, I. Yamada, T. Sasagawa, T. Hanaguri, M. Takano, and H. Takagi, J. Am. Chem. Soc. **124**, 12275 (2002).
[11] I. Yamada, A. A. Belik, M. Azuma, S. Harjo, T. Kamiyama, Y. Shimakawa, and M. Takano, Phys. Rev. B **72**, 224503 (2005).
[12] K. Foyevtsova, J. T. Krogel, J. Kim, P. R. C. Kent, E. Dagotto, and F. A. Reboredo, Phys. Rev. X **4**, 031003 (2014).
[13] L. K. Wagner and P. Abbamonte, Phys. Rev. B **90**, 125129 (2014).
[14] L. K. Wagner, Phys. Rev. B **92**, 161116 (2015).
[15] K. M. Shen, F. Ronning, D. H. Lu, F. Baumberger, N. J. C. Ingle, W. S. Lee, W. Meevasana, Y. Kohsaka, M. Azuma, M. Takano *et al.*, Science **307**, 901 (2005).
[16] T. Hanaguri, C. Lupien, Y. Kohsaka, D.-H. Lee, M. Azuma, M. Takano, H. Takagi, and J. C. Davis, Nature (London) **430**, 1001 (2004).
[17] K. Momma and F. Izumi, J. Appl. Crystallogr. **41**, 653 (2008).
[18] D. Vaknin, L. L. Miller, and J. L. Zarestky, Phys. Rev. B **56**, 8351 (1997).
[19] H. Müller-Buschbaum, Angewand. Chem. Int. Ed. Engl. **16**, 674 (1977).
[20] M. Moretti Sala, V. Bisogni, C. Aruta, G. Balestrino, H. Berger, N. B. Brookes, G. M. de Luca, D. D. Castro, M. Grioni, M. Guarise *et al.*, New J. Phys. **13**, 043026 (2011).
[21] V. N. Strocov, T. Schmitt, U. Flechsig, T. Schmidt, A. Imhof, Q. Chen, J. Raabe, R. Betemps, D. Zimoch, J. Krempasky *et al.*, J. Synch. Radiat. **17**, 631 (2010).
[22] T. Schmitt, V. N. Strocov, K.-J. Zhou, J. Schlappa, C. Monney, U. Flechsig, and L. Patthey, J. Electron Spectrosc. Relat. Phenom. **188**, 38 (2013).
[23] G. Ghiringhelli, A. Piazzalunga, C. Dallera, G. Trezzi, L. Braicovich, T. Schmitt, V. N. Strocov, R. Betemps, L. Patthey, X. Wang *et al.*, Rev. Sci. Instrum. **77**, 113108 (2006).
[24] L. J. P. Ament, G. Ghiringhelli, M. M. Sala, L. Braicovich, and J. van den Brink, Phys. Rev. Lett. **103**, 117003 (2009).
[25] M. W. Haverkort, Phys. Rev. Lett. **105**, 167404 (2010).
[26] J.-i. Igarashi and T. Nagao, Phys. Rev. B **85**, 064422 (2012).
[27] M. Le Tacon, G. Ghiringhelli, J. Chaloupka, M. M. Sala, V. Hinkov, M. W. Haverkort, M. Minola, M. Bakr, K. J. Zhou, S. Blanco-Canosa *et al.*, Nat. Phys. **7**, 725 (2011).
[28] L. Braicovich, M. M. Sala, L. J. P. Ament, V. Bisogni, M. Minola, G. Balestrino, D. D. Castro, G. M. D. Luca, M. Salluzzo, G. Ghiringhelli *et al.*, Phys. Rev. B **81**, 174533 (2010).
[29] M. P. M. Dean, A. J. A. James, R. S. Springell, X. Liu, C. Monney, K. J. Zhou, R. M. Konik, J. S. Wen, Z. J. Xu, G. D. Gu *et al.*, Phys. Rev. Lett. **110**, 147001 (2013).
[30] J. J. Lee, B. Moritz, W. S. Lee, M. Yi, C. J. Jia, A. P. Sorini, K. Kudo, Y. Koike, K. J. Zhou, C. Monney *et al.*, Phys. Rev. B **89**, 041104 (2014).
[31] M. Z. Hasan, E. D. Isaacs, Z.-X. Shen, L. L. Miller, K. Tsutsui, T. Tohyama, and S. Maekawa, Science **288**, 1811 (2000).
[32] M. d'Astuto, I. Yamada, P. Giura, L. Paulatto, A. Gauzzi, M. Hoesch, M. Krisch, M. Azuma, and M. Takano, Phys. Rev. B **88**, 014522 (2013).

[33] R. Coldea, S. M. Hayden, G. Aeppli, T. G. Perring, C. D. Frost, T. E. Mason, S.-W. Cheong, and Z. Fisk, Phys. Rev. Lett. **86**, 5377 (2001).
[34] A. Chubukov, E. Gagliano, and C. Balseiro, Phys. Rev. B **45**, 7889 (1992).
[35] S. Petit, in *Electronic Structure, Magnetism and Phonons*, *JDN 18–Neutrons et Simulations*, edited by N. M. M. Johnson and M. Plazanet (EDP Sciences, Les Ulis, 2011), Vol. 12, pp. 105–121.
[36] R. R. P. Singh, Phys. Rev. B **39**, 9760 (1989).
[37] B. Dalla Piazza, M. Mourigal, M. Guarise, H. Berger, T. Schmitt, K. J. Zhou, M. Grioni, and H. M. Rønnow, Phys. Rev. B **85**, 100508 (2012).
[38] Y. Y. Peng, G. Dellea, M. Minola, M. Conni, A. Amorese, D. Di Castro, G. M. De Luca, K. Kummer, M. Salluzzo, X. Sun *et al.*, arXiv:1609.05405.
[39] J.-Y. P. Delannoy, M. J. P. Gingras, P. C. W. Holdsworth, and A.-M. S. Tremblay, Phys. Rev. B **79**, 235130 (2009).
[40] F. Ronning, C. Kim, D. L. Feng, D. S. Marshall, A. G. Loeser, L. L. Miller, J. N. Eckstein, I. Bozovic, and Z.-X. Shen, Science **282**, 2067 (1998).
[41] W. Harrison, *Electronic Structure and the Properties of Solids: The Physics of the Chemical Bond* (Dover, New York, 1989).
[42] D. Vaknin, S. K. Sinha, C. Stassis, L. L. Miller, and D. C. Johnston, Phys. Rev. B **41**, 1926 (1990).
[43] O. Ivashko, N. E. Shaik, X. Lu, C. G. Fatuzzo, M. Dantz, P. G. Freeman, D. E. McNally, D. Destraz, N. B. Christensen, T. Kurosawa *et al.*, arXiv:1702.02782 (cond-mat.supr-con).
[44] E. Pavarini, I. Dasgupta, T. Saha-Dasgupta, O. Jepsen, and O. K. Andersen, Phys. Rev. Lett. **87**, 047003 (2001).
[45] www.overleaf.com.

III.4 Discussion & perspectives

The following sections give some perspectives of our continued study of the $Ca_2CuO_2Cl_2$ system in order to provide benchmarks for future many-body calculations. However, they report *preliminary* results which still need more detailed analysis and interpretation. The associated techniques and the interpretation of the data are only discussed very briefly.

III.4.1 High-resolution Cu L_3-edge RIXS and doping dependence

We performed high-resolution Cu L_3-edge RIXS on the ID32 beamline at the ESRF to study the evolution of the (para)magnons with doping. Our first measurements were repeating measurements on the undoped parent compound $Ca_2CuO_2Cl_2$ with the following goals in mind:

- We wanted to have a common reference on the same instrument for a clear comparison with the doped system. The width and intensity of the (para)magnon peaks are important to follow with doping. These are affected by the resolution function of the instrument and it is not very accurate to compare measurements on different instruments using convolution techniques.

- We noticed after a detailed analysis of our previous results on ADRESS and tests performed at the CSX beamline at the NSLSII that using a ceramic post was too "strong" for $Ca_2CuO_2Cl_2$ and leads to pitting which can affect the RIXS spectra. We found that Scotch or Kapton tape worked best for cleaving. We hoped that the increased resolution coupled with improved sample treatment could resolve the discrepancy between our magnon results and calculations.

- We performed the measurements using the four permutations of incident polarization (σ = LV and π = LH) and geometry (grazing-in and grazing-out) in order to decouple the bimagnon [99] and also determine the in-plane spin orientation [100].

The high-resolution spin wave dispersion is compared to our older low-resolution results in Fig. III.8. The extended Heisenberg model parameterized with the one band Hubbard model using $U = 3$ eV and $t = 340$ meV fits very well the new data. The corresponding effective exchange parameters are $J = 142$ meV, $J' = J'' = 2$ meV, and $J_c = 40$ meV. The parameters are very close to recent Cu L_3-edge RIXS results on La_2CuO_4 [101]. The zone boundary dispersion we find is less than before and now matches that of La_2CuO_4. Once we have fit the *dd*-excitations it would be interesting to see if the energy of Cu d_{z^2} matches the trend seen as a function of zone boundary dispersion [101]. The extraction of the bimagnon and analysis of the *dd*-excitations is still underway. We hope that the different experimental geometries and polarization will allow us to decouple the previously observed fluorescence line in this region. The preliminary energy, width, and intensity as a function of doping is shown in Fig. III.9 with a basic fitting procedure and no correction for self-absorption. The softening with doping in the middle along (π,0) could be due the existence of charge order. The intensity variation must be investigated in more detail by removing any multi-(para)magnon excitations and using an appropriate background. The width variation seems consistent with previous results on the cuprates in the underdoped regime.

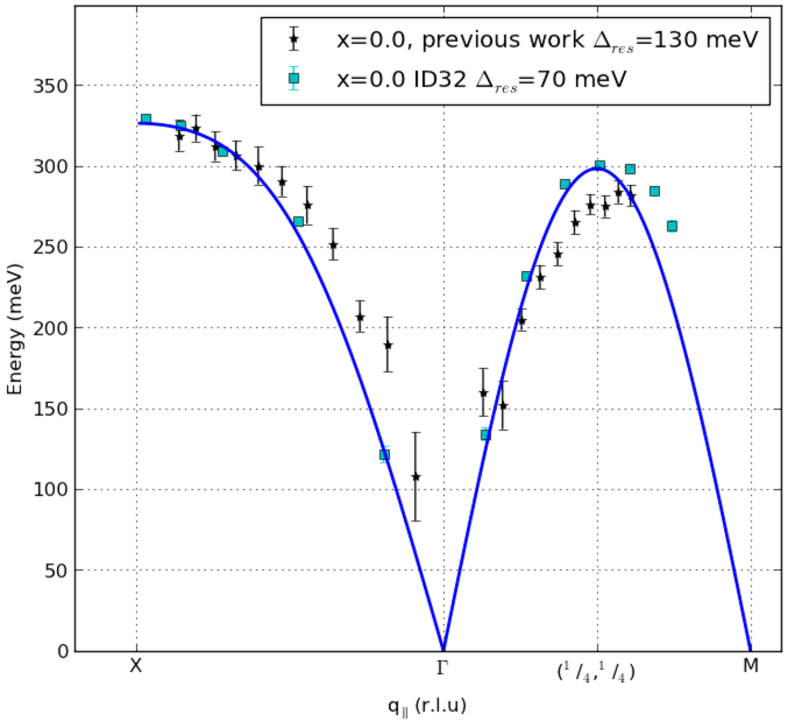

Figure III.8: Comparison of spin wave dispersion measured on ADRESS with 130 meV resolution and ID32 with 70 meV resolution. Another key difference between the experiments was using ceramic posts on ADRESS and tape on ID32 for cleaving. The fitting procedure was very basic and there is no correction for self-absorption. The blue line is the spin wave dispersion calculated as described in the text.

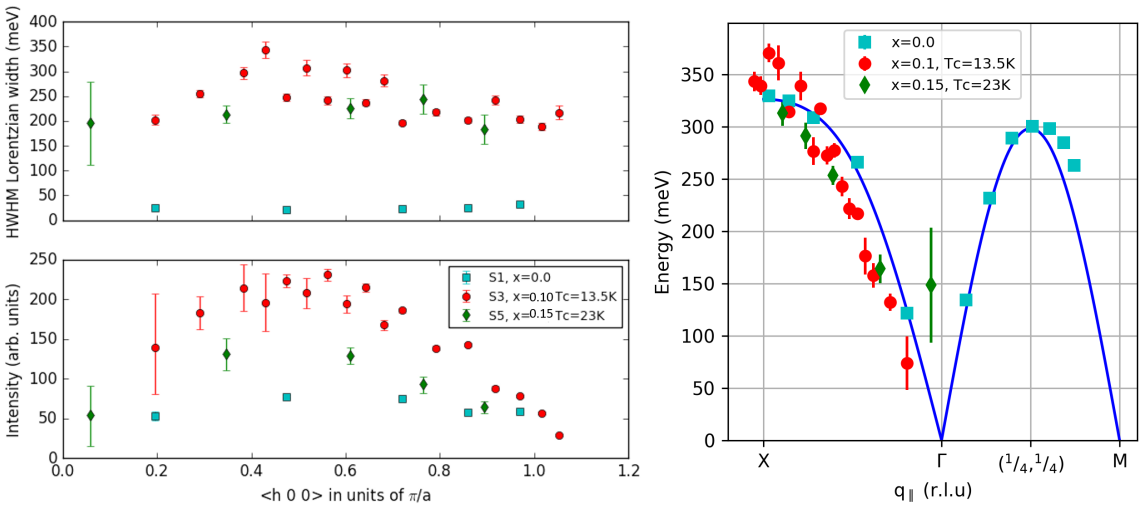

Figure III.9: Preliminary fitting parameters of the (para)magnon as a function of doping.

III.4.2 Bimagnon excitations

The bimagnon in the undoped parent compound $Ca_2CuO_2Cl_2$ was studied using three different x-ray edges in the spirit of Bisogni *et al.* [99]. In addition, we also measured the bimagnon using Raman spectroscopy. The key differences between measurements of the bimagnon at the O K-edge, Cu K-edge, and Cu L_3-edge is well-described in Ref. [99] and is summarized in Fig. III.10. As mentioned above, the Cu L_3-edge data is still under data treatment in order to extract the bimagnon, however at the end of this section a rough estimate is taken from the peak energy.

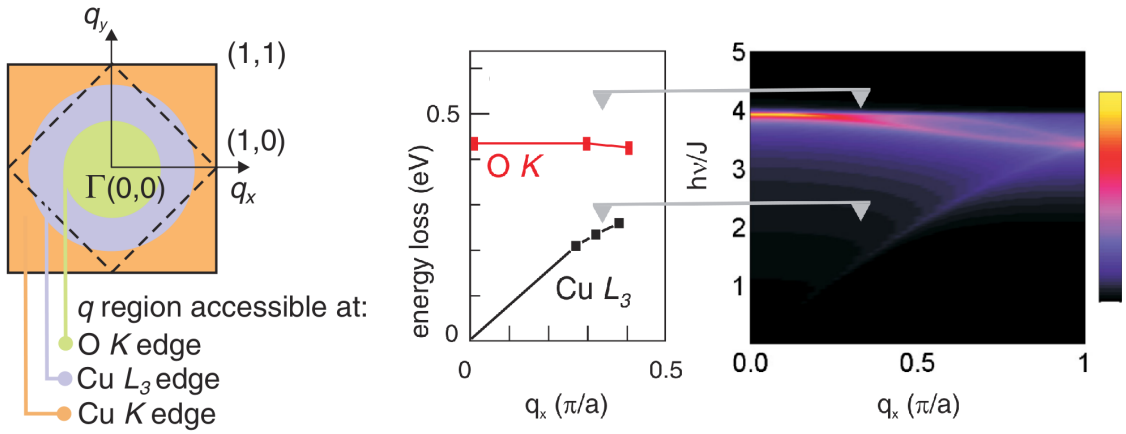

	O *K*	Cu L_3	Cu *K*
Transition	$1s \rightarrow 2p$	$2p_{3/2} \rightarrow 3d$	$1s \rightarrow 4p$
Typical energy	530 eV (soft x ray)	930 eV (soft x ray)	8990 eV (hard x ray)
Core-hole spin-orbit	No	Yes	No
Spin excitation	$\Delta S = 0$	$\Delta S = 0, \pm 1$	$\Delta S = 0$
Single magnon	Absent	Dominant	Absent
Physical information on the bimagnon	Upper ridge bimagnon (almost flat)	Lower ridge bimagnon (dispersing)	Lower ridge bimagnon (dispersing)
Momentum extension	~45% of the 1st BZ	~80% of the 1st BZ	Several BZs
RIXS contribution with respect to total emission	Small	Large	Small
Data handling needed to obtain bimagnon	Straightforward	Delicate separation from single magnon	Delicate background subtraction

Figure III.10: Overview of bimagnon measurements of cuprates at the three different x-ray edges [99]. (Left) The accessible q-space using the three techniques for a typical cuprate (Right) Comparison of experimental data on La_2CuO_4 compared to dispersion calculations (without self-interaction) shows that O K-edge and Cu L_3-edge probe different branches of the bimagnon dispersion (Bottom) A table summarizing the main features of each technique.

Our data at the Cu K-edge is shown and explained in more detail in App. B. The experiment at the Cu K-edge was extremely challenging and involved extensive masking on the cryostat window to reduce unnecessary Kα radiation which would backscatter from the helium in the bag to the detector. We only had a few hours for actual measurements at the very end, therefore we did not have time to redo the masking at different q-points. This is likely the cause of the intensity decrease towards Γ since the sample became masked as the analyzer was moved. The data is too noisy to conclusively say if we see dispersion of the

bimagnon peak as is predicted for the Cu K-edge.

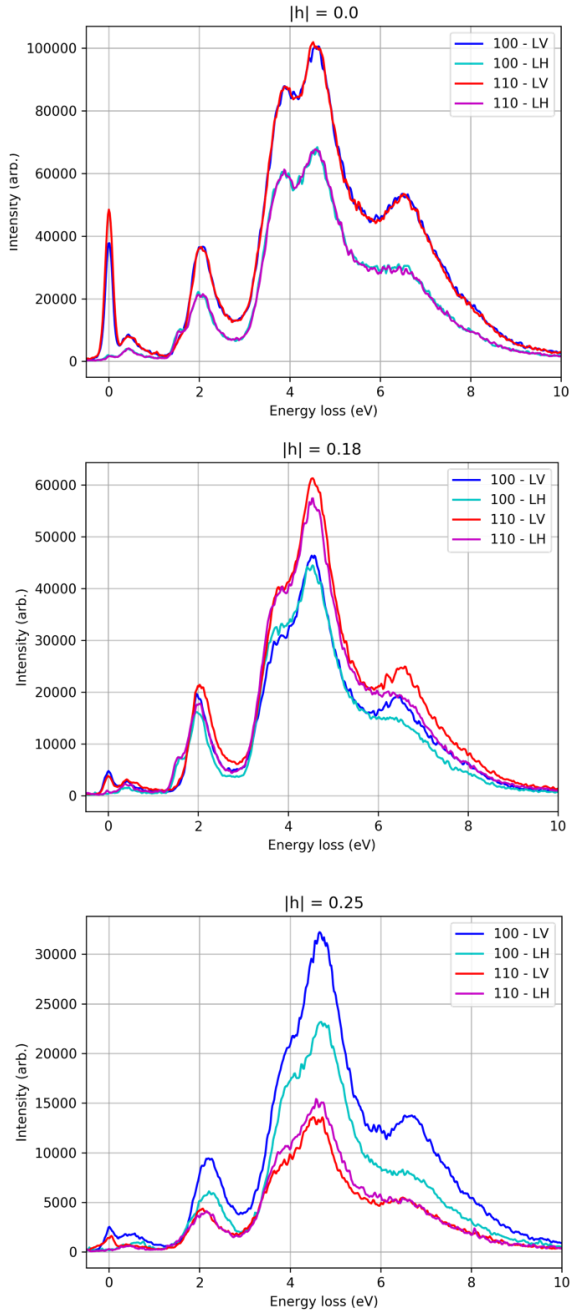

Figure III.11: O K-edge RIXS results on $Ca_2CuO_2Cl_2$. See text for details.

All of our raw measurements of $Ca_2CuO_2Cl_2$ using O K-edge RIXS, except some doping dependence measurements, are shown in Fig. III.11. The spectra are measured at three different angles, i.e. momentum transfers, whose magnitude is given by $|h| = |q_{\parallel}|$. As well, for each momentum transfer we measured with σ (LV) and π (LH) polarization along the two high-symmetry directions. The main features are a bimagnon at low energies, *dd* excitations

centered around 2 eV, and charge transfer excitations above 3 eV. The bimagnon has a peak energy of 450 ± 50 meV which does not show any dispersion within our current uncertainty. We will compare our data after a more thorough data treatment in order to determine if we see the same dispersion as Bisogni *et al.* [99], who observe a slight softening at higher momentum transfers as shown in Fig. III.10. We also performed a temperature study of the O K-edge RIXS spectra along ⟨100⟩ using LH and LV polarization which is shown in Fig. III.12. The in-plane momentum transfer was set to zero for these measurements. We see a change in the charge transfer excitations, while the bimagnon and *dd* excitations vary very little with temperature. The charge transfer excitations have increased spectral weight around 300–400 K, which is around the temperature where $Ca_2CuO_2Cl_2$ changes from a 3D antiferromagnetic state to a 2D antiferromagnetic state. This change is going to be investigated in more detail using cluster calculations [102].

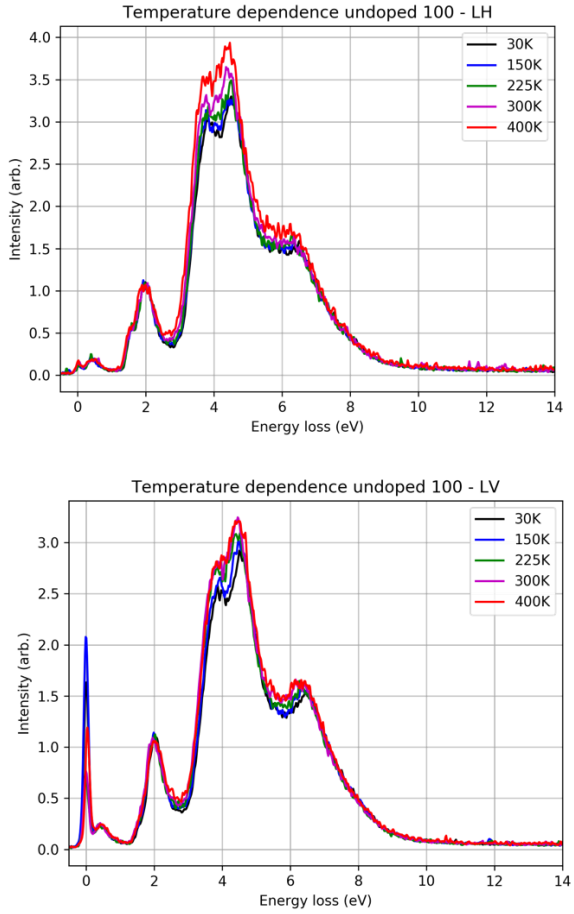

Figure III.12: Temperature dependence of O K-edge RIXS measured along ⟨100⟩ on $Ca_2CuO_2Cl_2$ with $|q_{\|}| = 0$. See text for details.

Raman spectroscopy can also probe bimagnon excitations near q ≈ 0. We used a Raman spectrometer at IMPMC which is specialized for following phonon transitions of samples under pressure but was never used before for polarized Raman spectroscopy. The study required a fair amount of commissioning since the need for a larger energy region to cap-

ture bimagnon meant stitching the spectra together. I noticed many issues concerning the background which were unnoticed before since they are only important in detailed studies of small and/or broad energy signals. I removed many sources of ambient light from LED indicators and lamps. I noticed the spectrometer efficiency varied with angle of the diffraction grating as we changed energy range, and was also sensitive to the incident polarization. We optimized the optical setup keeping the polarization in mind by always selecting linear vertical light to enter the spectrometer using a polarizer. For the (V,V) and (H,V) configurations we modified the incident polarization using a prism. The incident polarization was first reflected off a partially-silvered mirror at 90° towards the sample, reflected off the sample in back scattering, and returned through the partially-silvered mirror in transmission towards the polarizer before the spectrometer. In order to achieve other polarizations we would insert either a quarter or half wave-plate appropriately aligned between the cryostat holding the sample and the partially-silvered mirror. It can be shown that by switching the initial polarization between LH and LV with the prism and selecting LV polarization before the spectrometer entrance, we could probe the crossed and uncrossed configurations.

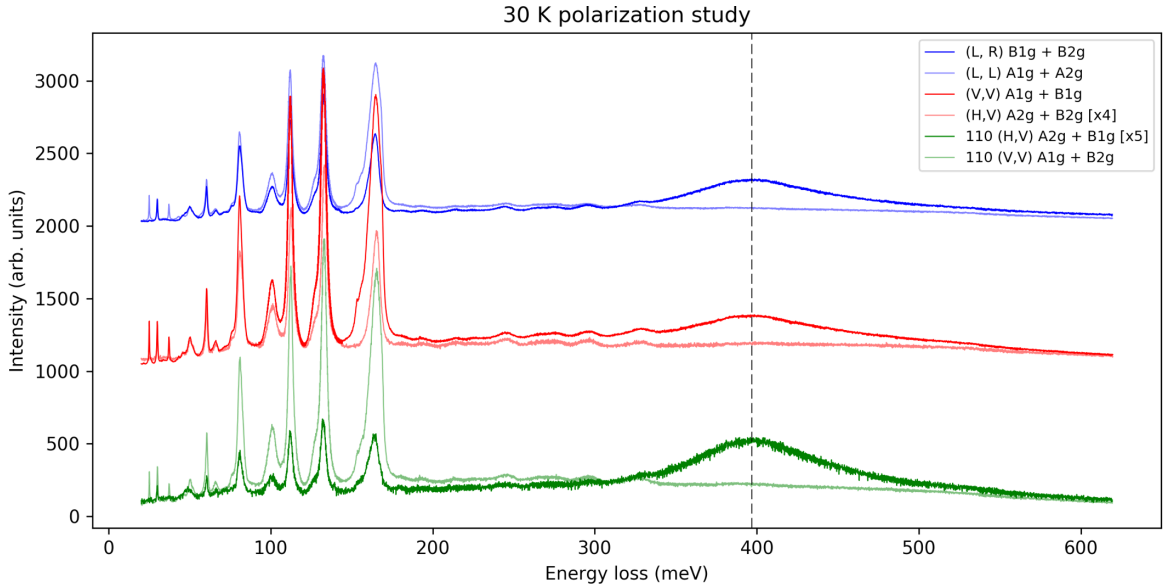

Figure III.13: Raman spectroscopy measurements of $Ca_2CuO_2Cl_2$ with (incident,exit) polarization in the back scattering geometry measured at 30 K. See Fig. III.14 for the experimental geometry. The spectra of a crossed/uncrossed pair are offset for clarity and plotted in the same color. The dashed gray vertical line indicates the peak energy of the bimagnon at 30 K.

We studied an undoped $Ca_2CuO_2Cl_2$ sample which was aligned such that linear horizontal polarization would be along the a-axis. The incident wavelength was 532 nm. Our study at 30 K with the crossed and uncrossed polarization for horizontal/vertical normal and rotated, as well as circular polarization is shown in Fig. III.13. A symmetry analysis finds that the bimagnon only appears when the B_{1g} symmetry is probed as expected. We performed a temperature study as well, which is shown in Fig. III.14, where we see a noticeable shift in the bimagnon energy. This also seems to be related to the change from 3D antiferromagnetic order to 2D antiferromagnetic order and will be investigated in more detail.

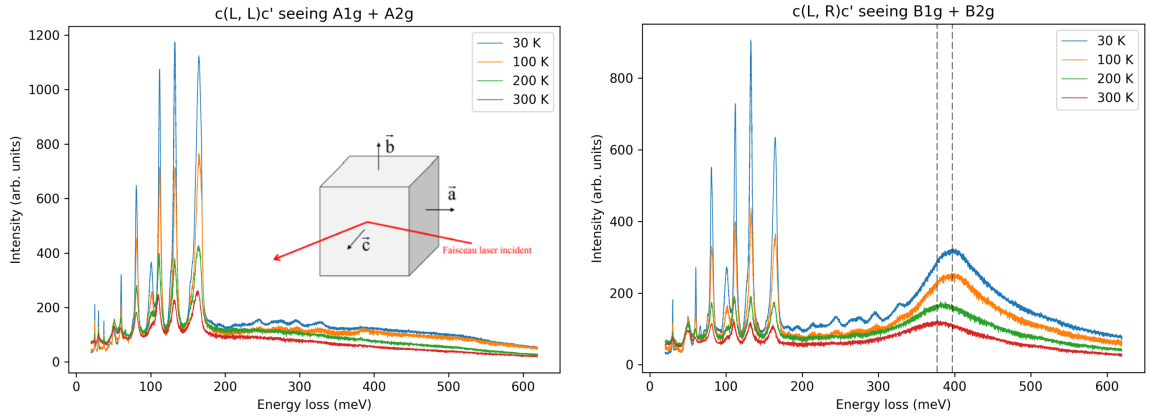

Figure III.14: Temperature study with uncrossed (left) and crossed (right) circular polarization. The inset show the scattering geometry we used except our incident and scattered light were directly along the *c*-axis. The bimagnon maximum shows a noticeable shift with temperature which is indicated with dashed vertical lines.

There are a few important points to mention about our Raman results. The first point is that we tuned the incident laser energy to below a threshold where we noticed visible sample damage with the camera. Nonetheless, I believe we were still using too much incident power and calculations I performed after show that a local increase in temperature of 50–100 K is plausible. This is consistent with the energy shift we see starting already at 200 K. The second point is that the we realized after the experiment that the waveplates we borrowed were not achromatic — the spectra shown have not yet been corrected for the use of a monochromatic waveplate. The correction will only affect the intensity with a smooth curve, giving extra weight further away from the elastic (thus increasing the intensity of the bimagnon slightly). Furthermore the correction will affect all spectra equally, therefore it does not change any of our conclusions. Finally, I realized the spectrometer has been operating in a sub-optimal configuration for many years. The partially-silvered mirror actually reflects $\approx 90\%$ of the light, therefore only 10% of the Raman signal is transmitted to the spectrometer. The incident laser power is a freely variable parameter (we operated at $< 5\%$ of the maximum power), therefore replacing the silvered-mirror with one which reflects 10% would increase the sensitivity of the spectrometer by roughly an order of magnitude!

A summary of the estimated bimagnon peak energies observed with the four techniques are summarized in the table below. According to the notation of Fig. III.10, the bimagnon energy for the dispersing Cu K-edge and Cu L_3-edge RIXS were taken at (1,0), while it was taken at (0,0) for O K-edge RIXS, in order to take the maximum energy of the bimagnon in each case. The error bars are large, however the bimagnon energies still do not match within the uncertainty. The x-rays results are consistent if we exclude the extremely noisy Cu K-edge results. The second column in the table expresses the bimagnon energy in terms of the NN exchange energy $J = 142$ meV found from our high-resolution Cu L_3-edge RIXS results. The expected energy without any self-interaction is $4J$. In general, we observe a higher bimagnon energy using the x-ray techniques than that seen with Raman spectroscopy. A detailed investigation into the excitation mechanism and the self-interaction is needed to resolve this discrepancy. Nonetheless, we note that our Raman measurements are consistent

with previous reports of a bimagnon energy in La_2CuO_4 of approximately $2.7J$ using the London-Fleury approach [103]. This approach approach is valid when the excitation is less than 2 times the charge transfer gap Δ. In the present study this is true: $\lambda = 532$ nm $= 2.33$ eV $< 2\Delta = 4.4$ eV.

Technique	$\hbar\omega$ (meV)	$\hbar\omega/J$
Cu L_3-edge	500 ± 50	3.17–3.87
Cu K-edge	550 ± 50	3.52–4.22
O K-edge	450 ± 50	2.81–3.52
Raman	400 ± 20	2.67–2.96

III.4.3 Phonon dispersion in $Ca_2CuO_2Cl_2$

We performed a high-resolution inelastic x-ray scattering (HR-IXS, see Ref. [104] for a review of the technique) experiment to study the the Cu-O bond stretching mode in $Ca_2CuO_2Cl_2$. This experiment was done in order to complete previous measurements on the vacancy doped system [74], which found a marked anisotropy in the dispersion of this bond stretching mode (E_{1u}) at optimal doping. The results showed that the dispersion along $\langle 100 \rangle$ softens towards the zone boundary, while the dispersion along $\langle 110 \rangle$ continues to harden (Fig. III.15).

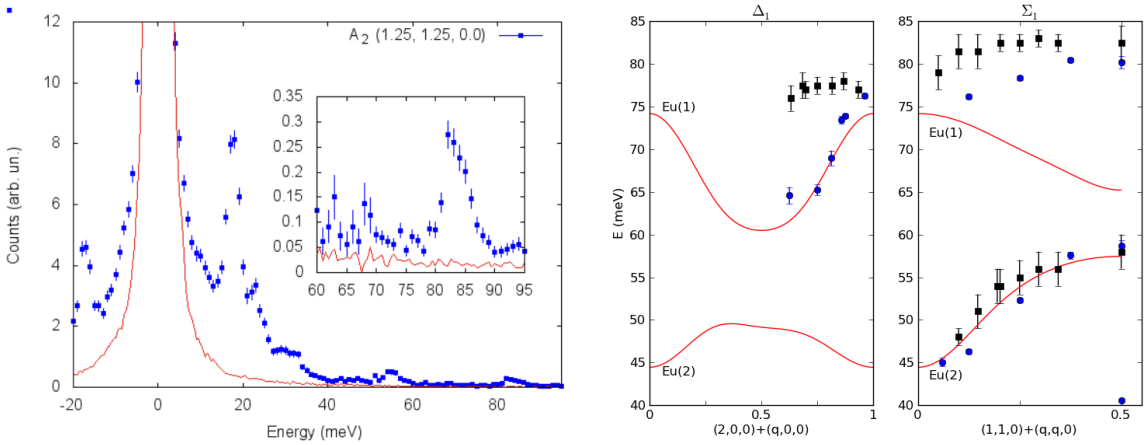

Figure III.15: (Left) An example of a HR-IXS spectra on undoped $Ca_2CuO_2Cl_2$ (blue squares) compared to the experimental resolution (red line). (Right) Preliminary data treatment on undoped (black) $Ca_2CuO_2Cl_2$ and previous results on optimally vacancy doped $Ca_2CuO_2Cl_2$ (blue) [74]. The red lines are DFT calculations.

Lattice dynamical calculations based on a shell model reproduce well the dispersion along $\langle 110 \rangle$, but overestimate the phonon softening along $\langle 100 \rangle$ by about 15 meV. This is due to the fact that shell models reproduce well ionic insulators and do not include electron-phonon coupling of the metallic phase, except for small screening contributions. On the other hand, DFT calculations predict an isotropic softening at the zone boundary. The predictions match fairly well the dispersion along $\langle 100 \rangle$ but have the opposite behavior as experimental observations along $\langle 110 \rangle$. The DFT calculations are likely also overestimating the screening

effects and would match the overdoped region, however in the optimally-doped region they accidentally match the ⟨100⟩ dispersion, which changes slightly from optimal to overdoped.

The previous results on vacancy doped $Ca_2CuO_2Cl_2$ did not also measure undoped $Ca_2CuO_2Cl_2$, therefore a direct proof of doping as the origin of the anisotropic softening could not be established. We measure undoped $Ca_2CuO_2Cl_2$ using HR-IXS on the BL35XU beamline of SPring-8 to firmly establish this fact. Our new results are plotted alongside the doped results in Fig. III.15, where we can clearly see that doping induces a large softening along ⟨100⟩, while there is a more modest softening along ⟨110⟩. This phonon anomaly upon doping could be due to increased screening caused by charge order along the ⟨100⟩ direction. The existence of charge order in the $Ca_2CuO_2Cl_2$ system is controversial and is discussed further in the next section.

III.4.4 Search for charge order

The easy cleavability of the the $Ca_2CuO_2Cl_2$ system has made it popular for surface-sensitive probes such as ARPES and STM. STM studies have detected charge order in $Ca_{2-x}Na_xCuO_2Cl_2$ over a wide range of doping [85, 86], yet attempts to find bulk charge order with resonant soft x-ray scattering have failed [88] (Fig. III.16). As well, the $Ca_2CuO_2Cl_2$ system lacks a 1/8 anomaly which is seen in the rest of the cuprates. Some authors suggest that the absence of buckling in the CuO_2 plane or the small alkaline metal radius (Ca < Sr < Ba) could explain the lack of this anomaly in the $Ca_2CuO_2Cl_2$ system [1]. Another interesting hypothesis is that charge order is statically pinned to disorder induced by Na doping such that, at least until optimal doping, charge order competes with superconductivity at all measured dopings. This agrees with the STM results which find charge order exists over a wide doping range. As well, the competition between charge and superconducting order in $Ca_{2-x}Na_xCuO_2Cl_2$ is one possible explanation why it has a lower T_c than $La_{2-x}Sr_xCuO_4$, despite the fact that it has more "ideal" CuO_2 planes [89].

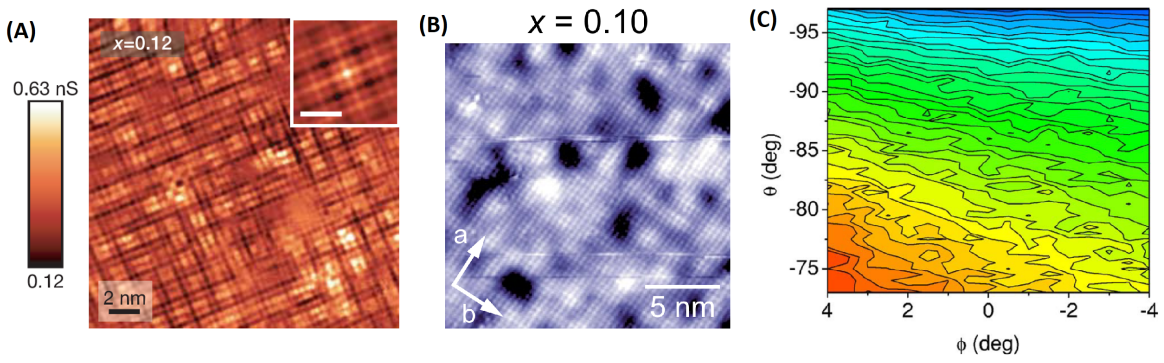

Figure III.16: STM differential conductance maps of $Ca_{2-x}Na_xCuO_2Cl_2$ shown from (A) Hanaguri *et al.* [86] and (B) Kohsaka *et al.* [85]. (C) Resonant soft x-ray scattering at the Cu L_3-edge find no evidence of charge order [88]. This region of reciprocal space is centered at (0.25, 0, 1.5) and ranges from H = 0.15 to H = 0.35 (r.l.u). The sloping background is caused by sample absorption variations.

STM experiments first reported charge modulations of $Ca_{2-x}Na_xCuO_2Cl_2$ in 2004 [86]. A Fourier transform of their measured differential conductance map $g(\mathbf{r}, E)$ found charge

modulations at (nq,0,0) with n integer $q \approx 0.25$, which corresponds to periodicity of $4a$. This first measurement reported a "checkerboard" modulation (Fig. III.16) which however was not confirmed by a later study [85]. This study found nanoscale charge order domains with a length scale of 4–5a and a preferred orientation along ⟨100⟩.

Our first attempt to measure a bulk signature of charge order in $Ca_{2-x}Na_xCuO_2Cl_2$ was on the CSX beamline at the NSLSII using resonant soft x-ray scattering at the Cu L_3-edge. Our tests showed that the Bragg peaks were severely spread in reciprocal space, which we attributed to poor cleaving with a post and strain from the strong epoxy we used which required high temperature curing. Nonetheless, with certain cuts of the reciprocal space there seemed to be hints of charge order.

These preliminary results motivated our next attempt on the ID32 beamline at the ESRF. In this case we used a silver paint which cures at room temperature to induce less strain and cleaved the samples using tape. We performed resonant soft x-ray scattering at Cu L_3-edge by using the RIXS spectrometer to measure the elastic peaks at $\mathbf{q}$ = (H, K, L) = (H, 0, 1.5). Our results are shown in Fig. III.17 at 10 K where we find a CDW-like peak around $\mathbf{q}$ = (-0.317, 0, 1.5). The peak width of this CDW-like peak corresponds to a correlation length of $\approx$ 250 Å.

The value of this wavevector is interesting for many reasons. First, it is similar to the wavevector for charge order in YBCO and BSCCO, rather than that of the 214 family, i.e. $La_{2-x}Sr_xCuO_4$. As well, this corresponds to a nesting vector in $Ca_{2-x}Na_xCuO_2Cl_2$ [84]. Finally, this is the same wavevector where we found the phonon anomaly with HR-IXS (Sec. III.4.3).

We performed a temperature study following the CDW-like peak and found that it persists until at least 100 K after which we lost the reflection. The reflection was likely lost due to the expansion of the sample holder since the peak showed no variations between 10 K and 100 K. The correlation length seems a bit long to be a real CDW-peak, therefore further investigation of this first hint of bulk charge order in $Ca_{2-x}Na_xCuO_2Cl_2$ is needed. A further study of the CDW-like peak would include measuring on and off resonance, measuring along ⟨100⟩ and ⟨110⟩, performing a more complete temperature study, and measuring its extent in L. In order to perform these experiments the sample preparation techniques should be improved. The $Ca_{2-x}Na_xCuO_2Cl_2$ crystals we measured on ID32 were much better than on CSX, however the alignment was extremely sensitive to the position of the sample (which is probably why we lost it upon heating). We should also consider gluing just a small corner of our sample to the sample holder in order to avoid introducing any extra strain in the crystal.

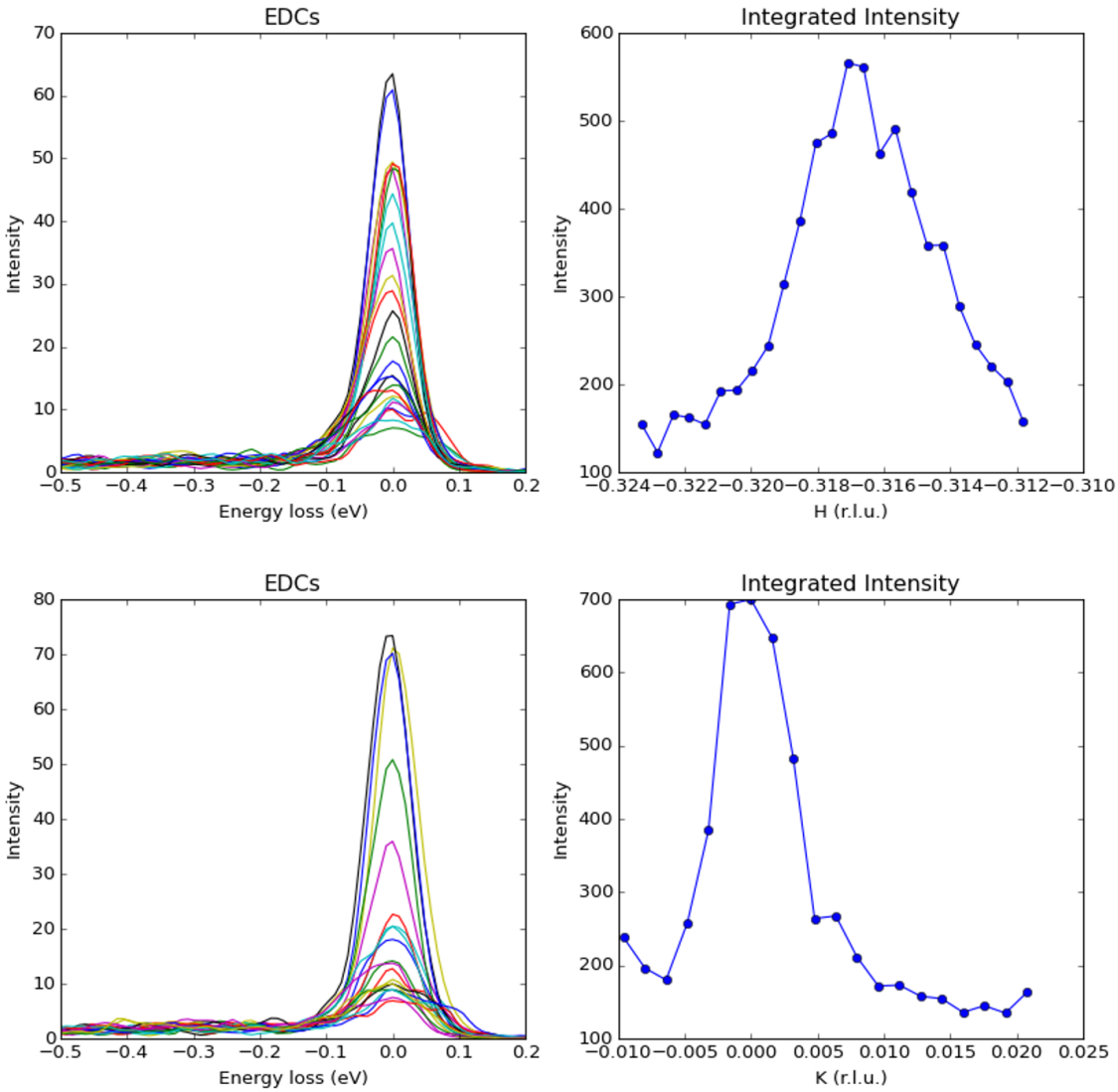

Figure III.17: Search for charge order in $Ca_{1.9}Na_{0.1}CuO_2Cl_2$ (Top) Elastic lines measured during scan of H at $\mathbf{q}$ = (H, 0, 1.5) and integrated intensity of elastic lines as a function of H. (Bottom) Elastic lines measured during scan of K at $\mathbf{q}$ = (-0.317, K, 1.5) and integrated intensity of elastic lines as a function of K.

Chapter IV

Magnetism of compressed iron

The second half of my thesis focused on the electronic and magnetic properties of compressed materials using two complementary techniques: x-ray emission spectroscopy (XES: Sec. II.2.2) and neutron powder diffraction (NPD: Sec. II.3). The x-ray and neutron experiments were performed using a diamond anvil cell (DAC: Sec. II.4.1) and a Paris-Edinburgh cell (PEC: Sec. II.4.2) respectively. This chapter discusses our study of iron while the next chapter discusses FeSe (Chap. V). The phase diagram of iron is shown in Fig. IV.1 and Fig. 1 in Sec. IV.2. The magnetic state of the ϵ-iron phase, and its connection to superconductivity in this region, has been debated for many decades and was the focus of this study.

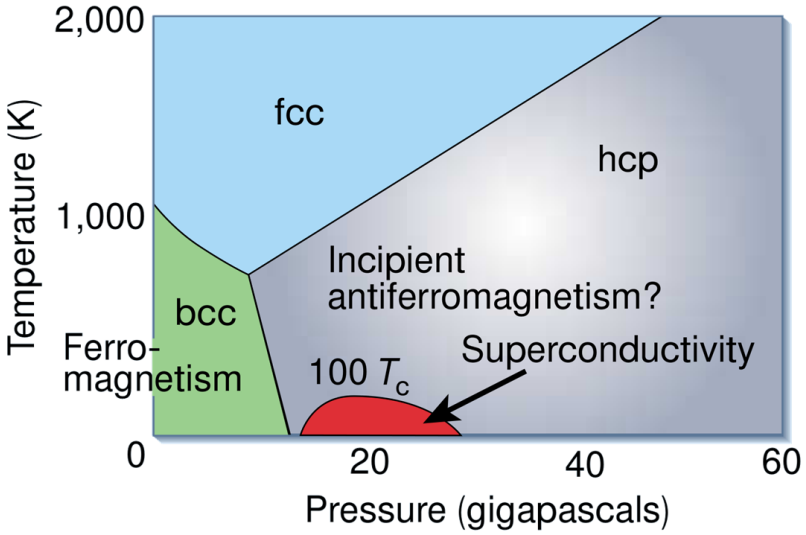

Figure IV.1: A schematic pressure-temperature phase diagram of iron [2]. The bcc (α), hcp (ϵ), and fcc (γ) phases are shown in green, gray, and blue respectively. A superconducting dome exists in the ϵ phase where the magnetic state is heavily debated.

IV.1 Introduction

Iron has shaped mankind's history for millennia due to its role in tool-making, construction, and warfare [105]. The Earth is largely composed of iron because of its galactic abundance caused by gradual enrichment due to supernovae coupled with iron's high nuclear binding energy. The last product formed during the final silicon-burning phase of nuclear fusion in massive stars is $^{56}_{28}$Ni, which rapidly decays into $^{56}_{27}$Co and then finally $^{56}_{26}$Fe [106]. The Earth's core has never been directly probed[1] but indirect evidence points to a core composed chiefly of iron, ≈10% nickel, and few percent of light elements (hydrogen, carbon, sulfur, oxygen, and/or silicon) [108–115]. Iron is also quite abundant in the Earth's crust, only behind oxygen, silicon, and aluminum [116]. Pure iron is rather soft, however alloying it with carbon increases its strength by many orders of magnitude producing steel. Around 90% of the world's metal production is iron due to steel's utility and iron's low cost due to its abundance.

The geophysical significance of iron makes it an important cornerstone of high pressure physics. Furthermore, the impact phenomena of steel is also an important application of iron's high pressure research. In 1956 Bancroft *et al.* made the "explosive" discovery of a high pressure polymorph of iron above 13 GPa in a dynamic pressure experiment [117]. Further static x-ray diffraction studies found that the new phase, dubbed ϵ-iron or hexaferrum, had a hexagonal close-packed crystal structure (hcp) compared to the body-centered cubic crystal structure (bcc) of the low pressure α-iron phase (also known as ferrite) [118–120]. The onset and width of the α-ϵ transition varied between experiments. As well, the transformation was found to be quite "sluggish" with a wide region of phase coexistence and large hysteresis. These are indicative of a first-order, martensitic transformation [121, 122], also known as a diffusion-less transformation. The transition occurs according to the Burgers mechanism [123] where the crystal undergoes simultaneous shear deformation with alternating shuffle of the adjacent atomic planes [124]. This atomic plane slippage results in the preservation of the crystal orientation according to Burgers orientation relationship: $(110)_{\text{bcc}} \parallel (0001)_{\text{hcp}}$ and $[\bar{1}11]_{\text{bcc}} \parallel [\bar{2}110]_{\text{hcp}}$ [123, 124]. Shear forces are clearly important for a martensitic transformation [125, 126] — the role of shear is seen in Fig. IV.2 by the increased onset pressure and reduced transition width for the pressure transmitting media which are more hydrostatic (and thus produce less shear force) [127]. The width of the transition is also due to its first-order nature and the fact that static pressure experiments using a DAC/PEC define a constant volume rather than pressure and the 4.7% volume reduction during the transition [128] must be compensated by the pressure medium.

The shear and shuffle steps of the Burgers transformation are not necessarily decoupled and the exact microscopic mechanism is still debated [124, 125, 129–132]. There are even intermediate orthorhombic [132] of fcc [133] phases predicted during the transition. However, very recently high-quality x-ray diffraction [128, 134, 135] and EXAFS [136] using helium as a pressure medium and a small incident beam size were performed. They both find a transition starting around just below 15 GPa and finishing just after 18 GPa. The EXAFS results find the shear step finishes almost instantly, while the shuffle step is gradual. The shuffling is nearly complete at 16.4 GPa and seems constant from 18–20.3 GPa (i.e transition finished above 18 GPa). EXAFS finds a better agreement with a slightly orthorhombic structure

[1] Although a fantastic, yet technically feasible, plan has been proposed [107]

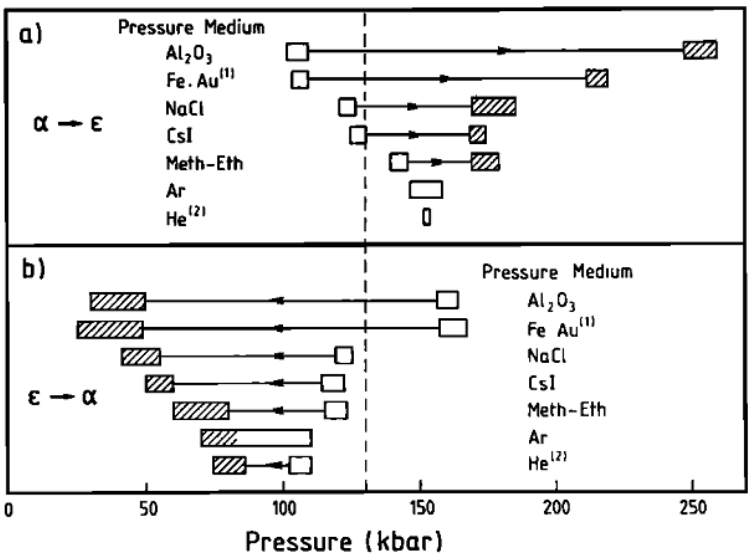

Figure IV.2: The α-ϵ transition in different pressure transmitting media measured using x-ray diffraction [127]. The top (bottom) panel represents compression (decompression) of iron, where the white rectangle is the start and the hatched rectangle is the end of the transition. The width of the rectangles represents their uncertainty. For quasi-hydrostatic media like helium and argon, only a white rectangle is visible during compression since their transition was very sudden and could not be distinguished within the uncertainty of their experiments. Realistic measurements of their transition widths are discussed in the text.

after the transition, however naturally the model has more fitting parameters so it is not direct evidence. On the contrary, x-ray diffraction finds no evidence of an intermediate phase or an orthorhombic structure above 18 GPa. However the EXAFS interpretation of an orthorhombic structure (at least locally) agrees with the broken hcp symmetry of ϵ-iron inferred from Raman spectroscopy [137]. The symmetry-breaking is postulated to be due to magnetism in ϵ-iron which is discussed further below. The transition width using helium as a pressure medium from recent experiments is larger than shown in Fig. IV.2 due to improvements in flux, resolution, and data treatment.

The previous two paragraphs highlight the importance of the pressure transmitting medium on the α-ϵ transition. During our XES measurements, we did not measure the structure simultaneously, neither by diffraction nor EXAFS. Our choice of pressure transmitting medium was therefore paramount to ensure we were measuring exclusively ϵ-iron above a certain pressure. Although helium is the best pressure transmitting medium, we performed our XES measurements using argon as the medium for practical reasons. According to Fig. IV.2, the α-ϵ transition occurs from 14.2–15.2 GPa with argon. However, as noted previously this data does not seem reliable for helium thus we should question its validity for argon. There is one other x-ray diffraction study using argon which finds the two phases coexisting still at 16.6 GPa and a complete transformation to ϵ-iron at the next highest pressure point, 21 GPa [138]. This study is also relatively dated, however a comparison with the hydrostaticity in a DAC (measured as the standard deviation of pressure, σ) for different pressure media [68] to Fig. IV.2 is convincing. The transition finishes at 18 GPa using helium

and $\sigma = 0.025$ GPa is constant at 17.5–20 GPa. The standard deviation in argon is slightly higher, $\sigma = 0.14$ GPa at 17.5 GPa and $\sigma = 0.25$ GPa at 20 GPa. It becomes much worse using 4:1 methanol-ethanol where $\sigma = 1.6$ GPa at 17.5 GPa and $\sigma = 2.1$ GPa at 20 GPa. According to Fig. IV.2, using 4:1 methanol-ethanol the transition completes at 18 GPa. This is the same as modern experiments find for helium and could be due to differences in pressure calibration. Nonetheless, argon is much closer to helium in terms of hydrostaticity and we should expect a complete transformation close to that of helium, i.e. 18 GPa. Furthermore, our NPD results presented in Sec. IV.2 were done without a pressure transmitting medium, but using hemispheres to increase hydrostaticity, and we find a complete transformation at 18.5 GPa. Therefore, a complete transformation (at most) above 19 GPa is a reasonable estimate for our XES measurements using argon as a pressure transmitting medium.

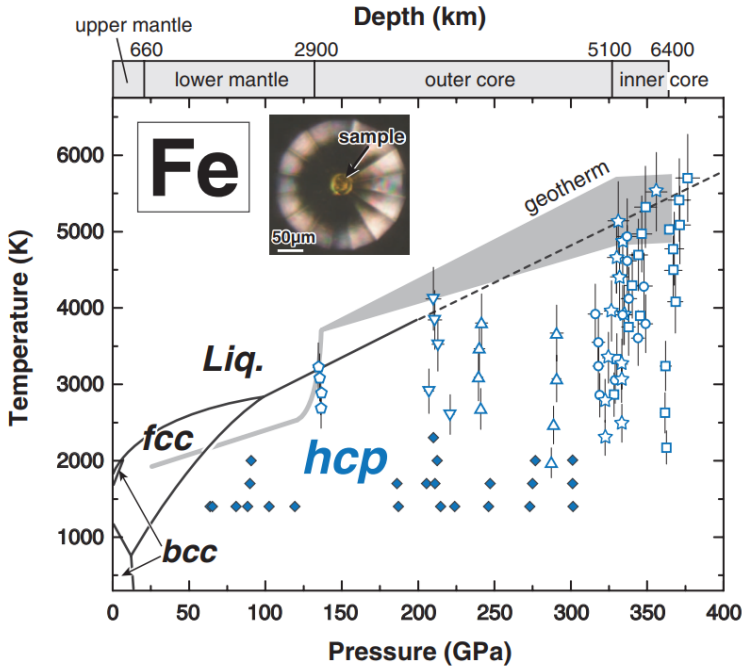

Figure IV.3: A schematic pressure-temperature phase diagram with points where x-ray diffraction was measured using a laser-heated diamond anvil cell [111]. The inferred temperature profile in the Earth is labelled by "geotherm". The inset is a photograph of the sample in the DAC at 335 GPa.

Iron has two other well-established phases, γ-iron and δ-iron. Their crystal structures are face-centered cubic (fcc) and body-centered cubic (bcc) respectively (the two high temperature phases in Fig. IV.3). Above at least 40 GPa and 1500 K there also have been experiments and theories reporting double-hcp, bcc, and unknown crystal structures [139–143]. However, recent x-ray diffraction results show that ϵ-iron is the stable polymorph up to the temperature and pressure range of the Earth's core [111] (Fig. IV.3). This extended phase diagram shows how γ-iron transforms into ϵ-iron at higher pressures and that the they form a triple point with the liquid phase around 100 GPa.

Iron is the archetypical ferromagnetic — the very word "ferro"magnetism is derived from the Latin word for iron, "ferrum". Iron is inextricably linked with magnetism because it is an

essential ingredient to understand iron's phase diagram: magnetism is needed to explain the stability of the α, γ, and δ phases [144–147]. Metals typically favor a close-packed structure, either hcp or fcc, since an increase in nearest neighbors reduces the ground state energy due to increased metallic bonding. On the contrary, at ambient condition phase, α-iron has a bcc structure (8 vs. 12 nearest neighbors) which is only predicted by theory if ferromagnetism is included [108]. The α-ϵ structural transition is coupled with a loss of ferromagnetism. The nature this transition, and whether it is magnetically-driven is heavily debated. A previous simultaneous EXAFS/XMCD study found the magnetic transition preceding the structural transition [148], however the same experiment performed with a smaller incident x-ray beam and a more hydrostatic pressure transmitting medium found that they are concomitant [136]. However, the uniform phonon dispersion found with inelastic x-ray scattering until 10 GPa [149] and nanoparticle experiments suggest the structural transition is driven by the loss of ferromagnetism [150].

The magnetic state after the structural transition, in the ϵ phase, is even more controversial. Early Mössbauer did not observe any measurable magnetic hyperfine field in ϵ-iron at temperatures as low as 30 mK [151] which agreed with the theoretical predictions of Wohlfarth in 1979 [152]. However, advances in first-principles calculations started to consistently predict afm ground states for ϵ-iron which should have been detected by Mössbauer spectroscopy, that is, all except one. The so-called afmII configuration is predicted to have a magnetic hyperfine field below the detection limits of Mössbauer due to an almost complete cancellation at the nucleus of the polarization from the core and valence electrons [6]. The afmII configuration and its predicted magnetic moment as a function of pressure are shown in Fig. IV.4. The afmII also neatly explains the splitting of a doubly-degenerate optical phonon as the orthorhombic structure breaks the original hcp symmetry.

Wohlfarth predicted that after becoming paramagnetic ϵ-iron would support superconductivity with a maximum T_c of 0.25 K, with the caveat that it could be inhibited by the existence of spin fluctuations [152]. At the turn of the millennium, an experiment measured a partial resistive transition in ϵ-iron and found its pressure dependence formed a superconducting dome from 15 to 32 GPa with a maximum T_c of 1.8 K (Fig. IV.5) [153]. A Meissner signal was also measured at 23 GPa confirming its superconducting nature [153], as well as a complete resistive transition a year later [154]. The sample quality was found to be very important for a complete resistive transition — a poor quality sample (RRR < 7) will not become superconducting at all, while annealed, high-quality iron whisker samples (RRR > 250) have a larger T_c of around 2.2 K. Calculations estimate a minimum mean free path ℓ =12 nm which is close to the estimated coherence length $\xi = 30$ nm. This points to superconductivity only in the clean limit which is a strong indication of unconventional superconductivity [154]. Other indications are that its T_c is an order of magnitude larger than predicted by Wohlfarth with phonon-mediated BCS theory and its critical field is an order of magnitude larger compared to other pure elements with a similar T_c (Fig. IV.5). Theoretical studies after the discovery of superconductivity in ϵ-iron found that indeed phonon-mediated BCS-based theories could not explain its "rapid" disappearance above 30 GPa and suggested that the pairing is mediated by spin fluctuations [155, 156].

Spin fluctuations are actually another reasonable candidate to explain the null Mössbauer results, other than the afmII state, since they could be fluctuating faster than the $\approx$ 100 ns timescale of ^{57}Fe Mössbauer. Besides their possible link to superconductivity, spin fluctuations are support by recent studies. A first-principles calculation including correlation

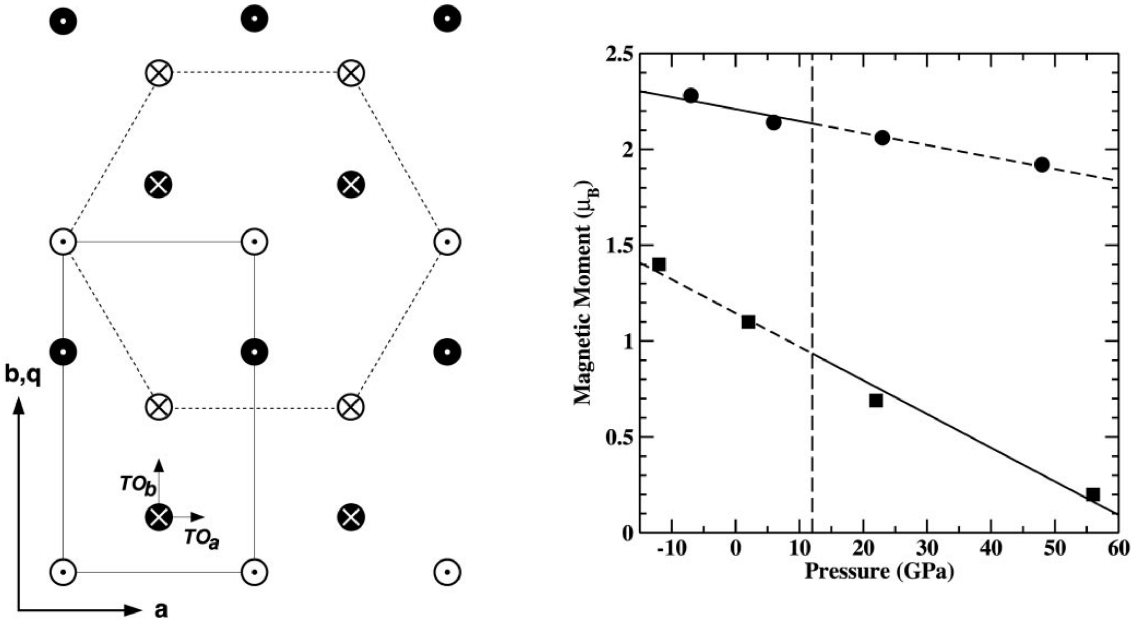

Figure IV.4: (Left) Orthorhombic afmII configuration which is the predicted by first-principles calculations to be the ground state of ϵ-iron [6]. The z-position of the atoms are z=1/4 (open) and z=3/4 (closed). The crosses and dots indicate spin in or out of plane respectively. (Right) The predicted magnetic moment per atom as a function of pressure [6]. The α-ϵ transition is indicated with a vertical dashed line.

effects found a paramagnetic ground state that currently gives the best agreement with ϵ-iron's equation of state and implies the importance of spin fluctuations due to the divergence of the calculations from experiments below 40 GPa [157]. Transport measurements also find non-Fermi liquid behavior in this same pressure region [158]. Finally, the same afmII state is predicted for a $Fe_{92}Ni_8$ alloy but with a large magnetic hyperfine field, but it was not observed with nuclear forward scattering from ^{57}Fe [159].

A magnet moment associated with spin fluctuations could be probed by Fe Kβ XES since it is sensitive to the atomic 3*d* orbital occupation, irrespective of the long range or fluctuations time scale. In fact, recently XES observed "remnant" magnetism in ϵ-iron [150]. We have improved upon these XES results by using a more hydrostatic pressure medium (argon), much higher statistics, and a new analysis technique. Our results allow us to see that the magnetic moment is not a ferromagnetic remnant due to a minority α-iron phase but that it is rather intrinsic to the ϵ-iron phase. As well, our XES results find zero magnetic moment at 30–40 GPa, which coincides with the end of the superconducting dome, strengthening the case of Cooper pairing by spin fluctuations as the mechanism behind ϵ-iron's unconventional superconductivity. Finally, our NPD results put an upper limit on the magnetic moment of a possible afmII phase which is four times less than its theoretical predictions.

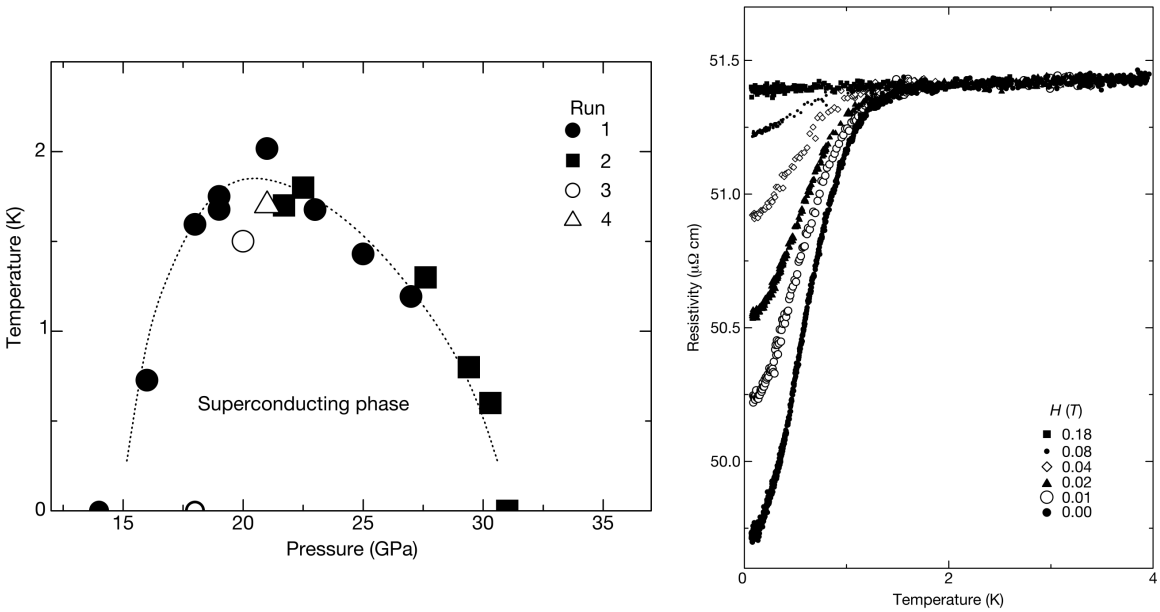

Figure IV.5: (Left) Superconducting transition of iron where T_c is defined as the onset of the transition [153]. The dotted line is a guide for the eye. Run 1 & 2 are from resistivity measurements while increasing pressure. Run 3 is from resistivity measurements decompressing from an initial 90 GPa compression. Run 4 is from the Meissner signal. (Right) Resistivity at 23 GPa measured in different applied fields [153]. The critical field is around 0.1 T, compared to 0.01 T for other elements with a similar T_c.

IV.2 Article 2: Spin fluctuations in the superconducting pressure region of ϵ-iron

Status: In preparation.

Author contributions: Matteo d'Astuto conceived this project and led the first XES run supported by Jean-Pascal Rueff, James Ablett, François Baudelet, and Pascal Munsch. François Baudelet conceived the cryogenic system for high-pressure XES and it was commissioned by him, Alain Polian, and Matteo d'Astuto. The second XES run was led by Blair Lebert with support from Amélie Juhin, Michele Casula, Alain Polian, Zailan Zhang, Gilles Le Marchand, and everyone from the first run. Blair Lebert analyzed the XES data with support from Jean-Pascal Rueff and Matteo d'Astuto. The NPD experiments were conceived and led by Stefan Klotz with support of Blair Lebert, Thierry Strässle, Thomas Hansen, and Matteo d'Astuto. The NPD data analysis was done by Blair Lebert with support from Stefan Klotz. Blair Lebert wrote the manuscript with feedback from Matteo d'Asutuo, Jean-Pascal Rueff, Stefan Klotz, Michele Casula, and the other co-authors.

Spin fluctuations in the superconducting pressure region of ϵ-iron

Blair W. Lebert[1,2], Jean-Pascal Rueff[2], Stefan Klotz[1], Amélie Juhin[1], Michele Casula[1], James M. Ablett[2], François Baudelet[2], Thierry Straessle[3], Thomas Hansen[4], Alain Polian[1,2], Pascal Munsch[1], Gilles Le Marchand[1,2], Zailan Zhang[1], and Matteo d'Astuto[1]

[1] *IMPMC, UMR CNRS 7590, Sorbonne Universités-UPMC University Paris 06, MNHN, IRD, 4 Place Jussieu, F-75005 Paris, France*

[2] *Synchrotron SOLEIL, L'Orme des Merisiers, BP-48 Saint-Aubin, 91192 Gif-sur-Yvette, France*

[3] *Paul Scherrer Institut, Villigen, Switzerland*

[4] *Institut Laue-Langevin, Grenoble, France*

November 17, 2017

Abstract

Compressed iron experiences a structural transition from the body-centered cubic α-iron phase to the hexagonal close-packed ϵ-iron phase. It is well-known that iron loses its ferromagnetism during the transition, however the magnetic state of ϵ-iron has been debated for many decades and experiments give seemingly contradictory results. Mössbauer spetroscopy finds no magnetism, while x-ray emission spectroscopy finds remnant magnetism. These paradoxical results are explained by either a paramagnetic state with spin fluctuations faster than Mössbauer timescales or an antiferromagnetic state, afmII, which is undetectable with Mössbauer spectroscopy [Steinle-Neumann G et al. (2004) *Proc. Natl. Acad. Sci. U. S. A.* 101(1):33–6]. We performed neutron powder diffraction measurements in ϵ-iron and do not observe afmII order down to 1.8 K, bolstering the theory of spin fluctuations. We confirmed the existence of a magnetic moment in ϵ-iron with x-ray emission spectroscopy and show it is intrinsic to this phase. This magnetic moment disappears at 30–40 GPa, the same pressure

region where superconductivity disappears, which is consistent with superconducting pairing mediated by spin fluctuations.

Iron is well-known since antiquity for its unique magnetic properties and continues to captivate scientists to this day. On a fundamental level, iron is intriguing since theory and experiment often contradict one other. For instance, even the most advanced first-principles methods [1] grossly overestimate the Curie temperature in the ferromagnetic (fm), body-centered cubic (bcc) α-iron phase (Fig. 1). The study of iron and its alloys has many applications, including steel production and geophysics. Regarding the latter, the hexagonal close-packed (hcp) ϵ-iron phase and its alloys are thought to compose the majority of the inner and outer Earth's core [2, 3]. Iron has been studied at increasingly high pressures and temperatures to this end, nonetheless the low pressure region of ϵ-iron has remained a mystery for many decades. Theory and experiments have produced paradoxical results regarding its magnetism, which became increasingly important after the discovery of superconductivity in this region (Fig. 1) [4, 5].

The application of pressure induces the martensitic α-ϵ structural transition coupled with a loss of ferromagnetism [7–10], however the existence of magnetism in ϵ-iron remains controversial. Mössbauer spectroscopy finds no magnetism down to 30 mK [11]. Conversely, Raman spectroscopy finds mode splitting until 40 GPa, possibly due to a magnetic state which lowers the hcp symmetry [12], and recent Kβ x-ray emission spectroscopy (XES) results finds a remnant magnetic moment [9]. Density functional theory (DFT) calculations predict a static collinear antiferromagnetic (afm) ground state, afmII, composed of alternating magnetization along the hcp a-axis [13, 14]. The afmII phase coincidentally has a hyperfine magnetic field below the detection limit of Mössbauer spectroscopy and also neatly explains Raman mode splitting due to its orthorhombic unit cell [14]. An alternative explanation is spin fluctuations faster than the timescale of Mössbauer spectroscopy, which are also thought to play a role in ϵ-iron's superconductivity [15–17].

A picture favoring the latter explanation is gradually emerging: recent studies support that ϵ-iron is a paramagnet with spin fluctuations, possibly with antiferromagnetic correlations, in the superconducting pressure region. DFT calculations predict an afmII phase in the $Fe_{92}Ni_8$

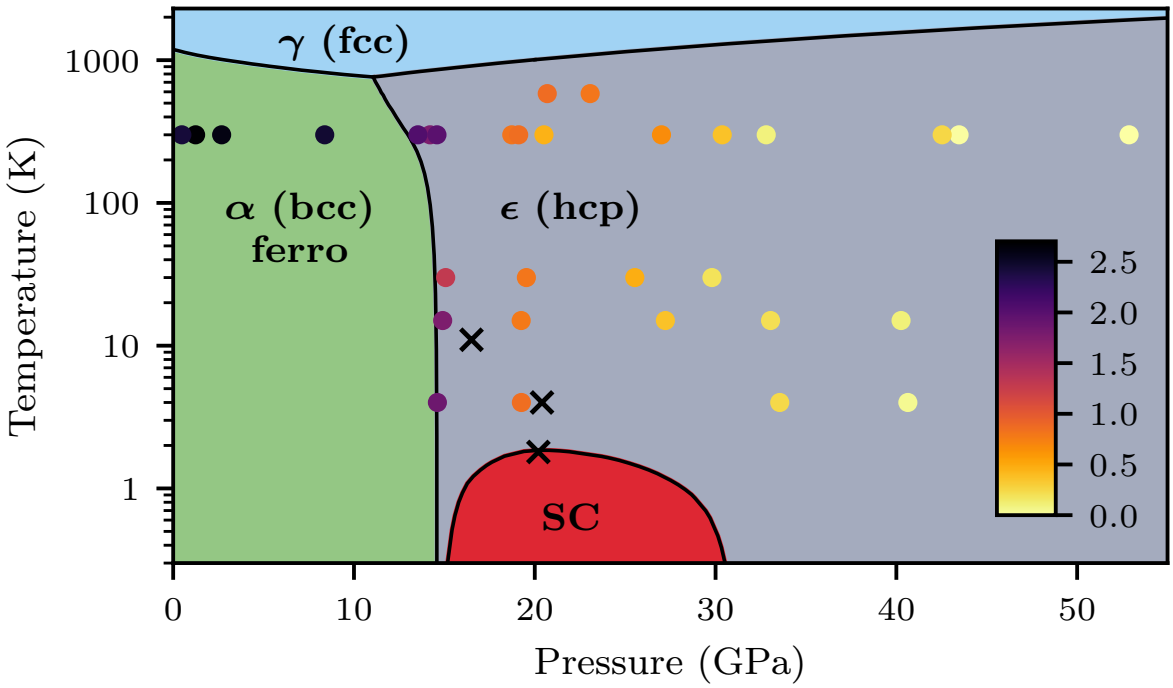

Figure 1: Schematic phase diagram of iron [4, 6]. Superconducting region labeled "SC". Our x-ray emission spectroscopy measurements are shown as circles, where the color represents the Kβ' satellite intensity as a percentage of the K$\beta_{1,3}$ mainline (see text for details). Low-temperature neutron powder diffraction measurements are shown as crosses.

alloy, but with a substantial hyperfine magnetic field unlike in pure iron, yet synchrotron Mössbauer spectroscopy detects no magnetism [18]. Transport measurements find non-Fermi liquid behavior indicative of spin fluctuations [19]. Calculations with local density approximation joined with dynamical mean-field theory (LDA+DMFT) predict a Pauli paramagnetic state which gives the closest agreement thus far with ϵ-iron's equation of state [20, 21]. Furthermore, their underestimation of resistivity and the divergence of their calculated equation of state in the superconducting pressure region hints at the importance of spin fluctuations.

We performed Kβ x-ray emission spectroscopy with considerably higher statistics, different analysis technique, and better pressure transmitting medium than past results [9, 22, 23]. We

confirm a magnetic moment persists in ϵ-iron [9] and also show that it is intrinsic to ϵ-iron rather than a remnant. We searched for possible magnetic order of these magnetic moments using neutron powder diffraction at record high-pressure and low-temperature conditions [24]. We found no static antiferromagnetism in ϵ-iron down to 1.8 K and put an upper limit of 0.2 μ_B for the magnetic moment of the afmII phase, which is four times less than theoretical predictions [14]. Overall our results reinforce the idea that ϵ-iron is paramagnetic with spin fluctuations. Furthermore, our Kβ XES results show the disappearance of the moment coincides with the the loss of superconductivity, suggesting that superconducting pairing is mediated by these spin fluctuations.

X-ray emission spectroscopy (XES)

Hard x-ray photon-in photon-out spectroscopy is well-suited to investigate magnetism in $3d$ compounds under high pressure [25, 26]. In particular, Kβ XES is an established probe of magnetism in iron [9, 22, 23] and iron oxides [27–29]. The Kβ ($3p \rightarrow 1s$) fluorescence has an intense mainline (K$\beta_{1,3}$) and a weaker, low-energy satellite region (Kβ'), as shown in our spectra in Fig. 2. This splitting is primarily due to the $3p - 3d$ exchange interaction between the $3p$ core hole and the majority-spin of the incomplete $3d$ shell in the final state [30, 31]. The $3p$ core hole acts as a probe of changes in the unpaired $3d$ spin occupation, in other words $3d$ spin angular momentum. In the case of iron, this corresponds approximately to the magnetic moment magnitude since the orbital angular momentum is mostly quenched. We stress that Kβ XES gives no information on the moment's direction nor spatial correlations, since it is only sensitive to the unpaired $3d$ occupancy.

The entire Kβ emission spectrum changes with the spin state. There is an overall redistribution of spectral weight from the mainline to the satellite for increasing spin angular momentum. This is due to a complex multiplet distribution in $3d$ transition metal compounds [32–39], however the crystal field multiplet approach is inappropriate for itinerant systems such as iron. Therefore, we instead follow the spin state semi-quantitatively by using the Kβ' satellite in-

tensity. Spin-resolved Kβ XES shows that the satellite is dominated by transitions involving unpaired 3d spin-up electrons [33, 34] and metal ions in similar chemical environments always show a stronger satellite for higher spin states [38]. An alternative anlysis technique is the integrated absolute difference (IAD) technique [38] which is shown to be a superior technique when studying two coexisting spin states during a transition at ambient pressure. We note first that in our case, a shoulder-like Kβ' satellite, with high statistics our technique is indistinguishable from the IAD technique, while with low statistics it varies from -12% to +2% [38]. Secondly, our measurements are performed under pressure and on an intinerant metal, not coexisting spin states in an extended transition. Pressure-induced effects on the Kβ mainline unrelated to 3d spin polarization have previously been observed, which is seen as large dichoric signal with the IAD technique, and tends to "stretch" the observed pressure transition region [40]. We believe this is also seen in previous x-ray magnetic circular dichorism (XMCD) and XES measurements on iron where the 10.3–18.4 GPa transition region found with XES is much larger than the 15.2–17.8 GPa transition region seen by XMCD [9].

We performed XES on iron over a large range of pressures and temperatures using an argon pressure transmitting medium (Fig. 1). The spectra are shown in Fig. 2 after alignment and normalization to the K$\beta_{1,3}$ mainline ($\approx$ 7057 eV). The satellite in iron is much weaker than in iron oxides, therefore in order to precisely follow its pressure evolution we measured with higher statistics than previous studies [9, 22, 23]. The pressure and temperature trends were studied in more detail by subtracting an ambient reference and finding the satellite intensity by fitting the Kβ' region of the resultant difference spectrum with a Gaussian lineshape (Fig. 2, inset). The results are shown together as a function of pressure in Fig. 1 and Fig. 3, where the highest pressure point is set to zero. The satellite intensity has no trend in temperature, therefore all the temperatures are considered equivalent when analyzing the pressure dependence. The lack of an observable temperature effect is unsurprising since XES is probing the 3d occupation which varies negligibly at these thermal energies (583 K $\approx$ 50 meV) in the absence of a phase transition.

The sharp drop in intensity and shift in position of the satellite around 15 GPa corresponds

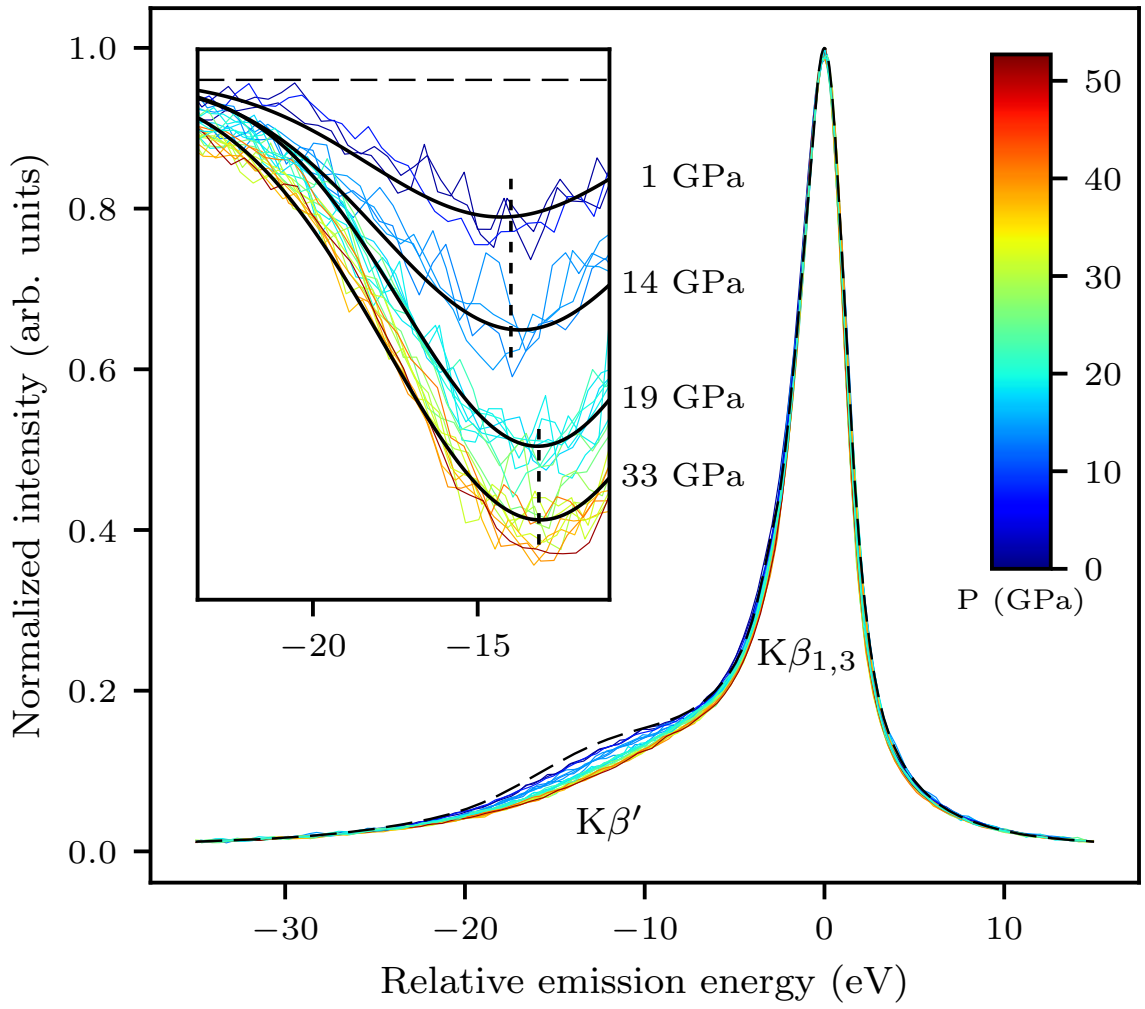

Figure 2: Pressure dependence of Kβ emission spectra of iron taken at various temperatures (no temperature trend found: see text and Fig. 1 & 3 for details). The spectra have been aligned and normalized to the K$\beta_{1,3}$ mainline. The inset is a zoom of the Kβ' satellite region after subtracting the ambient pressure/temperature reference (black dashed line). A selection of Gaussian fits are shown. The vertical dashed lines highlight the position shift during the α-ϵ transition.

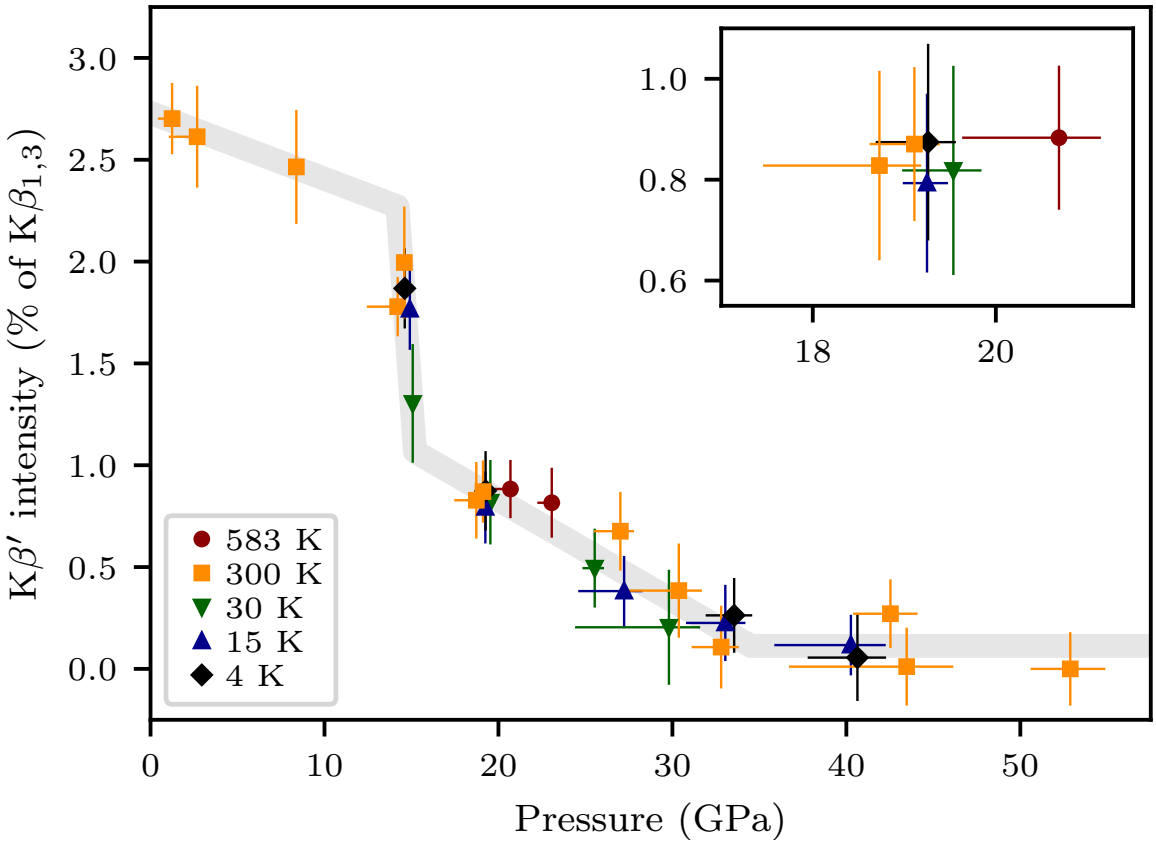

Figure 3: Pressure dependence of Kβ' intensity. The inset shows a zoom of the dense region around 20 GPa. The gray lines are guides for the eye.

to the α-ϵ transition. The use of a more hydrostatic pressure transmitting medium, coupled with increased statistics and a different analysis technique, leads to a narrower transition width than previous XES measurements [9]. The transition matches the structural transition [41, 42] and the Kβ' satellite shows a discontinuous change which indicates it is intrinsic to the ϵ-iron phase rather than a minority α-iron phase. Therefore, we find a magnetic moment in ϵ-iron after the α-ϵ transition which persists until 30–40 GPa. The drop in intensity at the transition cannot be unequivocally assigned to a smaller magnetic moment since the Fe local environment changes in the bcc-hcp transition which may also affect the satellite. However, the pressure

dependence of the magnetic moment for the afmII phase from first-principles calculations [14] shows a remarkable similarity to our results: a linear decrease in α-iron, a sharp drop during the transition, and finally a linear decrease in ϵ-iron with a larger slope. The calculations however predict zero magnetic moment above 60 GPa, while our results find it around 30–40 GPa. Nonetheless, a naive linear mapping of the Kβ' intensity to magnetic moment gives 0.7 μ_B at 20 GPa, which agrees well with 0.8 μ_B calculated for afmII.

Neutron powder diffraction (NPD)

We investigated the possible ordering of these magnetic moments in ϵ-iron using neutron powder diffraction. This technique is particularly suited to afm structures since their supercells imply certain Bragg peaks away from nuclear peaks towards lower scattering angles where the magnetic form factor is greatest. Using the techniques we describe in Ref. [24], we measured ϵ-iron above 20 GPa and down to 1.8 K. We see a complete α-ϵ transition during the pressure ramp (Fig. 4, top) to 18.5 GPa. The pressure increased further to 20.2 GPa upon cooling to 1.8 K (Fig. 4, bottom). The sample showed increased texturing in the α-iron phase during pressurization which agrees with Ref. [43]. This is seen mainly by the increasing intensity of the $(110)_{\mathrm{bcc}}$ peak, which becomes the $(002)_{\mathrm{hcp}}$ peak following the Burgers orientation relationship. Indeed, the preferred orientation is inherited by the ϵ-iron phase: we find a preferred orientation with the c-axis aligned $\approx 45°$ with respect to the scattering plane. This is clear by comparing the Rietveld refinements with and without preferred orientation (black and cyan lines in Fig. 4, bottom).

The low-2θ range is shown in Fig. 5 for three different pressures and temperatures. The top and middle panes are from run #1, where the middle is after pressurizing to 20.2 GPa and the top after depressurizing to 16.5 GPa. The bottom pane was from run #2 without cadmium shielding over the tungsten carbide of the pressure cell. The whole-pattern Rietveld refinement with ϵ-iron and diamond (and tungsten carbide for run #2) is shown as a black line. The peaks in this region are secondary reflections due to $\lambda/2$ contamination (0.2%). The two large peaks around 18.2° and 30.0° are from the (111) and (220) diamond secondary reflections. Run #2 has

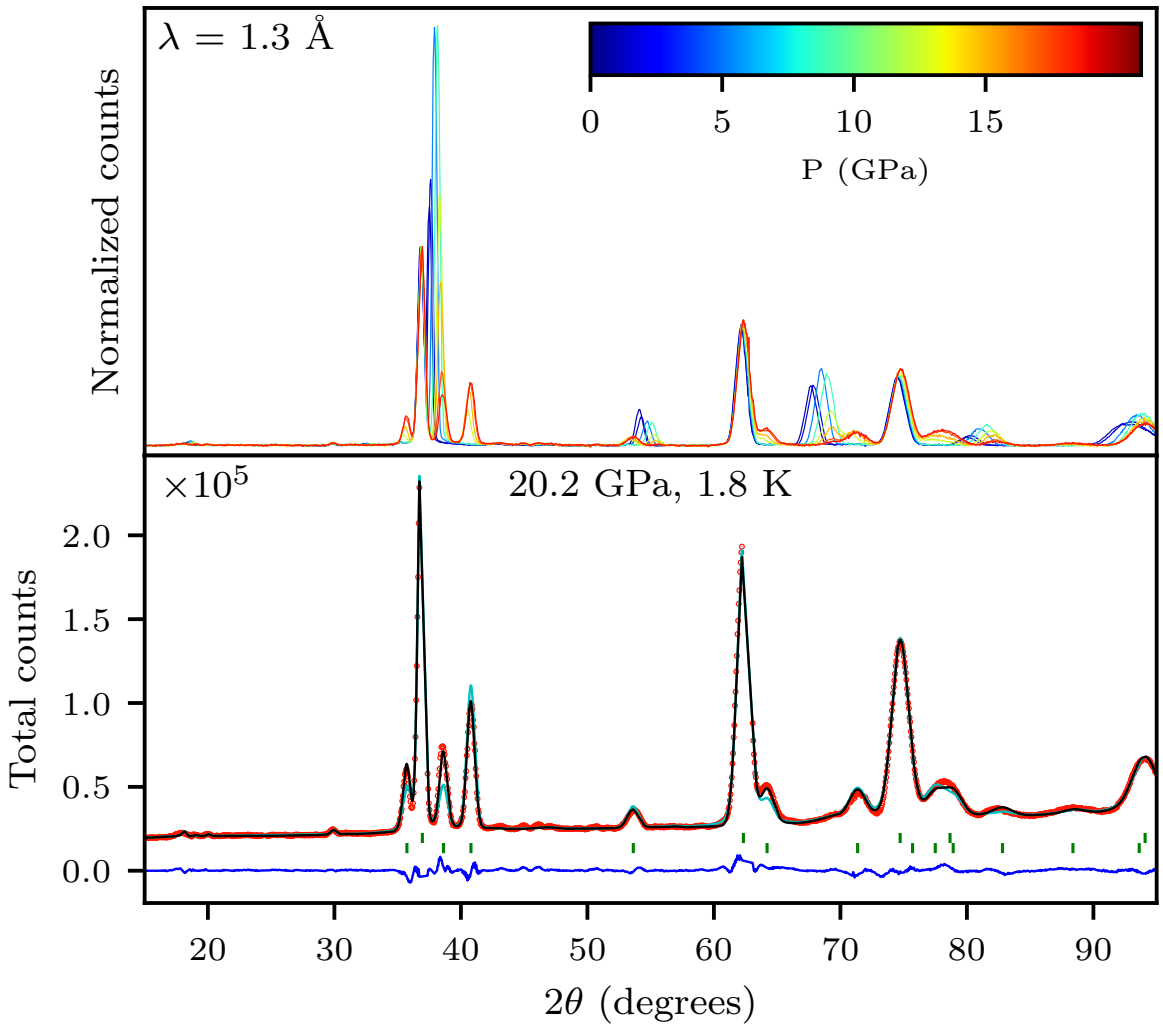

Figure 4: (Top) Neutron powder diffraction patterns showing a complete transformation to ϵ-iron during run #1. The temperature varied during the pressure ramp from 290 K (0 GPa) to 260 K (18.5 GPa). The spectra are normalized to the peak intensity of the diamond (111) Bragg reflection ($2\theta \approx 36.8°$) from the pressure cell. (Bottom) NPD pattern after cooling (red circles) with Rietveld refinement (black line) and their difference (blue line). Bragg reflections are marked with green ticks on the upper and lower row for diamond and ϵ-iron respectively, omitting reflections due to $\lambda/2$ contamination. A Rietveld refinement without any preferred orientation is shown as a cyan line.

a larger peak in the 30.0° region because of an additional tungsten carbide primary reflection. Weak secondary reflections from ϵ-iron are found at 17.6° (100), 19.0° (002), 20.1° (101), 26.1° (102), and 30.8° (110). Simulated afmII patterns are shown with 0.1 μ_B (blue), 0.2 μ_B (green), and 0.3 μ_B (red). Iron's magnetic moment in the afmII phase, assuming complete saturation, is therefore $\leq$ 0.2 μ_B for all three measurements. Our upper limit disagrees with afmII first-principles calculations [14] which predict 0.86 μ_B and 0.79 μ_B at 16.5 GPa and 20.2 GPa respectively.

The diffraction patterns show broad features centered around 21–24.5°, 25–27°, and 31–32.5° which are pressure-independent and more evident without shielding. We believe these are from graphite and graphite oxide residue left on the anvils after spark-erosion machining. We can remove these peaks by subtracting a high-temperature reference. The difference patterns are shown in Fig. 6 using an 18.5 GPa, 260 K reference for run #1 and a 20.8 GPa, 300 K reference for run #2. The difference spectra do not show any indication of short- or long-range magnetic order. Supposing that the Néel temperature (T_N) lies between the low and high temperature points, we find an upper limit of 0.15 μ_B for iron's magnetic moment in afmII (green simulation in Fig. 6).

Discussion

Our results reveal an intrinsic magnetic moment in ϵ-iron without any static afm order. The upper limit on the magnetic moment in afmII we find is four times smaller than DFT calculations [14]. Although mean-field calculations tend to overestimate magnetic moments, a four-fold difference is very unlikely. We did not simulate other afm arrangements, however no long- or short-range order was seen in the difference patterns and afmII is the only known arrangement with a hyperfine magnetic field smaller than the Mössbauer detection limit. There is always the possibility that T_N is below 1.8 K at 20.2 GPa and 11 K at 16.5 GPa. However, estimates using a multiscale approach find T_N = 75 K at 21 GPa for afmII [18] (and a different afm structure has an estimation of T_N = 69 K at 16 GPa [44]). The very similar c/a ratios and equations

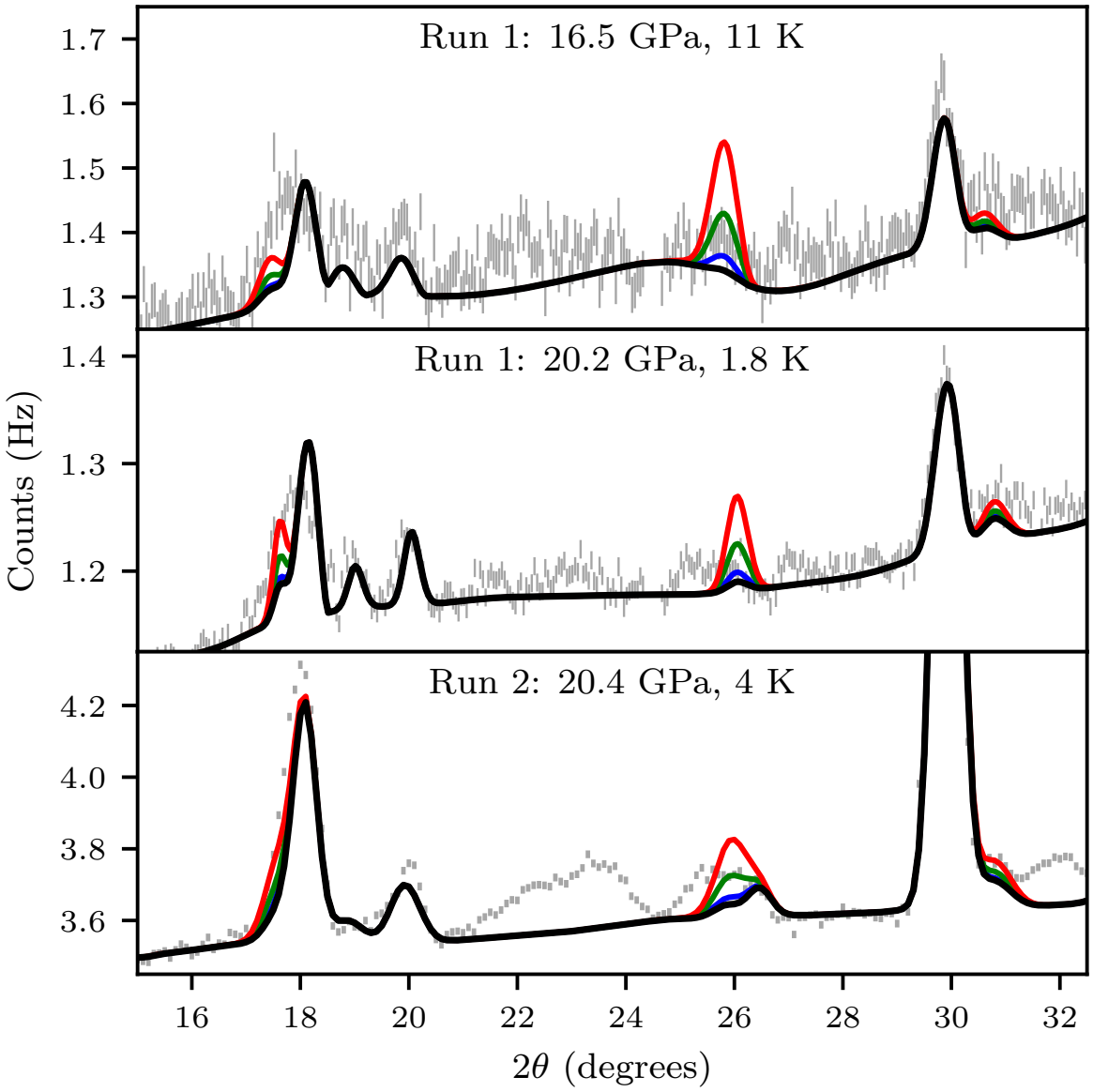

Figure 5: Neutron powder diffraction patterns (gray errors bars) with Rietveld refinement (black line). Simulations of afmII patterns shown with magnetic moments of 0.1 μ_B (blue), 0.2 μ_B (green), and 0.3 μ_B (red).

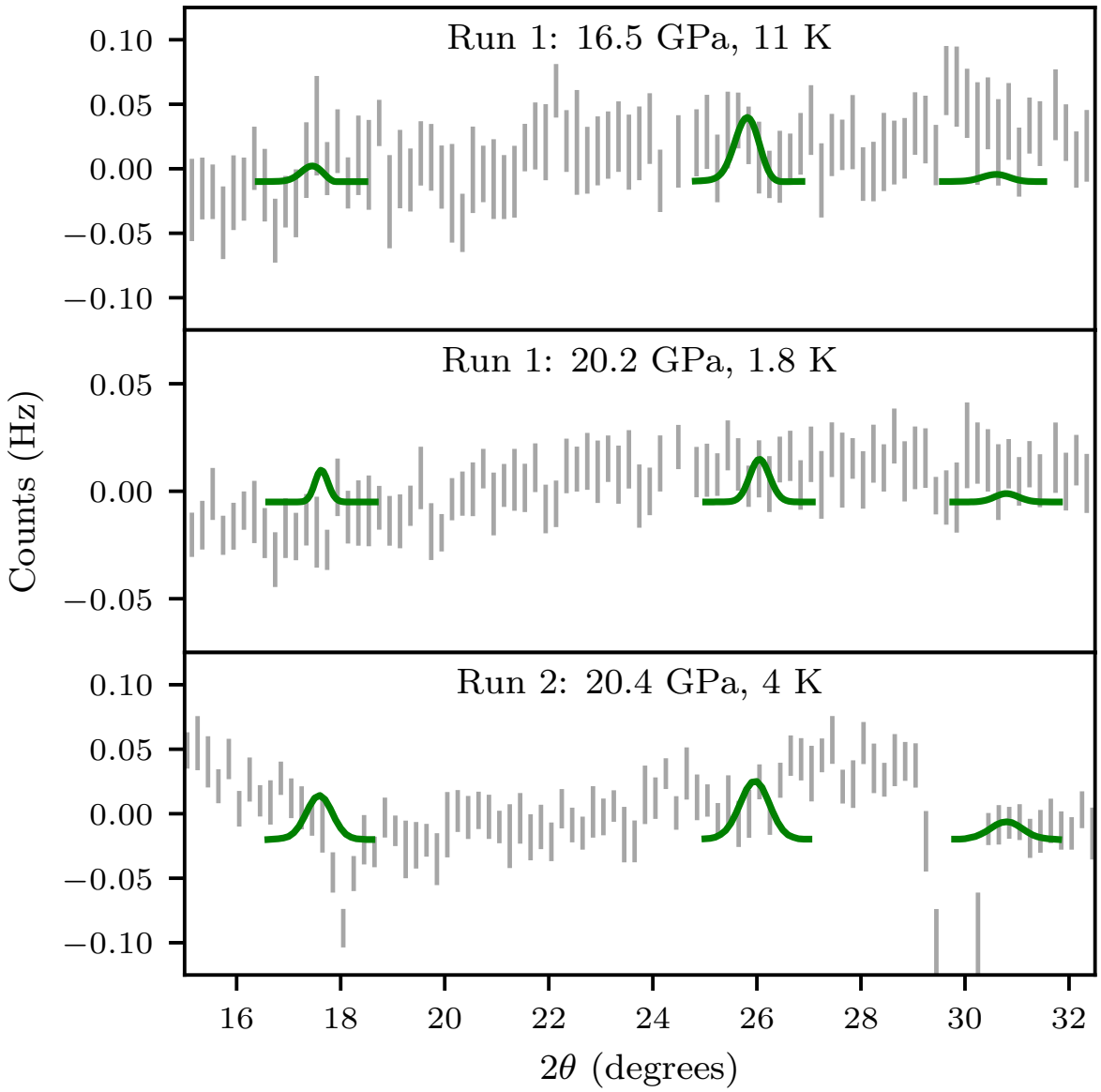

Figure 6: Neutron powder diffraction difference patterns with high temperature references (see text for details) binned to 0.2° shown as gray error bars. Simulation of afmII with 0.15 μ_B shown as green line.

of states measured in ϵ-iron at 15 K and 300 K means that if an afm structure exists the T_N should lie below or above said temperatures [21, 45, 46]. The addition of nickel impurities to iron creates an appreciable hyperfine magnetic field since they break the delicate balance between core and conduction electron polarization. However, synchrotron Mössbauer spectroscopy on the hcp-phase alloy $Fe_{92}Ni_8$ finds no magnetism, despite DFT predictions of an afmII state [18].

Our NPD results, coupled with previous results, strongly support the absence of afmII in ϵ-iron contrary to DFT calculations. A Pauli paramagnetic state was recently predicted using LDA+DMFT which shows the best agreement with ϵ-iron's equation of state, however spin fluctuations cannot be captured within this framework [20]. Nonetheless, spin fluctuations are inferred from the divergence in the calculated equation of state at 15–40 GPa (same pressure region as our XES results) and an underestimation of resistivity. Therefore, spin fluctuations are likely being probed in our Kβ XES measurements. In Mössbauer spectroscopy, spin fluctuations shorter than the lifetime of the 14.4 keV level of ^{57}Fe ($\approx$ 100 ns) [47] would effectively create a null hyperfine magnetic field. On the other hand, Kβ XES measures the 3d occupation and thus can measure the moment even with fluctuations.

The motion of compressed iron in response to an external magnet [48] is consistent with a picture of a paramagnetic state with spin fluctuations. Although if the pressure transmitting medium was truly hydrostatic as they state in this study due to heating, they could actually be measuring α-iron since shear forces are important for the α-ϵ transition. A study of saturation magnetization under pressure is also consistent with this picture [49]. The detection of saturation isothermal remnant magnetization at 21.5 GPa can only be explained by ferromagnetism and should be revisited with a more hydrostatic pressure transmitting medium [50].

Spin fluctuations have been studied in ϵ-iron for their connection to its superconductivity, however whether they are fm and/or afm, as well as their role in pairing is still unclear [15, 16, 51]. Antiferromagnetic spin fluctuations could possibly explain the second transverse optical peak seen with Raman spectroscopy if they are "afmII-like" and the increased width agrees qualitatively better with fluctuations rather than static afmII order [12, 14]. We should also note that band theory rarely "misses" the magnetic ground state. A plausible explanation is that

the inherent frustration of hcp lattice with respect to antiferromagnetism leads to a degenerate ground state and quantum spin fluctuations [52]. Frustrated antiferromagnets are known to have spins which fluctuate with a period on the order of 1 ns even near absolute zero [53]. Assuming afm spin fluctuations exist, we estimate their period in the high-temperature limit as 100 fs at 20 GPa, using Moriya's expression [53] and the nearest-neighbor exchange calculated in the Supplemental of Ref. [18]. On the other hand, ferromagnetic spin fluctuations are favored by transport measurements which report non-Fermi liquid behavior with $T^{5/3}$ dependence in this pressure region [5, 19, 54, 55].

We find the magnetic moment associated with spin fluctuations in ϵ-iron gradually decreases to zero around 30–40 GPa. The disappearance of spin fluctuations in ϵ-iron coinicides with the decreasing high pressure side of the superconducting dome [4, 55] and suggests p- or d-wave superconductivity where the spin fluctuations are pairing [15] (although calculations favor d-wave [16]). The loss of spin fluctuations around 30–40 GPa could also explain anomalous Debye sound velocity, c/a ratio [56], and Mössbauer center shift results around 40 GPa, which were originally proposed as due to an electronic topological transition in this pressure region [57]. X-ray diffraction results recently found no evidence of this electronic topological transition [21]. The pressure region where spin fluctuations disappear is also the same as the end of the non-Fermi liquid regime seen with transport and the disappearance of the extra Raman modeRegardless of the correlation, ϵ-iron's magnetic moment is gone above 40 GPa, much lower than relevant core pressures, therefore magnetism in ϵ-iron does not play an important geophysical role as was previously conjectured [58]. Our results also show that measurements of ϵ-iron below 40 GPa should not be extrapolated to higher pressures due the effects of magnetism in the lower pressure region.

In conclusion, we have used Kβ x-ray emission spectroscopy to show the existence of an intrinsic magnetic moment in ϵ-iron coinciding with the superconducting pressure region. Our neutron powder diffraction results exclude static antiferromagnetism in most of the low-pressure ϵ-iron P-T phase space. In particular, an afmII phase existing above 1.8 K at 20.2 GPa must have a moment four times smaller than theoretical predictions. With previous results we find a

coherent picture emerging of a paramagnetic state with spin fluctuations which mediate superconductivity in ϵ-iron. Extending inelastic neutron scattering [24, 59] and muon spin rotation spectroscopy to higher pressures would be useful to study the spin dynamics in ϵ-iron.

Materials and experimental methods

X-ray emission spectroscopy (XES)

We used a high-purity, 5 μm-thick iron foil for the XES experiment. It was performed in two separate synchrotron runs on the GALAXIES beamline at Synchrotron SOLEIL. The first run was performed using a He flow cryostat ($\leq$ 300 K) with three loadings, while the second run was performed using an external resisitive heater ($\geq$ 300 K) with two loadings. Pressure was applied using a membrane-driven diamond anvil cell equipped with 1.2 mm-thick diamonds with 300 μm culets. A 200 μm-thick rhenium gasket was pre-indented to 25 μm and drilled with a 150 μm diameter hole. The pressure was measured in-situ before and after each measurement using the fluorescence from ruby ($\leq$ 300 K) [60] or SrB_4O_7:Sm^{2+} ($\geq$ 300 K) [61]. The iron foil and manometer were cryogenically loaded with argon as the pressure medium. After changing the pressure we waited for relaxation, however pressure uncertainty was still dominated by this pressure creep. It has a shorter timescale ($\approx$ 1–2 h) than our measurements (8–16 h), therefore the error bars are asymmetric. Uncertainty due to the non-hydrostaticity of argon is also included [62].

We measured with the spectrometer in a transmission geometry. The sample, a spherically-bent Si(531) crystal analyzer, and an avalanche photodiode detector were arranged on a one-meter Rowland circle. The total energy resolution at the Fe K$\beta_{1,3}$ mainline (7057 eV, $\theta_B = 79°$) was 1.4 eV FWHM. The incident x-ray energy was either 9 or 10 keV for different loadings, both well above the Fe K-edge ($\approx$ 7112 eV). The spot size on the sample was 30(V) $\times$ 80(H) μm^2 and its position was recentered every half hour. Lead tape or an aluminum plate was used as a beam stop to block the direct beam after the pressure cell.

Many individual spectra are taken at each PT point and averaged into a single spectrum,

where the uncertainty is given by the standard deviation. Linear background subtraction and normalization/shift to the K$\beta_{1,3}$ mainline were performed before subtracting the ambient reference spectrum. Our reference spectrum was taken outside of a diamond anvil cell at ambient conditions for extremely high statistics to avoid introducing uncertainty in the difference spectra. The relative satellite intensity is extracted by fitting the difference spectra with a Gaussian lineshape in the satellite region (≤ -11 eV), using a Monte Carlo bootstrap technique to estimate the intensity uncertainty.

Neutron powder diffraction (NPD)

The NPD experiment was performed on the high-flux diffractometer D20 [63] at the Institut Laue-Langevin in two separate runs [64]. The techniques for NPD above 20 GPa and below 1.8 K are already presented in Ref. [24], including this specific experiment, therefore they will be presented only briefly. Thermal neutrons of $\lambda \approx 1.3$ Å were produced by reflection from a Cu (200) monochromator at a 42° take-off angle. A VX5 Paris-Edinburgh high pressure cell [65] applied pressure perpendicular to the scattering plane. We used sintered diamond anvils, surround by tungsten carbide and steel binding rings. The steel was shielded with cadmium in both runs, but the tungsten carbide was shielded only in run #1. The diamond anvils were machined using spark erosion into the double-toroidal configuration with reduced profile dimensions [24, 66]. Null-scattering TiZr gaskets were used with an inner set of encapsulating hemispheres. The sample was machined from a rod of 99.99+% pure iron into a roughly 9 mm^3 sphere (run #1 from Goodfellow ref. 203-947-27 and run #2 from Alfa Aesar). No pressure transmitting medium was used in order to increase signal and since all mediums are solid at these conditions. The pressure was determined from the sample itself since iron's equation of state is well-known [21, 45]. The maximum pressure we find is 2.2 GPa lower than Ref. [24] since we refined the wavelength in the current study and used all the acquisitions (15 times more than in Ref. [24]). The Rietveld refinement and pattern simulations were performed using FULLPROF [67]. The simulations assumed the magnetic form factor of an Fe^{3+} ion, although we note that at least in α-iron the form factor is slightly anisotropic [68].

Acknowledgements

We are grateful for beamtime and resources provided by SOLEIL, through in-house tests and projects (20130318 and 20120694). We are grateful to Guillaume Morard for lending us an iron foil and a diamond pair, as well as Jean-Paul Itié for fruitful discussions, a diamond pair, and a loan of another diamond pair. We acknowledge useful discussions with Abhay Shukla. We are grateful for beamtime and resources provided by ILL [64], as well as the ISIS facility for initial test measurements in 2003. We thank Xavier Tonon, Claude Payre and Alain Daramsy (ILL), as well as Gérard Hamel (IMPMC) for their aid during experiments. B.W.L acknowledges financial support from the French state funds managed by the ANR within the "Investissements dâĂŹAvenir" programme under reference ANR-11-IDEX-0004-02, and within the framework of the Cluster of Excellence MATISSE led by Sorbonne Université and from the LLB/SOLEIL PhD fellowship program.

References

[1] I. Leonov, A. I. Poteryaev, V. I. Anisimov & D. Vollhardt; "Electronic Correlations at the α-γ Structural Phase Transition in Paramagnetic Iron;" Phys. Rev. Lett. **106**, p. 106405 (2011).

[2] L. Stixrude, R. Cohen & D. Singh; "Iron at high pressure: Linearized-augmented-plane-wave computations in the generalized-gradient approximation;" Phys. Rev. B **50**, pp. 6442–6445 (1994).

[3] R. Jeanloz; "The Nature of the Earth's Core;" Annu. Rev. Earth Planet. Sci. **18**, pp. 357–386 (1990).

[4] K. Shimizu, T. Kimura, S. Furomoto, K. Takeda, K. Kontani, Y. Onuki & K. Amaya; "Superconductivity in the non-magnetic state of iron under pressure." Nature **412**, pp. 316–8 (2001).

[5] D. Jaccard, A. Holmes, G. Behr, Y. Inada & Y. Onuki; "Superconductivity of ϵ-Fe: complete resistive transition;" Phys. Lett. A **299**, pp. 282–286 (2002).

[6] F. P. Bundy; "Pressure—Temperature Phase Diagram of Iron to 200 kbar, 900 C;" J. Appl. Phys. **36**, p. 616 (1965).

[7] O. Mathon, F. Baudelet, J. Itié, a. Polian, M. D'Astuto, J. Chervin & S. Pascarelli; "Dynamics of the Magnetic and Structural α-ϵ Phase Transition in Iron;" Phys. Rev. Lett. **93**, p. 255503 (2004). doi:10.1103/PhysRevLett.93.255503.

[8] F. Baudelet, S. Pascarelli, O. Mathon, J. P. Itié, a. Polian, M. D. Astuto & J. C. Chervin; "X-ray absorption spectroscopy and x-ray magnetic circular dichroism simultaneous measurements under high pressure: the iron bcc–hcp transition case;" J. Phys. Condens. Matter **17**, pp. S957–S966 (2005).

[9] a. Monza, A. Meffre, F. Baudelet, J.-P. Rueff, M. D'Astuto, P. Munsch, S. Huotari, S. Lachaize, B. Chaudret & A. Shukla; "Iron Under Pressure: "Kohn Tweezers" and Remnant Magnetism;" Phys. Rev. Lett. **106**, p. 247201 (2011).

[10] N. Ishimatsu, Y. Sata, H. Maruyama, T. Watanuki, N. Kawamura, M. Mizumaki, T. Irifune & H. Sumiya; "αâĹŠϵ transition pathway of iron under quasihydrostatic pressure conditions;" Phys. Rev. B **90**, p. 014422 (2014). doi:10.1103/PhysRevB.90.014422.

[11] G. Cort, R. Taylor & J. Willis; "Search for magnetism in hcp epsilon-Fe;" J. Appl. Phys. **53**, p. 2064 (1982).

[12] S. Merkel, A. Goncharov, H. Mao, P. Gillet & R. Hemley; "Raman spectroscopy of iron to 152 gigapascals: implications for Earth's inner core;" Science **288**, pp. 1626–9 (2000).

[13] G. Steinle-Neumann, L. Stixrude & R. Cohen; "First-principles elastic constants for the hcp transition metals Fe, Co, and Re at high pressure;" Phys. Rev. B **60**, pp. 791–799 (1999).

[14] G. Steinle-Neumann, L. Stixrude & R. E. Cohen; "Magnetism in dense hexagonal iron." Proc. Natl. Acad. Sci. U. S. A. **101**, pp. 33–6 (2004).

[15] I. Mazin, D. Papaconstantopoulos & M. Mehl; "Superconductivity in compressed iron: Role of spin fluctuations;" Phys. Rev. B **65**, p. 100511 (2002).

[16] S. Bose, O. Dolgov, J. Kortus, O. Jepsen & O. Andersen; "Pressure dependence of electron-phonon coupling and superconductivity in hcp Fe: A linear response study;" Phys. Rev. B **67**, p. 214518 (2003).

[17] T. Jarlborg; "Spin fluctuations, electron–phonon coupling and superconductivity in near-magnetic elementary metals—-Fe, Co, Ni and Pd;" Phys. C Supercond. **385**, pp. 513–524 (2003).

[18] a. Papandrew, M. Lucas, R. Stevens, I. Halevy, B. Fultz, M. Hu, P. Chow, R. Cohen & M. Somayazulu; "Absence of Magnetism in Hcp Iron-Nickel at 11 K;" Phys. Rev. Lett. **97**, p. 087202 (2006).

[19] a. T. Holmes, D. Jaccard, G. Behr, Y. Inada & Y. Onuki; "Unconventional superconductivity and non-Fermi liquid behaviour of -iron at high pressure;" J. Phys. Condens. Matter **16**, pp. S1121–S1127 (2004).

[20] L. V. Pourovskii, J. Mravlje, M. Ferrero, O. Parcollet & I. A. Abrikosov; "Impact of electronic correlations on the equation of state and transport in ϵ -Fe;" Phys. Rev. B - Condens. Matter Mater. Phys. **90**, pp. 1–6 (2014). doi:10.1103/PhysRevB.90.155120.

[21] A. Dewaele & G. Garbarino; "Low temperature equation of state of iron;" Appl. Phys. Lett. **111**, pp. 2–6 (2017). doi:10.1063/1.4989688.

[22] J. Rueff, M. Krisch, Y. Cai, A. Kaprolat, M. Hanfland, M. Lorenzen, C. Masciovecchio, R. Verbeni & F. Sette; "Magnetic and structural α-ϵ phase transition in Fe monitored by x-ray emission spectroscopy;" Phys. Rev. B **60**, pp. 14510–14512 (1999).

[23] J.-P. Rueff, M. Mezouar & M. Acet; "Short-range magnetic collapse of Fe under high pressure at high temperatures observed using x-ray emission spectroscopy;" Phys. Rev. B **78**, p. 100405 (2008).

[24] S. Klotz, T. Strässle, B. Lebert, M. d'Astuto & T. Hansen; "High pressure neutron diffraction to beyond 20 GPa and below 1.8 K using Paris-Edinburgh load frames;" High Pressure Research **36**, pp. 73–78 (2016). doi:10.1080/08957959.2015.1136624.

[25] J.-P. Rueff & A. Shukla; "Inelastic x-ray scattering by electronic excitations under high pressure;" Rev. Mod. Phys. **82**, pp. 847–896 (2010).

[26] M. d'Astuto, A. Barla, N. Kernavanois, J.-P. Rueff, F. Baudelet, R. Rüffer, L. Paolasini & B. Couzinet; "Magnetism under Pressure with Synchrotron Radiation;" in "Magnetism: Synchrotron Radiation Approach," , *Lect Notes Phys*, volume 697, edited by E. Beaurepaire, H. Bulou, F. Scheurer & J.-P. Kappler; p. 375 (Springer-Verlag, Berlin, Heidelberg, New York) (2006).

[27] J. Badro, G. Fiquet, F. Guyot, J.-P. Rueff, V. V. Struzhkin, G. Vankó & G. Monaco; "Iron partitioning in Earth's mantle: toward a deep lower mantle discontinuity." Science **300**, pp. 789–91 (2003).

[28] J. Badro, J.-P. Rueff, G. Vankó, G. Monaco, G. Fiquet & F. Guyot; "Electronic transitions in perovskite: possible nonconvecting layers in the lower mantle." Science **305**, pp. 383–6 (2004).

[29] A. Mattila, J.-P. Rueff, J. Badro, G. Vankó & A. Shukla; "Metal-Ligand Interplay in Strongly Correlated Oxides: A Parametrized Phase Diagram for Pressure-Induced Spin Transitions;" Phys. Rev. Lett. **98**, p. 196404 (2007). doi:10.1103/PhysRevLett.98.196404.

[30] K. Tsutsumi; "The X-ray Non-diagram Lines K β' of Some Compounds of the Iron Group;" J. Phys. Soc. Japan **14**, pp. 1696–1706 (1959).

[31] K. Tsutsumi, H. Nakamori & K. Ichikawa; "X-ray Mn Kβ emission spectra of manganese oxides and manganates;" Phys. Rev. B **13**, pp. 929–933 (1976).

[32] F. M. F. de Groot, A. Fontaine, C. C. Kao & M. Krisch; "Charge transfer multiplet calculations of the K beta X-ray emission spectra of divalent nickel compounds;" Journal of Physics: Condensed Matter **6**, p. 6875 (1994). http://stacks.iop.org/0953-8984/6/i=34/a=019.

[33] G. Peng, X. Wang, M. M. Crush, S. P. Cramer, F. M. DeGroot, K. Hämäläinen, J. A. Moore, J. B. Hastings, D. P. Siddons, W. H. Armstrong & O. C. Mullins; "High-resolution manganese x-ray fluorescence spectroscopy. Oxidation-state and spin-state sensitivity;" J. Am. Chem. Soc. **116**, pp. 2914–2920 (1994). doi:10.1021/ja00086a024.

[34] G. Peng, X. Wang, C. R. Randall, J. A. Moore & S. P. Cramer; "Spin selective x-ray absorption spectroscopy: Demonstration using high resolution Fe Kβ fluorescence;" Appl. Phys. Lett. **65**, pp. 2527–2529 (1994). doi:10.1063/1.112625.

[35] X. Wang, F. M. F. de Groot & S. P. Cramer; "Spin-polarized x-ray emission of 3d transition-metal ions: A comparison via $K\alpha$ and $K\beta$ detection;" Phys. Rev. B **56**, pp. 4553–4564 (1997). doi:10.1103/PhysRevB.56.4553.

[36] F. de Groot; "High-Resolution X-ray Emission and X-ray Absorption Spectroscopy;" Chem. Rev. **101**, pp. 1779–1808 (2001).

[37] P. Glatzel, J. Yano, U. Bergmann, H. Visser, J. H. Robblee, W. Gu, F. M. de Groot, S. P. Cramer & V. K. Yachandra; "Resonant inelastic X-ray scattering (RIXS) spectroscopy at the Mn K absorption pre-edge—a direct probe of the 3d orbitals;" J. Phys. Chem. Solids **66**, pp. 2163–2167 (2005).

[38] G. Vankó, T. Neisius, G. Molnar, F. Renz, S. Karpati, A. Shukla & F. M. F. de Groot; "Probing the 3d spin momentum with X-ray emission spectroscopy: the case of molecular-spin transitions." J. Phys. Chem. B **110**, pp. 11647–53 (2006).

[39] G. Vankó & F. de Groot; "Comment on "Spin crossover in (Mg,Fe)O: A Mössbauer effect study with an alternative interpretation of x-ray emission spectroscopy data";" Phys. Rev. B **75**, p. 177101 (2007).

[40] Z. Mao, J.-F. Lin, J. Yang, J. Wu, H. C. Watson, Y. Xiao, P. Chow & J. Zhao; "Spin and valence states of iron in Al-bearing silicate glass at high pressures studied by synchrotron Mossbauer and X-ray emission spectroscopy;" American Mineralogist **99**, pp. 415–423 (2014).

[41] R. Boehler; "The phase diagram of iron to 430 kbar;" Geophys. Res. Lett. **13**, pp. 1153–1156 (1986).

[42] R. Boehler, N. von Bargen & A. Chopelas; "Melting, thermal expansion, and phase transitions of iron at high pressures;" J. Geophys. Res. **95**, p. 21731 (1990).

[43] S. Merkel, H.-R. Wenk, P. Gillet, H. kwang Mao & R. J. Hemley; "Deformation of polycrystalline iron up to 30GPa and 1000K;" Physics of the Earth and Planetary Interiors **145**, pp. 239 – 251 (2004). doi:https://doi.org/10.1016/j.pepi.2004.04.001.

[44] V. Thakor, J. Staunton, J. Poulter, S. Ostanin, B. Ginatempo & E. Bruno; "Ab initio calculations of incommensurate antiferromagnetic spin fluctuations in hcp iron under pressure;" Phys. Rev. B **67**, p. 180405 (2003).

[45] A. Dewaele, P. Loubeyre, F. Occelli, M. Mezouar, P. Dorogokupets & M. Torrent; "Quasihydrostatic Equation of State of Iron above 2 Mbar;" Phys. Rev. Lett. **97**, p. 215504 (2006).

[46] A. Dewaele, C. Denoual, S. Anzellini, F. Occelli, M. Mezouar, P. Cordier, S. Merkel, M. Véron & E. Rausch; "Mechanism of the $\alpha - \epsilon$ phase transformation in iron;" Phys. Rev. B **91**, p. 174105 (2015). doi:10.1103/PhysRevB.91.174105.

[47] P. Gütlich, E. Bill & A. Trautwein; *Mössbauer Spectroscopy and Transition Metal*

Chemistry: Fundamentals and Applications (Springer Berlin Heidelberg) (2010); ISBN 9783540884286; https://books.google.fr/books?id=nAqkEHuoiM0C.

[48] S. Gilder; "Magnetic Properties of Hexagonal Closed-Packed Iron Deduced from Direct Observations in a Diamond Anvil Cell;" Science (80-.). **279**, pp. 72–74 (1998). doi:10.1126/science.279.5347.72.

[49] X. Wang, T.-L. Hu, B. Han, H.-C. Jin, Y. Li, Q. Zhou & T. Zhang; "Ferromagnetic materials under high pressure in a diamond-anvil cell: A magnetic study;" Chinese Phys. B **23**, p. 070701 (2014). doi:10.1088/1674-1056/23/7/070701.

[50] Q. Wei & S. A. Gilder; "Ferromagnetism of iron under pressure to 21.5 GPa;" Geophys. Res. Lett. **40**, pp. 5131–5136 (2013). doi:10.1002/grl.51004.

[51] T. Jarlborg; "Ferromagnetic and antiferromagnetic spin fluctuations and superconductivity in the hcp-phase of Fe;" Phys. Lett. A **300**, pp. 518–523 (2002).

[52] R. Moessner & A. P. Ramirez; "Geometrical frustration;" Phys. Today **59**, pp. 24–29 (2006). doi:10.1063/1.2186278.

[53] S. R. Dunsiger, J. S. Gardner, J. A. Chakhalian, A. L. Cornelius, M. Jaime, R. F. Kiefl, R. Movshovich, W. A. MacFarlane, R. I. Miller, J. E. Sonier & B. D. Gaulin; "Low temperature spin dynamics of the geometrically frustrated antiferromagnetic garnet Gd3Ga5O12;" Phys. Rev. Lett. **85**, pp. 3504–3507 (2000). doi:10.1103/PhysRevLett.85.3504.

[54] D. Jaccard & A. T. Holmes; "Spin and Valence-Fluctuation Mediated Superconductivity in Pressurized Fe and CeCu_2(Si/Ge)_2;" Phys. B **359–361**, pp. 333–340 (2005). doi:10.1016/j.physb.2005.01.056.

[55] C. S. Yadav, G. Seyfarth, P. Pedrazzini, H. Wilhelm, R. Černý & D. Jaccard; "Effect of pressure cycling on iron: Signatures of an electronic instability and unconventional superconductivity;" Phys. Rev. B **88**, p. 054110 (2013).

[56] S. Ono, T. Kikegawa, N. Hirao & K. Mibe; "High-pressure magnetic transition in hcp-Fe;" Am. Mineral. **95**, pp. 880–883 (2010).

[57] K. Glazyrin, L. Pourovskii, L. Dubrovinsky, O. Narygina, C. McCammon, B. Hewener, V. Schünemann, J. Wolny, K. Muffler, a. Chumakov, W. Crichton, M. Hanfland, V. Prakapenka, F. Tasnádi, M. Ekholm, M. Aichhorn, V. Vildosola, a. Ruban, M. Katsnelson & I. Abrikosov; "Importance of Correlation Effects in hcp Iron Revealed by a Pressure-Induced Electronic Topological Transition;" Phys. Rev. Lett. **110**, p. 117206 (2013).

[58] S. S. Saxena & P. B. Littlewood; "Superconductivity. Iron cast in exotic role." Nature **412**, pp. 290–1 (2001).

[59] S. Klotz & M. Braden; "Phonon Dispersion of bcc Iron to 10 GPa;" Phys. Rev. Lett. **85**, pp. 3209–3212 (2000).

[60] A. Dewaele, M. Torrent, P. Loubeyre & M. Mezouar; "Compression curves of transition metals in the Mbar range: Experiments and projector augmented-wave calculations;" Phys. Rev. B **78**, p. 104102 (2008).

[61] F. Datchi, a. Dewaele, P. Loubeyre, R. Letoullec, Y. Le Godec & B. Canny; "Optical pressure sensors for high-pressure–high-temperature studies in a diamond anvil cell;" High Press. Res. **27**, pp. 447–463 (2007).

[62] S. Klotz, J.-C. Chervin, P. Munsch & G. L. Marchand; "Hydrostatic limits of 11 pressure transmitting media;" Journal of Physics D: Applied Physics **42**, p. 075413 (2009). http://stacks.iop.org/0022-3727/42/i=7/a=075413.

[63] T. C. Hansen, P. F. Henry, H. E. Fischer, J. Torregrossa & P. Convert; "The D20 instrument at the ILL: a versatile high-intensity two-axis neutron diffractometer;" Meas. Sci. Technol. **19**, p. 034001 (2008). doi:10.1088/0957-0233/19/3/034001.

[64] S. Klotz, M. d'Astuto, T. Hansen, B. Lebert & T. Straessle; "Search for magnetic order in epsilon-iron at 20 GPa;" (2015). doi:10.5291/ill-data.5-31-2443.

[65] S. Klotz; *Techniques in High Pressure Neutron Scattering* (Taylor & Francis) (2016); ISBN 9781138199217.

[66] S. Klotz, J. M. Besson, G. Hamel, R. J. Nelmes, J. S. Loveday, W. G. Marshall & R. M. Wilson; "Neutron powder diffraction at pressures beyond 25 GPa;" Applied Physics Letters **66**, pp. 1735–1737 (1995). doi:10.1063/1.113350.

[67] J. Rodríguez-Carvajal; "Recent advances in magnetic structure determination by neutron powder diffraction;" Physica B **192**, pp. 55–69 (1993). doi:10.1016/0921-4526(93)90108-I.

[68] C. Shull & Y. Yamada; "MAGNETIC ELECTRON CONFIGURATION IN IRON;" J. Phys. Soc. Japan **Vol: 17: Suppl. B-III** (1962).

IV.3 Discussion & perspectives

The Kβ XES technique is a double-edged sword: its strength in being able to measure spin fluctuations via the 3*d* occupation is also its weakness since it does not provide us with any information about the spin fluctuations correlation, direction, or timescale. Therefore, we turned towards first-principles calculations to help interpret our experimental results. With the success of Pourovskii *et al.* in describing the experimental equation of state (EOS) by including correlations [157], we tried the less computational intensive technique DFT+U to include correlations and study the magnetic state of ϵ-iron. The U and J parameters were fit to match α-iron's experimental EOS and magnetic moment and then were applied to the ϵ-iron state for the Pauli paramagnetic and afmII configurations. The results are shown in Fig. IV.6 alongside the results of Pourovskii *et al.*. The LDA+DMFT results for a Pauli paramagnetic state underestimate the EOS below 60 GPa, while our DFT+U results for the afmII state overestimates the EOS below 60 GPa. They both converge around 60 GPa where the magnetic moment approaches zero using the generalized gradient approximation for the exchange functional. These rough results emphasize the importance of magnetism in this low pressure region where superconductivity is found in order to properly describe the EOS. The fact that the static afmII state overestimates the EOS suggests spin fluctuations rather than a static phase.

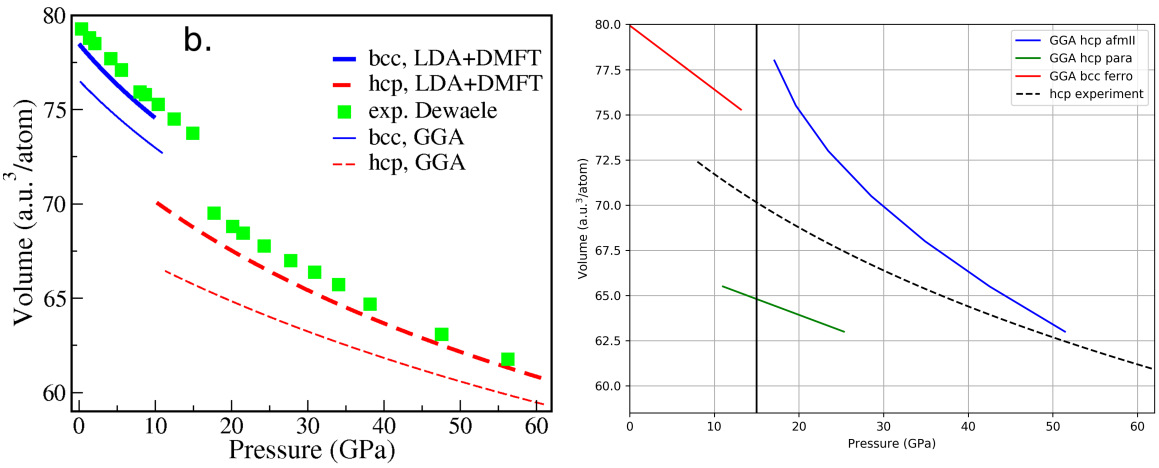

Figure IV.6: (Left) Equation of state calculated using DFT with a generalized gradient approximation exchange functional (GGA) and using the LDA+DMFT technique compared to experimental results [157]. (Right) Our preliminary calculations using DFT+U with the GGA exchange functional.

With the aid of Michele Casula, I began calculating the ground state of ϵ-iron using a higher convergence than previously reported studies and supercells larger than the afmII supercell. We discovered a new collinear magnetic ground state with a slightly lower energy than the afmII state. This state has three inequivalent atomic sites with unequal magnetic moments, yet the state is still antiferromagnetic since their sum over the supercell is zero. The work is being continued by Michele Casula and Tommaso Gorni, who have identified two more nearly degenerate states for a total of four. The results have been verified with different pseudo-potentials and a simple exchange model similar to one for a spin ice has been

developed. Currently they are performing a classical Monte Carlo study to investigate the effect of these degenerate states on the predicted Néel temperature of the afmII state. The description they are providing for itinerant spin fluctuations is unique because the magnitude of the moments is fluctuating rather than just the direction, as in previous treatments of itinerant spin fluctuations. These results support the idea that the afmII state is destabilized due to the frustration of the hcp lattice with respect to antiferromagnetism which leads to quantum spin fluctuations.

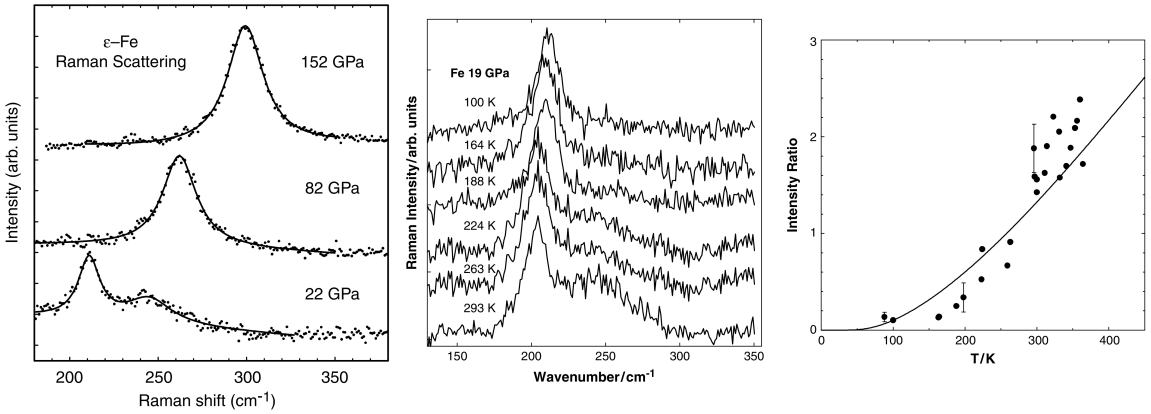

Figure IV.7: (Left) Raman spectroscopy finds a splitting of the E_{2g} optical phonon mode present at low pressures in ϵ-iron [137] (Center) Sample of Raman spectra at 19 GPa and different temperatures shows the disappearance of the second peak at low temperatures [160] (Right) The temperature dependence of the extra Raman peak's intensity from the same study.

At first glance, our DFT results suggest that afm correlations should exist between spins. This is consistent with Raman spectroscopy measurements at 300 K [137], however low-temperature Raman measurements show a decreased intensity in the anomalous peak with lower temperatures (Fig. IV.7) [160]. A fit of the temperature dependence predicts a complete disappearance below 50 K [160]. They believe this second peak probably does not have a magnetic origin and suggest that it can be qualitatively explained by the anharmonicity of the optical mode whose response factor changes drastically with temperature. However, it is worth repeating that the second peak disappears around 30–40 GPa, the same as seen by XES and transport studies, which suggests they all have a common origin. The transport results are shown in Fig. IV.8. The data has been fit at low temperatures with the function $\rho = \rho_0 + AT^n$. The temperature dependence is $n = 5/3$ which is the predicted dependence for fm fluctuations in traditional itinerant spin fluctuations theory. We can see that the intensity of this non-Fermi fluid scattering contribution, A, as well as the temperature region below which this fit is valid, T^*, both decrease with pressure. The pre-factor A in particular tends towards zero in agreement with XES and Raman. It is interesting to note that the fit validity region ends around 35 K, while the Raman measurements find no peak below 50 K. A very speculative hypothesis is that for some unknown reason fm fluctuations are gradually replaced by afm fluctuations at higher temperatures. This could be due to a ferromagnetic instability at low temperatures near the transition, although the non-Fermi liquid regime extends up to at least 30 GPa. Another possible explanation is due to entropic effects between competing

ground states and will be investigated further in our first-principles calculations. We would also like to attempt a prediction of the expected temperature dependence of resistivity when the spins fluctuate in intensity, rather than just direction. EXAFS and XMCD have not been reported for ϵ-iron below 300 K. A low-temperature EXAFS/XMCD study could help shed more information on the correlation of spin fluctuations in this region. Spin-resolved EXAFS is another technique which could be interesting, however the count rates are likely exorbitantly low.

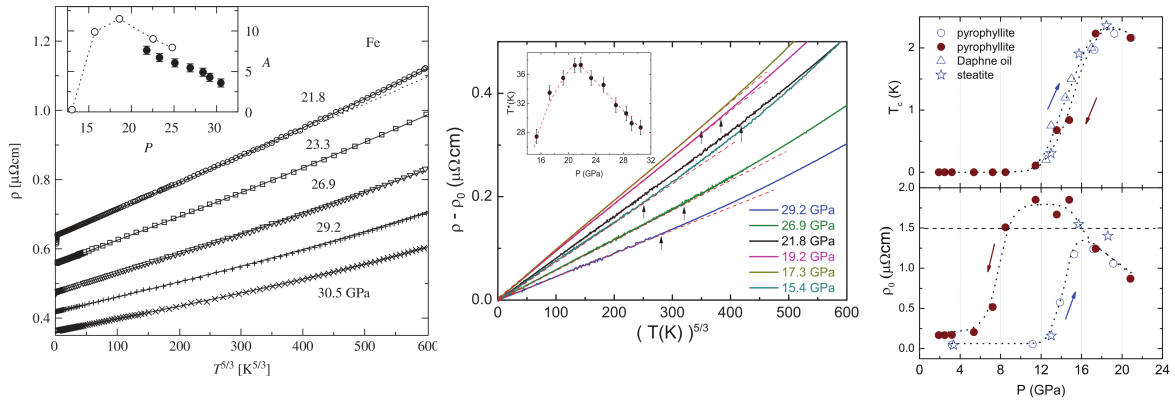

Figure IV.8: (Left) Transport measurements of ϵ-iron in the superconducting pressure region [161]. The inset shows the pressure dependence of the pre-factor A (see text for details). (Center) A different transport study where the inset shows T*, the validity range of the non-Fermi liquid fitting with $n = 5/3$ temperature dependence [162] (Right) Pressure-cycling dependence of T_c and residual resistivity ρ_0 from the same study.

In the background section (Sec. I.4.1), heavy fermion superconductors with ferromagnetism in their phase diagrams were introduced with the allusion that there could be a connection with pure iron. However, in the end it seems that pure iron is completely unrelated to heavy fermion superconductors. The magneto-structural phase transition in iron means that ferromagnetism does not seem to play a role in ϵ-iron. However, it is interesting that ϵ-iron's superconducting dome starts directly after the α-ϵ transition, which is a completely different behavior than in silicon [163, 164] which after the structural transition already has a finite T_c. This suggests that ferromagnetic impurities due to an α-iron minority are destroying the superconductivity directly after transition. Transport measurements are not done with best pressure transmitting mediums and it is reasonable that the minority phase is competing until the pressure of maximum T_c. The destruction of superconductivity due to these impurities, coupled with the pressure dependence of the spin fluctuations, would naturally explain the observed superconducting dome shape. A pressure-cycling transport study however finds very little hysteresis for T_c, contrary to the direction dependent transition behavior of the α-ϵ transition (Fig. IV.8) [162]. However, in the figure there is also presented a plausible explanation: the residual resistivity increases upon decompression due to cold working and the associated decrease in the mean free path of the electrons means that iron is no longer in the required clean limit. These considerations should be studied in more detail by performing pressure-cycling experiments with more hydrostatic pressure mediums and in-situ annealing of the sample.

Chapter V

Magnetism of compressed FeSe

The second compressed material I studied using XES and NPD was FeSe, whose pressure phase diagram is an incredible example of intertwined magnetic, nematic, and superconducting orders (Fig. V.1). The critical temperature shows a four-fold increase under compression and there are T_c anomalies where the superconducting and magnetic orders intersect. The high-pressure T_c anomaly at 7 GPa coincides with the loss of antiferromagnetic order, the maximum T_c, and a structural transition from a 2D layered structure to an environment with 3D connectivity, making it an ideal region to study the interplay between these orders.

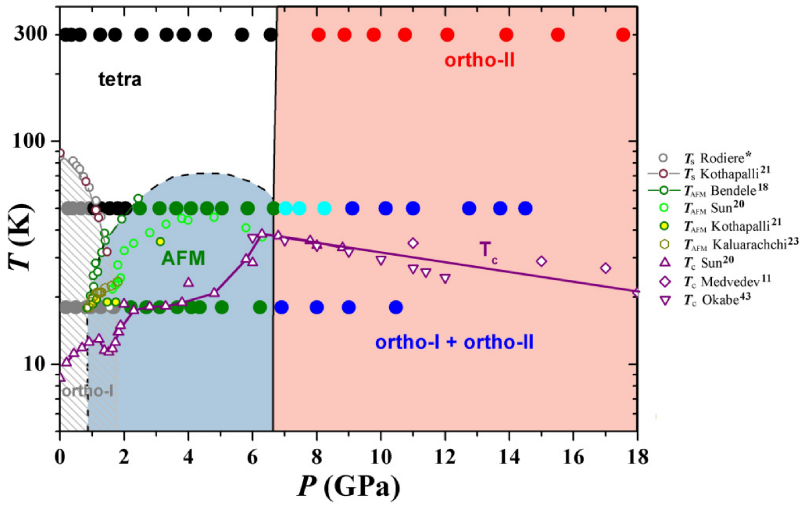

Figure V.1: The pressure-temperature phase diagram of FeSe [3]. The color of the large filled circles indicates their structure: black, tetragonal phase; gray, ortho-I phase; green, AFM phase; red, ortho-II phase; blue, a mixture of ortho-I and ortho-II phases; cyan, possible onset of the formation of the ortho-II phase. T_s is the ordering temperatures of nematicity-induced orthogonal structure, T_{AFM} the Néel temperature, and T_c the superconducting critical temperature.

V.1 Introduction

At ambient conditions there are two stable polymorphs of FeSe, a tetragonal PbO-type structure ($P4/nmm$) known as β-FeSe [165] and a hexagonal NiAs-type type structure ($P6_3/mmc$). We are interested in the tetragonal polymorph (referred to as simply FeSe in this thesis) since it belongs to the Fe-based superconductor family [166]. It is one of the few compounds in this family which exhibits superconductivity without long-range afm order at ambient conditions. Coupled with its simple 11 structure, which consists of solely FeSe "planes", this makes FeSe an ideal material to study superconductivity in FeSC. Its critical temperature is modified significantly with pressure with a non-monotonic increase from 8–9 K up to $\approx$ 37 K [167]. FeSe monolayers also show a significant increase of T_c up to 65–100 K [168, 169].

FeSe has a second-order transition below $\approx$ 1 GPa to an orthorhombic ($Cmma$) structure (delineated by T_s in Fig. V.1) which is driven by the appearance of nematic order as it is cooled [165]. FeSe does not have long-range afm order unlike other FeSCs, therefore certain studies claim the nematic order is driven by orbital order rather than spin fluctuations [170, 171]. However, there are some first-principle studies which predict spin fluctuations due to the degeneracy of the ground state [172]. This structure, which we refer to as ortho-I, continues to exist at low temperatures until around 7 GPa (see Fig. 1 in Sec. V.2), although its nature and orthorhombicity change [3]. Below T_N, muon spin-relaxation (μSR) spectroscopy find afm order with a small magnetic moment [173–175]. These measurements were below 2.4 GPa, although transport measurements follow its signature up to 6 GPa, above which it falls below T_c [176]. The existence of an afm dome in the middle of a superconducting "dome" is quite unique. The afm order is unknown although a μSR rotational study predicts either a collinear or bicollinear structure (Fig. V.2) [175]. The afm order coexists with superconductivity, although it is still unclear if they are distinctly separate phases or coexisting electronic orders in a single phase. The phase diagram shows an anti-correlation between afm ordering temperature, T_N, and superconducting critical temperature. There is a clear dip in the T_c at the onset of afm order around 1 GPa, while similarly at higher pressures the T_c increase coincides with the T_N decrease, which is subsequently followed by a decrease of T_c as the pressure in further increased. The final "decrease" is related to a structural transition discussed further below (in Sec. V.3 I argue that perhaps it is not decreasing). The first "T_c anomaly" at 1 GPa has been studied in detail and it is attributed to a reduction in the density of states due to a reconstruction of the Fermi surface [177], however the second anomaly has received much less attention.

Single-crystal x-ray diffraction has found that ortho-I has a first-order transition to a new structure above 7–8 GPa which we call ortho-II [3]. The ortho-I structure is pseudo-tetragonal and has the same layered structure as the ambient tetragonal form (Fig. V.3). On the other hand, ortho-II has a MnP-type structure ($Pnma$) which is dramatically different than ortho-I. The ortho-II phase has a 3D structure characterized by a network of face-sharing $FeSe_6$ octahedra, rather than the quasi-2D layer structure seen in ortho-I (Fig. V.3). The ortho-II structure can also be thought of as a distorted hexagonal NiAs-type arrangement ($P6_3/mmc$), which partly explains why previous diffraction studies on powders believed this phase was hexagonal. There is a 10% volume change during this first-order ortho-I to ortho-II transition which makes the transition destructive and irreversible.

The majority of magnetic probes, such μSR and NMR spectroscopy, have focused on

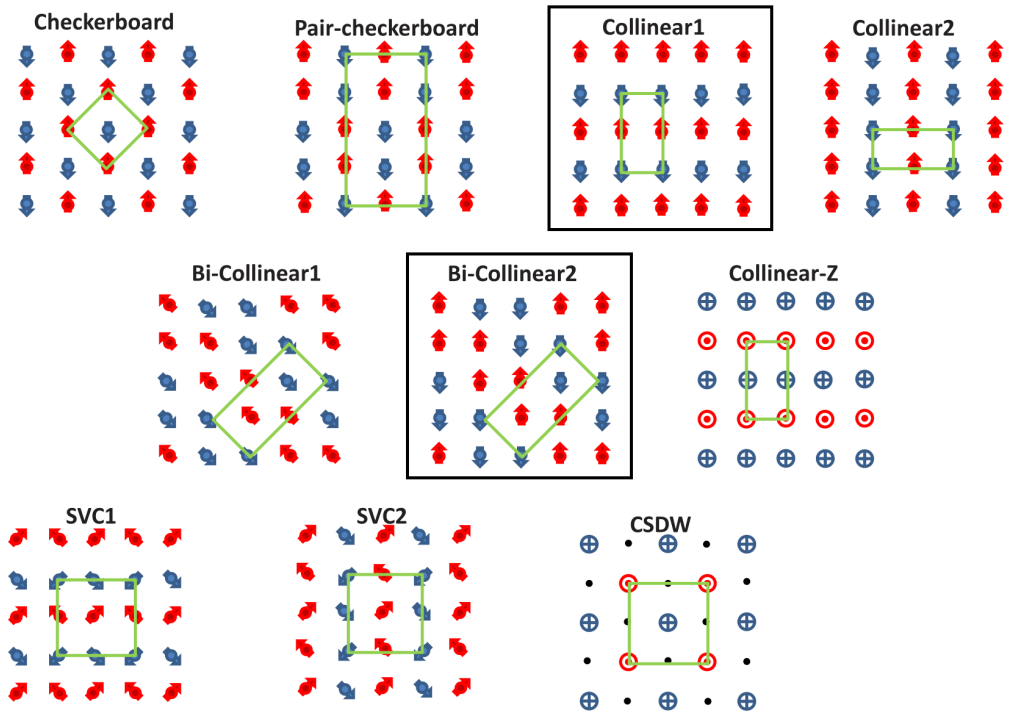

Figure V.2: Ten different afm magnetic orders that are possible for FeSe [175]. The Fe moments are shown in the Fe plane (Se above/below plane not shown) as red and blue arrows pointing in the plane and circles pointing out of the plane. The afm in-plane supercells are shown with a green rectangle. The moments can order ferromagnetically or antiferromagnetically along the c-axis for a total of 20 different configurations. The two (four including c-axis ordering) configurations which are supported by μSR studies, Collinear1 and Bi-Collinear2, are outlined in black [175].

the low-pressure T_c anomaly. Nonetheless, XES and Mössbauer spectroscopy have been performed at higher pressures, however they used polycrystalline, first-generation FeSe rather than high-quality single crystal FeSe. The XES results from two previous studies are shown in Fig. V.4 [178, 179]. The pressure dependence of the XES intensity[1] is very similar in the two cases with a fairly monotonic decrease with pressure, although they both show a small change change in slope near the structural transition. Kumar *et al.* and Chen *et al.* find the change at 6 GPa and 12 GPa respectively. Our results presented in Sec. V.2 show a completely different trend than these results. This discrepancy is discussed in our article and Sec. V.3. The Mössbauer spectra in Fig. V.5 (b) have an increased width above 7 GPa which the authors attribute to a new coexisting phase (thought to be hexagonal but now known to be ortho-II) [180]. This interpretation is puzzling since since recent x-ray diffraction sees an almost complete transformation at 10.5 GPa (Fig. V.5 (d)) [3]. This will be discussed in more detail in Sec. V.3, along with the transport results shown in this figure, where I present a speculation about nanoscale phase separation of the two orthorhombic phases during the

[1]Kumar *et al.* [178] used the integrated intensity of the satellite and Chen *et al.* [179] used the integrated absolute difference (IAD). See Sec. II.2.2 for a detailed discussion about the different XES techniques.

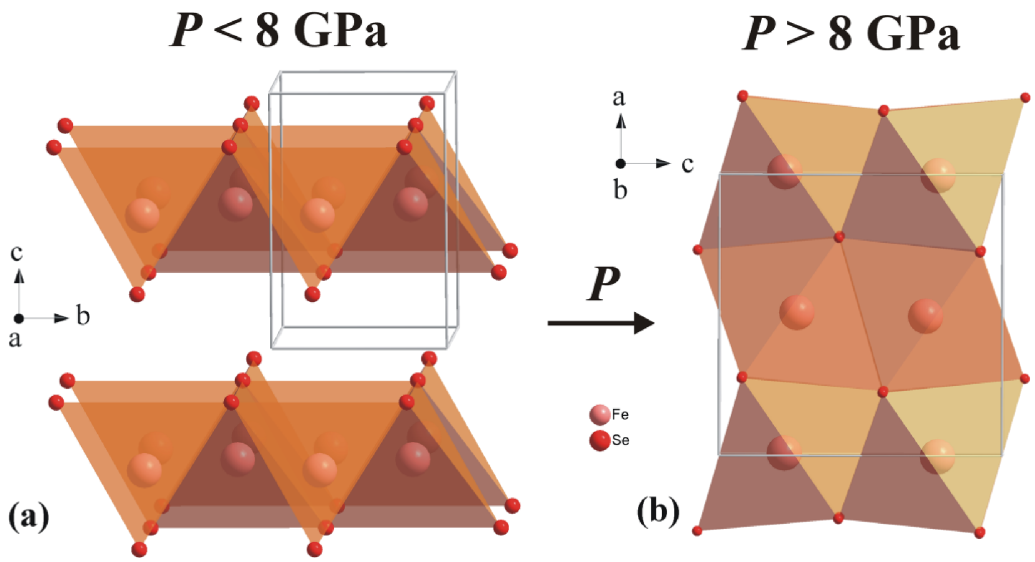

Figure V.3: Low-pressure and high-pressure phases of FeSe [3]. (a) The low-pressure phase has a tetragonal PbO-type ($P4/nmm$) structure and is composed of layers of edge-shared $FeSe_4$ tetrahedra. The low-pressure, low-temperature ortho-I phase ($Cmma$) is similar except for a slight orthorhombic distortion in the ab plane. (b) The high-pressure, MnP-type ortho-II structure ($Pnma$) is composed of chains of face-shared $FeSe_6$ octahedra. (Note the change of axes between the two figures).

transition.

In the next section our article is presented where we performed a high pressure XES and NPD study of FeSe. Completely opposite of previous reports, our XES measurements evidence a very clear low-spin to high-spin transition as FeSe is compressed. By measuring PFY-XAS as well at each pressure step, we find that this transition is concomitant with the ortho-I to ortho-II transition previously observed with low-temperature XRD [3]. A first-principles calculation of the high-pressure spectrum agrees qualitatively with the high-spin state observed by XES. These two states realize the recently predicted band-dependent Mottness in Fe-based superconductors and shed a new light on the interplay between structure, magnetism and superconductivity in these compounds. Our NPD results on the ortho-I phase is presented in the Supplementary Information of the article. We find more stringent upper limits than previous NPD studies which strongly suggest that the afm order has a Collinear1 configuration (Fig. V.2).

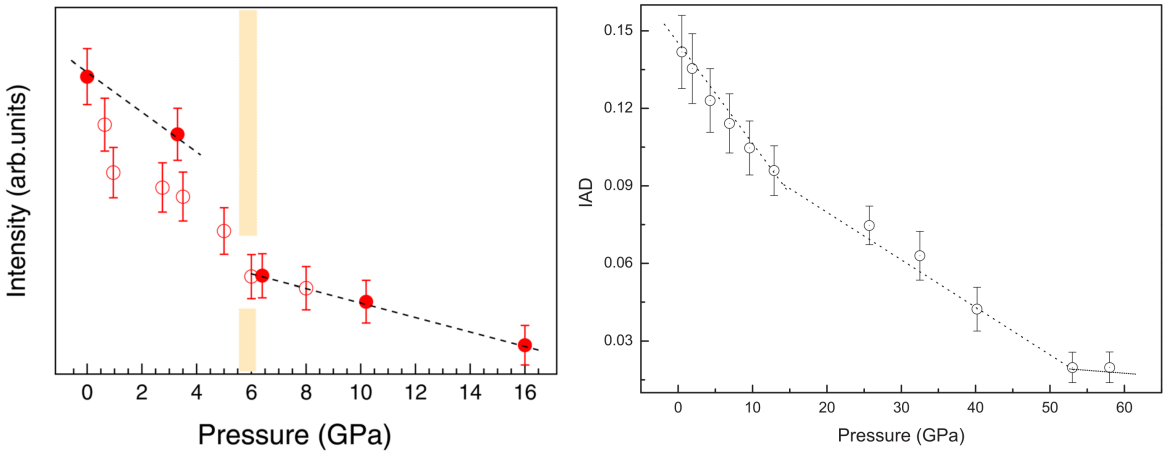

Figure V.4: X-ray emission spectroscopy (XES) studies of FeSe under pressure done in 2011. (left) The results of Kumar *et al.* [178] using integrated intensity, where measurements at 300 K are shown as closed red circles and at 8 K as open red circles. (right) Measurements from Chen *et al.* [179] at 300 K using integrated absolute difference (IAD).

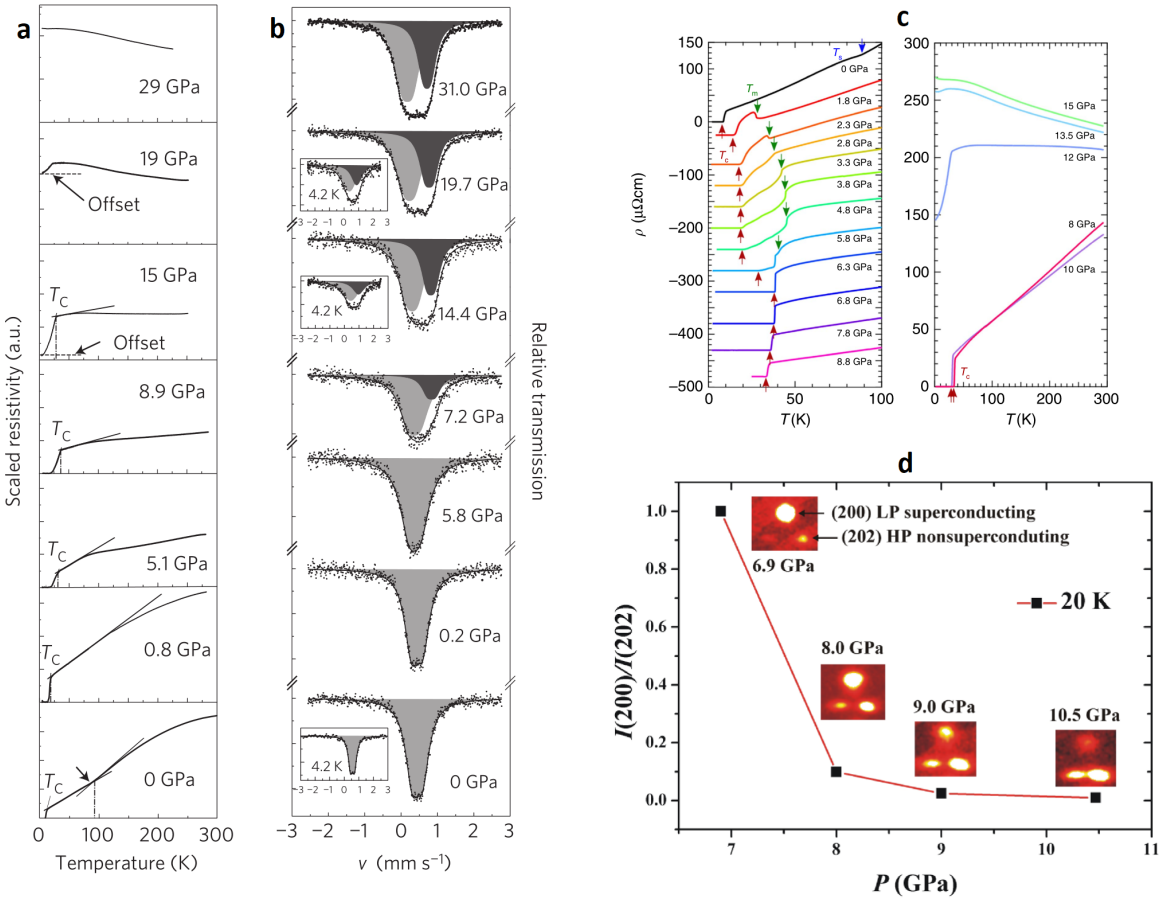

Figure V.5: High-pressure transport (a) and Mössbauer (b) measurements of polycrystalline FeSe from Medvedev *et al.* [180]. (c) Transport measurements by Sun *et al.* on high-quality single crystals [176]. (d) Estimation of ortho-I phase fraction from x-ray diffraction [3].

V.2 Article 3: Emergent high-spin state above 7 GPa in superconducting FeSe

Status: Submitted on 20 October 2017 - arXiv:1708.04805 [7]

Author contributions: The FeSe samples used in this study were grown and prepared by Pierre Toulemonde. The XES/XAS experiments were performed by Blair Lebert, Jean-Pascal Rueff, Pierre Toulemonde, Victor Balédent, and James Ablett. The XES/XAS data treatment was done by Blair Lebert with the aid of Jean-Pascal Rueff. The FDMNES simulations were performed by Blair Lebert, Jean-Pascal Rueff, and Victor Balédent. The NPD experiment was performed by Blair Lebert, Victor Balédent, Pierre Toulemonde, Stefan Klotz, Pierre Rodière, M Raba, and Thomas Hansen. The NPD data treatment was done by Blair Lebert with the aid of Pierre Toulemonde, Victor Balédent, and Stefan Klotz. The article was written by Blair Lebert with input principally from Jean-Pascal Rueff, Pierre Toulemonde, and Victor Balédent and minor comments from the other authors.

Emergent high-spin state above 7 GPa in superconducting FeSe

B. W. Lebert,[1,2] V. Balédent,[3] P. Toulemonde,[4,5] J. M. Ablett,[2]
S. Klotz,[1] T. Hansen,[6] P. Rodière,[4,5] M. Raba,[4,5] and J.-P. Rueff[2,7]

[1]*IMPMC-Sorbonne Universités, Université Pierre et Marie Curie, CNRS, IRD, MNHN 4, place Jussieu, 75252 Paris, France*

[2]*Synchrotron SOLEIL, L'Orme des Merisiers, BP 48 St Aubin, 91192 Gif sur Yvette*

[3]*Laboratoire de Physique des Solides, CNRS, Univ. Paris-Sud, Université Paris-Saclay 91405 Orsay cedex, France*

[4]*CNRS, Institut Néel, F-38000 Grenoble, France*

[5]*Université Grenoble-Alpes, Institut Néel, F-38000 Grenoble, France*

[6]*Institut Laue-Langevin, B.P. 156, 38042 Grenoble Cedex 9, France*

[7]*LCPMR-Sorbonne Universités, Université Pierre et Marie Curie, CNRS, 4 place Jussieu, 75252 Paris, France*

(Dated: November 17, 2017)

Abstract

The local electronic and magnetic properties of superconducting FeSe have been investigated by Kβ x-ray emission and simultaneous x-ray absorption spectroscopy at the Fe K-edge at high pressure and low temperature. Our results indicate a sluggish decrease of the local Fe spin moment under pressure up to 6–7 GPa, in line with previous reports, followed by a sudden increase at higher pressure that has gone unnoticed until now. The magnetic surge coincides with an abrupt change of the Fe local structure as observed by the decrease of the Fe-K pre-edge region intensity and corroborated by the simulations of the absorption spectra. This pressure corresponds to a structural transition, previously detected by x-ray diffraction, from the *Cmma* form to the denser *Pbnm* form with octahedral coordination of iron. Finally, the near-edge region of the x-ray absorption spectra shows a change before this transition at 5 GPa, corresponding well with the onset pressure of the previously observed enhancement of T_c. Our results emphasize the delicate interplay between structural, magnetic, and superconducting properties in FeSe under pressure.

PACS numbers: 74.25.-q,78.70.En,78.70.Dm

FeSe is the simplest form of the Fe superconductors (FeSC), yet one of the more fascinating members, as seen in its many overlapping phases and their apparent correlation with the superconducting critical temperature T_c (Fig. 1). Below 6–7 GPa, FeSe has a PbO-type tetragonal structure ($P4/nmm$) at ambient temperature which is slightly distorted to an orthorhombic structure ($Cmma$) [1] below the structural and magnetic transition temperatures (T_s and T_N). The low-temperature orthorhombic phase, denoted here as "ortho-I", is characterized by nematic order with two distinct origins: below T_s, it is a second-order structural transition driven by orbital order [2, 3]; while below T_N, it is a simultaneous first-order magneto-structural transition driven by stripe-type spin fluctuations [4–6]. Muon spin relaxation (μSR) [7–9] and nuclear forward scattering [6] find anti-ferromagnetic (AFM) order with a small magnetic moment in the 0.8–2.4 GPa range below T_N, although the exact type is unknown. Transport measurements show that this AFM order exists to at least 6.3 GPa [10]. Above 6–7 GPa, a structural transition is observed [11–14] to a MnP-type orthorhombic phase ($Pnma$ or equivalently $Pbnm$), denoted here as "ortho-II", with the Fe ion site symmetry changing from T_d to O_h. This transition was observed with ^{57}Fe Mössbauer spectroscopy above 7 GPa as an additional component in the spectrum, however no magnetic hyperfine splitting is observed at 4.2 K [15].

The superconducting critical temperature in FeSe shows drastic changes with pressure. After an initial increase, T_c dips at the onset of AFM order, which is attributed to a reduction in the density of states due to a reconstruction of the Fermi surface [16, 17]. Increasing the pressure further enhances both the magnetic and superconducting orders, with T_N reaching a maximum of 45–55 K [8, 10] at $\sim$ 4.2 GPa and T_c plateauing around 20 K below this pressure [10, 18]. Above this pressure magnetic order decreases and coincides with a sharp rise in T_c to a maximum around 37 K at $\sim$ 6.2 GPa [10, 12, 13, 15, 19]. After this maximum T_c has a discontinuous change from a positive to negative slope, coinciding with the transition to the ortho-II phase [11]. An AFM region in the middle of a superconducting "dome" is quite unique, and the phase diagram shows their intimate connection as two T_c anomalies where the two intersect. The low pressure anomaly in T_c evolution around 1 GPa has been thoroughly studied, however the high pressure one at 5–7 GPa has received relatively little attention, despite that fact that it is interesting due to the ortho-I $\rightarrow$ ortho-II transition in the same region. X-ray spectroscopy in the hard x-ray range is well-suited to investigate the local Fe properties in this pressure region [20]. In particular, Kβ ($3p \rightarrow 1s$ transition)

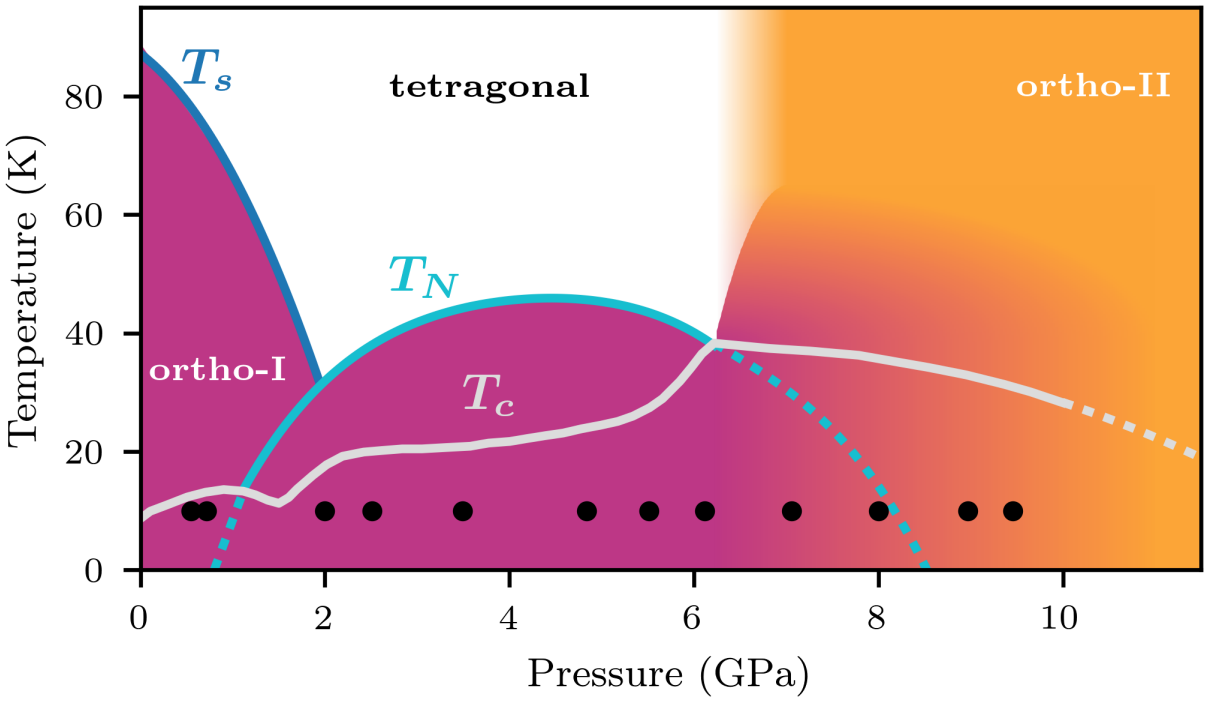

FIG. 1. Schematic P-T phase diagram of FeSe [10, 11]. Tetragonal (white), ortho-I (purple), and ortho-II (orange) structures are described in introduction. T_s, T_N and T_c are the structural, magnetic and superconducting transitions, with dashed lines represent extrapolations. P-T measurement points for XES/XAS are indicated with circles.

x-ray emission spectroscopy (XES) and x-ray absorption spectroscopy (XAS) at the K-edges are well-established probes of the local electronic, magnetic, and structural properties. As a primarily atomic probe, XES can access the local magnetic moment of a selected atom regardless of the magnetic order, while XAS provides a view of the local electronic and structural properties. In recent works [21, 22], Kumar *et al.* and Chen *et al.* have used XES to probe Fe magnetism in FeSe under high pressure. Their results show a decrease of the Fe spin state with a discontinuous change in slope near the ortho-I $\rightarrow$ ortho-II transition. This is interpreted as a high-spin (HS) to low-spin (LS) transition [21] or a state with a smaller magnetic moment [22]. However, as demonstrated in this Letter, the HS state is excluded at low pressures. Furthermore, their experiments were performed with polycrystalline samples including the hexagonal polymorph of FeSe (11% in the sample of Chen *et al.*) and at room temperature or only up to 8 GPa at 8 K for Kumar *et al.*. In this work, we perform a high-pressure study of FeSe single crystals at 10 K until 9.5 GPa using Fe-Kβ XES and XAS

at the Fe K-edge. Our results demonstrate a previously unobserved LS $\rightarrow$ HS transition that coincides with the onset of the ortho-II phase and maximum of T_c. More generally, they highlight the strong interplay between the structural, magnetic and superconducting properties in FeSe under pressure.

The XES/XAS experiment was performed on the GALAXIES beamline [23] at the SOLEIL synchrotron facility. We used high purity FeSe single crystals from the Institut Néel (Grenoble) grown by chemical vapor transport [24]. Pressure was applied using a membrane-driven diamond anvil cell equipped with 1.2 mm thick diamonds with 300 μm culets. Several FeSe single crystals were loaded in a 150 μm hole of a CuBe gasket, along with ruby chips for in-situ pressure measurement [25] and silicone oil as a pressure transmitting medium. XES/XAS were measured with the spectrometer in a transmission geometry using a 1-meter radius spherically bent Ge(620) crystal analyzer and an avalanche photodiode detector arranged in the Rowland circle geometry. The total energy resolution at the Fe Kβ line ($\sim$7057 eV, $\theta_B = 79°$) was 1.2 eV FWHM. The XES spectra were measured with 10 keV incident x-rays. The XAS spectra was measured using the partial-fluorescence yield (PFY) method with the spectrometer fixed to the Fe Kβ line. This technique leads to an intrinsic sharpening effect due to the shallower $3p$ core hole left in the final state with respect to the deeper $1s$ level [20].

Our XES spectra measured at 10 K are shown in Fig. 2 for increasing pressure up to 9.5 GPa. The spectra are aligned to the main peak at 7057 eV and normalized to the maximum intensity. There is a weak satellite located around -12 eV from the main line, which is well-established as a signature of the local magnetic moment [27]. The satellite can be seen more clearly by subtracting the zero-spin reference [26], FeS_2, as shown in the inset of Fig. 2. The fitted intensity of the satellite from the difference spectra is shown in Fig. 3 as red squares. FeSe exhibits a LS state with a gradually decreasing magnetic moment until 6 GPa, followed by a jump between 6–7 GPa to a HS state which plateaus around 9.5 GPa. The low-pressure behavior is consistent with previous results [21, 22] and is understood to be due to band structure effects in the compressed lattice, however the sudden increase around 7 GPa was previously unobserved. The onset pressure and coexistence region of this LS $\rightarrow$ HS transition coincides with the ortho-I $\rightarrow$ ortho-II transition at low temperature [11].

To gain insight on the Fe local structure, we also measured high-resolution XAS at each pressure point after each XES measurement. The series of PFY-XAS spectra taken at the

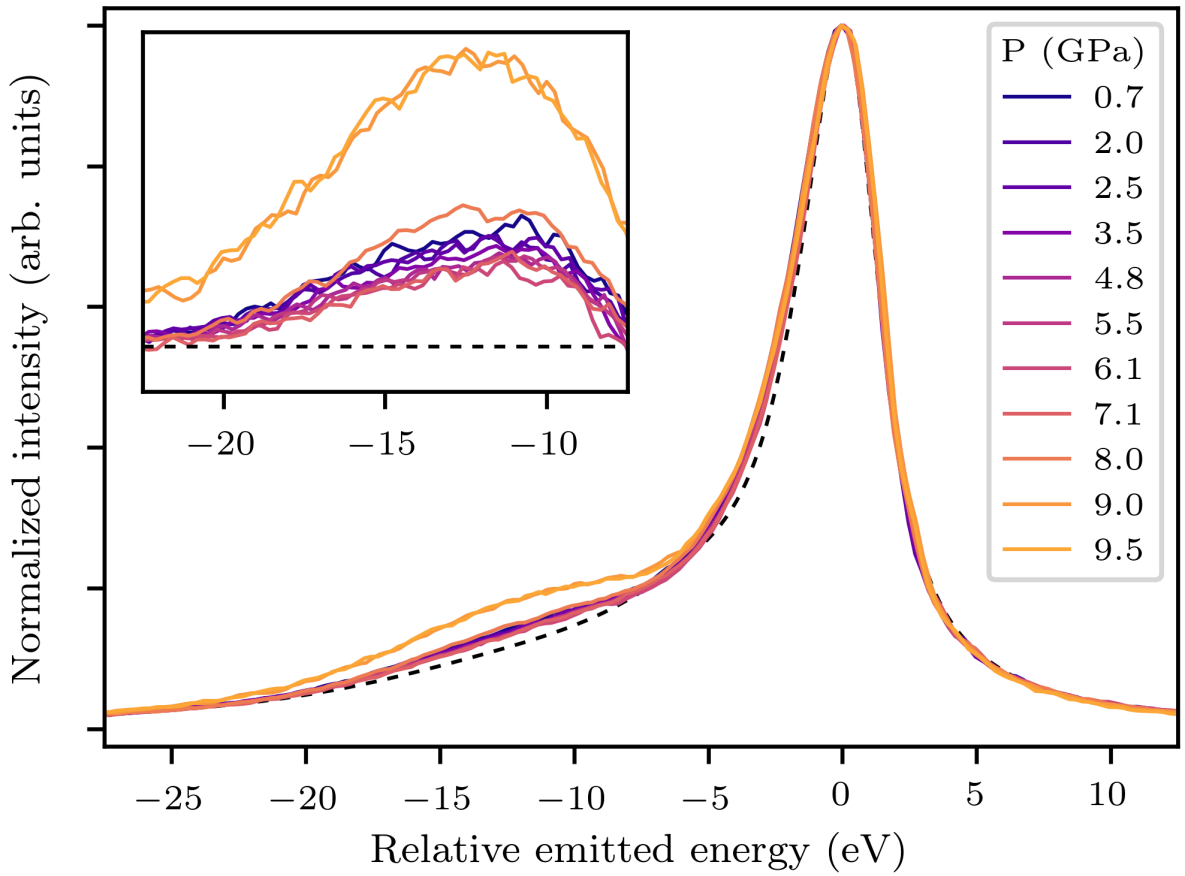

FIG. 2. Fe Kβ x-ray emission in FeSe as a function of pressure measured at 10 K. The inset is a zoom of the satellite region showing the difference with the FeS_2 zero-spin reference [26], shown as a black dashed line in the main plot.

same pressures as XES is shown in Fig. 4, where the inset emphasizes the pre-edge region. The spectra are normalized and flattened using the software ATHENA [28]. The pre-peak feature A in FeSe at low pressure is mainly due to the dipole transitions from Fe 1s to Fe 3d-Se 4p hybrid bands as expected in T_d symmetry, with a small contribution from Fe quadrupole $1s \rightarrow 3d$ transitions [22, 29–31]. Fe 3d-Se 4p hybridization is sensitive to the local geometry, therefore the pre-peak can be used to study the pressure evolution of the structure. To clarify its pressure dependence, it was fitted by a Gaussian lineshape after subtraction of a Victoreen background to account for the rising edge. This pre-edge area is shown as blue inverted triangles in Fig. 3 using the right scale and the label "XAS A". Under increasing pressure, the area slowly increases until 6–7 GPa, where it suddenly

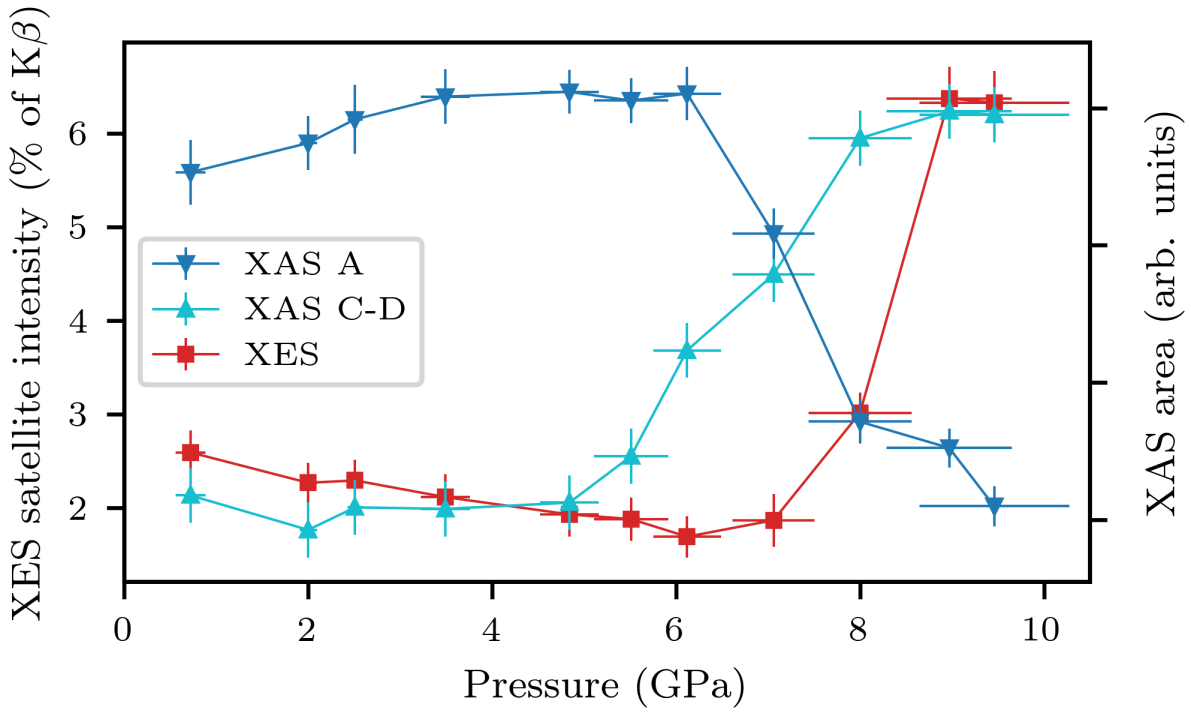

FIG. 3. Pressure dependence of XES and XAS spectra. (Left scale) Intensity of Kβ satellite shown as red squares. (Right scale) Area of the Fe pre-edge feature A shown as blue inverted triangles and area between XAS features C and D shown as cyan triangles (scaled and offset).

decreases, which is the same trend (albeit opposite direction) as the satellite intensity in XES. The decreased intensity is due to a reduced hybridization as the coordination of iron increases during the ortho-I (tetrahedral coordination) $\rightarrow$ ortho-II (octahedral coordination) transition [11]. The increased coordination is also supported by the change of the hyperfine splitting at high pressure [15]. The remarkable parallel evolution of the magnetic (XES) and structural (XAS) properties shows the interplay between the electronic and lattice degrees of freedoms. Moreover, The absorption features B, C, and D can be assigned as Fe dipole $1s \rightarrow 4p$ transitions, where C and D also have significant contribution from Fe $1s$ to Fe $4p$-Se $3d$ hybrid band transitions [22, 29–31]. The features at higher energies are dominated by multiple scattering of the photoelectron with the nearest neighbors. The feature around 7160 eV shows a clear shift (arrow in Fig. 4) supporting the change of local structure we see with the pre-peak. A significant spectral change is observed in the region between features C and D, even before the concomitant structural and magnetic transition. The change is shown in Fig. 3 (cyan triangles) by taking the area between C and D. The onset of the increased

intensity corresponds remarkably well with the sudden increase in T_c around 5 GPa [10]. The trend is continuous until the ortho-II dominant phase at 9.5 GPa, which puts into question the possible connection between ortho-II and superconductivity since ortho-II is not believed to support superconductivity [11] and a negative dρ/dT suggests it is semiconductor [10, 15].

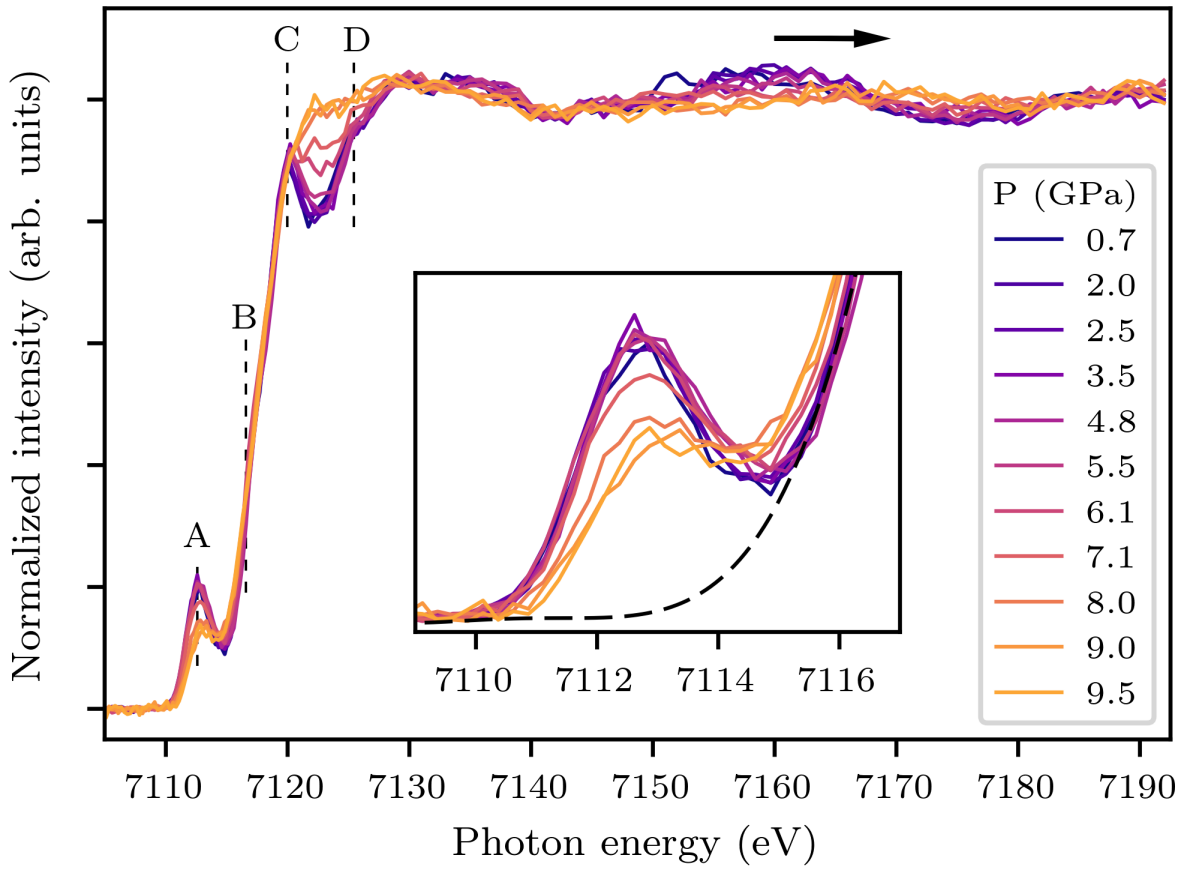

FIG. 4. Partial-fluorescence yield x-ray absorption at the Fe K-edge in FeSe as a function of pressure measured at 10 K. The inset is a zoom of the pre-edge region, with the Victoreen background (at 0 GPa) shown with dashed line.

To further understand the structural and electronic transitions, the XAS spectra were simulated using the FDMNES code [32]. A cluster radius of 12 Å (10 Å) for the low-pressure (high-pressure) reached full convergence. Spin-orbit coupling was included by relativistic effect corrections and the Fermi level was set self-consistently [33]. The crystal structures were taken from Ref. [1] for the low-pressure ortho-I phase and from Ref. [14] for the high-pressure ortho-II phase. To simulate the pressure-induced spin-state transition, the calculations in

the orthoII phase were carried out using either a LS or a HS ground state configuration. The results are shown in Fig. 5 along with the experimental spectra measured at 0.7 GPa and 9.5 GPa. We do not expect to yield an accurate description of the d electronic structure in absence of correlations — more accurate approaches do show that many-body correlations lead to a renormalization of the d bands and changes of the d density of states close to the Fermi edge [34] — but the K-edge should be well-described since it mostly connects to a single particle picture. Indeed, the low-pressure spectrum is reproduced well in the pre-edge and near-edge regions, while calculations for the high-pressure spectrum reproduces well the near-edge, however it finds a pre-edge that is too intense. The deviation in the pre-edge region from the experiment is more pronounced in the LS configuration, whereas in the HS configuration the pre-edge is flattened and yields a better agreement with the experimental data. The less-pronounced pre-peak is consistent with high-spin Fe^{II} in an octahedral environment [35]. This agrees with our XES results that there is a transition to a high-spin state above 7 GPa at 10 K in FeSe.

The main outcome of our study is the original observation of a high-spin state above 7 GPa as FeSe adopts the ortho-II phase. This follows the initial decrease of the local moment in the ortho-I phase which has been reported elsewhere [21, 22] and confirmed here. Both XAS and XES indicate that the magnetic surge at high pressure is consistent with a pressure-induced LS to HS transition. The electronic change is likely resulting from the change of Fe site symmetry: in the ortho-I phase, Fe occupies a tetrahedral (T_d) site that becomes increasingly distorted with pressure whereas Fe sits in an octahedral (O_h) site in the ortho-II phase [11–13]. At first glance, the spin state of FeSe is surprising. According to ligand field theory, one would expect Fe to be high-spin in the ortho-I phase since tetrahedral coordination normally favors a high-spin state. However, the iron superconductor's electronic structure was also shown to be controlled by the correlated and specific "Mottness" of d electrons with band-dependent correlations yielding e_g states less correlated than t_{2g} states [36]. We suggest that the T_d low-spin state is stabilized because it minimizes the on-site electron correlations by filling preferentially the e_g bands. At high pressure, correlation becomes less effective as the band width broadens which eventually allows a high-spin configuration as the Fe symmetry turns O_h. That the spin state transition coincides with the structural transition and T_c slope change demonstrates the strong interplay between electronic and lattice degrees of freedom in FeSe.

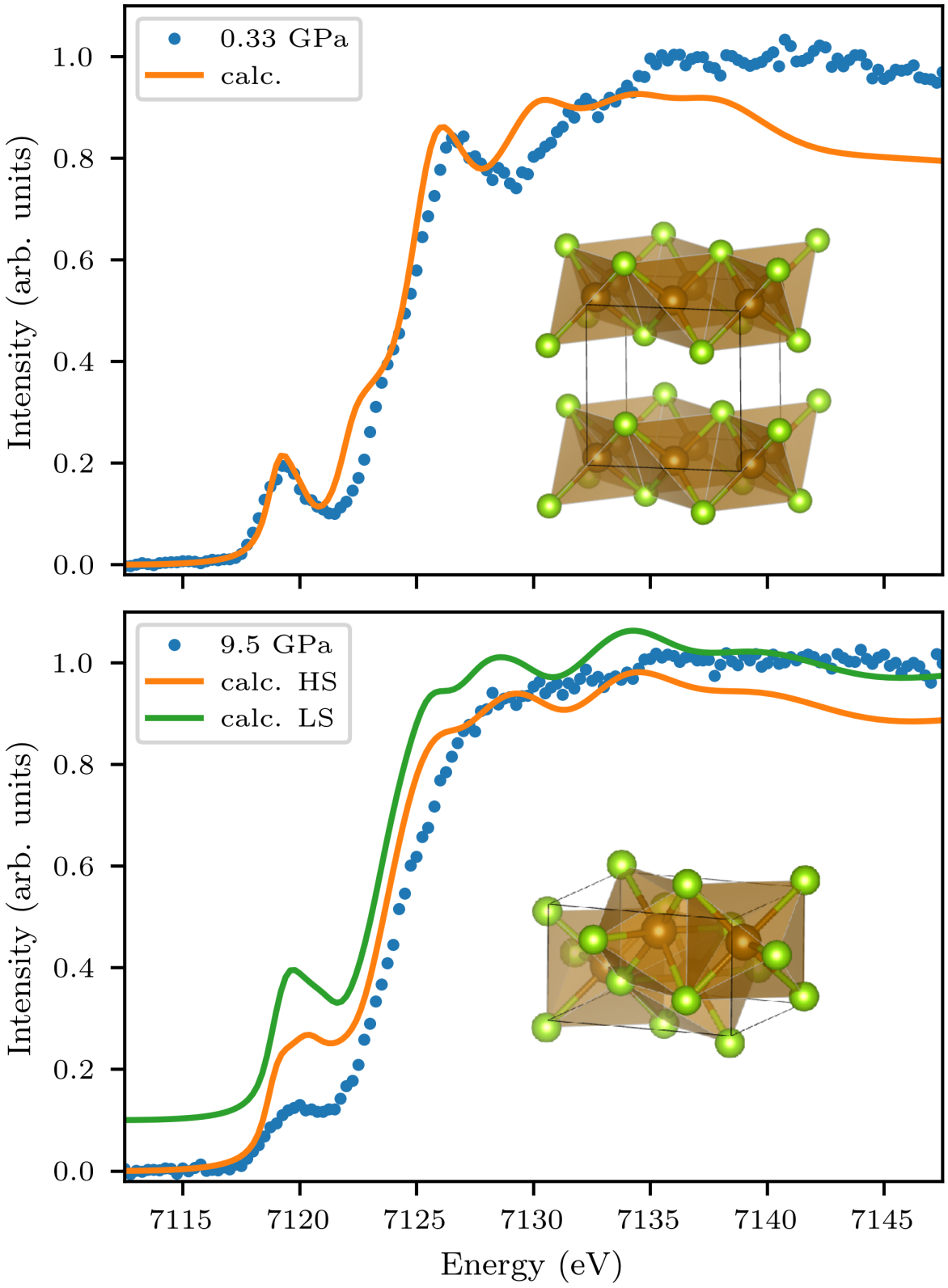

FIG. 5. Calculated XAS spectra (solid lines) at the Fe K-edge in FeSe in the ortho-I (top panel) and ortho-II phases (bottom panel). The insets illustrate the tetrahedral and octahedral symmetry of the Fe site in the ortho-I and ortho-II phase respectively. The experimental data at 0.7 and 9.5 GPa are displayed with solid circles. Low-spin (LS) and high-spin (HS) state configurations were

We lack here the knowledge of the magnetic order as x-ray spectroscopy are local probes. We performed neutron powder diffraction until ∼12 GPa, yet did not detect a significant amount of the ortho-II phase in order to search for magnetic order (see Supplemental Material). This calls for neutron powder diffraction at even higher pressures, which was shown to be feasible to at least 20 GPa at low temperatures [37].

We acknowledge SOLEIL for provision of synchrotron radiation facilities (proposal 201511119) and help from the high pressure laboratory for cell loading. We acknowledge ILL for provision of neutron facilities (proposal 5-31-2517 [38]). We acknowledge P. Strobel and S. Karlsson from Institut Néel, Grenoble, France, for their help in the growth of the FeSe crystals using the CVT method. B.W.L acknowledges financial support from the French state funds managed by the ANR within the "Investissements d'Avenir" programme under reference ANR-11-IDEX-0004-02, and within the framework of the Cluster of Excellence MATISSE led by Sorbonne Université and from the LLB/SOLEIL PhD fellowship program. Sample synthesis and preparation was done by P.T. The XES/XAS experiment was performed by B.W.L, J.P.R, P.T, V.B, and J.M.A. The XES/XAS data treatment was done by B.W.L and J.P.R. The NPD experiment was performed by B.W.L, V.B, P.T, S.K, P.R, M.R, and T.H. The NPD data was treated by B.W.L, P.T, and V.B. The FDMNES simulations were performed by V.B, J.P.R, and B.W.L. The paper was written by B.W.L, J.P.R, P.T, V.B, and J.M.A.

[1] S. Margadonna, Y. Takabayashi, M. T. McDonald, K. Kasperkiewicz, Y. Mizuguchi, Y. Takano, A. N. Fitch, E. Suard, and K. Prassides, Chem. Commun. , 5607 (2008).

[2] S.-H. Baek, D. V. Efremov, J. M. Ok, J. S. Kim, J. van den Brink, and B. Büchner, Nat. Mater. **14**, 210 (2015).

[3] P. Massat, D. Farina, I. Paul, S. Karlsson, P. Strobel, P. Toulemonde, M.-A. Méasson, M. Cazayous, A. Sacuto, S. Kasahara, T. Shibauchi, Y. Matsuda, and Y. Gallais, Proc. Natl. Acad. Sci. **113**, 9177 (2016).

[4] Q. Wang, Y. Shen, B. Pan, Y. Hao, M. Ma, F. Zhou, P. Steffens, K. Schmalzl, T. R. Forrest, M. Abdel-Hafiez, X. Chen, D. A. Chareev, A. N. Vasiliev, P. Bourges, Y. Sidis, H. Cao, and J. Zhao, Nat. Mater. **15**, 159 (2016).

[5] P. S. Wang, S. S. Sun, Y. Cui, W. H. Song, T. R. Li, R. Yu, H. Lei, and W. Yu, Phys. Rev. Lett. **117**, 237001 (2016).

[6] K. Kothapalli, A. E. Böhmer, W. T. Jayasekara, B. G. Ueland, P. Das, A. Sapkota, V. Taufour, Y. Xiao, E. Alp, S. L. Bud'ko, P. C. Canfield, A. Kreyssig, and A. I. Goldman, Nat. Comm. **7**, 12728 (2016).

[7] M. Bendele, A. Amato, K. Conder, M. Elender, H. Keller, H.-H. Klauss, H. Luetkens, E. Pomjakushina, A. Raselli, and R. Khasanov, Phys. Rev. Lett. **104**, 087003 (2010).

[8] M. Bendele, A. Ichsanow, Y. Pashkevich, L. Keller, T. Strässle, A. Gusev, E. Pomjakushina, K. Conder, R. Khasanov, and H. Keller, Phys. Rev. B **85**, 064517 (2012).

[9] R. Khasanov, Z. Guguchia, A. Amato, E. Morenzoni, X. Dong, F. Zhou, and Z. Zhao, Phys. Rev. B **95**, 180504 (2017).

[10] J. P. Sun, K. Matsuura, G. Z. Ye, Y. Mizukami, M. Shimozawa, K. Matsubayashi, M. Yamashita, T. Watashige, S. Kasahara, Y. Matsuda, J. Q. Yan, B. C. Sales, Y. Uwatoko, J. G. Cheng, and T. Shibauchi, Nat. Comm. **7**, 12146 (2016).

[11] V. Svitlyk, M. Raba, V. Dmitriev, P. Rodière, P. Toulemonde, D. Chernyshov, and M. Mezouar, Phys. Rev. B **96**, 014520 (2017).

[12] G. Garbarino, A. Sow, P. Lejay, A. Sulpice, P. Toulemonde, M. Mezouar, and M. Nunez-Regueiro, EPL **86**, 27001 (2009).

[13] S. Margadonna, Y. Takabayashi, Y. Ohishi, Y. Mizuguchi, Y. Takano, T. Kagayama, T. Nakagawa, M. Takata, and K. Prassides, Phys. Rev. B **80**, 064506 (2009).

[14] R. S. Kumar, Y. Zhang, S. Sinogeikin, Y. Xiao, S. Kumar, P. Chow, A. L. Cornelius, and C. Chen, J. Phys. Chem. B **114**, 12597 (2010).

[15] S. Medvedev, T. M. McQueen, I. A. Troyan, T. Palasyuk, M. I. Eremets, R. J. Cava, S. Naghavi, F. Casper, V. Ksenofontov, G. Wortmann, and C. Felser, Nat. Mater. **8**, 630 (2009).

[16] T. Terashima, N. Kikugawa, A. Kiswandhi, D. Graf, E.-S. Choi, J. S. Brooks, S. Kasahara, T. Watashige, Y. Matsuda, T. Shibauchi, T. Wolf, A. E. Böhmer, F. Hardy, C. Meingast, H. v. Löhneysen, and S. Uji, Phys. Rev. B **93**, 094505 (2016).

[17] T. Terashima, N. Kikugawa, S. Kasahara, T. Watashige, Y. Matsuda, T. Shibauchi, and S. Uji, Phys. Rev. B **93**, 180503 (2016).

[18] K. Miyoshi, K. Morishita, E. Mutou, M. Kondo, O. Seida, K. Fujiwara, J. Takeuchi, and

S. Nishigori, J. Phys. Soc. Jpn. **83**, 013702 (2014).

[19] D. Braithwaite, B. Salce, G. Lapertot, F. Bourdarot, C. Marin, D. Aoki, and M. Hanfland, J. Phys.: Condens. Matter **21**, 232202 (2009).

[20] J.-P. Rueff and A. Shukla, Rev. Mod. Phys. **82**, 847 (2010).

[21] R. S. Kumar, Y. Zhang, Y. Xiao, J. Baker, A. Cornelius, S. Veeramalai, P. Chow, C. Chen, and Y. Zhao, Appl. Phys. Lett. **99**, 061913 (2011).

[22] J. M. Chen, S. C. Haw, J. M. Lee, T. L. Chou, S. A. Chen, K. T. Lu, Y. C. Liang, Y. C. Lee, N. Hiraoka, H. Ishii, K. D. Tsuei, E. Huang, and T. J. Yang, Phys. Rev. B **84**, 125117 (2011).

[23] J.-P. Rueff, J. M. Ablett, D. Céolin, D. Prieur, T. Moreno, V. Balédent, B. Lassalle, J. E. Rault, M. Simon, and A. Shukla, J. Synchrotron Rad. **22**, 175 (2015).

[24] S. Karlsson, P. Strobel, A. Sulpice, C. Marcenat, M. Legendre, F. Gay, S. Pairis, O. Leynaud, and P. Toulemonde, Supercond. Sci. Technol. **28**, 105009 (2015).

[25] A. Dewaele, M. Torrent, P. Loubeyre, and M. Mezouar, Phys. Rev. B **78**, 104102 (2008).

[26] J. F. Lin, H. Watson, G. Vankó, E. E. Alp, V. B. Prakapenka, P. Dera, V. V. Struzhkin, A. Kubo, J. Y. Zhao, C. McCammon, and W. J. Evans, Nat. Geosci. **1**, 688 (2008).

[27] G. Peng, F. M. F. de Groot, K. Hämäläinen, J. A. Moore, X. Wang, M. M. Grush, J. B. Hastings, D. P. Siddons, W. H. Amstrong, O. C. Mullins, and S. P. Cramer, J. Am. Chem. Soc. **116**, 2914 (1994).

[28] B. Ravel and M. Newville, J. Synchrotron Rad. **12**, 537 (2005).

[29] J. M. Chen, S. C. Haw, J. M. Lee, S. A. Chen, K. T. Lu, M. J. Deng, S. W. Chen, H. Ishii, N. Hiraoka, and K. D. Tsuei, J. Chem. Phys **137**, 244702 (2012).

[30] M. Bendele, C. Marini, B. Joseph, L. Simonelli, P. Dore, S. Pascarelli, M. Chikovani, E. Pomjakushina, K. Conder, N. L. Saini, and P. Postorino, J. Phys.: Condens. Matter **25**, 425704 (2013).

[31] B. Joseph, A. Iadecola, L. Simonelli, Y. Mizuguchi, Y. Takano, T. Mizokawa, and N. L. Saini, J. Phys.: Condens. Matter **22**, 485702 (2010).

[32] S. A. Guda, A. A. Guda, M. A. Soldatov, K. A. Lomachenko, A. L. Bugaev, C. Lamberti, W. Gawelda, C. Bressler, G. Smolentsev, A. V. Soldatov, and Y. Joly, J. Chem. Theory Comput. **11**, 4512 (2015).

[33] O. Bunău and Y. Joly, J. Phys.: Condens. Matter **21**, 345501 (2009).

[34] M. Aichhorn, S. Biermann, T. Miyake, A. Georges, and M. Imada, Phys. Rev. B **82**, 064504

(2010).

[35] T. E. Westre, P. Kennepohl, J. G. DeWitt, B. Hedman, K. O. Hodgson, and E. I. Solomon, Journal of the American Chemical Society **119**, 6297 (1997).

[36] L. de' Medici, G. Giovannetti, and M. Capone, Phys. Rev. Lett. **112**, 177001 (2014).

[37] S. Klotz, T. Strässle, B. Lebert, M. d'Astuto, and T. Hansen, High Press. Res. **36**, 73 (2016).

[38] P. Toulemonde, L. Amand, V. Balédent, T. Hansen, S. Klotz, B. W. Lebert, M. Raba, and P. Rodière, (2017), 10.5291/ill-data.5-31-2517.

Supplemental Material for "Emergent high-spin state above 7 GPa in superconducting FeSe"

B.W. Lebert, V. Balédent, P. Toulemonde, J. M. Ablett,
S. Klotz, T. Hansen, P. Rodière, M. Raba, and J.-P. Rueff

Neutron powder diffraction study of FeSe

Neutron powder diffraction (NPD) is complementary to the local probes XES/XAS, since it is sensitive to magnetic order. The NPD experiment was performed on the high-flux diffractometer D20 [1] at the Institut Laue-Langevin. Thermal neutrons of $\lambda = 2.414$ Å were produced by reflection from a pyrolitic graphite HOPG (002) monochromator at a take-off angle of 42° with a HOPG filter on the incident beam. Pressure was produced using a VX5 Paris-Edinburgh high pressure cell [2], toroidal cBN anvils, and null-scattering TiZr gaskets with an inner set of encapsulating hemispheres. Single crystals from the same batch as the XES/XAS experiments were crushed into a powder and loaded into the hemispheres with Pb as the pressure standard and deuterated 4:1 methanol-ethanol as the pressure transmitting medium.

NPD patterns were measured up to ∼12 GPa and from 300 K down to 6.5 K [3]. Unfortunately we did not observe clearly the ortho-I → ortho-II transition (because the sample signal becomes very weak above 10 GPa and the conversion of ortho-I phase was insufficient) and therefore could not characterize the magnetic order of the ortho-II phase. This is likely due to the radically different pressure medium, pressure device, and P-T path. Here we focus on NPD patterns measured with high statistics at 4.5 GPa and 7.8 GPa after cooling down to 6.5 K. Our measurement at 4.5 GPa, which corresponds with the maximum T_N of the pressure-induced AFM phase, is shown in Fig. 1 and a zoom of its low-2θ region where the most intense magnetic peaks are expected is shown in Fig. 2.

A whole-pattern Rietveld refinement was performed (shown in black) with the ortho-I FeSe and Pb phases using FULLPROF [4] and then the parameters were fixed in order to test different possible AFM configurations (shown in blue in Fig. 2). The ortho-I (001) nuclear reflection is visible as well as a ferrimagnetic peak due to a <5% contamination from hexagonal FeSe. Using the notation of Khasanov et al. [5], we tested the Collinear1 (CI/CII) and Bi-collinear2 (BI/BII) types of AFM structures, where the Roman numeral I and II correspond to without and with AFM coupling along the c-axis. Fig. 2 shows the

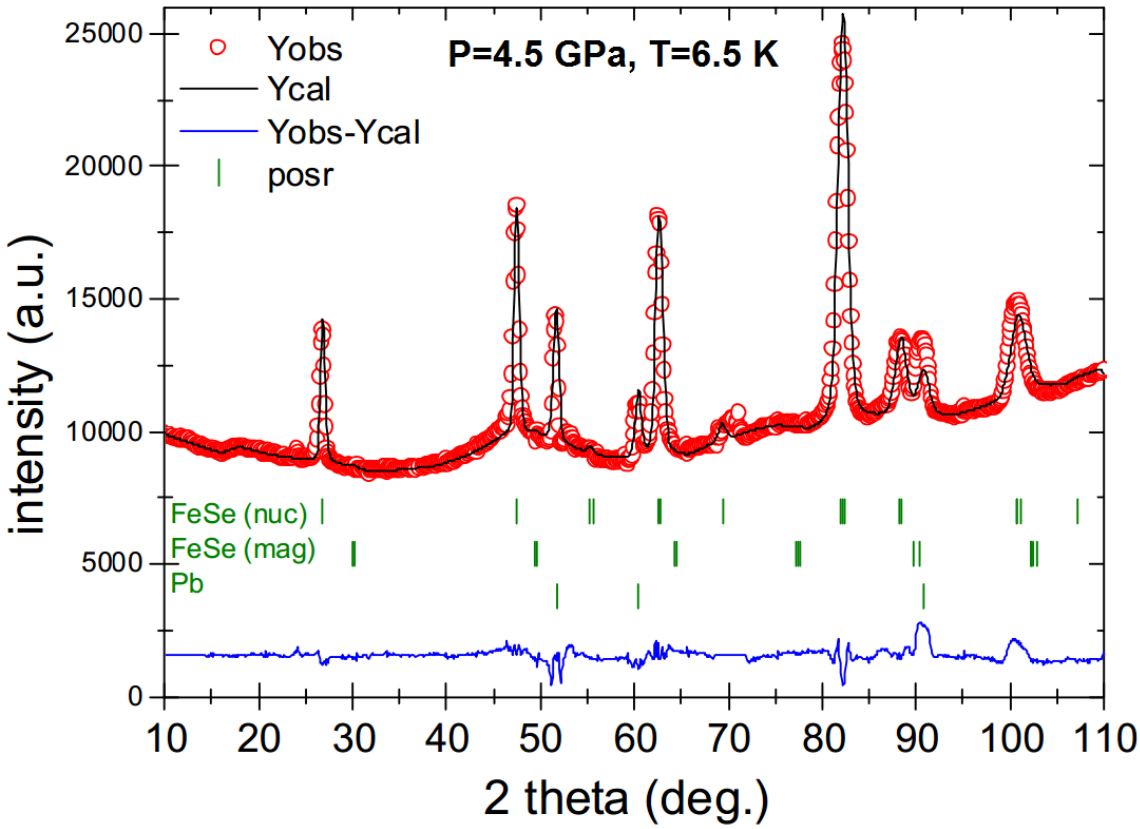

Figure 1: Neutron powder diffraction pattern of FeSe at 6.5 K and 4.5 GPa. FeSe (mag) is representing the Collinear1-II structure (see text for details).

calculated pure magnetic peaks in the low-2θ range with our suggested upper limit for the magnetic moment of 0.3 μ_B for CI/II and 0.2 μ_B for BI/II. Extrapolations from μSR [6] predict a moment of $\sim$0.35 μ_B. A moment of this magnitude should be visible in our data for the Bi-collinear2 AFM configurations, however it is not visible. Therefore our results indicate a Collinear1 AFM structure for this pressure-induced AFM phase present in the 0.8 GPa-6 GPa range. This is the same type of AFM structure as in other FeAs-based FeSCs. No magnetic peak was observed at 7.8 GPa and the upper limits were $\sim$0.1 μ_B higher due to reduced statistics. Finally, difference patterns taken between 6.5 K and 300 K at both pressures show no indication of long-range order.

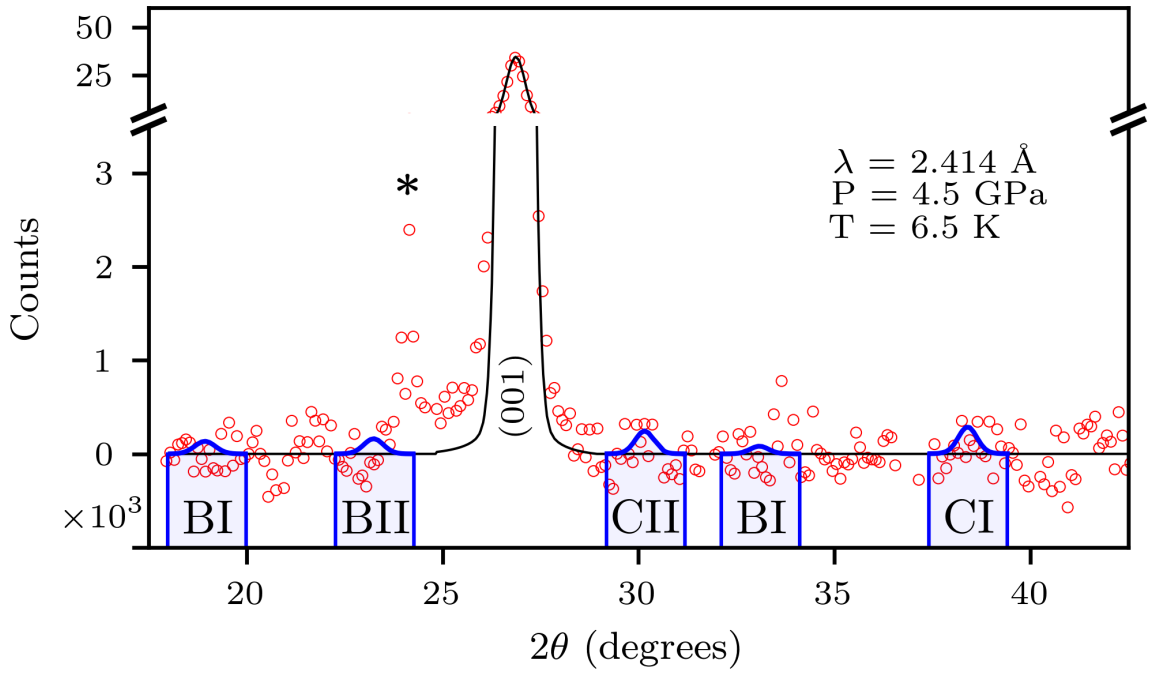

Figure 2: Low-2θ portion of neutron powder diffraction pattern on FeSe at 6.5 K and 4.5 GPa with smooth polynomial background removed. The data is shown as open red circles, Rietveld refinement in black, and AFM simulations in blue (see text for details). A ferrimagnetic peak due to contamination from hexagonal FeSe is shown with an asterisk.

References

[1] T. C. Hansen, P. F. Henry, H. E. Fischer, J. Torregrossa & P. Convert; "The D20 instrument at the ILL: a versatile high-intensity two-axis neutron diffractometer;" Meas. Sci. Technol. **19**, p. 034001 (2008). doi:10.1088/0957-0233/19/3/034001.

[2] S. Klotz; *Techniques in High Pressure Neutron Scattering* (Taylor & Francis) (2016); ISBN 9781138199217.

[3] P. Toulemonde, L. Amand, V. Balédent, T. Hansen, S. Klotz, B. W. Lebert, M. Raba & P. Rodière; "High pressure magnetic phases of the pressure - temperature phase diagram of FeSe;" (2017). doi:10.5291/ill-data.5-31-2517.

[4] J. Rodríguez-Carvajal; "Recent advances in magnetic structure determination by

neutron powder diffraction;" Physica B **192**, pp. 55–69 (1993). doi:10.1016/0921-4526(93)90108-I.

[5] R. Khasanov, Z. Guguchia, A. Amato, E. Morenzoni, X. Dong, F. Zhou & Z. Zhao; "Pressure-induced magnetic order in FeSe: A muon spin rotation study;" Phys. Rev. B **95**, p. 180504 (2017). doi:10.1103/PhysRevB.95.180504.

[6] M. Bendele, A. Ichsanow, Y. Pashkevich, L. Keller, T. Strässle, A. Gusev, E. Pomjakushina, K. Conder, R. Khasanov & H. Keller; "Coexistence of superconductivity and magnetism in $FeSe_{1-x}$ under pressure;" Phys. Rev. B **85**, p. 064517 (2012). doi:10.1103/PhysRevB.85.064517.

V.3 Discussion & perspectives

Our XES results are completely different than the previous results of Kumar *et al.* and Chen *et al.* (Fig. V.4). If we compare the experiments there are four key differences between them we should consider, listed in order of my believed importance:

- *Form*: Our sample was single crystals, while previous studies used a powder.
- *Quality*: Significant improvements were made in FeSe sample quality after 2011 by the perfection of the chemical vapor transport synthesis technique for FeSe.
- *Pressure medium*: Chen *et al.* used silicone oil as well, while Kumar *et al.* used helium as the pressure transmitting medium.
- *Temperature*: The measurements presented in our article are taken at 10 K. Previous results were measured at 300 K with the exception of P $\leq$ 8 GPa in Kumar *et al.* were also measured at 8 K.

Starting from the bottom of the list, I don't believe temperature plays a large role because we know that XES is measuring the occupation and should be relatively temperature-independent (like ϵ-iron results). Actually, we have performed XES at room temperature, but the results were not published since we did could not go very high in pressure due to a small leak in the diamond anvil cell's membrane (Fig. V.6). When these results are scaled to match our plot in the article we see the start of the low-spin to high-spin transition, therefore temperature cannot explain the discrepancy with previous results. Before discussing the three other differences, it is interesting to note the small increase in XES intensity from 0.8–1.5 GPa. This is the same pressure region as the low-pressure T_c anomaly when afm order appears, therefore it seems that XES is sensitive to the Fermi surface reconstruction. This was not observed in our XES measurements at 10 K shown in the article since we jump from 0.7 GPa to 2.0 GPa directly.

The pressure medium does not seem important since Chen *et al.* used silicone oil as well. The sample quality could be a large factor, however it is difficult to be certain. FeSe single crystals are plaquette-shaped, where the *ab*-plane (i.e. Fe-layers) of the tetragonal phase form the large flat surface and the *c*-axis is parallel to the surface normal. Therefore, the sample shape could play a major role since the DAC compression axis was parallel to the *c*-axis. As the pressure medium became less hydrostatic there would be an increased uniaxial force compressing the *c*-axis and squeezing the FeSe planes together. To be certain if the shape or quality was more important, a high-quality single crystal could be ground into a powder and measured in a DAC with XES. If we find the same XES results then we confirm that sample quality was the problem of past XES experiments. We performed neutron *powder* diffraction with FeSe crystals of identical quality, however we only observed a 10% conversion of ortho-I to ortho-II. We went to pressures well above what was needed with XES for a complete conversion, which leads me to believe that the form (powder versus single crystal) is the leading explanation for why this transition was not observed in previous XES experiments.

The Mössbauer results of Mevedev *et al.* [180] shown in Fig. V.5 are interesting since they show an identical ortho-I/"hexagonal" ratio from 15 GPa to 31 GPa. This could be again an issue due to using a powder, or, it could be a widening due to an increased hyperfine

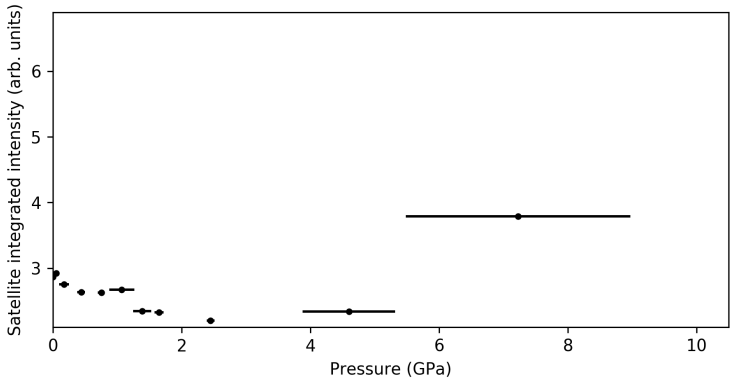

Figure V.6: Unpublished XES data measured at ambient temperature. The data treatment is simpler than in the article — it is the integrated intensity (scaled), rather than an intensity extracted from a fit. However, the fit was well-described by a Gaussian shape with a fixed width, therefore the area is proportional to the intensity. The uncertainty in intensity was not estimated and pressure estimate represents only the pressure difference between the start and end of a measurement.

magnetic field. In the case of the latter, the fact that the low and high temperature patterns are the same suggests robust magnetic ordering up to ambient temperature.

The increase of the C-D near-edge XAS feature at 5 GPa before the structural transition must be investigated in more detail. I have a very speculative theory that it is somehow sensitive to a minority ortho-II phase before the main transition. The intercalation of potassium between FeSe planes in $K_xFe_{2-y}Se_2$ is known to lead to a nano-scale phase separation of an afm high-spin phase, $K_{0.8}Fe_{1.6}Se_2$, and a superconducting phase, KFe_2Se_2 [181]. Simonelli *et al.* [181] suggest that an interaction between these phases causes the increase in T_c from 8 K to 32 K in these compounds. I speculate that if a high-spin ortho-II minority appears at lower pressures in FeSe, this could be what is inducing the sharp increase in T_c. This is plausible since the phase proportion shown in Fig. V.5 from Svitlyk *et al.* [3] is plotting I(200)/I(202) rather than the correct measure of phase fraction, I(200)/(I(200) + I(202)). At 6.9 GPa the figure shows 100% ortho-I phase, yet the diffraction image shows a minority ortho-II phase. Finally the transport measurements in Fig. V.5 should be considered in this context. How much the crystals are destroyed should be quantified since this will severely impact the transport measurements. The ortho-II phase has been been interpreted as a semiconducting state due to the negative temperature dependence of its resistivity, however I suggest that this could also be due to electronic scattering from increased domain boundaries at lower temperatures. As well, in the measurements from both Sun *et al.* and Medvedev *et al.* the high pressure curves (for example 15 GPa in Fig. V.5) seem to consist of two components. These kinks could be interpreted as a small partial resistive drop from the minority ortho-I, suggesting that the T_c actually continues to increase to at least 55 K.

This high pressure region is still quite mysterious and is starting to be explored vigorously. There are some recent articles and unpublished results that are not included in our article which are worth mentioning. The first is Hall resistivity measurements which find a large Hall coefficient near 6 GPa, corresponding with the maximum T_c due to afm spin fluctuations

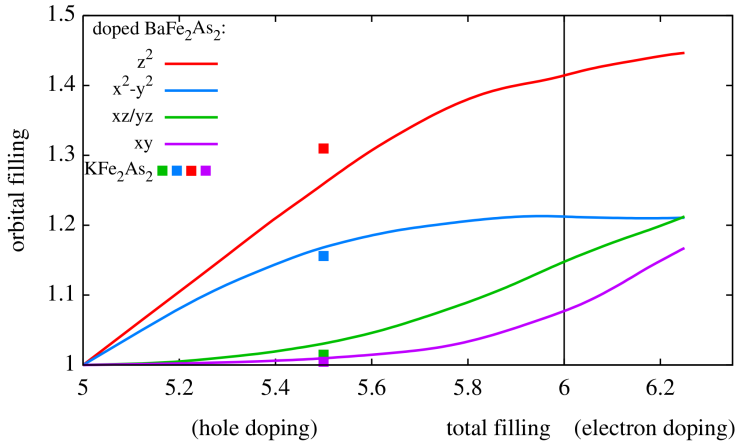

Figure V.7: Slave-spins mean field calculations of the electron population as a function of doping for $BaFe_2Se_2$ and stoichiometric KFe_2As_2 [182]. There are 6 electrons in FeSe that must fill the $3d$ orbitals (vertical line).

as the afm phase destabilizes [183]. There is also recent high-energy x-ray diffraction results which find an intermediate tetragonal phase of only 1–2 GPa width existing between the ortho-I and ortho-II phases[2]. They also performed nuclear forward scattering, however the measurement in this intermediate region could be fit equally well with either a high-spin or low-spin model. Finally, our argument that the ortho-I low-spin state is due to band-dependent correlations is logical, but the fact that increased pressure decreases correlations and leads to a high-spin ortho-II state is a bit more tenuous. Tetrahedral coordination usually favors a high-spin state since the crystal field energy is smaller than the spin pairing energy so all the $3d$ orbitals will be filled with one electron before pairing. However, as shown for $BaFe_2As_2$ in Fig. V.7, calculations suggest that the e_g bands (z^2 and $x^2 - y^2$) are preferentially filled to avoid on-site electron correlations which leads to a low-spin state. We argue that O_h high-spin state is a result of decreased correlation with pressure, likely aided by the structural transition, such that band-dependent correlations no longer play an important role. In this case, we assume the ratio of the correlation and bandwidth, U/W, is still small enough such that electrons prefer filling the $3d$ orbitals equally before pairing which leads to a high-spin state. Work needs to continue to quantify the correlation and bandwidth before and after the structural transition. Another possible explanation comes from recent band structure calculations on the NiAs-type hexagonal FeSe structure that found strong magnetism arising from a Van Hove singularity [184] associated with the direct Fe-Fe c-axis chains (Fig. V.8). The ortho-II structure is slightly distorted from a NiAs-type hexagonal cell, therefore it is not unlikely that ortho-II will also exhibit a Van Hove singularity. We plan to perform DFT calculations in the ortho-II phase using the same parameters to study the band structure near the Fermi level in more detail.

The small jump we find in our room temperature XES signal (Fig. V.6) reveals the utility of using small pressure steps. As well, if we would like to study in more detail the ortho-I to ortho-II transition, smaller pressure steps and pressure cycling would be useful tools to study

[2]Personal communication with Anna Böhmer

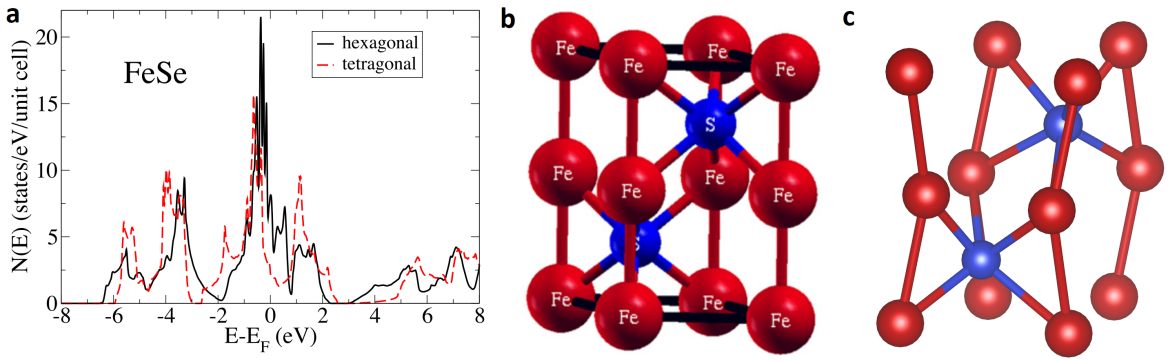

Figure V.8: (a) Calculated electronic density of states for hexagonal (black) and tetragonal (red) FeSe [184]. (b) Crystal structure of FeSe in the hexagonal ($P6_3/mmc$) structure [184] (c) and ortho-II ($Pnma$). The bonds have been drawn to match those shown in (b), although it differs from the accepted NiAs-type structure found by x-ray diffraction.

the role of irreversibility. Membrane DACs are in use all over France, yet their continuously variable pressure has not been exploited to its maximum potential. I suggest future experiments should couple a mass flow controller with the gas delivery system to the membrane of the DAC. This would allow slow ramping speeds which has many advantages. A slow continuous ramp would eliminate pressure drifts due to relaxation effects and the large density of points would put techniques such as XES on par with transport measurements, where small anomalies indicate changes of the electronic structure. The ramping speed could also be varied in a series of experiments in order to study kinetic effects during structural transitions. The addition of electromagnetic valves could also allow automated pressure cycling experiments. Finally, the slow ramping speed could be beneficial to help reach extremely high pressures. It would avoid large pressure jumps which could break the diamonds and allow data acquisition up to the very final point before a blow-out. Lab-based XES spectrometers are becoming more common place with recent instrumentation developments and are a natural fit with this technique.

There are many experiments that could help shed more light on the high-pressure ortho-II phase and the associated transition. Pushing the pressure limits of μSR spectroscopy could provide a valuable tool. Neutron diffraction should be attempted again, however we must first study the importance of the sample form (powder versus single crystal) on the structural transition. Finally, the introduction nanoscale XAS/XES beamlines around the world opens up the opportunity to study possible nano-scale phase separation of the ortho-I and ortho-II phases during the transition.

Chapter VI
Conclusion

I present a variety of experimental measurements in this thesis, mostly related to magnetism, applied to three completely different unconventional superconductors. My results emphasize the intimate connection between magnetism and superconductivity which seems ubiquitous in unconventional superconductors. The main results of these studies are:

- The magnon dispersion in the undoped parent compound $Ca_2CuO_2Cl_2$ is measured and we estimate the super-exchange parameter $J = 141$ meV. Our high-resolution measurements are well-fit with further exchange terms parameterized by a one-band Hubbard model.

- We provide a set of benchmarks characterizing magnetic excitations in the $Ca_2CuO_2Cl_2$ system for comparison with future many-body calculations. These results include the doping dependence of the paramagnon and an extensive study of the bimagnon using a multitude of techniques. We also find the first hints of bulk charge order in the $Ca_2CuO_2Cl_2$ system.

- Our neutron powder diffraction results on ϵ-iron rebuts the existence of static afmII order. Therefore, we find spin fluctuations must exist in order to explain previous experimental results.

- The magnetic moment in ϵ-iron measured with x-ray emission spectroscopy tends towards zero between 30–40 GPa, the same region where the superconducting state disappears. This strongly supports the previous predicted theories of Cooper pairing mediated by spin fluctuations in ϵ-iron.

- Our preliminary calculations suggest that spin fluctuations arise in ϵ-iron due to degenerate ground states in the geometrically frustrated hcp lattice.

- We find an unforeseen low-spin to high-spin transition in FeSe associated with its structural transition. The origin of this unusual effect is explained well by recently predicted band-dependent correlation effects in Fe-based superconductors.

- A spectroscopic signature of the increased T_c in FeSe around 5 GPa is found and needs to be investigated further. I speculate that nanoscale separation of the low- and high-spin states induces spin fluctuations which enhance the T_c in this region.

- The upper limits we set for the magnetic moment of different antiferromagnetic configurations in the ortho-I phase of FeSe agree with a stripe-type collinear arrangement which is in common with other FeSe-based superconductors.

As is often the case in science, the answers I found in this thesis naturally lead to even more questions than I answered! Further studies on these unconventional superconductors are needed to truly understand magnetism and its connection to superconductivity in these systems.

In the case of the $Ca_2CuO_2Cl_2$ system, the major missing piece is many-body calculations. We plan to collaborate with a theorist on the next paper discussing bimagnons in the parent compound. The doping dependence is still incomplete and we plan to measure the dispersion along the $\langle 110 \rangle$ direction, as well as with optimal doping (x = 0.2). Our high-resolution RIXS results can already see the bond-stretching phonon and future studies with < 30 meV resolution will help provide more information about the electron-phonon coupling, which may naturally provide an explanation of the phonon anomaly observed with IXS outside of charge order. The CDW-like peak we found is the first hint of bulk charge order in this system and we plan to improve our sample quality and preparation techniques in order to conclusively confirm our results.

The ϵ-iron phase still holds many mysteries as well. The most important point is to finish our calculations to better interpret the data we have already gathered. Nonetheless, there are many future measurements which could help elucidate the magnetic state of ϵ-iron even further. Inelastic neutron scattering and muon spin rotation spectroscopy would be useful to probe the spin excitations directly. Indirectly, an isobaric EXAFS/XMCD temperature study could investigate the picture of a locally distorted orthorhombic structure due to afm spin fluctuations near room temperature which disappears at low temperatures as fm fluctuations become dominant. The low-pressure side of the superconducting dome should be investigated with pressure-cycling transport measurements using helium as the transport medium, as well as using a laser to anneal the sample in-situ.

We are currently investigating the band structure of the ortho-II phase to determine if a Van Hove singularity exists as predicted for the hexagonal phase. The effect of sample shape/orientation and high pressure method on the structural transition in FeSe needs to be investigated in more detail to explain why our NPD studies and previous XES studies did not observe a transition. The easiest experiment is to perform two quick XES measurements at room temperature, one which uses a ground powder from high-quality single crystals and another which just uses high-quality single crystals. Armed with this knowledge we would like to repeat neutron diffraction measurements in order to determine the magnetic moment and magnetic structure in the ortho-II phase. The possibility of nanoscale phase separation could be investigated with nano-XES mapping measurements. As well, measurements of the Meisner effect to determine the T_c instead of transport could be instructive. Finally, the irreversible, destructive nature of the transition should be investigated in more detail, including measurements on samples depressurized to room temperature and comparisons with hexagonal FeSe.

Our results on FeSe show the importance of the pressure application technique in these quasi-2D systems. The structural transition could be investigated further using uniaxial strain instead of quasi-hydrostatic pressure techniques. Besides being able to tune quite differently quasi-2D materials, uniaxial stress can also be applied in a UHV environment

making it compatible with many more techniques (soft x-ray RIXS as one example). Uniaxial strain would also be a useful to study further the $Ca_2CuO_2Cl_2$ system. Measurements of the T_c in $Ca_{2-x}Na_xCuO_2Cl_2$ under pressure show a linear decrease with pressure, which is the complete opposite behavior observed in isostructural $La_{2-x}Sr_xCuO_4$ [185]. This should be studied further using uniaxial strain in and out of the CuO_2 plane. Uniaxial strain in $Ca_{2-x}CuO_2Cl_2$ and $Ca_{2-x}Na_xCuO_2Cl_2$ can also help determine the influence of the Cu-Cl bond length on T_c in order to explain why $Ca_{2-x}CuO_2Cl_2$ has a higher T_c.

I have investigated magnetic order, which is due to repulsive interactions, near superconducting order, which is due to attractive interactions. Very broadly speaking, a common theme is emerging from the study of unconventional superconductors in which the additional degree of freedom from magnetism leads to degenerate states that induce magnetic fluctuations implicated with superconductivity. In FeSe and $Ca_2CuO_2Cl_2$ this is a natural consequence of their strongly correlated nature, while in ϵ-iron it appears to arise due to geometric frustration.

Appendix A

Article 4: High pressure neutron diffraction to beyond 20 GPa and below 1.8 K using Paris-Edinburgh load frames

Status: Published in *High Pressure Research* **36:1**, 73-78 [186] on 22 January 2016

Author contributions: The high pressure techniques were developed by Stefan Klotz and previous collaborators. Thierry Strässle was the first to attempt low temperatures for neutron powder diffraction by pumping on helium. Blair Lebert, Stefan Klotz, Thierry Strässle, Matteo d'Asuto, and Thomas Hansen participated in the iron experiment which is presented as proof of concept. The article was written by Stefan Klotz with input of Blair Lebert and other co-authors.

HIGH PRESSURE RESEARCH, 2016
VOL. 36, NO. 1, 73–78
http://dx.doi.org/10.1080/08957959.2015.1136624

Taylor & Francis
Taylor & Francis Group

High pressure neutron diffraction to beyond 20 GPa and below 1.8 K using Paris-Edinburgh load frames

S. Klotz[a], Th. Strässle[b], B. Lebert[a], M. d'Astuto[a] and Th. Hansen[c]

[a]IMPMC, CNRS UMR 7590, Université P&M Curie, Paris, France; [b]Paul Scherrer Institut, Villigen, Switzerland; [c]Institut Laue-Langevin, Grenoble, France

ABSTRACT

We describe a method for collecting neutron diffraction patterns simultaneously at high pressure (>22 GPa) and low temperature (<1.8 K). The system uses ~5–10 mm^3 samples compressed by double-toroidal sintered diamond anvils, with the required forces generated by a Paris-Edinburgh press of 30 kg mass. Technical details are given and diffraction data of ε-iron at 22.6 GPa and 1.79 K are presented.

ARTICLE HISTORY
Received 15 December 2015
Accepted 22 December 2015

KEYWORDS
Neutron diffraction; high pressure; iron; Paris-Edinburgh press; low temperatures

A large part of neutron diffraction deals with physical phenomena which appear only at very low temperatures close to 0 K, such as many magnetic ordering and quantum critical phenomena. There is a growing interest to investigate these phenomena with high pressure since the interatomic distances, and thus the interaction parameters controlling these phenomena, can be tuned in a continuous and controlled fashion. The simultaneous generation of high pressure and very low temperatures is a well-known problem in neutron scattering, in particular for pressures in the multi-GPa range where the pressure cells are rather massive and therefore need a more complex cryogenic solution.

Here we discuss a method which allows neutron diffraction to at least 22 GPa and 1.8 K using samples of typically 5–10 mm^3. The technique uses a VX5 Paris-Edinburgh high pressure cell of 130 tonnes capacity,[1] double-toroidal anvils,[2,3] and cryogenic equipment which was already briefly presented.[4] Figure 1 shows schematically the set-up. The pressure cell is attached to, and cooled by, a two-stage closed-cycle refrigerator (CCR) with a base temperature of 3.6 K. A key feature of this cryogenic set-up is that during operation the cell is in contact with He-exchange gas inside a sealed Al-container (item 6). This ensures efficient heat exchange and small temperature gradients compared to more conventional CCR solutions where the sample or pressure cell is in vacuum and only cooled/heated by thermal contact to the cold head. A second Al container (item 7) is attached to the first stage of the CCR and acts as a heat shield towards the outer vacuum container (item 8). Temperature changes with the 30 kg mass of the VX5 cell are rather slow using the CCR only, typically 0.1 K/min. A practical modus operandi is therefore to pre-cool the cell with liquid nitrogen injected into the inner Al container through a

CONTACT S. Klotz stefan.klotz@impmc.jussieu.fr

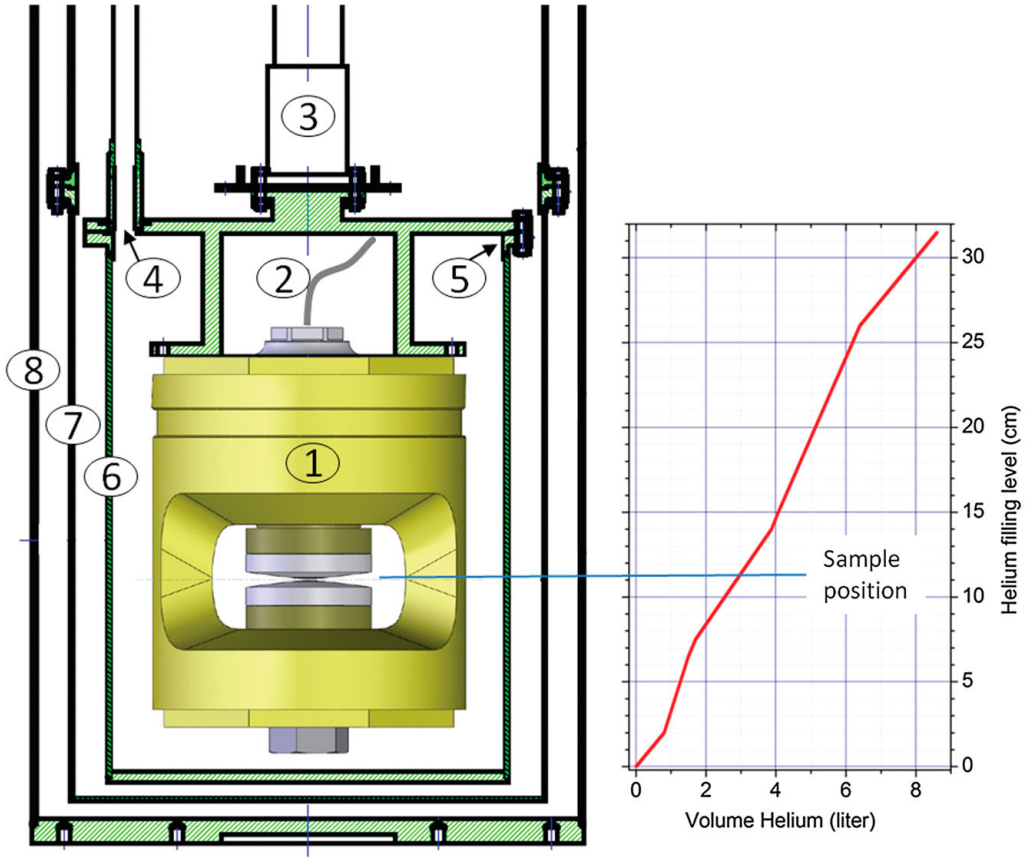

Figure 1. Left: High pressure cell in its cryostat. Right: Helium volume as a function of filling level. (1) pressure cell, (2) He-capillary, (3) CCR cold head, (4) vent, (5) indium-seal, (6) inner Al container, (7) 30 K Al-heat shield, (8) outer vacuum container. Filling levels are measured from the bottom of the inner Al-container.

vent inlet (item 4). This method allows reaching 80 K within approximately 2 h, including the removal of the remaining liquid and purging with He-gas.

In initial experiments at the Swiss neutron source SINQ at the Paul Scherrer Institute (PSI), we realised that this cryogenic equipment is perfectly adapted to reach much lower temperatures. For this purpose the cell is cooled to a base temperature of typically 4–6 K using the CCR. The inner Al-container is then filled with liquid helium. Figure 1 (right panel) gives the volume of He stored in the Al-container as a function of filling height with respect to the bottom of the inner Al-container (item 6). It is seen that the container can accept approximately 3 L of helium up to the sample level, and up to 8.5 L in total. Pumping on the fluid through one of the two vents (diametre 12 mm) leads to a rapid decrease in temperature; the lambda point (2.17 K) is reached within 15 min, while 1.8 K is reached within 30 min. The He consumption to 2 K is approximately 30–40% and mainly consumed to cool the fluid He itself, not the cell, which has a much lower heat capacity at this temperature. With helium filled up to ~20 cm from the bottom of the Al-container, the He-level drops to below the sample/beam height when temperatures below 2 K are reached, *i.e.* at the point where neutron data can be collected. In fact, even when the sample is below the liquid He level, diffraction data can be collected, although attenuated by approximately 40%. From this moment onward, the He-consumption is very low as a consequence of the CCR still running and hence screening the heat

flow from above. With the remaining 3 L of He, we have kept temperatures below 2 K for 7 h, with 80% of this time below 1.8 K (base temperature 1.79 K). This period is sufficient for most diffraction experiments, even on small samples.

We have used this set-up to investigate the ε-phase of iron which is stable beyond ~15 GPa. For this purpose, double-toroidal anvils [2,3] were used with their profile dimensions reduced by a factor 0.8 compared to previous designs,[5] see inset Figure 2. To generate the required forces we used a VX5 Paris-Edinburgh cell with a capacity of 130 tonnes and a mass of 30 kg, as shown in Fig. 1. See Ref. [1] for details concerning this type of large volume cell and its application to neutron scattering. Null scattering TiZr gaskets were used with an inner set of encapsulating hemispheres. The solid sample was machined from a rod of pure iron (Goodfellow Ref. 203-947-27, 99.99+% purity) into a roughly 9 mm^3 sphere. No pressure medium was used since all pressure transmitting fluids are solid anyway at our target pressure and temperature conditions. However, the spherical shape of the sample chamber seems to ensure quasi-hydrostatic conditions, judged by the measured onset pressure of the α–ε transition (14.5 GPa) and the pressure where the α-phase disappears (19.5 GPa), in comparison with previous investigations on the effect of non-hydrostaticity on this transition.[9] Temperatures were measured with a calibrated CX-1050-AA Cernox resistance sensor attached to the cell body approximately 10 cm from the sample. Pressure values were obtained directly from the measured (refined) unit cell volume and the known equations-of-state of α- [6] and ε-iron.[7,10] Initial tests at 300 K were carried out in 2003 at the PEARL station of the UK. ISIS facility using D_2O ice VII as a sample. These indicated that using this anvil profile (inset Figure 2), pressures in excess

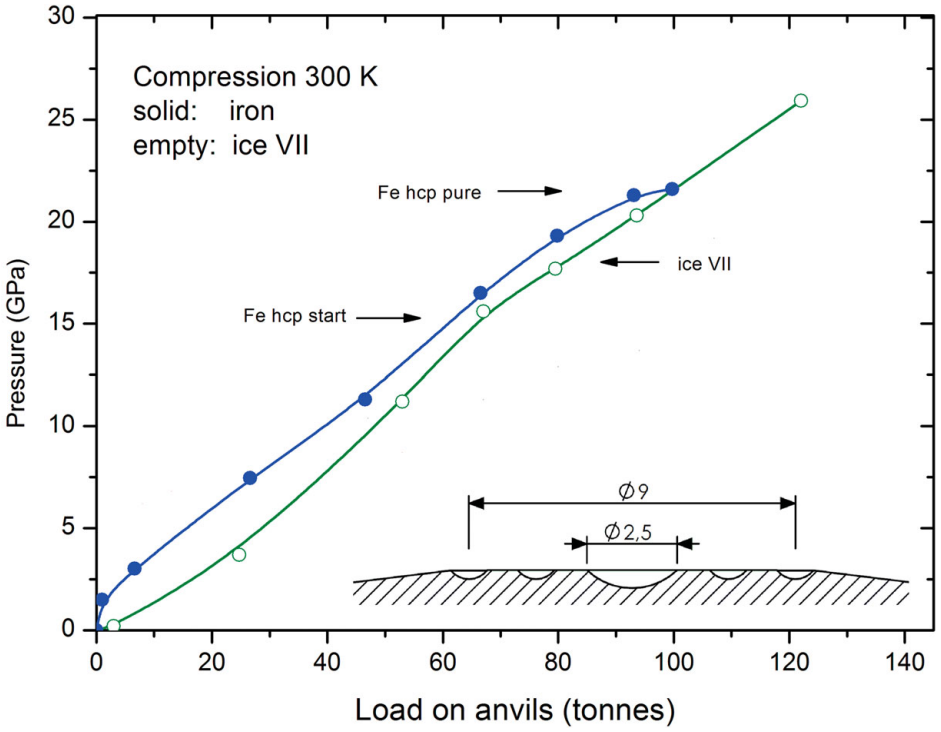

Figure 2. Pressure-load curve for a 9 mm^3 sample of iron and ice VII, at 300 K. Pressure values were obtained using equations of state from Refs. [6,7] (iron) and Ref. [8] (ice VII). Lines are guides to the eye. The inset shows the cross section of the anvil profile used in the experiments with dimensions given in mm.

of 25 GPa can be generated with a force of less than 130 tonnes which is within reach of a VX5 press.

The data reported here were collected at the high-intensity diffractometer D20 [11] at the Institut Laue-Langevin, Grenoble, France, using a wavelength of 1.30 Å, produced by a copper (200) monochromator at a take-off angle of 42°. This instrumental configuration gives maximal neutron flux at reasonable resolution up to $2\theta \sim 60°$ and degraded resolution above. Figure 3 shows a diffraction pattern obtained at 1.79 K and 22.6 GPa, after 10 min of beam time. Apart from a scale factor and background, the Rietveld fit to the pattern (line through the data) includes refinements of lattice parameters, isotropic thermal displacement factors as well as preferred orientation. Unavoidably, the strongest reflections are due to the anvil material, polycrystalline diamond. These can be readily included into the fits and pose no serious problem for structural investigations. The initial room temperature compression to 100 tonnes gave patterns of pure ε-Fe (plus diamond) with refined unit cell parameters of $a = 2.44232(20)$ Å and $c = 3.92918(39)$ Å, *i.e.* $V = 20.297(3)$ Å^3, hence a pressure of 21.3 GPa according to the Vinet-Rydberg equation-of-state of Ref. [7] ($V_0 = 11.214$ Å^3/atom, $B_0 = 163.4$ GPa, $B_0' = 5.38$). After cooling at constant load, the refinements of the pattern at 1.79 K shown in Figure 3 give $a = 2.43873(22)$ Å and $c = 3.91908(40)$ Å, *i.e.* $V = 20.186(3)$ Å^3. This indicates a pressure of 22.6 GPa using unpublished X-ray synchrotron data of ε-Fe obtained at 15 K [10] and the same type of equation-of-state with $V_0 = 11.207$ Å^3/atom, $B_0 = 163.6$ GPa and $B_0' = 5.33$. [10] The 13 K difference with our measurements is completely negligible because the thermal expansion of any solid at such temperatures is virtually zero. After decompression at ~200 K the anvils were recovered undamaged. A complete analysis of these results

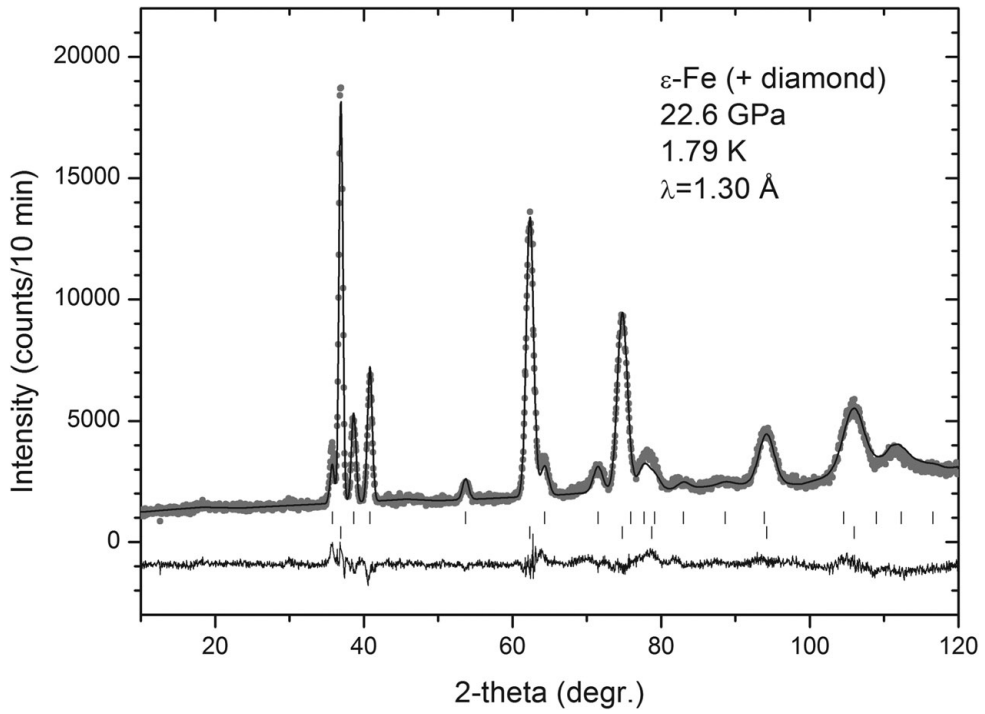

Figure 3. Diffraction pattern of ε-iron at 22.6 GPa and 1.79 K. The line is a Rietveld fit to the data (dots), the difference curve is given below. Upper tick marks indicate ε-Fe peak positions, lower tick marks those of diamond from the anvils. The pattern represents raw data, *i.e.* no background was subtracted. The accumulation time is 10 min.

including the search for the potential presence of magnetism in ε-Fe will be given separately.[12]

It should be admitted that iron's large scattering length and simple structure produce high-intensity diffraction patterns. Nevertheless, the method described here might be applicable for a large number of materials where relatively low resolution is required at high scattering angles, for example studies with a focus on magnetism. With the ever-increasing performance of neutron focusing techniques the method described here might become more widespread in the future.

Acknowledgements

We are grateful for beamtime [13] and other resources provided by ILL for these experiments, as well as the ISIS facility for beamtime in initial test measurements in 2003. We thank X. Tonon, Claude Payre and Alain Daramsy (ILL) as well G. Hamel (IMPMC) and J. White (PSI) for their help during the experiments.

Funding

Blair Lebert acknowledges a PhD grant from the French excellence initiative under the MATISSE programme and support from the LLB-SOLEIL PhD grant programme.

Disclosure statement

No potential conflict of interest was reported by the authors.

References

[1] Klotz S. Techniques in high pressure neutron scattering. Boca Raton (FL): CRC Press – Taylor and Francis; 2013.
[2] Khvostantsev LG, Vereshchagin LF, Novikov AP. Device of toroid type for high pressure generation. High Temp-High Pressures. 1977;9:637–639.
[3] Semerchan AA, Kuzin NN, Davidova TN, Bibaev KK. High-pressure and high-temperature apparatus with a working volume of 85 cm^3, operating at pressure and temperatures for synthesis of carbonado, for a press with load of 50,000 tons. Sov Phys Dokl. 1983;28:64–65.
[4] Bourgeat-Lami E, Chapuis JF, Chastagnier J, et al. Overview of the projects recently developed by the advanced neutron environment team at the ILL. Phys B: Condens Matter. 2006;385–386:1303–1305.
[5] Klotz S, Besson JM, Hamel G, et al. Neutron powder diffraction at pressures beyond 25 GPa. Appl Phys Lett. 1995;66:1735–1737.
[6] Mao HK, Bassett WA, Takahashi T. Effect of pressure on crystal structure and lattice parameters of iron up to 300 kbar. J Appl Phys. 1967;38:272–276.
[7] Dewaele A, Loubeyre P, Occelli F, Mezouar M, Dorogokupets PI, Torrent M. Quasihydrostatic equation of state of iron above 2 Mbar. Phys Rev Lett. 2006;97:215504-4.
[8] Wolanin E, Pruzan Ph, Chervin JC, et al. Equation of state of ice VII up to 106 GPa. Phys Rev B. 1997;56:5781–5785.
[9] Von Bargen N, Boehler R. Effect of non-hydrostaticity on the α–ε transition of iron. High Pressure Res. 1990;6:133–140.
[10] Dewaele A. Low temperature equation-of-state of ε-iron. ESRF Exp. Report HC-1679. Grenoble: ESRF; 2014.

[11] Hansen TC, Henry PF, Fischer HE, Torregrossa J, Convert P. The D20 instrument at the ILL: a versatile high-intensity two-axis neutron diffractometer. Meas Sci Technol. 2008;19:034001-6.
[12] Lebert B, et al. to be published.
[13] Klotz S, d'Astuto M, Lebert B, Strässle Th, Hansen Th. Search for magnetic order in ε-iron at 20 GPa. Grenoble: Institut Laue-Langevin (ILL); 2013. Available from: http://doi.ill.fr/10.5291/ILL-DATA.5-31-2443

Appendix B

News brief: Resonant inelastic x-ray scattering (RIXS) at very high resolution

Status: Published 26 April 2017 at https://www.synchrotron-soleil.fr/en/news/resonant-inelastic-x-ray-scattering-rixs-very-high-resolution

Author contributions: The high resolution commissioning was performed by Blair Lebert, Jean-Pascal Rueff, James Ablett, and Dominique Prieur. The experiment presented as a proof of concept was performed by Blair Lebert, Jean-Pascal Rueff, Matteo d'Astuto, James Ablett, Simo Huotari, Mary Upton, Kari Ruotsalainen, and Alessandro Nicolaou. Blair Lebert and Jean-Pascal Rueff wrote the news brief.

Resonant inelastic x-ray scattering (RIXS) at very high resolution

The measurement of elementary excitations in a material requires high resolution spectroscopic probes with momentum resolution. RIXS is a powerful technique to characterize these low energy excitations. On GALAXIES beamline, a new High Resolution RIXS setup is available to users for investigating complex materials.

Material properties are fundamentally controlled by the behavior of low energy electrons. The knowledge of this electronic ground state is a primary, yet insufficient, ingredient to understand the physical properties. To characterize the full response of the material to external perturbation, it is equally essential to understand the elementary excitations, whose energy and dispersion in the momentum space will affect the overall material behavior. Clearly, the measurement of these excitations requires high resolution spectroscopic probes with momentum resolution. Resonant inelastic x-ray scattering (RIXS) has emerged as a powerful technique to characterize these low energy excitations. This technique complements traditional inelastic neutron scattering because it is element selective, is available for small samples, and can be performed in challenging sample environments. The GALAXIES team has recently succeeded in measuring their beamline's first high resolution RIXS results, offering users a new tool for investigating complex materials.

The setup is illustrated in Figure 1. The scattered x-rays are collected by a 100 mm diameter 'diced' crystal analyzer. The analyzer is an array of mm-size crystalline cubes arranged on a spherical substrate. The role of the analyzer is to filter the scattered x-rays (by Bragg diffraction) and focus them onto a 2D detector. The unstrained single crystal quality of the analyzer ensures very high resolution. In addition, each cube acts as a dispersive element, providing extra resolving power. By scanning the analyzer Bragg and post-processing the detector images, it is possible to reconstruct high resolution RIXS spectra as shown in Figure 2.

.

Figure 1: Schematic of the high resolution RIXS setup. The scattered x-ray beam is reflected by a 100 mm diameter spherically bent 'diced' crystal analyzer. The analyzer filters, disperses and focuses the x-ray photons on to a 2D pixelated detector

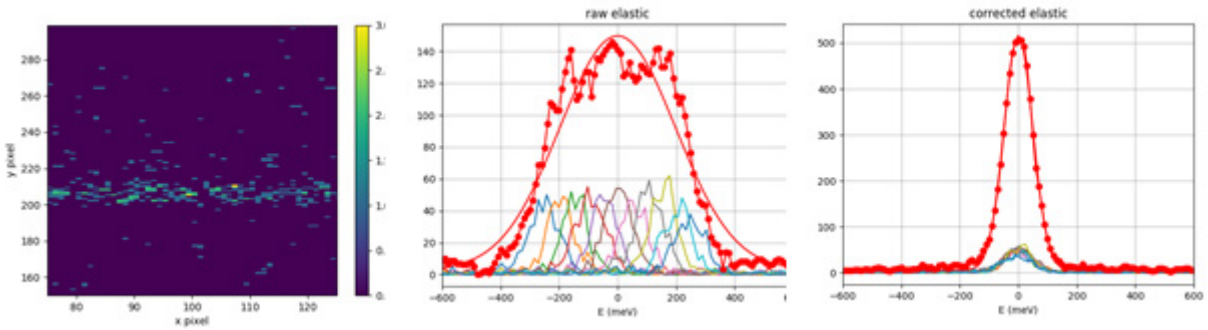

Figure 2: (left) Image of an elastic peak on the 2D detector at a given Bragg angle. (center) When scanning the Bragg angle, the elastic line moves on the detector (right) The correct spectrum can be reconstructed from the energy dispersion and pixel-energy correlation. A Gaussian fit provides a FWHM of 115 meV.

The method has recently been applied to investigate the low energy magnetic excitations in the high temperature superconducting (HTS) cuprate parent compound, $Ca_2CuO_2Cl_2$. Magnetic excitations have been intensively studied for their possible role in the pairing mechanism in HTS cuprates. However, the interpretation of the experiments remains highly controversial because of the lack of theoretical understanding of electronic correlations in realistic systems. The cuprate family $Ca_2CuO_2Cl_2$ offers a unique opportunity to bridge state-of-the-art theory and experiment, due to its reduced number of electrons and relatively simple structure. However, since it is only available as small single crystals, it was infeasible to

study the material with inelastic neutron scattering and it is just becoming possible to study it with RIXS due to advances in high resolution instrumentation.

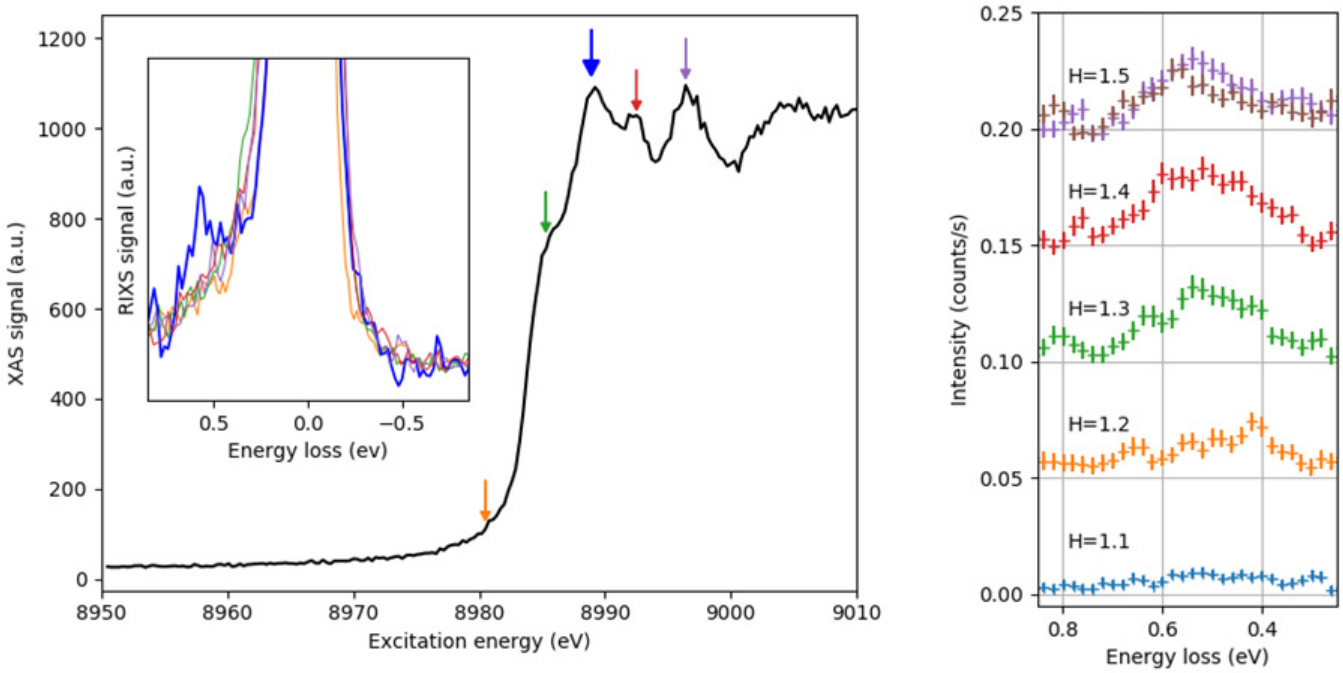

Figure 3: (left) RIXS spectra at different incident energies shows a resonance at 8989 eV. (right) High resolution RIXS spectra in $Ca_2CuO_2Cl_2$ at the Cu K-edge after subtracting elastic peak taken at different positions in reciprocal space (H, 0, 14). Spectra are offset by 0.05 counts/s for clarity and two different measurements are shown for H=1.5.

The measurements were performed at the Cu K-edge using a Ge(733) diced analyzer from APS at a Bragg angle of ~88° and a MERLIN 2D detector. The overall resolution was 115 meV at 8980 eV as estimated from the FWHM of the elastic line, yielding a resolving power of ~80000. Despite an intense elastic line, a clear excitation can be seen around 540 meV which resonates in the near edge region at 8989 eV (Figure 3). The excitation – interpreted here as primarily a bimagnon – decreases in intensity towards low momentum transfer as expected by theory. However, the expected dispersion is not clearly seen and there is a complex multi-magnon structure. Future experiments on $Ca_2CuO_2Cl_2$ in both the undoped and doped regimes will be coupled with quantum Monte Carlo calculations which will help us shed light on the complex structure of these magnetic excitations in the cuprates and elucidate their possible role in Cooper pairing.

The bimagnon measured was incredibly weak, only about 2 photons/min/channel with an incident flux of 6 x 10^{12} photons/min. Future experiments will benefit greatly from the GALAXIES newly installed high resolution monochromator which will be commissioned soon.

CONTACT

Jean-Pascal RUEFF

ADDITIONAL RESOURCES

GALAXIES Beamline

READ ALSO

Solidification of an Al-Cu Alloy (4 w% Cu) using X-ray Microtomography

SOLEIL, accélérateur de recherche et d'innovation pour l'industrie cosmétique : témoignage de Lucien BILDSTEIN, chercheur et responsable de laboratoire chez L'OREAL

Evidences of the self-assembly of graphene oxide sheets at the air-water interface

Bibliography

[1] K. Ohishi, I. Yamada, A. Koda, W. Higemoto, S. R. Saha, R. Kadono, K. M. Kojima, M. Azuma & M. Takano; "Magnetic phase diagram of hole-doped Ca 2-xNa xCuO 2Cl 2 cuprate superconductor;" J. Phys. Soc. Japan **74**, pp. 2408–2412 (2005). doi:10.1143/JPSJ.74.2408.

[2] S. S. Saxena & P. B. Littlewood; "Iron cast in exotic role;" Nature **412**, pp. 290–291 (2001). doi:10.1038/35085681.

[3] V. Svitlyk, M. Raba, V. Dmitriev, P. Rodière, P. Toulemonde, D. Chernyshov & M. Mezouar; "Complex biphase nature of the superconducting dome of the FeSe phase diagram;" Phys. Rev. B **96**, pp. 1–7 (2017). doi:10.1103/PhysRevB.96.014520.

[4] B. W. Lebert, M. P. M. Dean, A. Nicolaou, J. Pelliciari, M. Dantz, T. Schmitt, R. Yu, M. Azuma, J.-P. Castellan, H. Miao, A. Gauzzi, B. Baptiste & M. D'Astuto; "Resonant inelastic x-ray scattering study of spin-wave excitations in the cuprate parent compound Ca2CuO2Cl2;" Phys. Rev. B **95**, p. 155110 (2017). doi:10.1103/PhysRevB.95.155110.

[5] G. Steinle-Neumann, R. Cohen & L. Stixrude; "Magnetism in iron as a function of pressure;" J. Phys. Condens. Matter **16**, pp. S1109—-S1119 (2004). doi:10.1088/0953-8984/16/14/020.

[6] G. Steinle-Neumann, L. Stixrude & R. Cohen; "Magnetism in dense hexagonal iron." Proc. Natl. Acad. Sci. U. S. A. **101**, pp. 33–36 (2004). doi:10.1073/pnas.2237239100.

[7] B. W. Lebert, V. Balédent, P. Toulemonde, J. M. Ablett & J. P. Rueff; "Electronic transition in FeSe at high pressure and low temperature;" (2017). http://arxiv.org/abs/1708.04805.

[8] H. K. Onnes; "The superconductivity of mercury;" Comm. Phys. Lab. Univ. Leiden **122**, p. 124 (1911).

[9] P. J. Ray; *Figure 2.4 in Master's thesis, "Structural investigation of La(2-x)Sr(x)CuO(4+y) - Following staging as a function of temperature"*; Ph.D. thesis; University of Copenhagen; Copenhagen (2015).

[10] Y. Kamihara, T. Watanabe, M. Hirano & H. Hosono; "Iron-Based Layered Superconductor La[O 1- x F x]FeAs (x = 0.05-0.12) with T c = 26 K;" J. Am. Chem. Soc. **130**, pp. 3296–3297 (2008). doi:10.1021/ja800073m.

[11] A. P. Drozdov, M. I. Eremets, I. A. Troyan, V. Ksenofontov & S. I. Shylin; "Conventional superconductivity at 203 kelvin at high pressures in the sulfur hydride system;" Nature **525**, pp. 73–76 (2015). doi:10.1038/nature14964.

[12] G. F. Sun, K. W. Wong, B. R. Xu, Y. Xin & D. F. Lu; "Tc enhancement of HgBa2Ca2Cu3O8+δ by Tl substitution;" Phys. Lett. A **192**, pp. 122–124 (1994). doi:https://doi.org/10.1016/0375-9601(94)91026-X.

[13] L. Gao, Y. Y. Xue, F. Chen, Q. Xiong, R. L. Meng, D. Ramirez, C. W. Chu, J. H. Eggert & H. K. Mao; "Superconductivity up to 164 K in HgBa2Cam-1CumO2m+2+δ (m=1, 2, and 3) under quasihydrostatic pressures;" Phys. Rev. B **50**, pp. 4260–4263 (1994). doi:10.1103/PhysRevB.50.4260.

[14] "The rise of quantum materials;" Nat. Phys. **12**, pp. 105–105 (2016). doi:10.1038/nphys3668.

[15] J.-P. Rueff & A. Shukla; "Inelastic x-ray scattering by electronic excitations under high pressure;" Rev. Mod. Phys. **82**, pp. 847–896 (2010). doi:10.1103/RevModPhys.82.847.

[16] "Crystal Field Theory;" https://chem.libretexts.org/Core/Inorganic{_}Chemistry/Crystal{_}Field{_}Theory/Crystal{_}Field{_}Theory.

[17] C. Kittel; *Introduction to solid state physics, 7th edition* (Wiley India Pvt. Limited) (2007); ISBN 9788126510450; https://books.google.fr/books?id=F9Qu5c{_}hUaUC.

[18] L. P. Levy; *Magnetism and Superconductivity*; Texts and monographs in physics (Springer) (2000); ISBN 9783540666882; https://books.google.ca/books?id=pN4uR30PK9kC.

[19] M. Tinkham; *Introduction to Superconductivity: Second Edition*; Dover Books on Physics (Dover Publications) (2004); ISBN 9780486435039; https://books.google.ca/books?id=JOQoAwAAQBAJ.

[20] "Meissner effect - Wikipedia;" https://en.wikipedia.org/wiki/Meissner{_}effect.

[21] K. H. Bennemann & J. B. Ketterson; "History of Superconductivity: Conventional, High-Transition Temperature and Novel Superconductors;" in "Superconductivity," , edited by K. H. Bennemann & J. B. Ketterson; pp. 3–26 (Springer Berlin Heidelberg, Berlin, Heidelberg) (2008); ISBN 978-3-540-73253-2.

[22] J. P. Carbotte; "Properties of boson-exchange superconductors;" Rev. Mod. Phys. **62**, pp. 1027–1157 (1990). doi:10.1103/RevModPhys.62.1027.

[23] F. S. Si, O. Stockert, S. Wirth, C. Geibel, H. Q. Yuan, S. Kirchner & Q; "Routes to heavy-fermion superconductivity;" J. Phys. Conf. Ser. **449**, p. 12028 (2013). http://stacks.iop.org/1742-6596/449/i=1/a=012028.

[24] S. S. Saxena, P. Agarwal, K. Ahilan, F. M. Grosche, R. K. W. Haselwimmer, M. J. Steiner, E. Pugh, I. R. Walker, S. R. Julian, P. Monthoux, G. G. Lonzarich, A. Huxley, I. Sheikin, D. Braithwaite & J. Flouquet; "Superconductivity on the border of itinerant-electron ferromagnetism in UGe2;" Nature **406**, pp. 587–592 (2000). doi:10.1038/35020500.

[25] N. D. Mathur, F. M. Grosche, S. R. Julian, I. R. Walker, D. M. Freye, R. K. W. Haselwimmer & G. G. Lonzarich; "Magnetically mediated superconductivity in heavy fermion compounds;" Nature **394**, pp. 39–43 (1998). doi:10.1038/27838.

[26] J. Orenstein; "Advances in the Physics of High-Temperature Superconductivity;" Science (80-.). **288**, pp. 468–474 (2000). doi:10.1126/science.288.5465.468.

[27] D. J. Scalapino; "A common thread: The pairing interaction for unconventional superconductors;" Rev. Mod. Phys. **84**, pp. 1383–1417 (2012). doi:10.1103/RevModPhys.84.1383.

[28] J. M. Tranquada; "Spins, stripes, and superconductivity in hole-doped cuprates;" AIP Conf. Proc. **1550**, pp. 114–187 (2013). doi:10.1063/1.4818402.

[29] B. Keimer, S. A. Kivelson, M. R. Norman, S. Uchida & J. Zaanen; "From quantum matter to high-temperature superconductivity in copper oxides;" Nature **518**, pp. 179–186 (2015). doi:10.1038/nature14165.

[30] R. Coldea, S. M. Hayden, G. Aeppli, T. G. Perring, C. D. Frost, T. E. Mason, S. W. Cheong & Z. Fisk; "Spin waves and electronic interactions in La2CuO4;" Phys. Rev. Lett. **86**, pp. 5377–5380 (2001). doi:10.1103/PhysRevLett.86.5377.

[31] J. Paglione & R. L. Greene; "High-temperature superconductivity in iron-based materials;" Nat. Phys. **6**, pp. 645–658 (2010). doi:10.1038/nphys1759.

[32] A. Chubukov & P. J. Hirschfeld; "Iron-based superconductors, seven years later;" Phys. Today **68**, pp. 46–52 (2015). doi:10.1063/PT.3.2818.

[33] "Inelastic Scattering;" http://www.mlz-garching.de/englisch/neutron-research/experimental-methods/inelastic-scattering.html.

[34] J. B. Parise; "Introduction to Neutron Properties and Applications;" Rev. Mineral. Geochemistry **63**, pp. 1–25 (2006). doi:10.2138/rmg.2006.63.1.

[35] A. C. T. Vaughan & D.; *X-ray Data Booklet*; 2nd edition (Lawrence Berkeley National Laboratory, University of California) (2001).

[36] H. Marsh; "Synchrotron Radiation Interaction with Matter;" http://slideplayer.com/slide/5857920/.

[37] P. Glatzel & U. Bergmann; "High resolution 1s core hole X-ray spectroscopy in 3d transition metal complexes - Electronic and structural information;" Coord. Chem. Rev. **249**, pp. 65–95 (2005). doi:10.1016/j.ccr.2004.04.011.

[38] Munzarin; "File:XASFig.jpg;" https://commons.wikimedia.org/wiki/File:XASFig.jpg.

[39] J. P. Rueff & A. Shukla; "A rixs cookbook: Five recipes for successful rixs applications;" J. Electron Spectros. Relat. Phenomena **188**, pp. 10–16 (2013). doi:10.1016/j.elspec.2013.04.014.

[40] G. Vankó, T. Neisius, G. Molnár, F. Renz, S. Kárpáti, A. Shukla & F. M. F. De Groot; "Probing the 3D spin momentum with X-ray emission spectroscopy: The case of molecular-spin transitions;" J. Phys. Chem. B **110**, pp. 11647–11653 (2006). doi:10.1021/jp0615961.

[41] K. Gilmore, J. Vinson, E. Shirley, D. Prendergast, C. Pemmaraju, J. Kas, F. Vila & J. Rehr; "Efficient implementation of core-excitation Bethe–Salpeter equation calculations;" Comput. Phys. Commun. **197**, pp. 109–117 (2015). doi:10.1016/j.cpc.2015.08.014.

[42] J. Vinson, J. J. Rehr, J. J. Kas & E. L. Shirley; "Bethe-Salpeter equation calculations of core excitation spectra;" Phys. Rev. B **83**, p. 115106 (2011). doi:10.1103/PhysRevB.83.115106.

[43] W. Schülke; *Electron Dynamics by Inelastic X-Ray Scattering*; Oxford Science Publications (OUP Oxford) (2007); ISBN 9780198510178; https://books.google.ca/books?id=EXwSDAAAQBAJ.

[44] M. P. M. Dean; "Insights into the high temperature superconducting cuprates from resonant inelastic X-ray scattering;" J. Magn. Magn. Mater. **376**, pp. 3–13 (2015). doi:10.1016/j.jmmm.2014.03.057.

[45] Rixs2010; "File:RIXS excitations.jpg;" https://commons.wikimedia.org/wiki/File:RIXS{_}excitations.jpg.

[46] L. Braicovich, M. Moretti Sala, L. J. Ament, V. Bisogni, M. Minola, G. Balestrino, D. Di Castro, G. M. De Luca, M. Salluzzo, G. Ghiringhelli & J. Van Den Brink; "Momentum and polarization dependence of single-magnon spectral weight for Cu L3 -edge resonant inelastic x-ray scattering from layered cuprates;" Phys. Rev. B - Condens. Matter Mater. Phys. **81**, pp. 1–5 (2010). doi:10.1103/PhysRevB.81.174533.

[47] N. S. Headings, S. M. Hayden, R. Coldea & T. G. Perring; "Anomalous high-energy spin excitations in the high-Tc superconductor-parent antiferromagnet La2CuO4;" Phys. Rev. Lett. **105**, pp. 1–4 (2010). doi:10.1103/PhysRevLett.105.247001.

[48] M. P. M. Dean, R. S. Springell, C. Monney, K. J. Zhou, J. Pereiro, I. Božović, B. Dalla Piazza, H. M. Rønnow, E. Morenzoni, J. van den Brink, T. Schmitt & J. P. Hill; "Spin excitations in a single La2CuO4 layer;" Nat. Mater. **11**, p. 850 (2012). doi:10.1038/nmat3409.

[49] G. Ghiringhelli, A. Piazzalunga, C. Dallera, G. Trezzi, L. Braicovich, T. Schmitt, V. N. Strocov, R. Betemps, L. Patthey, X. Wang & M. Grioni; "SAXES, a high resolution spectrometer for resonant x-ray emission in the 400-1600 eV energy range;" Rev. Sci. Instrum. **77**, pp. 1–9 (2006). doi:10.1063/1.2372731.

[50] L. J. P. Ament, M. V. Veenendaal & J. V. D. Brink; "Determining the electron-phonon coupling strength from Resonant Inelastic X-ray Scattering at transition metal L-edges;" **95** (2011).

[51] A. Lanzara, P. V. Bogdanov, X. J. Zhou, S. A. Kellar, D. L. Feng, E. D. Lu, T. Yoshida, H. Eisaki, A. Fujimori, K. Kishio, J.-I. Shimoyama, T. Noda, S. Uchida, Z. Hussain & Z.-X. Shen; "Evidence for ubiquitous strong electron–phonon coupling in high-temperature superconductors;" Nature **412**, p. 510 (2001). doi:10.0.4.14/35087518.

[52] S. Johnston, F. Vernay, B. Moritz, Z.-X. Shen, N. Nagaosa, J. Zaanen & T. P. Devereaux; "Systematic study of electron-phonon coupling to oxygen modes across the cuprates;" Phys. Rev. B **82**, p. 64513 (2010). doi:10.1103/PhysRevB.82.064513.

[53] P. Willmott; *An Introduction to Synchrotron Radiation* (John Wiley & Sons, Ltd, Chichester, UK) (2011); ISBN 9781119970958.

[54] V. N. Strocov, T. Schmitt, U. Flechsig, T. Schmidt, A. Imhof, Q. Chen, J. Raabe, R. Betemps, D. Zimoch, J. Krempasky, X. Wang, M. Grioni, A. Piazzalunga & L. Patthey; "High-resolution soft X-ray beamline ADRESS at the Swiss Light Source for resonant inelastic X-ray scattering and angle-resolved photoelectron spectroscopies;" J. Synchrotron Radiat. **17**, pp. 631–643 (2010). doi:10.1107/S0909049510019862.

[55] J.-P. Rueff, J. M. Ablett, D. Céolin, D. Prieur, T. Moreno, V. Balédent, B. Lassalle-Kaiser, J. E. Rault, M. Simon & A. Shukla; "The GALAXIES beamline at the SOLEIL synchrotron: inelastic X-ray scattering and photoelectron spectroscopy in the hard X-ray range;" J. Synchrotron Radiat. **22**, pp. 175–179 (2015). doi:10.1107/S160057751402102X.

[56] S. Huotari, F. Albergamo, G. Vankó, R. Verbeni & G. Monaco; "Resonant inelastic hard x-ray scattering with diced analyzer crystals and position-sensitive detectors;" Rev. Sci. Instrum. **77**, pp. 1–6 (2006). doi:10.1063/1.2198805.

[57] S. Huotari, G. Vankó, F. Albergamo, C. Ponchut, H. Graafsma, C. Henriquet, R. Verbeni & G. Monaco; "Improving the performance of high-resolution X-ray spectrometers with position-sensitive pixel detectors;" J. Synchrotron Radiat. **12**, pp. 467–472 (2005). doi:10.1107/S0909049505010630.

[58] E. Collart, A. Shukla, F. Gélébart, M. Morand, C. Malgrange, N. Bardou, A. Madouri & J. L. Pelouard; "Spherically bent analyzers for resonant inelastic X-ray scattering with intrinsic resolution below 200 meV;" J. Synchrotron Radiat. **12**, pp. 473–478 (2005). doi:10.1107/S090904950501472X.

[59] T. C. Hansen, P. F. Henry, H. E. Fischer, J. Torregrossa & P. Convert; "The D20 instrument at the ILL: a versatile high-intensity two-axis neutron diffractometer;" Meas. Sci. Technol. **19**, p. 034001 (2008). doi:10.1088/0957-0233/19/3/034001.

[60] J. R. Copley; *The Fundamentals of Neutron Powder Diffraction* (National Institute of Standards and Technology) (2001).

[61] D. S. Sivia; *Elementary Scattering Theory: For X-ray and Neutron Users* (OUP Oxford) (2011); ISBN 9780199228676; https://books.google.ca/books?id=vvpAqv5o6zUC.

[62] D. G. Henshaw & D. G. Hurst; "Neutron Diffraction by Liquid Helium;" Phys. Rev. **91**, p. 1222 (1953). doi:10.1103/PhysRev.91.1222.

[63] L. Dubrovinsky, N. Dubrovinskaia, V. B. Prakapenka & A. M. Abakumov; "Implementation of micro-ball nanodiamond anvils for high-pressure studies above 6 Mbar;" Nat. Commun. **3**, p. 1163 (2012). doi:10.1038/ncomms2160.

[64] A. Jayaraman; "Ultrahigh pressures;" Rev. Sci. Instrum. **57**, pp. 1013–1031 (1986). doi:10.1063/1.1138654.

[65] A. Jayaraman; "Diamond anvil cell and high-pressure physical investigations;" Rev. Mod. Phys. **55**, pp. 65–108 (1983). doi:10.1103/RevModPhys.55.65.

[66] R. Letoullec, J. P. Pinceaux & P. Loubeyre; "The membrane diamond anvil cell: A new device for generating continuous pressure and temperature variations;" High Press. Res. **1**, pp. 77–90 (1988). doi:10.1080/08957958808202482.

[67] R. J. Angel, M. Bujak, J. Zhao, G. D. Gatta & S. D. Jacobsen; "Effective hydrostatic limits of pressure media for high-pressure crystallographic studies;" J. Appl. Crystallogr. **40**, pp. 26–32 (2007). doi:10.1107/S0021889806045523.

[68] S. Klotz, J.-C. Chervin, P. Munsch & G. Le Marchand; "Hydrostatic limits of 11 pressure transmitting media;" J. Phys. D. Appl. Phys. **42**, p. 075413 (2009). doi:10.1088/0022-3727/42/7/075413.

[69] R. A. Forman, G. J. Piermarini, J. D. Barnett & S. Block; "Pressure Measurement Made by the Utilization of Ruby Sharp-Line Luminescence;" Science (80-.). **176**, pp. 284–285 (1972). doi:10.1126/science.176.4032.284.

[70] A. Dewaele, M. Torrent, P. Loubeyre & M. Mezouar; "Compression curves of transition metals in the Mbar range: Experiments and projector augmented-wave calculations;" Phys. Rev. B - Condens. Matter Mater. Phys. **78**, pp. 1–13 (2008). doi:10.1103/PhysRevB.78.104102.

[71] F. Datchi, R. LeToullec & P. Loubeyre; "Improved calibration of the SrB 4 O 7: Sm 2+ optical pressure gauge: Advantages at very high pressures and high temperatures;" J. Appl. Phys. **81**, pp. 3333–3339 (1997). doi:10.1063/1.365025.

[72] S. Klotz; *Techniques in High Pressure Neutron Scattering* (CRC Press, Boca Raton) (2013); ISBN 9781138199217; https://www.crcpress.com/Techniques-in-High-Pressure-Neutron-Scattering/Klotz/p/book/9781138199217.

[73] S. Adachi, T. Tatsuki, C. Q. Jin, X. J. Wu, a. Tokiwa-Yamamoto, T. Tamura, Y. Moriwaki & K. Tanabe; "High pressure syntheses of copper oxychlorides with K2NiF4-type and related structures;" J. Low Temp. Phys. **105**, pp. 1505–1510 (1996). doi:10.1007/BF00753913.

[74] M. D'Astuto, I. Yamada, P. Giura, L. Paulatto, A. Gauzzi, M. Hoesch, M. Krisch, M. Azuma & M. Takano; "Phonon anomalies and lattice dynamics in the superconducting oxychlorides Ca2-xCuO2Cl2;" Phys. Rev. B - Condens. Matter Mater. Phys. **88**, pp. 1–9 (2013). doi:10.1103/PhysRevB.88.014522.

[75] L. K. Wagner & P. Abbamonte; "Effect of electron correlation on the electronic structure and spin-lattice coupling of high- Tc cuprates: Quantum Monte Carlo calculations;" Phys. Rev. B **90**, p. 125129 (2014). doi:10.1103/PhysRevB.90.125129.

[76] L. K. Wagner; "Ground state of doped cuprates from first-principles quantum Monte Carlo calculations;" Phys. Rev. B - Condens. Matter Mater. Phys. **92**, pp. 1–6 (2015). doi:10.1103/PhysRevB.92.161116.

[77] K. Foyevtsova, J. T. Krogel, J. Kim, P. R. C. Kent, E. Dagotto & F. A. Reboredo; "Ab initio Quantum Monte Carlo Calculations of Spin Superexchange in Cuprates: The Benchmarking Case of Ca 2 CuO 3;" Phys. Rev. X **4**, p. 031003 (2014). doi:10.1103/PhysRevX.4.031003.

[78] D. Vaknin, L. Miller & J. Zarestky; "Stacking of the square-lattice antiferromagnetic planes in Ca2CuO2Cl2;" Phys. Rev. B **56**, pp. 8351–8359 (1997). doi:10.1103/PhysRevB.56.8351.

[79] F. Ronning, T. Sasagawa, Y. Kohsaka, K. M. Shen, A. Damascelli, C. Kim, T. Yoshida, N. P. Armitage, D. H. Lu, D. L. Feng, L. L. Miller, H. Takagi & Z.-X. Shen; "Evolution of a metal to insulator transition in Ca2-xNaxCuO2Cl2 as seen by angle-resolved photoemission;" Phys. Rev. B **67**, p. 165101 (2003). doi:10.1103/PhysRevB.67.165101.

[80] Z. Hiroi, N. Kobayashi & M. Takano; "Synthesis, structure and superconductivity of Ca 2-x Na x Cu O 2 Cl 2;" Phys. C **266**, pp. 191–202 (1996).

[81] D. Hechel & I. Felner; "Antiferromagnetic order in Ca2CuO2Cl2, Sr2CuO2Cl2 and Sr2CuO3+x;" Phys. C Supercond. **235-240**, pp. 1601–1602 (1994). doi:10.1016/0921-4534(94)92026-5.

[82] D. Meyers, H. Miao, A. C. Walters, V. Bisogni, R. S. Springell, M. D'Astuto, M. Dantz, J. Pelliciari, H. Y. Huang, J. Okamoto, D. J. Huang, J. P. Hill, X. He, I. Božović, T. Schmitt & M. P. M. Dean; "Doping dependence of the magnetic excitations in La2-xSrxCuO4;" Phys. Rev. B **95**, p. 75139 (2017). doi:10.1103/PhysRevB.95.075139.

[83] Y. Kohsaka, Y. Kohsaka, M. Azuma, M. Azuma, I. Yamada, I. Yamada, T. Sasagawa, T. Sasagawa, T. Hanaguri, T. Hanaguri, M. Takano, M. Takano, H. Takagi & H. Takagi; "Growth of Na-Doped Ca 2 CuO 2 Cl 2 Single Crystals under High Pressures of Several GPa;" Adv. Mater. Process. **9**, pp. 12275–12278 (2002).

[84] K. M. Shen; "Nodal Quasiparticles and Antinodal Charge Ordering in Ca2-xNaxCuO2Cl2;" Science (80-.). **307**, pp. 901–904 (2005). doi:10.1126/science.1103627.

[85] Y. Kohsaka, K. Iwaya, S. Satow, T. Hanaguri, M. Azuma, M. Takano & H. Takagi; "Imaging nanoscale electronic inhomogeneity in the lightly doped mott insulator Ca2-xNaxCuO2Cl2;" Phys. Rev. Lett. **93**, pp. 7–10 (2004). doi:10.1103/PhysRevLett.93.097004.

[86] T. Hanaguri, C. Lupien, Y. Kohsaka, D.-H. Lee, M. Azuma, M. Takano, H. Takagi & J. C. Davis; "A 'checkerboard' electronic crystal state in lightly hole-doped Ca2-xNaxCuO2Cl2;" Nature **430**, pp. 1001–1005 (2004). doi:10.1038/nature02861.

[87] K. Fujita, M. H. Hamidian, S. D. Edkins, C. K. Kim, Y. Kohsaka, M. Azuma, M. Takano, H. Takagi, H. Eisaki, S.-i. Uchida, A. Allais, M. J. Lawler, E.-A. Kim, S. Sachdev & J. C. S. Davis; "Direct phase-sensitive identification of a d-form factor density wave in underdoped cuprates;" Proc. Natl. Acad. Sci. **111**, pp. E3026–E3032 (2014). doi:10.1073/pnas.1406297111.

[88] e. Smadici, P. Abbamonte, M. Taguchi, Y. Kohsaka, T. Sasagawa, M. Azuma, M. Takano & H. Takagi; "Absence of long-ranged charge order in NaxC2-xCuO2Cl2 (x=0.08);" Phys. Rev. B **75**, p. 075104 (2007). doi:10.1103/PhysRevB.75.075104.

[89] D. Hirai, T. Sasagawa & H. Takagi; "Is there 1/8-anomaly of Tc in Ca2 s(-) xNax-CuO2Cl2 with a checkerboard-type charge ordering?" Phys. C Supercond. its Appl. **463-465**, pp. 56–59 (2007). doi:10.1016/j.physc.2007.01.034.

[90] Z. Hiroi, N. Kobayashi & M. Takano; "Probable hole-doped superconductivity without apical oxygens in (Ca, Na)2CuO2CI2;" (1994).

[91] N. D. Zhigadlo, J. Karpinski, S. Weyeneth, R. Khasanov, S. Katrych, P. Wägli & H. Keller; "Synthesis and bulk properties of oxychloride superconductor Ca 2-x Na x CuO 2 Cl 2;" J. Phys. Conf. Ser. **97**, p. 012121 (2008). doi:10.1088/1742-6596/97/1/012121.

[92] I. Yamada, A. A. Belik, M. Azuma, S. Harjo, T. Kamiyama, Y. Shimakawa & M. Takano; "Single-layer oxychloride superconductor Ca2-xCuO2Cl2 with A-site cation deficiency;" Phys. Rev. B - Condens. Matter Mater. Phys. **72**, pp. 1–5 (2005). doi:10.1103/PhysRevB.72.224503.

[93] M. Azuma, T. Saito, I. Yamada, Y. Kohsaka, H. Takagi & M. Takano; "Single Crystal Growth of Ca2-xNaxCuO2Cl2 and Related Compounds at High Pressures of Several GPa;" J. Low Temp. Phys. **131**, pp. 671–679 (2003). doi:10.1023/A:1022904815038.

[94] N. D. Zhigadlo & J. Karpinski; "High-pressure synthesis and superconductivity of Ca2-xNaxCuO2Cl2;" Phys. C Supercond. its Appl. **460-462 I**, pp. 372–373 (2007). doi:10.1016/j.physc.2007.03.292.

[95] K. H. Satoh, M. Hiraishi, M. Miyazaki, S. Takeshita, A. Koda, R. Kadono, I. Yamada, K. Oka, M. Azuma, Y. Shimakawa & M. Takano; "Effect of Zn substitution for Cu on near the hole concentration of per Cu;" Phys. B Condens. Matter **404**, pp. 713–716 (2009). doi:10.1016/j.physb.2008.11.191.

[96] T. Tatsuki, S. Adachi, M. Itoh, T. Tamura, X. Wu, C. Jin, N. Koshizuka & K. Tanabe; "High-pressure synthesis of superconducting(Ca, K) 2CuO2C12;" **255**, pp. 61–64 (1995).

[97] I. Yamada, M. Azuma, Y. Shimakawa & M. Takano; "Single crystal growth of A-site deficient superconductor Ca2-xCuO2Cl2;" Phys. C Supercond. its Appl. **460-462 I**, pp. 420–421 (2007). doi:10.1016/j.physc.2007.03.106.

[98] J. M. Wallace & P. V. Hobbs; "Introduction and Overview;" in "Atmos. Sci.", pp. 1–23 (Elsevier) (2006); ISBN 9780127329512.

[99] V. Bisogni, L. Simonelli, L. J. P. Ament, F. Forte, M. Moretti Sala, M. Minola, S. Huotari, J. Van Den Brink, G. Ghiringhelli, N. B. Brookes & L. Braicovich; "Bimagnon studies in cuprates with resonant inelastic x-ray scattering at the O K edge. I. Assessment on La 2CuO 4 and comparison with the excitation at Cu L 3 and Cu K edges;" Phys. Rev. B - Condens. Matter Mater. Phys. **85**, pp. 1–9 (2012). doi:10.1103/PhysRevB.85.214527.

[100] M. Moretti Sala, V. Bisogni, C. Aruta, G. Balestrino, H. Berger, N. B. Brookes, G. M. De Luca, D. Di Castro, M. Grioni, M. Guarise, P. G. Medaglia, F. Miletto Granozio, M. Minola, P. Perna, M. Radovic, M. Salluzzo, T. Schmitt, K. J. Zhou, L. Braicovich & G. Ghiringhelli; "Energy and symmetry of dd excitations in undoped layered cuprates measured By Cu L3 resonant inelastic x-ray scattering;" New J. Phys. **13** (2011). doi:10.1088/1367-2630/13/4/043026.

[101] Y. Y. Peng, G. Dellea, M. Minola, M. Conni, A. Amorese, D. Di Castro, G. M. De Luca, K. Kummer, M. Salluzzo, X. Sun, X. J. Zhou, G. Balestrino, M. Le Tacon, B. Keimer, L. Braicovich, N. B. Brookes & G. Ghiringhelli; "Influence of apical oxygen on the extent of in-plane exchange interaction in cuprate superconductors;" Nat. Phys. (2017). doi:10.1038/nphys4248.

[102] C. Monney, V. Bisogni, K.-J. Zhou, R. Kraus, V. N. Strocov, G. Behr, J. Málek, R. Kuzian, S.-L. Drechsler, S. Johnston, A. Revcolevschi, B. Büchner, H. M. Rønnow, J. van den Brink, J. Geck & T. Schmitt; "Determining the Short-Range Spin Correlations in the Spin-Chain Li2CuO2 and CuGeO3 Compounds Using Resonant Inelastic X-Ray Scattering;" Phys. Rev. Lett. **110**, p. 87403 (2013). doi:10.1103/PhysRevLett.110.087403.

[103] K. B. Lyons, P. A. Fleury, J. P. Remeika, A. S. Cooper & T. J. Negran; "Dynamics of spin fluctuations in lanthanum cuprate;" Phys. Rev. B **37**, pp. 2353–2356 (1988). doi:10.1103/PhysRevB.37.2353.

[104] A. Q. R. Baron; "Introduction to High-Resolution Inelastic X-Ray Scattering;" arXiv: **1504.01098**, pp. [cond–mat.mtrl–sci] (2015).

[105] M. E. Weeks; "The discovery of the elements. I. Elements known to the ancient world;" J. Chem. Educ. **9**, pp. 4–10 (1932). doi:10.1021/ed009p4.

[106] B. W. Carroll & D. A. Ostlie; *An Introduction to Modern Astrophysics* (Pearson Addison-Wesley) (2007); ISBN 9780805304022; https://books.google.fr/books?id=M8wPAQAAMAAJ.

[107] D. J. Stevenson; "Planetary science: Mission to Earth's core — a modest proposal;" Nature **423**, pp. 239–240 (2003). doi:10.1038/423239a.

[108] L. Stixrude, R. E. Cohen & D. J. Singh; "Iron at high pressure: Linearized-augmented-plane-wave computations in the generalized-gradient approximation;" Phys. Rev. B **50**, pp. 6442–6445 (1994). doi:10.1103/PhysRevB.50.6442.

[109] L. Stixrude & R. E. Cohen; "Constraints on the crystalline structure of the inner core: Mechanical instability of BCC iron at high pressure;" Geophys. Res. Lett. **22**, pp. 125–128 (1995). doi:10.1029/94GL02742.

[110] L. Stixrude, E. Wasserman & R. E. Cohen; "Composition and temperature of Earth's inner core;" J. Geophys. Res. Solid Earth **102**, pp. 24729–24739 (1997). doi:10.1029/97JB02125.

[111] S. Tateno, K. Hirose, Y. Ohishi & Y. Tatsumi; "The Structure of Iron in Earth's Inner Core;" Science (80-.). **330**, pp. 359–361 (2010). doi:10.1126/science.1194662.

[112] R. Jeanloz; "The Nature of the Earth's Core;" Annu. Rev. Earth Planet. Sci. **18**, pp. 357–386 (1990). doi:10.1146/annurev.ea.18.050190.002041.

[113] T. Sakamaki, E. Ohtani, H. Fukui, S. Kamada, S. Takahashi, T. Sakairi, A. Takahata, T. Sakai, S. Tsutsui, D. Ishikawa, R. Shiraishi, Y. Seto, T. Tsuchiya & A. Q. R. Baron; "Constraints on Earth's inner core composition inferred from measurements of the sound velocity of hcp-iron in extreme conditions;" Sci. Adv. **2** (2016). doi:10.1126/sciadv.1500802.

[114] Y. Nakajima, S. Imada, K. Hirose, T. Komabayashi, H. Ozawa, S. Tateno, S. Tsutsui, Y. Kuwayama & A. Q. R. Baron; "Carbon-depleted outer core revealed by sound velocity measurements of liquid iron–carbon alloy;" **6**, p. 8942 (2015). doi:10.1038/ncomms9942.

[115] J. Badro, A. S. Côté & J. P. Brodholt; "A seismologically consistent compositional model of Earth's core;" Proc. Natl. Acad. Sci. **111**, pp. 7542–7545 (2014). doi:10.1073/pnas.1316708111.

[116] A. A. Yaroshevsky; "Abundances of chemical elements in the Earth's crust;" Geochemistry Int. **44**, pp. 48–55 (2006). doi:10.1134/S001670290601006X.

[117] D. Bancroft, E. L. Peterson & S. Minshall; "Polymorphism of iron at high pressure;" J. Appl. Phys. **27**, pp. 291–298 (1956). doi:10.1063/1.1722359.

[118] J. C. Jamieson & A. W. Lawson; "X-ray diffraction studies in the 100 kilobar pressure range;" J. Appl. Phys. **33**, pp. 776–780 (1962). doi:10.1063/1.1777167.

[119] H. K. Mao, W. A. Bassett & T. Takahashi; "Effect of pressure on crystal structure and lattice parameters of iron up to 300 kbar;" J. Appl. Phys. **38**, pp. 272–276 (1967). doi:10.1063/1.1708965.

[120] R. Clendenen & H. Drickamer; "The effect of pressure on the volume and lattice parameters of ruthenium and iron;" J. Phys. Chem. Solids **25**, pp. 865–868 (1964). doi:10.1016/0022-3697(64)90098-8.

[121] P. M. Giles & A. R. Marder; "The effect of composition on the pressure-induced HCP transformation in iron;" Metall. Trans. **2**, pp. 1371–1378 (1971). doi:10.1007/BF02913362.

[122] P. M. Giles, M. H. Longenbach & A. R. Marder; "High-Pressure α-ϵ Martensitic Transformation in Iron;" J. Appl. Phys. **42**, pp. 4290–4295 (1971). doi:10.1063/1.1659768.

[123] W. G. Burgers; "On the process of transition of the cubic-body-centered modification into the hexagonal-close-packed modification of zirconium;" Physica **1**, pp. 561–586 (1934). doi:10.1016/S0031-8914(34)80244-3.

[124] J. B. Liu & D. D. Johnson; "Bcc-to-hcp transformation pathways for iron versus hydrostatic pressure: Coupled shuffle and shear modes;" Phys. Rev. B - Condens. Matter Mater. Phys. **79**, pp. 1–9 (2009). doi:10.1103/PhysRevB.79.134113.

[125] K. J. Caspersen, A. Lew, M. Ortiz & E. A. Carter; "Importance of shear in the bcc-to-hcp transformation in iron;" Phys. Rev. Lett. **93**, pp. 1–4 (2004). doi:10.1103/PhysRevLett.93.115501.

[126] Y. Ma, E. Selvi, V. I. Levitas & J. Hashemi; "Effect of shear strain on the α–ϵ phase transition of iron: a new approach in the rotational diamond anvil cell;" J. Phys. Condens. Matter **18**, pp. S1075–S1082 (2006). doi:10.1088/0953-8984/18/25/S14.

[127] R. Boehler, N. von Bargen & A. Chopelas; "Melting, thermal expansion, and phase transition of iron at high pressures;" J. Geophys. Res. **95**, pp. 21731–21736 (1990). doi:10.1029/JB095iB13p21731.

[128] A. Dewaele, C. Denoual, S. Anzellini, F. Occelli, M. Mezouar, P. Cordier, S. Merkel, M. V??ron & E. Rausch; "Mechanism of the alpha-epislon Phase transformation in iron;" Phys. Rev. B - Condens. Matter Mater. Phys. **91**, pp. 1–8 (2015). doi:10.1103/PhysRevB.91.174105.

[129] P. Tolédano, H. Katzke & D. Machon; "Symmetry-induced collapse of ferromagnetism at the α–ϵ phase transition in iron;" J. Phys. Condens. Matter **22**, p. 466002 (2010). doi:10.1088/0953-8984/22/46/466002.

[130] N. Gunkelmann, E. M. Bringa, K. Kang, G. J. Ackland, C. J. Ruestes & H. M. Urbassek; "Polycrystalline iron under compression: Plasticity and phase transitions;" Phys. Rev. B - Condens. Matter Mater. Phys. **86**, pp. 1–11 (2012). doi:10.1103/PhysRevB.86.144111.

[131] B. Dupé, B. Amadon, Y. P. Pellegrini & C. Denoual; "Mechanism for the alpha-epsilon phase transition in iron;" (2013); arXiv:1301.1623v1.

[132] Z. Lu, W. Zhu, T. Lu & W. Wang; "Does the fcc phase exist in the Fe bcc–hcp transition? A conclusion from first-principles studies;" Model. Simul. Mater. Sci. Eng. **22**, p. 025007 (2014). doi:10.1088/0965-0393/22/2/025007.

[133] F. M. Wang & R. Ingalls; "Iron bcc-hcp transition: Local structure from x-ray-absorption fine structure;" Phys. Rev. B **57**, pp. 5647–5654 (1998). doi:10.1103/PhysRevB.57.5647.

[134] A. Dewaele, P. Loubeyre, F. Occelli, M. Mezouar, P. I. Dorogokupets & M. Torrent; "Quasihydrostatic equation of state of Iron above 2 Mbar;" Phys. Rev. Lett. **97**, pp. 29–32 (2006). doi:10.1103/PhysRevLett.97.215504.

[135] A. Dewaele & G. Garbarino; "Low temperature equation of state of iron;" Appl. Phys. Lett. **111**, pp. 2–6 (2017). doi:10.1063/1.4989688.

[136] N. Ishimatsu, Y. Sata, H. Maruyama, T. Watanuki, N. Kawamura, M. Mizumaki, T. Irifune & H. Sumiya; "α-ϵ transition pathway of iron under quasihydrostatic pressure conditions;" Phys. Rev. B **90**, p. 014422 (2014). doi:10.1103/PhysRevB.90.014422.

[137] S. Merkel; "Raman Spectroscopy of Iron to 152 Gigapascals: Implications for Earth's Inner Core;" Science (80-.). **288**, pp. 1626–1629 (2000). doi:10.1126/science.288.5471.1626.

[138] A. P. Jephcoat, H. K. Mao & P. M. Bell; "Static Compression of Iron to 78 GPa With Rare Gas Solids as Pressure-Transmitting Media;" J. Geophys. Res. **91**, pp. 4677–4684 (1986). doi:10.1029/JB091iB05p04677.

[139] C. S. Yoo, P. Söderlind, J. A. Moriarty & A. J. Cambell; "dhcp as a possible new epsilon' phase of iron at high pressures and temperatures;" Phys. Lett. A **214**, pp. 65–70 (1996). doi:https://doi.org/10.1016/0375-9601(96)00160-0.

[140] S. K. Saxena, G. Shen & P. Lazor; "Experimental Evidence for a New Iron Phase and Implications for Earth's Core." Science **260**, pp. 1312–1314 (1993). doi:10.1126/science.260.5112.1312.

[141] S. K. Saxena, L. S. Dubrovinsky, P. Häggkvist, Y. Cerenius, G. Shen & H. K. Mao; "Synchrotron X-ray Study of Iron at High Pressure and Temperature." Science **269**, pp. 1703–1704 (1995). doi:10.1126/science.269.5231.1703.

[142] M. Ross, D. A. Young & R. Grover; "Theory of the iron phase diagram at Earth core conditions;" J. Geophys. Res. Solid Earth **95**, pp. 21713–21716 (1990). doi:10.1029/JB095iB13p21713.

[143] R. Boehler; "Temperatures in the Earth's core from melting-point measurements of iron at high static pressures;" Nature **363**, pp. 534–536 (1993). http://dx.doi.org/10.1038/363534a0.

[144] J.-P. Rueff, M. Mezouar & M. Acet; "Short-range magnetic collapse of Fe under high pressure at high temperatures observed using x-ray emission spectroscopy;" Phys. Rev. B **78**, p. 100405 (2008). doi:10.1103/PhysRevB.78.100405.

[145] M. V. You, V. Heine, A. J. Holden & P. J. Lin-Chung; "Magnetism in Iron at High Temperatures;" Phys. Rev. Lett. **44**, pp. 1282–1284 (1980). doi:10.1103/PhysRevLett.44.1282.

[146] H. Hasegawa; "Finite-temperature surface properties of itinerant-electron ferromagnets;" J. Phys. F Met. Phys. **16**, pp. 347–364 (1986). doi:10.1088/0305-4608/16/3/013.

[147] Y. Tsunoda; "Spin-density wave in cubic γ-Fe and γ-Fe 100-x Co x precipitates in Cu;" J. Phys. Condens. Matter **1**, pp. 10427–10438 (1989). doi:10.1088/0953-8984/1/51/015.

[148] O. Mathon, F. Baudelet, J. P. Itié, A. Polian, M. D'Astuto, J. C. Chervin & S. Pascarelli; "Dynamics of the Magnetic and Structural alpha-epsilon Phase Transition in Iron;" Phys. Rev. Lett. **93**, p. 255503 (2004). doi:10.1103/PhysRevLett.93.255503.

[149] S. Klotz & M. Braden; "Phonon dispersion of bcc iron to 10 GPa;" Phys. Rev. Lett. **85**, pp. 3209–3212 (2000). doi:10.1103/PhysRevLett.85.3209.

[150] A. Monza, A. Meffre, F. Baudelet, J. P. Rueff, M. D'Astuto, P. Munsch, S. Huotari, S. Lachaize, B. Chaudret & A. Shukla; "Iron under pressure: "Kohn Tweezers" and remnant magnetism;" Phys. Rev. Lett. **106**, pp. 1–4 (2011). doi:10.1103/PhysRevLett.106.247201.

[151] G. Cort, R. D. Taylor & J. O. Willis; "Search for magnetism in hcp ϵ-Fe;" J. Appl. Phys. **53**, pp. 2064–2065 (1982). doi:10.1063/1.330745.

[152] E. Wohlfarth; "The possibility that epsilon-Fe is a low temperature superconductor;" (1979).

[153] K. Shimizu, T. Kimura, S. Furomoto, K. Takeda, K. Kontani, Y. Onuki & K. Amaya; "Superconductivity in the non-magnetic state of iron under pressure." Nature **412**, pp. 316–318 (2001). doi:10.1038/35085536.

[154] D. Jaccard, A. T. Holmes, G. Behr, Y. Inada & Y. Onuki; "Superconductivity of ϵ-Fe: Complete resistive transition;" Phys. Lett. Sect. A Gen. At. Solid State Phys. **299**, pp. 282–286 (2002). doi:10.1016/S0375-9601(02)00725-9.

[155] I. I. Mazin, D. A. Papaconstantopoulos & M. J. Mehl; "Superconductivity in compressed iron: Role of spin fluctuations;" Phys. Rev. B **65**, p. 100511 (2002). doi:10.1103/PhysRevB.65.100511.

[156] S. Bose, O. Dolgov, J. Kortus, O. Jepsen & O. Andersen; "Pressure dependence of electron-phonon coupling and superconductivity in hcp Fe: A linear response study;" Phys. Rev. B **67**, p. 214518 (2003). doi:10.1103/PhysRevB.67.214518.

[157] L. V. Pourovskii, J. Mravlje, M. Ferrero, O. Parcollet & I. A. Abrikosov; "Impact of electronic correlations on the equation of state and transport in ϵ -Fe;" Phys. Rev. B - Condens. Matter Mater. Phys. **90**, pp. 1–6 (2014). doi:10.1103/PhysRevB.90.155120.

[158] a. T. Holmes, D. Jaccard, G. Behr, Y. Inada & Y. Onuki; "Unconventional superconductivity and non-Fermi liquid behaviour of -iron at high pressure;" J. Phys. Condens. Matter **16**, pp. S1121–S1127 (2004). doi:10.1088/0953-8984/16/14/021.

[159] A. B. Papandrew, M. S. Lucas, R. Stevens, I. Halevy, B. Fultz, M. Y. Hu, P. Chow, R. E. Cohen & M. Somayazulu; "Absence of magnetism in hcp iron-nickel at 11 K;" Phys. Rev. Lett. **97**, pp. 2–5 (2006). doi:10.1103/PhysRevLett.97.087202.

[160] a. F. Goncharov & V. V. Struzhkin; "Raman spectroscopy of metals, high-temperature superconductors and related materials under high pressure;" J. Raman Spectrosc. **34**, pp. 532–548 (2003). doi:10.1002/jrs.1030.

[161] P. Pedrazzini, D. Jaccard, G. Lapertot, J. Flouquet, Y. Inada, H. Kohara & Y. Onuki; "Probing the extended non-Fermi liquid regimes of MnSi and Fe;" Phys. B Condens. Matter **378-380**, pp. 165–166 (2006). doi:10.1016/j.physb.2006.01.062.

[162] C. S. Yadav, G. Seyfarth, P. Pedrazzini, H. Wilhelm, R. Černý & D. Jaccard; "Effect of pressure cycling on iron: Signatures of an electronic instability and unconventional superconductivity;" Phys. Rev. B - Condens. Matter Mater. Phys. **88**, pp. 1–7 (2013). doi:10.1103/PhysRevB.88.054110.

[163] T. H. Lin, W. Y. Dong, K. J. Dunn, C. N. Wagner & F. P. Bundy; "Pressure-induced superconductivity in high-pressure phases of Si;" Phys. Rev. B **33**, pp. 7820–7822 (1986). doi:10.1103/PhysRevB.33.7820.

[164] K. J. Chang, M. M. Dacorogna, M. L. Cohen, J. M. Mignot, G. Chouteau & G. Martinez; "Superconductivity in high-pressure metallic phases of Si;" Phys. Rev. Lett. **54**, pp. 2375–2378 (1985). doi:10.1103/PhysRevLett.54.2375.

[165] S. Margadonna, Y. Takabayashi, M. T. McDonald, K. Kasperkiewicz, Y. Mizuguchi, Y. Takano, A. N. Fitch, E. Suard & K. Prassides; "Crystal structure of the new FeSe(1-x) superconductor." Chem. Commun. (Camb). pp. 5607–5609 (2008). doi:10.1039/b813076k.

[166] F.-C. Hsu, J.-Y. Luo, K.-W. Yeh, T.-K. Chen, T.-W. Huang, P. M. Wu, Y.-C. Lee, Y.-L. Huang, Y.-Y. Chu, D.-C. Yan & M.-K. Wu; "Superconductivity in the PbO-type structure α-FeSe;" Proc. Natl. Acad. Sci. **105**, pp. 14262–14264 (2008). doi:10.1073/pnas.0807325105.

[167] S. Margadonna, Y. Takabayashi, Y. Ohishi, Y. Mizuguchi, Y. Takano, T. Kagayama, T. Nakagawa, M. Takata & K. Prassides; "Pressure evolution of the low-temperature crystal structure and bonding of the superconductor FeSe (Tc =37 K);" Phys. Rev. B - Condens. Matter Mater. Phys. **80**, pp. 1–6 (2009). doi:10.1103/PhysRevB.80.064506.

[168] S. He, J. He, W. Zhang, L. Zhao, D. Liu, X. Liu, D. Mou, Y.-B. Ou, Q.-Y. Wang, Z. Li, L. Wang, Y. Peng, Y. Liu, C. Chen, L. Yu, G. Liu, X. Dong, J. Zhang, C. Chen, Z. Xu, X. Chen, X. Ma, Q. Xue & X. J. Zhou; "Phase diagram and electronic indication of high-temperature superconductivity at 65 K in single-layer FeSe films;" Nat. Mater. **12**, p. 605 (2013). doi:10.1038/nmat3648.

[169] J.-F. Ge, Z.-L. Liu, C. Liu, C.-L. Gao, D. Qian, Q.-K. Xue, Y. Liu & J.-F. Jia; "Superconductivity above 100 K in single-layer FeSe films on doped SrTiO3;" Nat. Mater. **14**, p. 285 (2014). doi:10.1038/nmat4153.

[170] S.-H. Baek, D. V. Efremov, J. M. Ok, J. S. Kim, J. van den Brink & B. Büchner; "Orbital-driven nematicity in FeSe;" Nat. Mater. **14**, pp. 210–214 (2014). doi:10.1038/nmat4138.

[171] P. Massat, D. Farina, I. Paul, S. Karlsson, P. Strobel, P. Toulemonde, M.-A. Méasson, M. Cazayous, A. Sacuto, S. Kasahara, T. Shibauchi, Y. Matsuda & Y. Gallais; "Charge-induced nematicity in FeSe;" Proc. Natl. Acad. Sci. **113**, pp. 9177–9181 (2016). doi:10.1073/pnas.1606562113.

[172] J. K. Glasbrenner, I. I. Mazin, H. O. Jeschke, P. J. Hirschfeld & R. Valentí; "Effect of magnetic frustration on nematicity and superconductivity in Fe chalcogenides;" **11** (2015). doi:10.1038/nphys3434.

[173] M. Bendele, A. Amato, K. Conder, M. Elender, H. Keller, H. H. Klauss, H. Luetkens, E. Pomjakushina, A. Raselli & R. Khasanov; "Pressure induced static magnetic order in superconducting FeSe1-x;" Phys. Rev. Lett. **104**, pp. 1–4 (2010). doi:10.1103/PhysRevLett.104.087003.

[174] M. Bendele, A. Ichsanow, Y. Pashkevich, L. Keller, T. Strässle, A. Gusev, E. Pomjakushina, K. Conder, R. Khasanov & H. Keller; "Coexistence of superconductivity and magnetism in FeSe 1-x under pressure;" Phys. Rev. B - Condens. Matter Mater. Phys. **85**, pp. 1–11 (2012). doi:10.1103/PhysRevB.85.064517.

[175] R. Khasanov, Z. Guguchia, A. Amato, E. Morenzoni, X. Dong, F. Zhou & Z. Zhao; "Pressure-induced magnetic order in FeSe: A muon spin rotation study;" Phys. Rev. B **95**, pp. 1–5 (2017). doi:10.1103/PhysRevB.95.180504.

[176] J. P. Sun, K. Matsuura, G. Z. Ye, Y. Mizukami, M. Shimozawa, K. Matsubayashi, M. Yamashita, T. Watashige, S. Kasahara, Y. Matsuda, J. Q. Yan, B. C. Sales, Y. Uwatoko, J. G. Cheng & T. Shibauchi; "Dome-shaped magnetic order competing with high-temperature superconductivity at high pressures in FeSe;" Nat. Commun. **7**, p. 12146 (2016). doi:10.1038/ncomms12146.

[177] T. Terashima, N. Kikugawa, A. Kiswandhi, D. Graf, E. S. Choi, J. S. Brooks, S. Kasahara, T. Watashige, Y. Matsuda, T. Shibauchi, T. Wolf, A. E. Böhmer, F. Hardy, C. Meingast, H. V. Löhneysen & S. Uji; "Fermi surface reconstruction in FeSe under high pressure;" Phys. Rev. B **93** (2016). doi:10.1103/PhysRevB.93.094505.

[178] R. S. Kumar, Y. Zhang, Y. Xiao, J. Baker, A. Cornelius, S. Veeramalai, P. Chow, C. Chen & Y. Zhao; "Pressure induced high spin-low spin transition in FeSe superconductor studied by x-ray emission spectroscopy and ab initio calculations;" Appl. Phys. Lett. **99**, pp. 6–9 (2011). doi:10.1063/1.3621859.

[179] J. M. Chen, S. C. Haw, J. M. Lee, T. L. Chou, S. A. Chen, K. T. Lu, Y. C. Liang, Y. C. Lee, N. Hiraoka, H. Ishii, K. D. Tsuei, E. Huang & T. J. Yang; "Pressure dependence of the electronic structure and spin state in Fe 1.01Se superconductors probed by x-ray absorption and x-ray emission spectroscopy;" Phys. Rev. B - Condens. Matter Mater. Phys. **84**, pp. 1–6 (2011). doi:10.1103/PhysRevB.84.125117.

[180] S. Medvedev, T. M. McQueen, I. A. Troyan, T. Palasyuk, M. I. Eremets, R. J. Cava, S. Naghavi, F. Casper, V. Ksenofontov, G. Wortmann & C. Felser; "Electronic and magnetic phase diagram of β-Fe1.01Se with superconductivity at 36.7 K under pressure;" Nat. Mater. **8**, pp. 630–633 (2009). doi:10.1038/nmat2491.

[181] L. Simonelli, T. Mizokawa, M. M. Sala, H. Takeya, Y. Mizuguchi, Y. Takano, G. Garbarino, G. Monaco & N. L. Saini; "Temperature dependence of iron local magnetic moment in phase-separated superconducting chalcogenide;" Phys. Rev. B **90**, p. 214516 (2014). doi:10.1103/PhysRevB.90.214516.

[182] L. de' Medici, G. Giovannetti & M. Capone; "Selective Mott Physics as a Key to Iron Superconductors;" Phys. Rev. Lett. **112**, p. 177001 (2014). doi:10.1103/PhysRevLett.112.177001.

[183] J. P. Sun, G. Z. Ye, P. Shahi, J. Q. Yan, K. Matsuura, H. Kontani, G. M. Zhang, Q. Zhou, B. C. Sales, T. Shibauchi, Y. Uwatoko, D. J. Singh & J. G. Cheng; "High- Tc Superconductivity in FeSe at High Pressure: Dominant Hole Carriers and Enhanced Spin Fluctuations;" Phys. Rev. Lett. **118**, pp. 1–6 (2017). doi:10.1103/PhysRevLett.118.147004.

[184] D. S. Parker; "Strong 3D and 1D magnetism in hexagonal Fe-chalcogenides FeS and FeSe vs. weak magnetism in hexagonal FeTe;" Sci. Rep. **7**, p. 3388 (2017). doi:10.1038/s41598-017-03502-5.

[185] R. Yu, Q. Liu, S. Zhang, X. Wang, W. Han & C. Jin; "High-pressure growth of Ca2-xNaxCuO2Cl2 single crystals and pressure effect on superconductivity;" Phys. C Supercond. **478**, pp. 29–31 (2012). doi:10.1016/j.physc.2012.03.028.

[186] S. Klotz, T. Strässle, B. Lebert, M. D'Astuto & T. Hansen; "High pressure neutron diffraction to beyond 20 GPa and below 1.8 K using Paris-Edinburgh load frames;" High Press. Res. **36**, pp. 73–78 (2016). doi:10.1080/08957959.2015.1136624.

Blair LEBERT **26 janvier 2018**

Sujet : Propriétés magnétiques des supraconducteurs non conventionnels epsilon-Fe, FeSe, et $Ca_2CuO_2Cl_2$ étudiés par diffusion des rayons X et des neutrons

Résumé : La proximité omniprésente de l'ordre magnétique et supraconducteur dans les supraconducteurs non conventionnels implique l'importance de comprendre le magnétisme dans ces matériaux. Dans ce contexte, cette thèse porte sur l'étude du magnétisme dans trois supraconducteurs non conventionnels. Les excitations magnétiques dans le système d'oxychlorure de cuivre de l'élément léger $Ca_2CuO_2Cl_2$ ont été étudiées en fonction du dopage et de la température en utilisant principalement la diffusion inélastique résonante aux rayons X. L'effet de la pression sur le magnétisme dans ϵ-fer et le β-FeSe a été étudié en utilisant la spectroscopie d'émission des rayons X et la diffraction des neutrons sur poudre.

Mots clés : magnétisme, supraconductivité, Ca2CuO2Cl2, epsilon-fer, FeSe

Subject :Magnetic properties of the unconventional superconductors epsilon-Fe, FeSe and $Ca_2CuO_2Cl_2$ investigated by x-ray and neutron scattering

Abstract: The ubiquitous proximity of magnetic and superconducting order in unconventional superconductors implies the importance of understanding magnetism in these materials. In this context, this thesis concerns the study of magnetism in three unconventional superconductors. The magnetic excitations in the light element copper oxychloride system $Ca_2CuO_2Cl_2$ were studied as a function of doping and temperature using primarily resonant inelastic x-ray scattering. The effect of pressure on magnetism in ϵ-iron and β-FeSe was studied using x-ray emission spectroscopy and neutron powder diffraction.

Keywords : magnetism, superconductivity, Ca2CuO2Cl2, epsilon-iron, FeSe